Investigating Nonequilibrium Ionization and Recombination Processes in Solar Wind and Transient Plasma

by

Yeimy J. Rivera

A dissertation submitted in partial fulfillment
of the requirements for the degree of
Doctor of Philosophy
(Climate and Space Sciences and Engineering)
in The University of Michigan
2020

Doctoral Committee:

Professor Enrico Landi, Co-Chair
Professor Susan T. Lepri, Co-Chair
Professor Nuria Calvet
Research Scientist Jason A. Gilbert
Professor Justin C. Kasper
Research Scientist Jim Raines

Yeimy J. Rivera

yrivera@umich.edu

ORCID iD: 0000-0002-8748-2123

© Yeimy Rivera 2020

This thesis is dedicated to everyone that has been a part of this journey.

ACKNOWLEDGEMENTS

This thesis is the product of several years of confusion of which all came together at the end. This journey would have not been as successful without the thoughtful guidance and support of my PhD advisors, Enrico Landi and Susan Lepri.

I would like to thank Jim Raines for the valuable mentoring sessions that helped shape my scientific interests and my future career. Also, Justin Kasper which opened my eyes to the complexity of solar wind during his plasma physics course which inspired my postdoctoral research.

In addition, I attribute my fundamental understanding of space physics to Xianzhe Jia and Shasha Zou. Their dedication to teaching and support of students in the department had a fundamental effect to the rest of my PhD research.

I would like to thank my previous advisor, Cristina Cadavid, for her support, advice, and motivation early in my career that paved the way to where I am now.

A very special 'thank you' to my CLaSP colleagues which have provided constant support in all aspects of my PhD life (and hopefully I have returned the favor). Abby Azari has been incredibly inspirational through the growing pains of figuring it all out. Samantha Basile has been kind and supportive in all matters of self-care.

In addition, I have forged life-long friendships at CLaSP from our mutual PhD struggle. Camilla Harris has been an incredibly supportive friend and a colleague that I have always admired. However, what I appreciated the most was that she constantly humored me for the numerous times I have snuck up on her in the office. Doğa Can Su Öztürk helped me navigate my first two years at CLaSP by listening to 'the woes of a newbie doctoral student which had no idea of what was to come'. Ryan Dewey has proved to be an exceptional drinking companion and a scientist I aspire to. Ben Alterman has been incredibly influential to building confidence in my abilities as a scientist.

I wholeheartedly thank the departmental staff which were instrumental in navigating my entire PhD experience: Sandy Pytlinski, Elaine Meinzer, Claire Miller, EJ Olsen, Lindsay Coleman, Debby Eddy. Also, the IT staff which saved me from destroying my work countless times: Faye Ogasawara, Darren Britten-Bozzone, and Bryan White.

I would like to thank everyone at the High Altitude Observatory in Boulder, CO which have been an incredibly kind and supportive group of friends and colleagues; Steve Tomczyk, Scott McIntosh, Paul Bryans, Ian Hewins, Sheryl Shapiro, Alice Lecinski.

Lastly, despite the numerous times I have failed throughout my life, my mother has always been a positive light in my life. It is fair to say that this thesis would have not been possible without the encouragement and love from my mother, sister, and boyfriend. A sincere 'thank you' to my family for their unwavering support and confidence that I could get to where I wanted.

TABLE OF CONTENTS

CHAPTER

LIST OF FIGURES

Figure

LIST OF TABLES

Table

ABSTRACT

In this work, I investigated the evolution of coronal mass ejections (CMEs) and the solar wind by combining remote sensing, in situ observations, and nonequilibrium ionization modeling using the Michigan Ionization Code (MIC). The work investigates physical processes governing the plasma's radial evolution and the injection of energy to the system. The aim of this thesis is to investigate low ionized charge states in CMEs and He^+ in the solar wind to understand their origin and formation.

Through simulations of charge states with the MIC, the modeling work reconstructed the thermodynamic evolution of several plasma structures within the expansion of a coronal mass ejection (CME) by examining heliospheric ion composition within the ejecta. The reconstructed CME contained rare, low charge states, which are often absent within CMEs, along with typical highly ionized coronal plasma. Modeling results show that the source of the low ionized material in the CME measurements is from prominence material and is not a result of recombination from cooling of the plasma. However, part of the prominence also exists in a highly ionized form. These results provide important constraints to the evolution of prominence material that is often observed at the Sun but rarely measured in situ.

In addition, this study indicated the CME components experienced rapid, continuous, and non-uniform heating as they travelled away from the Sun. Motivated by these results, I identified useful spectral lines to study the eruption with future solar telescopes. This study investigated the diagnostic potential of several spectral lines spanning the EUV to near-Infrared and ranging between chromospheric and sub-flare

temperatures to enable a comprehensive examination of solar eruptions that can be coupled with in situ and nonequilibrium modeling. I present a list of recommended spectral lines along with a discussion of their diagnostic capability. Results show that several of the most observable lines will be within the planned observations of future solar telescopes; Daniel K. Inouye Solar Telescope (DKIST), and Upgraded COronal Multi-channel Polarimeter (UCoMP), and instruments on Solar Orbiter, e.g. Spectral Imaging of the Coronal Environment (SPICE) and Multi-Element Telescope for Imaging and Spectroscopy (METIS).

Furthermore, I investigated the presence of singly ionized He in the solar wind, that are outside of CME cores and pick up ions, to determine their origin and formation mechanism using the MIC. Current ionization models of the solar wind cannot account for the enhanced density of He^+ observed at 1AU, therefore we reconcile the additional He^+ through charge exchange of solar wind alphas and outgassed interplanetary dust neutrals. We find that charge exchange processes can be an important mechanism in the formation of solar He^+ from alpha particles below $10 - 15R_\odot$, and due to this, may potentially shape ion densities for other species in the solar wind as well.

CHAPTER I

Introduction

1.1 The Sun and Heliosphere

1.1.1 Internal Structure of the Sun

The Sun is a G-type main sequence star mid way through its stellar lifespan as predicted by the Hertzsprung-Russell diagram (Strömgren et al., 1933). Its internal structure is comprised of a rigidly rotating core undergoing nuclear fusion, surrounded by a radiative zone, that is encompassed by a convective zone, as shown in Figure 1.1[1] (Eddington, 1920). Energy production at the core is governed by Hydrogen fusion reactions dominated by the proton-proton chain, making up 98.3% of the energy, while the Carbon-Nitrogen-Oxygen reactions supplies the remaining amount. The energy from the core is then transported through the radiative region of the Sun, in the form of radiation, which is separated from the convection zone by the tachocline boundary (Weizsäcker, 1935; Bethe & Critchfield, 1938). The tachocline is a layer where the main energy transport mechanism shifts between radiation to convection. In the convective zone, the hot, dense plasma is transported from deep in the Sun towards the surface where is cools and descends back down.

---

[1] `https://commons.wikimedia.org/wiki/File:The_solar_interior.svg`

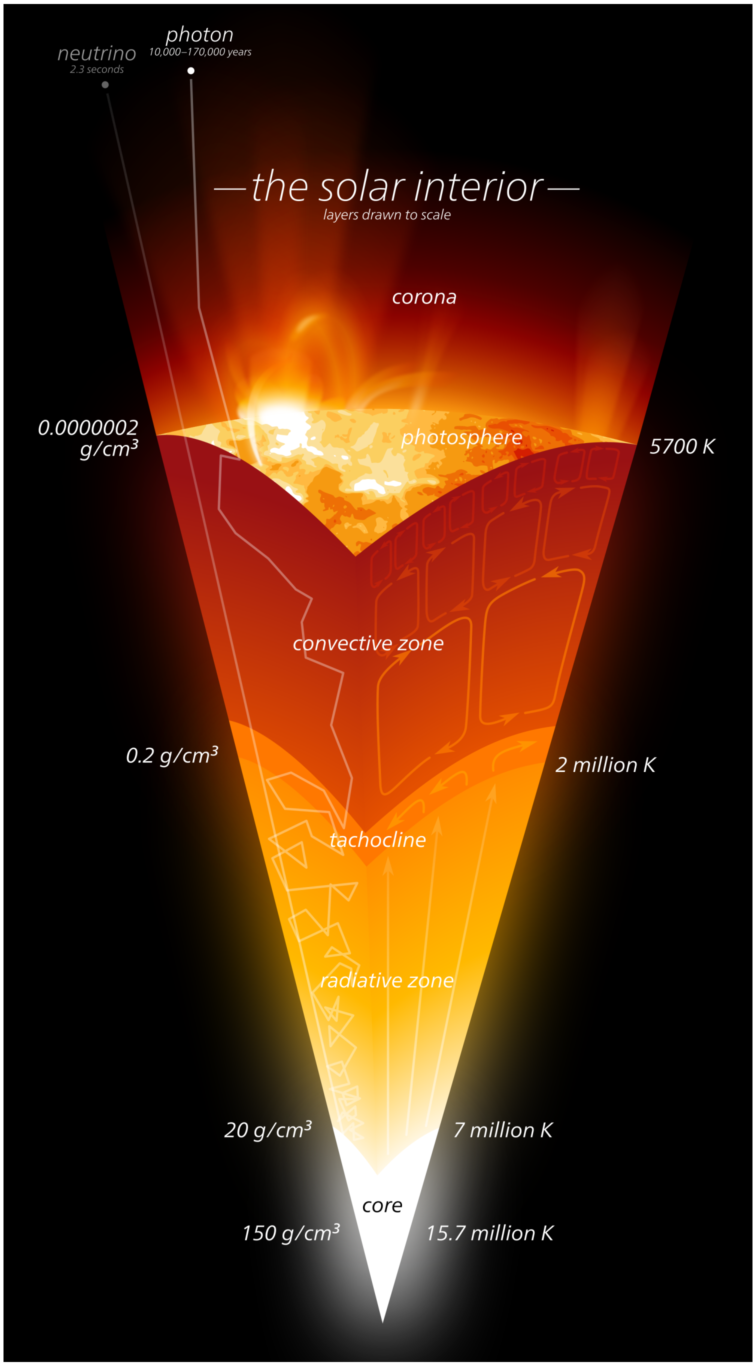

Figure 1.1: An illustration of the solar interior of the Sun from Wikipedia Commons.

1.1.2 The Surface and Structures at the Sun

At the outer edge of the convective zone, where the opacity of the Sun shifts from optically thick to optically thin, defines the beginning of the solar surface called the photosphere. The photosphere appears as the first visible layer of the Sun and is characterized by a temperature of approximately 5770K. The convection below the surface appear as multiscale granular structures churning on the surface.

Up to this point, the temperature and density radially decrease from the center of the Sun. However, above the photosphere, in the chromosphere, marks the beginning of an unexpected rise in temperature. Between the chromosphere and the solar corona is known as the transition region where plasma undergoes a sharp temperature and density gradient as the temperature rises while the density descends rapidly. This region is shown on the left plot of Figure 1.2 where the solid line represents the temperature and the dashed line is the density with increasing distance above the photosphere on the vertical axis. Above the transition region is a tenuous and hot atmosphere, known as the corona, and outward propagating solar wind.

The plasma beta, β, is a useful quantity for insight to the governing processes within the rapidly changing regions described. The plasma β is defined as the ratio of the thermal to magnetic pressure of the plasma as,

$$\beta = \frac{P_{thermal}}{P_{magnetic}} = \frac{nk_BT}{B^2/2\mu_0}, \tag{1.1}$$

where P is the thermal and magnetic pressure, n is the number density, k_B is the Boltzmann constant, T is the plasma temperature, B is the magnetic field magnitude, and μ_0 is permeability of free space. In the case where the plasma $\beta > 1$, this indicates that magnetic field lines are dragged along with the plasma flow while a $\beta < 1$ indicates the plasma is dominated by the magnetic field. As shown on the right plot of Figure 1.2, $\beta > 1$ below the photosphere, however this values shifts from a plasma to a magnetically dominated regime between the photosphere and outer corona, and transitions back above 1 in the outer corona (Gary, 2001; Bourdin, 2017).

The plasma β governs the structure of the global magnetic field at the different so-

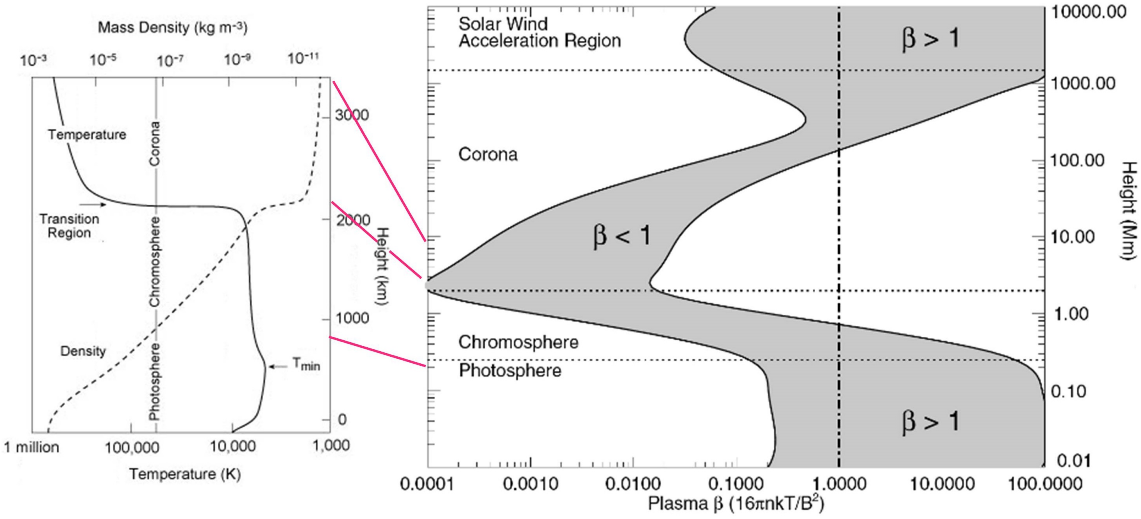

Figure 1.2: Temperature and density and plasma beta, β, with increasing height above the photosphere, taken from Gary (2001).

lar boundaries. The Sun's magnetic field is generated deep inside the Sun and extends the entire heliosphere. At the convection zone, where plasma $\beta > 1$, the magnetic field flows with the motion of the plasma which can breach the surface creating a network of multi-scale loops and different structures far into the corona and interplanetary medium. Figure 1.3 is a cartoon picture that illustrates the magnetic field topology of different solar structures as the plasma β changes along the vertical axis between the photopshere and the corona. There are regions of *open* and *closed* field that form. Coronal holes are typically regions of weak, open magnetic field, shown in black. Coronal helmet streamers are unipolar structures that form as elongated loops, dragged out by emanating solar wind, often extending several solar radii from the surface, as shown in green. Pseudostreamers contain multipolar regions at the base and stretch out similarly to helmet streamers, shown in blue. In addition, complex, twisted magnetic field structures can form which are often sites of large scale reconnection and plasma release, as will be further discussed.

Plasma is constantly released from the Sun as part of the solar wind, as well as through large scale eruptions called coronal mass ejections (CMEs). Solar plasma engulfs the entire solar system, as illustrated in Figure 1.4[2]. The termination shock is the boundary where solar particles decelerate to below the sound speed, all of which is encompassed by the heliosphere. The heliopase denotes the main separation between material from the Sun and the local interstellar medium. Moreover, solar and Heliospheric science is not only the study of solar material itself, but also the interaction between the Sun and objects in the heliosphere, such as planets, comets, interplanetary dust, and interstellar material that penetrates the heliosphere. Observations of these interactions have been key to the progress in our understanding of the Sun.

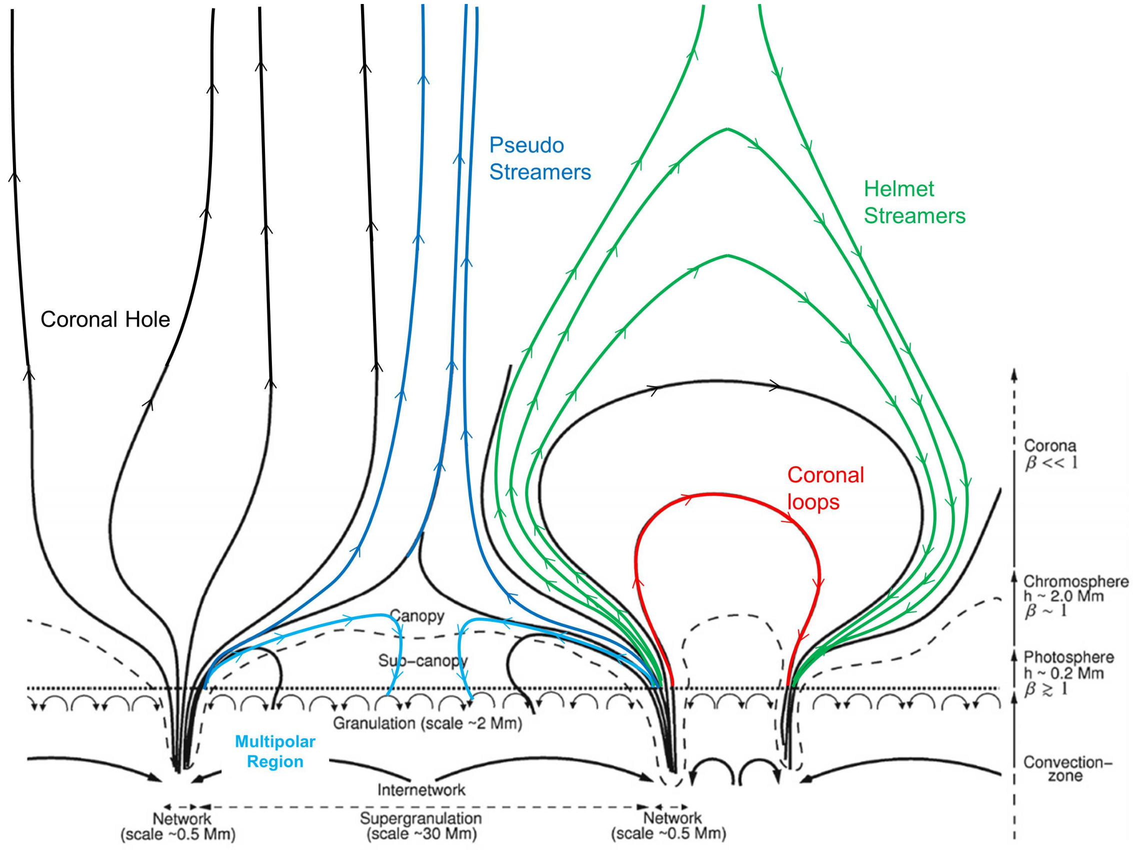

Figure 1.3: Open and closed magnetic field structures at the solar surface. Adapted from Wiegelmann et al. (2014).

---

[2] https://photojournal.jpl.nasa.gov/catalog/PIA22835

1.2 Early History of the Solar Wind and Coronal Mass Ejections

For millennia, humanity has been fascinated with the motion of the celestial sky. Many cultures, like the Babylonians, Egyptians, and Greeks, associated the Sun, moon, comets, planets, and stars with deities and gods. The celestial bodies have not only provided a sense of wonderment and curiosity but also a method of tracking time and the passage of seasons. For example, the Mayan culture monitored the Sun to develop a sophisticated solar calendar. Studies of the movement of the Sun and planets gave way to the exploration of our solar system and to the field of solar and heliospheric physics. Throughout this time, there have been crucial discoveries that have led to our current understanding of the Sun and the solar system.

1.2.1 Key Observations Which Have Led to the Present Model of the Sun

The darkness of space was long thought to be an empty vacuum; however, some of the first evidence that the Sun was ejecting material and what, ultimately, led to the discovery of the solar wind was through observations of comets in the 19th and 20th century (see Festou et al. 1993 for details of comet history). Comets are composed of a main body and surrounding atmosphere, known as the nucleus and coma, respectively. While traveling in the heliosphere, the mixture of frozen gasses and dust that make up the nucleus begins to vaporize and ionize as it approaches the Sun, forming the coma. The material lost from the coma forms the comet's distinctive dust tail, trailing the comet along its trajectory, and an ion tail, pointed in the antisolar direction, as shown in Figure 1.5. The direction of the tails was an indication that the comet was immersed in a flow of radiation, while their distinctive shape indicated that each were under the influenced of different forces; the dust tail formed through radiation

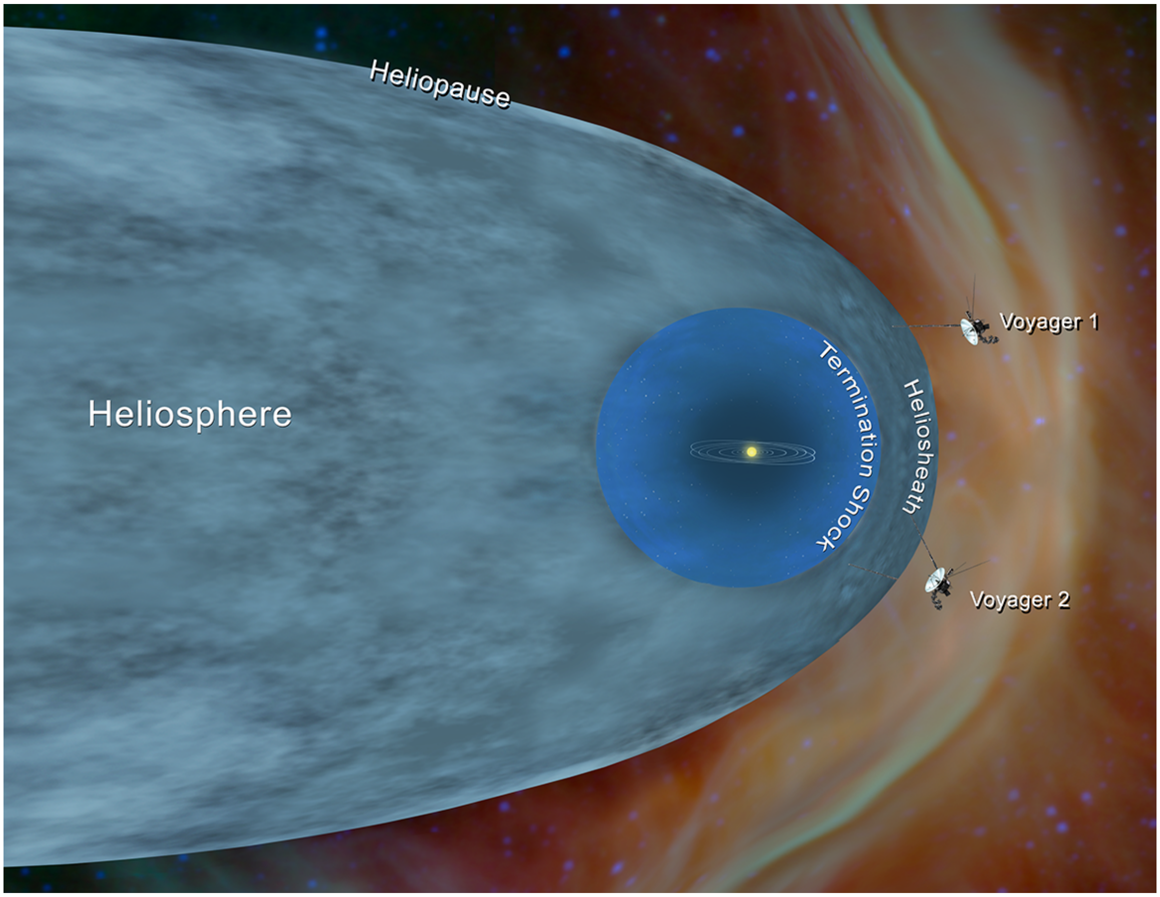

Figure 1.4: The heliosphere includes the bubble within the heliopause, where the heliopause is a boundary that separates solar from interstellar material. Image credit: NASA/JPL.

pressure, and the ion tail shaped by local electromagnetic forces. This additional force would later be understood as the Lorentz force arising from the interplanetary electromagnetic field carried by the solar wind. Comet tails prompted scientists to hypothesize that the Sun was constantly releasing particles, which they referred to as 'solar corpuscular radiation', along with the observed sunlight, which became the basis of what we now know as the solar wind (Hoffmeister, 1944; Biermann, 1951).

Simultaneously, magnetic disturbances at the Earth had long indicated a solar-terrestrial connection. A strong indication of a correlation between solar and geomagnetic activity began with the discovery of the solar sunspot cycle (Sabine, 1852; Wolf, 1852). Sunspots, appearing as dark spots on the solar disk in white light, have

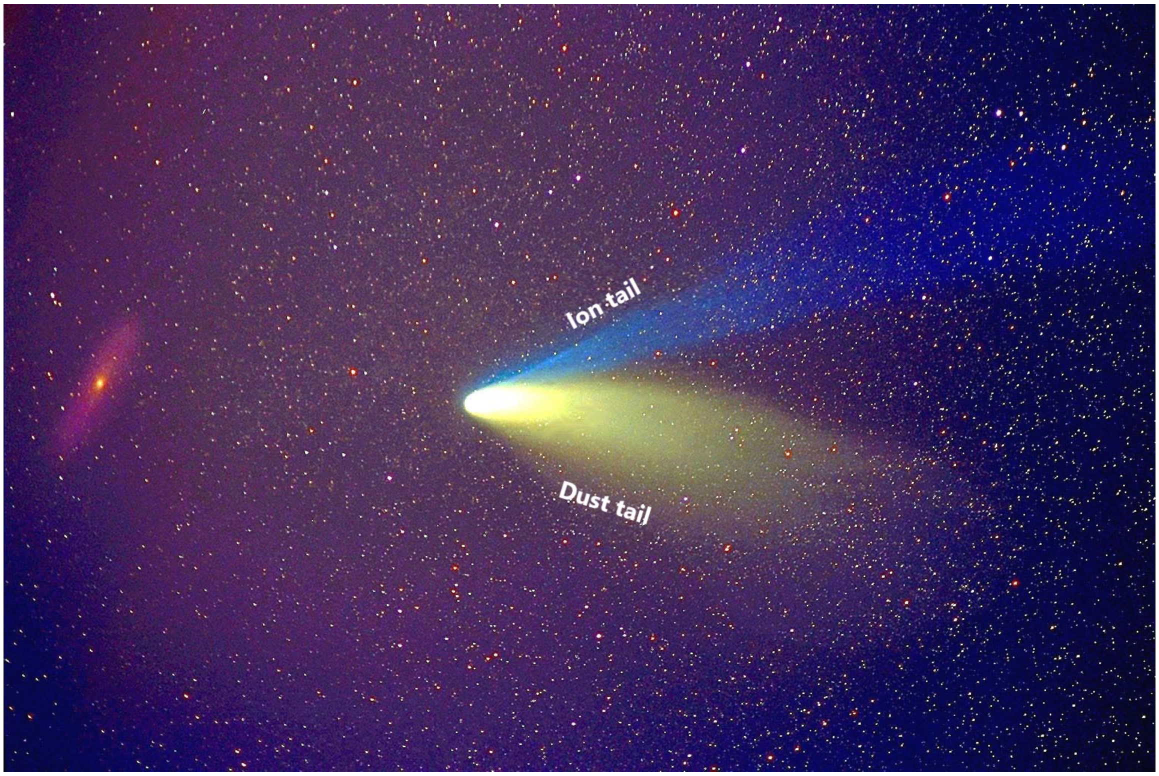

Figure 1.5: Comet Hale Bopp adapted from the Astronomy Picture of the Day on August 13, 2006.

been recorded consistently since the 1600s. Figure 1.6 is a record of sunspots between 1874 – 2020, where the top panel plots the sunspot's solar disk latitude in time, and the bottom panel shows the sunspot area coverage in time. The sunspots are shown to follow an 11 year cyclic pattern where they are observed to migrate from higher to lower latitudes on the solar disk, during which the number of sunspots peaks halfway. The 11 year solar periodicity defines the solar cycle which was shown to match well with the magnetic activity pattern recorded on Earth. This indicated a connection between the solar sunspot number and geomagnetic storms at Earth, however it was still unclear how exactly they were linked.

One of the earliest examples of a Sun-Earth connection took place on September 1, 1859 when Richard Carrington reported observing a bright flash at the Sun as he routinely examined and documented the location of sunspots on the solar disk

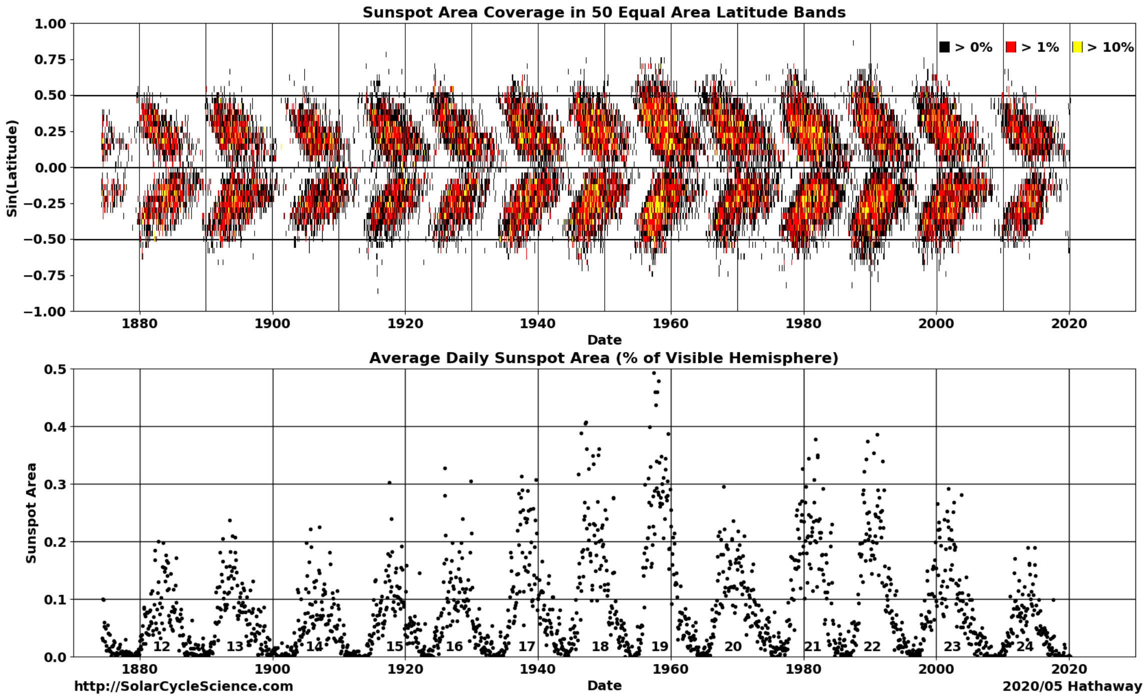

Figure 1.6: Variation of sunspots on the solar disk between 1874 – 2020.

(Carrington, 1859). Separately, Richard Hodgson also witnessed the enhancement of light while observing the Sun nearby. The flash observed was a violent flare. Nearly 16 hours later, a 'great magnetic storm' was detected by the Kew Observatory in London (Stewart, 1861). Carrington recognized the connection between the solar event and geomagnetic storm, however the field remained skeptical given that it had been a singular event. This connection prompted further investigation to the relationship between solar activity and the near-Earth environment, however it would take over half a century later for this relationship to be well accepted.

Furthermore, alongside sunspot observations, solar eclipses provided a unique perspective of the Sun in which to study solar activity. Solar eclipses have long provided unparalleled views to the Sun's atmosphere by blocking the majority of the light from the solar disk. This enables observations of dynamics in the corona that would otherwise be too faint to observe. In fact, during totality, when the moon completely obstructs the solar surface, structures in the corona can be observed with the naked

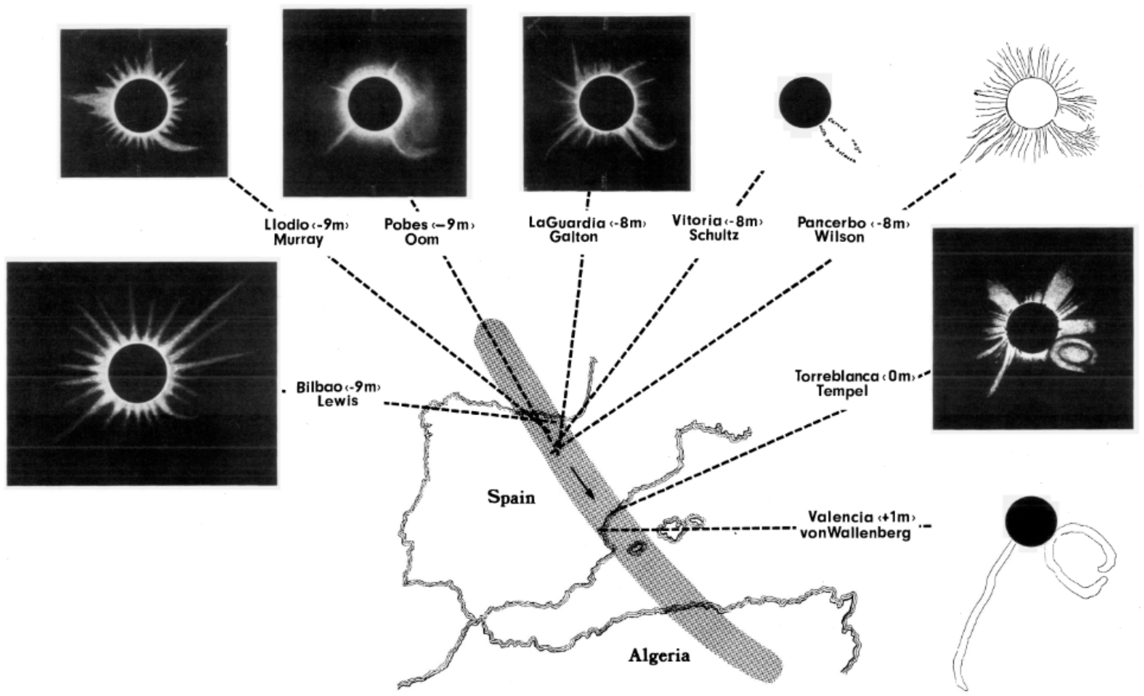

Figure 1.7: Solar eclipse of 1860 drawings and observations from several observers along the path of totality.

eye. This is a unique opportunity in which the community can participate in solar observations without the need of a telescope, extending observations to anyone along the eclipse path. This was advantageous during the Solar Eclipse of 1860, where through several accounts along the path of totality across Spain, it was confirmed that material directed out from the Sun as shown in Figure 1.7 taken from (Eddy, 1974). One drawing in particular, by G. Tempel in Torreblanca, depicted a CME moments after its eruption as it accelerated through the corona, shown on the left of Figure 1.8. This image is one of the first recorded observations of material leaving the Sun in the typical flux rope shape that is routinely observed with present day coronagraphs, shown on the right of the same figure. Subsequent solar observations in the upcoming decades revealed solar transients in white light, described as 'gaseous matter projecting from the Sun', providing more and more evidence of a magnetically active Sun (Ranyard, 1872, 1878).

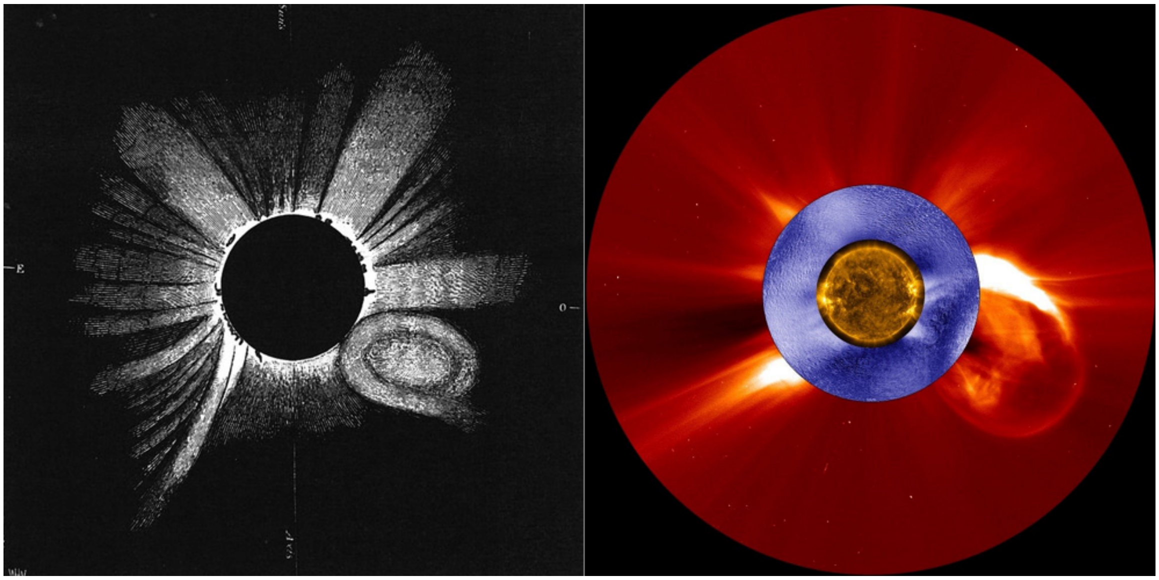

Figure 1.8: Solar eclipse drawing from G. Tempel during the Solar Eclipse of 1860 (left) and a composite image of a CME (right) taken with SDO/AIA in the center, K-Cor between solar surface to $1R_\odot$, and SOHO/LASCO C2 between $1R_\odot$ to $3.5R_\odot$.

In 1892, George Hale provided some of the first narrowband images of eruptions in Hα and the Calcium K line with his invention of the spectroheliograph and, its updated version, the spectrohelioscope (Hale, 1892, 1929). The spectrohelioscope, akin to modern slit spectrometers, was able to isolate a spectral line with the capability to quickly scan the entire Sun, enabling observations of transient phenomena. In the upcoming decades, transient observations from several spectrohelioscopes around the world confirmed a clear connection between observations of eruptions at the Sun and subsequent global magnetic storms (Hale, 1931).

Parallel to observations of transient phenomena, spectroscopic observations of the Sun were being carried out to determine the thermodynamic and compositional properties of the Sun's corona. One of the first comprehensive analysis of the Sun's spectrum, shown in Figure 1.9, was carried out during a solar eclipse in 1869 by Professor Young. Several of the spectral lines from the solar eclipse observations were identified as Fraunhofer absorption lines, however spectroscopy was in its infancy at

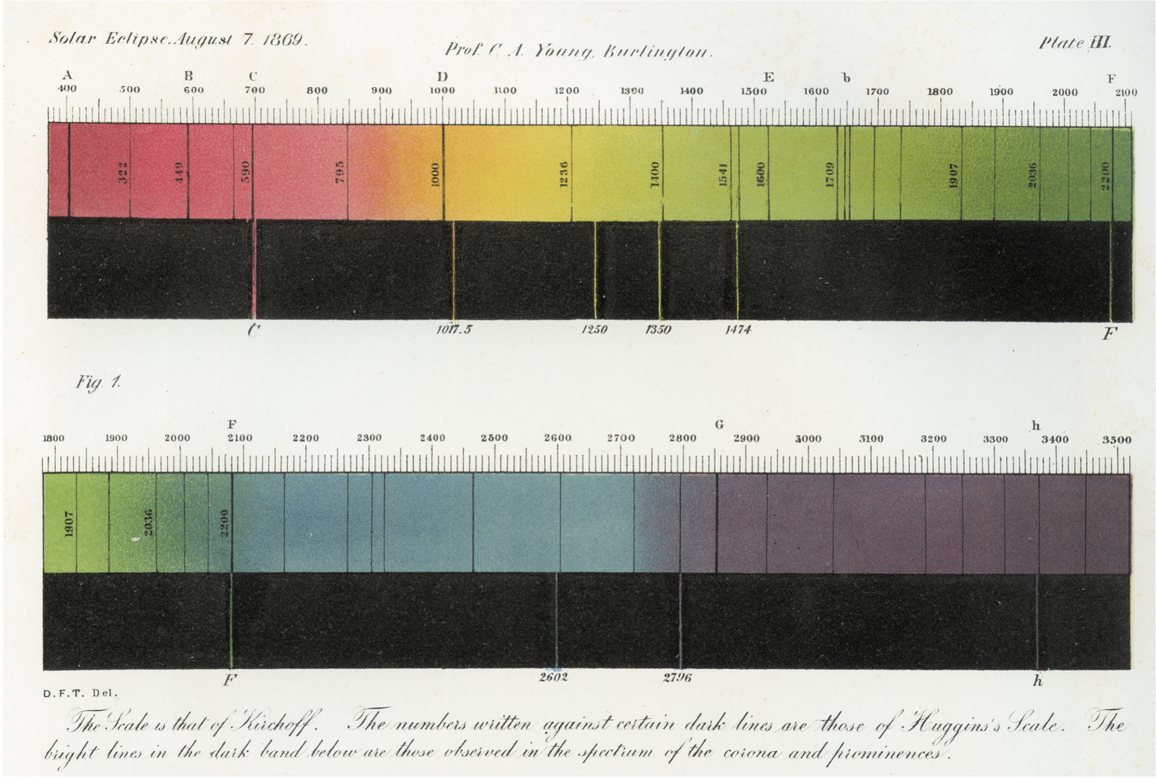

Figure 1.9: Solar spectrum during solar eclipse of 1869 by Professor C. A. Young.

the time, therefore some spectral lines were unknown, notably, the λλ5303 Å spectra line on the green part of the spectrum. Unable to determine their origin, scientists misinterpreted the spectra as a new element which was given the name 'coronium'. It was not until the work of Grotian (1939) and Edlén (1943) where the mislabeled spectrum was correctly identified to contain Fe XIV 5303 Å and several other highly ionized Fe, Ca, and Ni ions, e.g. Fe X, XI, Ca XII, XIII, and Ni XII, XIII, XV. The correct identification of the spectral lines indicated a much higher ionization level of charge states in the corona which corresponded to a multi-million Kelvin temperature, a value that was an order of magnitude larger than the solar surface at 5770K. This was counter-intuitive to the 2nd law of thermodynamics which dictates the energy transferred between adjacent structures flows in the direction of lower temperature until equilibrium is reached. This meant that the state of the corona would not be stable unless there was an unaccounted energy source maintaining its high temperature, such as the Sun's magnetic field. Major strides towards understanding this phenomena have been made by way of magnetohydrodynamic (MHD) waves (Alfvén & Lindblad, 1947; Osterbrock, 1961; Tu & Marsch, 2001; Cranmer et al., 2007; Tomczyk et al., 2007; Kasper et al., 2008; McIntosh et al., 2011; Kasper et al., 2017) and the nanoflare theory (Parker, 1988; Cargill & Klimchuk, 1997; Aschwanden, 1999; Klimchuk et al., 2008; Jess et al., 2014), however this so-called 'coronal heating problem' has continued to puzzle the solar community.

Together, comet tail observations and the connection of solar eruptions to magnetic disturbances at the Earth indicated that magnetized material was perpetually, not just episodically, flowing from the Sun and interacting with bodies in the heliosphere. Eugene Parker's historical paper (Parker, 1958), connected these discoveries by proposing a supersonic expansion of the corona that forms a continuous solar wind flow. His theory assumed a non-hydrostatic, isothermal, spherically symmetric corona, such that the single fluid MHD equations for the conservation of mass, momentum, and energy are as follows,

$$\frac{1}{r^2}\frac{d}{dr}\left(r^2\rho u\right) = 0 \tag{1.2}$$

$$\rho u\frac{du}{dr} + \frac{dp}{dr} + \frac{\rho G M_\odot}{r^2} = 0 \tag{1.3}$$

$$\frac{3}{2}u\frac{dp}{dr} + \frac{5}{2}\frac{1}{r^2}\frac{d}{dr}\left(r^2 u\right) = 0 \tag{1.4}$$

for a fully ionized gas, i.e. quasi neutral, where the negative charges is approximately equal to the positive charges, $n_e \approx Zn_i$, and where heat conduction effects are negligible. r is the radial distance from the Sun, ρ is the plasma's mass density, u is the solar wind speed, G is the gravitational constant, $M_\odot$ is the mass of the Sun, and p is the momentum. Combining equation 1.3 and 1.4,

$$\frac{du}{dr} = \frac{2ru_s^2 - g_\odot R_\odot^2}{u^2 - u_s^2}\left(\frac{u}{r^2}\right) \tag{1.5}$$

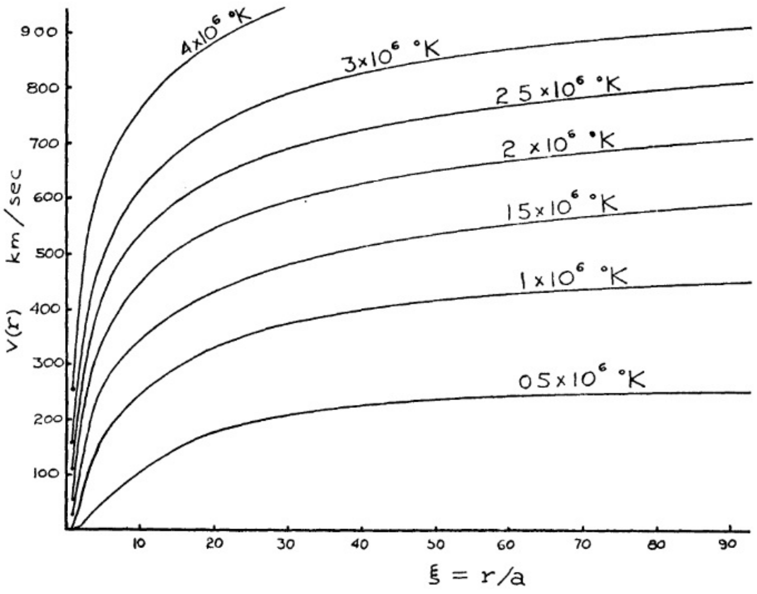

Figure 1.10: Solutions to equation 1.6, showing the solar wind velocity with distance from the Sun for several coronal temperatures, taken from Parker (1958). ξ is the distance from the Sun, r, divided by the radius of the corona, a.

where $g_\odot$ is the gravity at the solar surface, $R_\odot$ is the radius of the Sun, and $u_s = \sqrt{\gamma kT/m}$ is the speed of sound where γ is the adiabatic index, k is the Boltzmann constant, and T is temperature. The solution to the differential equation is,

$$\frac{1}{2}u^2 - u_s^2 \ln(u) = 2u_s^2 \ln(r) + g_\odot \frac{R_\odot^2}{r} + C \tag{1.6}$$

where C is a constant. This equation has several possible solutions of which the most physical interpretation was for the description where solar wind accelerates up to a super sonic speed at some critical point and gradually reaches an asymptotic velocity. The solutions to the speed as a function of distance from the Sun for this scenario are given in Figure 1.10 for several corresponding coronal temperatures, T.

Initially, Parker's work was met with skepticism from the field. However, the beginning of space exploration would soon lend credence to Parker's solar wind model. A timeline of relevant solar and heliospheric space missions is included in Figure 1.11,

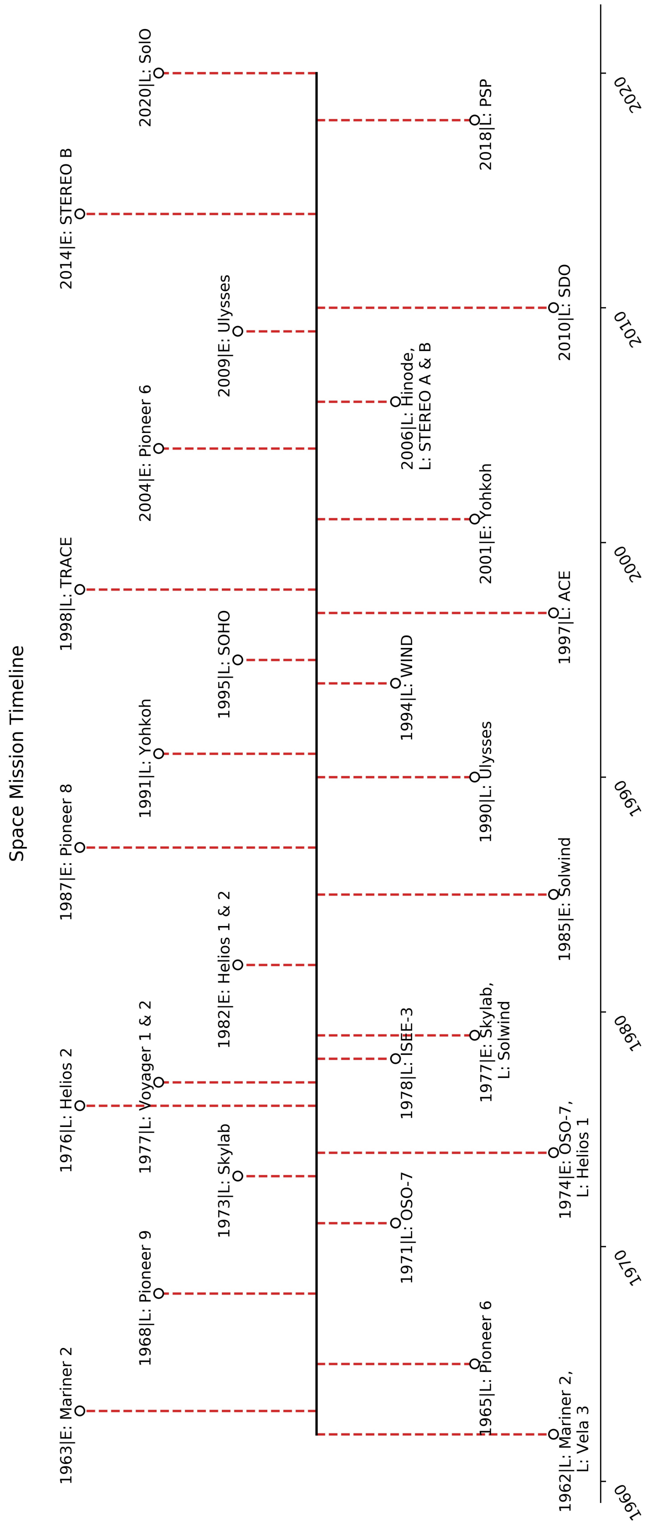

Figure 1.11: Timeline of relevant solar and heliospheric missions between 1962−2020. Each mission is denoted as L, launched, and E, ended.

beginning with the launch of Mariner 2 en route to Venus in 1962. Mariner 2 carried several instruments, including a solar mass spectrometer to probe the planetary and space plasma environment. One of the many discoveries of Mariner 2 was the measurement of the flux and velocity distribution of solar wind particles, H and He, revealing that the plasma was traveling between $400 - 700$ km s^{-1} during a span of several days (Neugebauer & Snyder, 1962). These observations validated the Parker solar wind solutions and constrained the temperature of the corona as well.

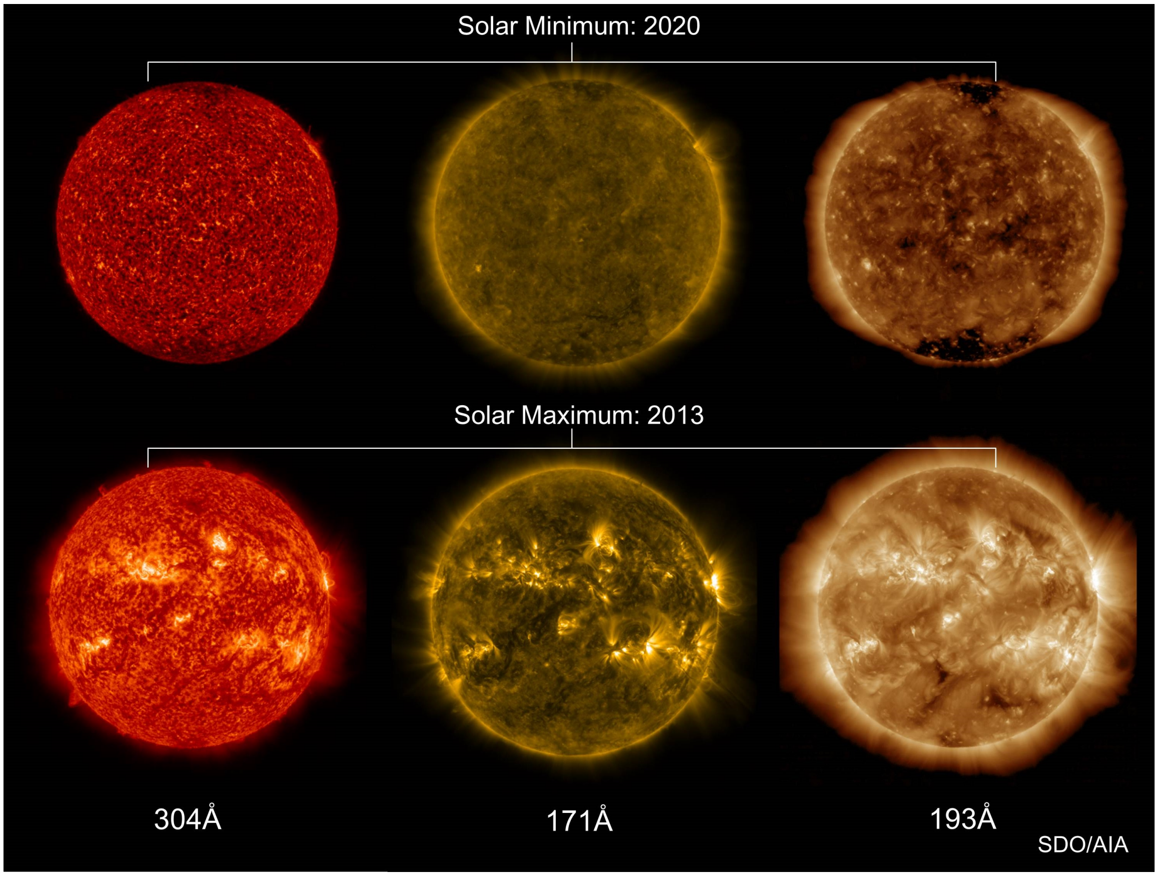

Figure 1.12: EUV broadband images of the Sun during solar minimum (top row) and maximum (bottom) in SDO/AIA 304, 171, ad 193 Å. Images downloaded from Helioviewer.org.

1.3 Solar Activity

Within the continuous flow of solar wind are transients that perturb the ambient heliosphere. The Sun operates at several time and spatial scales, one of which is its 11 year solar cycle which largely governs magnetic activity, such as flares and CMEs, that give rise to transient phenomena. Figure 1.12 are images of the Sun in three broadband EUV channels from the Solar Dynamics Observatory (SDO) taken by the Atmospheric Imaging Assembly (AIA; Lemen et al. 2012) instrument. The top row shows the Sun in the descending phase of cycle 24 (year: 2020), during solar minimum, and the bottom row are taken near the peak of solar activity in solar maximum (year: 2013). The channel centered around 304Å corresponds primarily to He II associated with temperature, $\log_{10}(T[\mathrm{K}]) = 4.7$, 171Å corresponds to Fe IX associated with temperature $\log_{10}(T[\mathrm{K}]) = 5.8$, and 193Å to Fe XII, XXIV associated with temperatures $\log_{10}(T[\mathrm{K}]) = 6.2$, and $\log_{10}(T[\mathrm{K}]) = 7.3$ during flares. Solar minimum is characterized by a dipole-like magnetic field, low magnetic activity, and a minimally structured Sun. The progression of the solar cycle as it ascends into solar maximum is observed through the appearance of bright features made up of a dense network of multipolar magnetic field regions, known as active regions. Also, through the appearance of dark features, coronal holes, at lower latitudes as a result of the magnetic field becoming more disorganized and less dipole-like.

1.3.1 CME Structure and Evolution

The progression into solar maximum sees an increase of CMEs, as can be seen in Figure 1.13, which plots the daily CME rate, in red and blue, throughout solar cycle 23 as indicated by the sunspot number in gray. Evidence for episodic releases of plasma clouds from the Sun began in the 1800s and was further refined in the 1900s (Webb & Howard, 2012). Figure 1.14 shows the progression of the description of CMEs throughout the 20th century. Initially, the eruptions were thought of as gusts of, mostly, neutral material that was violently released from the Sun and propagated radially into the interplanetary medium. However, as the community began to discover the connection between solar and geomagnetic activity, the idea of CMEs progressed towards a magnetized plasma clouds that rapidly expanded and transported magnetic field flux into the interplanetary medium.

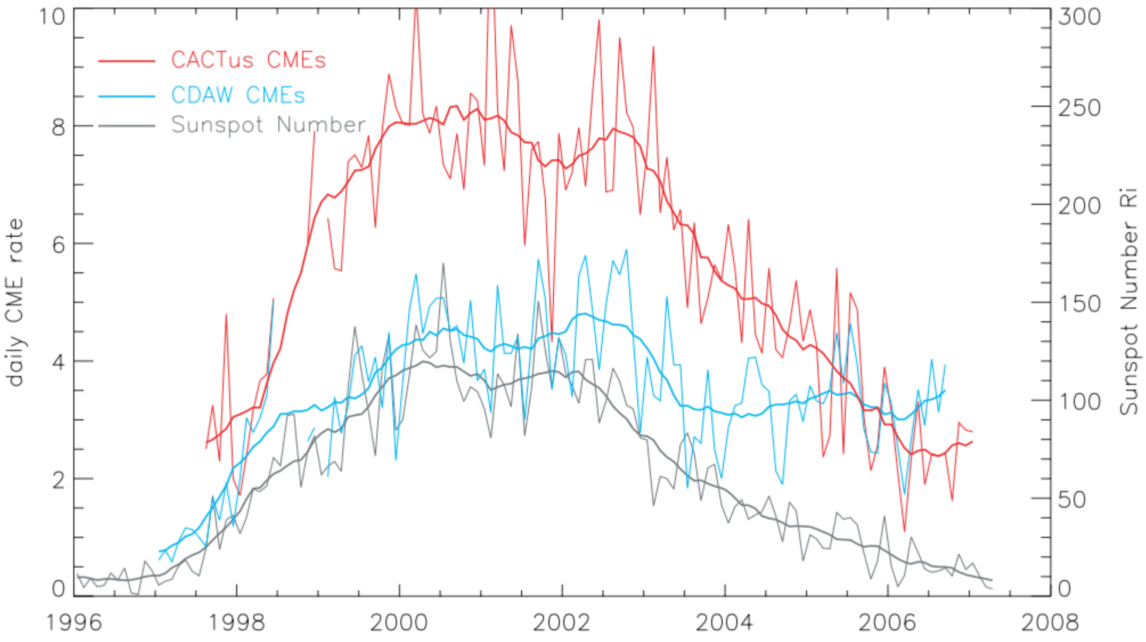

Figure 1.13: Daily CME rate between 1996−2018, taken from Robbrecht et al. (2009).

Solar eclipses proved useful to monitor and study eruptive phenomena. However, their rarity, limited duration, dependence on adequate weather, and inaccessibility made it difficult to study the Sun systematically. The invention of the coronagraph by Bernard Lyot in the early 1900s offered astronomers the ability to recreate solar eclipse conditions at any place and time, and extended the length in which observations could be taken (Lyot, 1930, 1939). Since its invention, coronagraphs have been constructed for ground- and space-based observations. The Mauna Loa Solar Observatory has built a series of white light coronagraphs which have near-continuously observed the Sun's corona between 1956, with the MK I K-coronameter instrument,

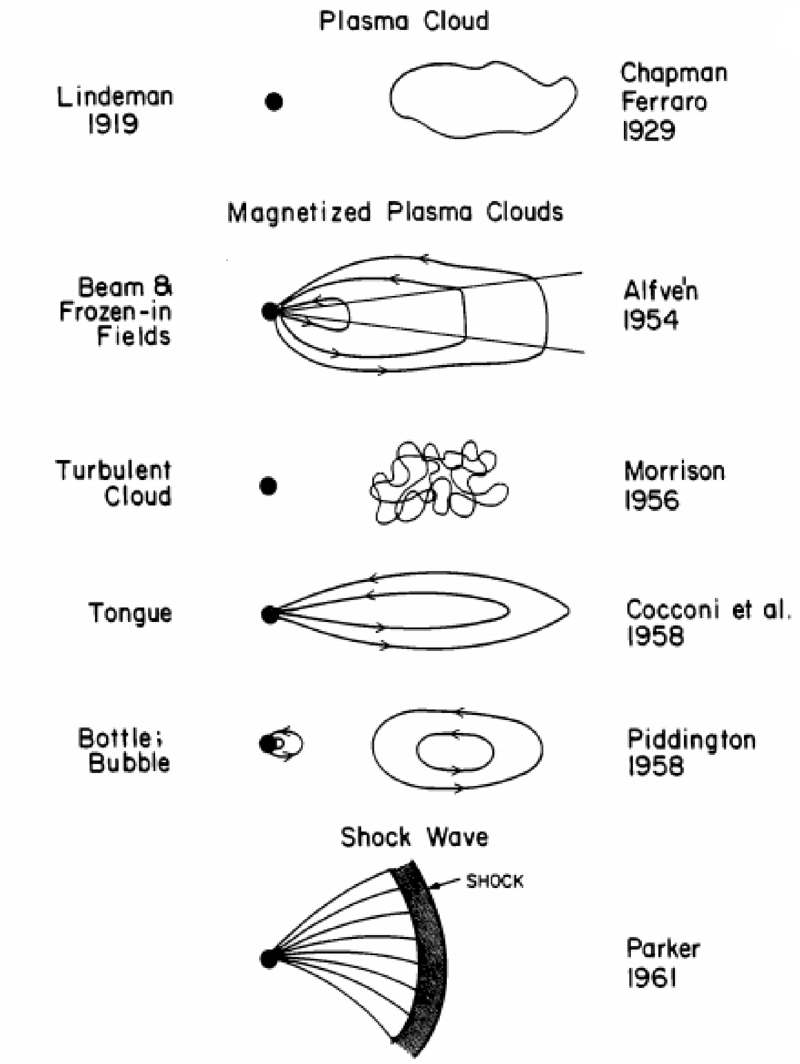

Figure 1.14: Some of the first representations of CMEs in the literature, taken from Burlaga et al. (1981).

to the present, with the K-cor coronagraph[3]. Space-based white light coronagraphs, such as the Large Angle Spectroscopic Coronagraph (LASCO; Brueckner et al. 1995) on SOlar and Heliospheric Observatory (SOHO) C1 (operational only towards the beginning of the mission), C2 & C3 with a combined field of view (FOV) between $1.1 - 30R_\odot$, that launched in 1995 and remains operational, has provided decades of systematic observations of coronal activity on the Sun-Earth line. The Solar Terrestrial Relations Observatory (STEREO; Kaiser et al. 2008) Cor 1 (inner) and Cor

---

[3] `https://www2.hao.ucar.edu/mlso/mlso-instruments`

2 (outer) coronagraphs, with coverage between $1.5 - 15R_\odot$, are mounted on identical spacecrafts that drift ahead and behind along the orbit of the Earth providing coronagraph images from different vantage points of the Sun.

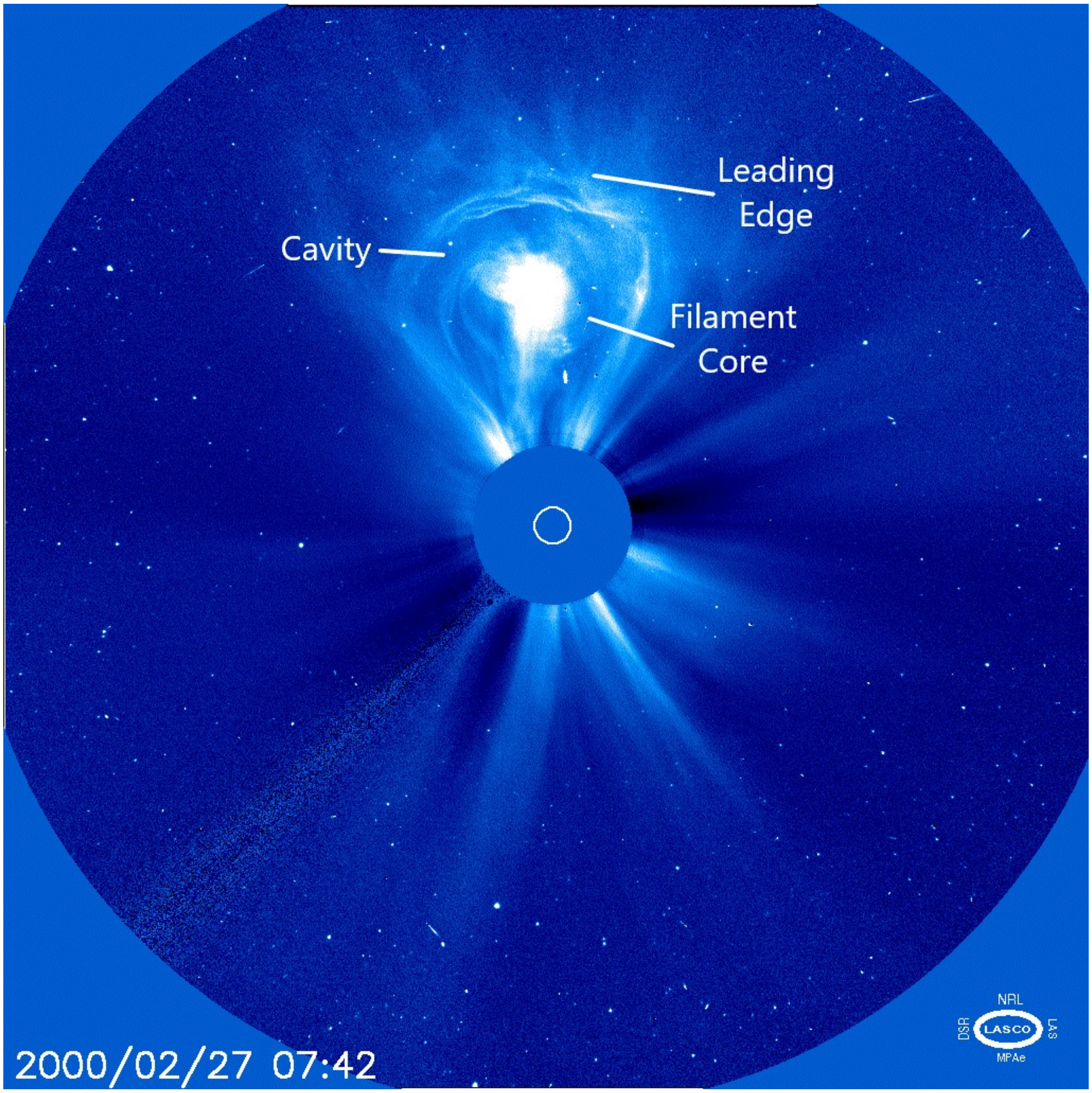

Figure 1.15: Traditional multipart CME structure during an eruption on February 27, 2000 observed by LASCO coronagraph C3. The image is in white light with a FOV between $5 - 30R_\odot$. The white circle in the center outlines the surface of the Sun.

Over half a century of coronagraph observations have enabled the study of CME structure, frequency, kinematics, evolution, and solar cycle dependence Webb &

Howard (2012). From decades of observations, CMEs appear to exhibit a multi-part structure that forms as the plasma leaves the solar surface, as shown in Figure 1.15. The leading edge is formed as the plasma accelerates into the slower moving solar wind, resulting in a compressed front that leads the main CME body. Following the leading edge is a low density cavity and a dense filament core. Generally, the eruption is triggered by magnetic reconnection that destabilizes the magnetic field arcade. The eruption violently releases plasma onto newly open field lines that was previously confined to closed loops in the corona.

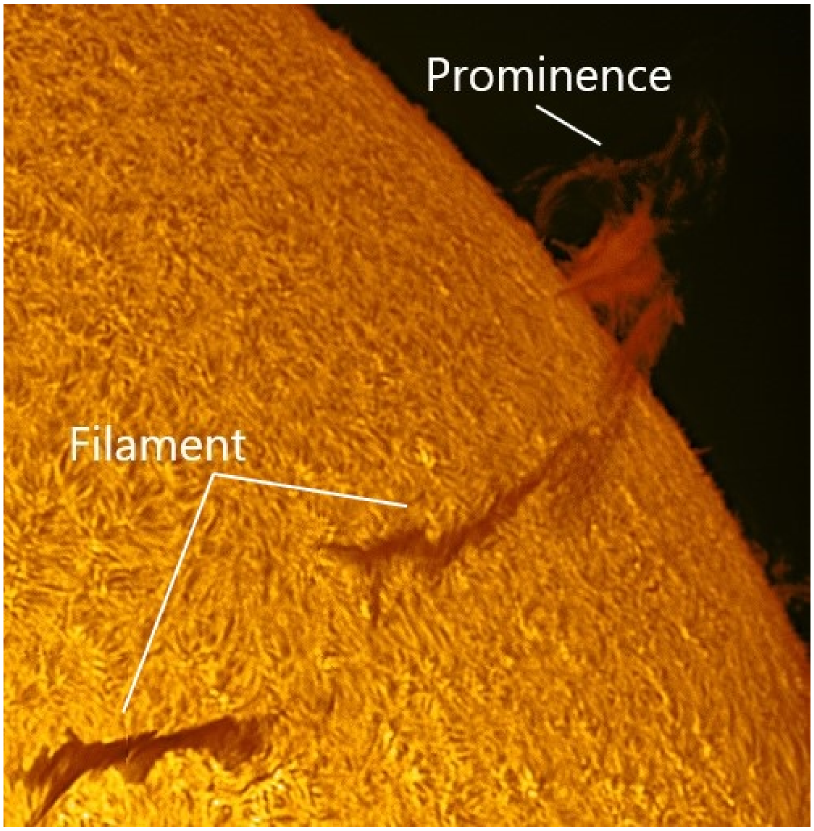

Figure 1.16: Hα image of a filament, on the solar disk, and prominence, observed on the limb.

The core of the CME is typically the brightest feature in white light coronagraph images, with notably contrasting thermodynamic properties to the surrounding plasma. The CME cores are made up of pockets of relatively cool (10^{3-4}K) and dense (10^{9-12} cm^{-3}) plasma structures, called prominences or filaments (Parenti, 2014). Solar prominences, as referred to when observed on the limb or filaments when observed on the solar disk as shown in Figure 1.16, are immersed within a tenuous (10^{7-8} cm^{-3}), multi-million Kelvin corona which can hover up to 100 Mm above the photosphere. Filaments are typically found within active regions but they can also appear in low magnetic field regions of the quiet Sun, as well as at the border of active regions and coronal holes. Their lifetime can span between days to months, during which they maintain a relatively constant thermodynamic state. The prominence-corona transition region (PCTR) is a thin boundary that surrounds the cool filament core, separating the filament from the corona (Engvold, 1988; Cirigliano et al., 2004; Parenti & Vial, 2013; Parenti, 2015). The PCTR appears less dense, 10^{6-8} cm^{-3}, and warmer, 10^{4-6} K, compared to the main prominence body and is thought to provide insulating properties to the filament body. Furthermore, filaments are not monolithic structures but rather thought to be composed of smaller, thread-like structures whose scale is below the resolution of present telescopes. For this reason, the density filling factor is not well constrained, however several studies have estimated the filament and adjacent PCTR filling factor to be on the order of 10^{-3} to 10^{-1} (Labrosse et al., 2010). The large uncertainties in the density filling factor have long inhibited the accurate determination of filament mass and density which have important implications to the computation of CME energetics, that are key to understanding the CME's energy budget, and its presence in the heliosphere, which is futher discussed in Section 1.3.2.

1.3.2 Overview of Signatures Used in Interplanetary CME Detection

Once in the heliosphere, CMEs are referred to as Interplanetary CMEs (ICMEs). In the last half century, several spacecraft throughout the heliosphere have analyzed ICMEs at different stages of their evolution. Remote observations of the multipart structure seen accelerating from the Sun have provided distinguishing features that

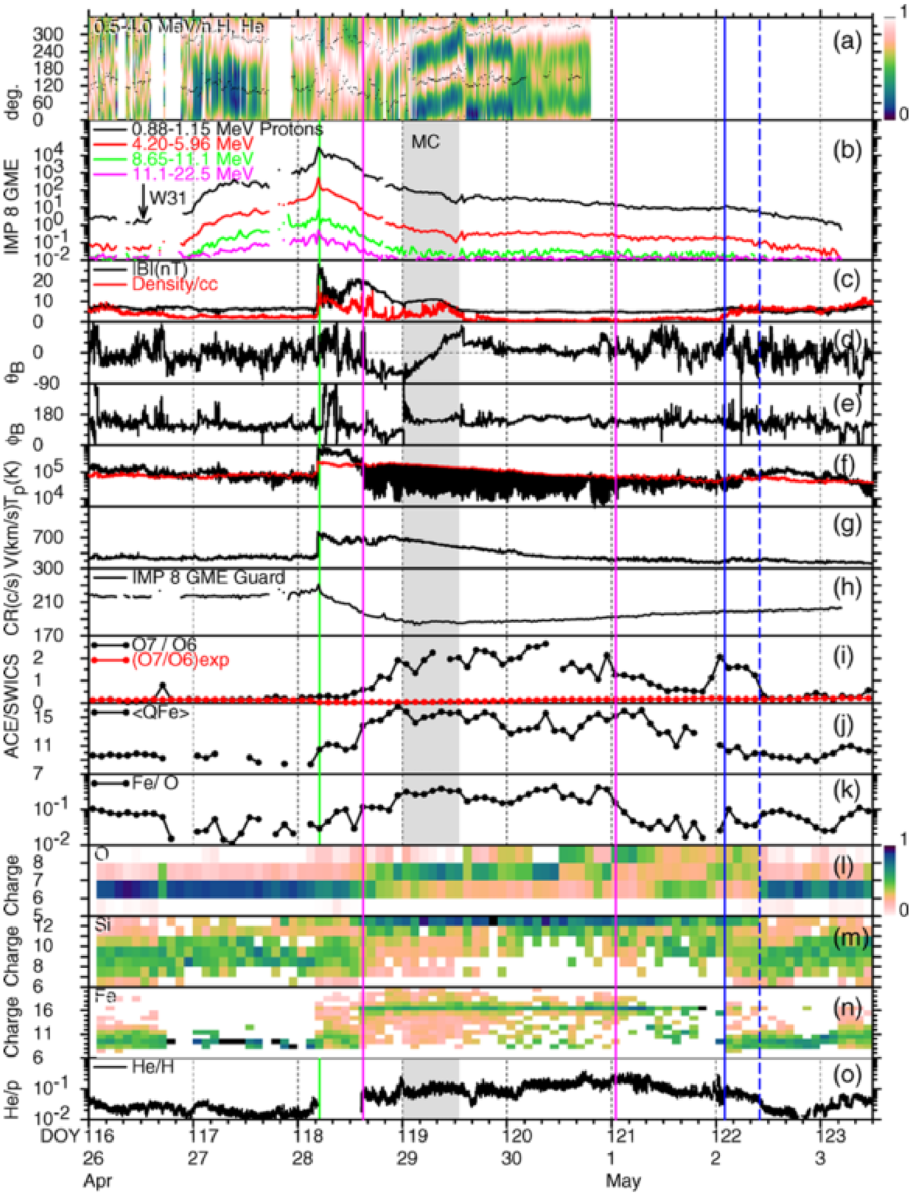

Figure 1.17: Taken from Richardson & Cane (2010), (a) angular distributions of protons, (b) 0.88 – 22 MeV proton intensities, (c) magnetic field magnitude, in black, and proton density, in red, (d-e) the θ and ϕ components of the magnetic field, respectively, (f) proton temperature, in black, with predicted temperature, in red, (g) speed, (h) cosmic ray count rate, (i) O^{7+}/O^{6+}, in black, and predicted, in red, (j) average Fe charge state, (k) Fe/O density ratio, (l-n) normalized charge state distribution of O, Si, Fe, respectively, and (o) He/H density ratio. The green line represents the shock arrival, the purple lines define the ICME boundary, and the magnetic cloud is shaded in grey. The blue lines are associated with the trailing Fe, O and Si charge states.

guide the identification of CMEs within the continuous solar wind. Through these features, a comprehensive ICME event list has been compiled from near-Earth spacecraft measurements of magetic field, plasma state, ionic composition, and energetic particles (Cane & Richardson, 2003; Richardson & Cane, 2010). Throughout this section, I will refer to the multi-panel vertical plot in Figure 1.17, displaying in situ measurements of an ICME in 2001 at L1 from Richardson & Cane (2010) which illustrates several of the properties discussed below. In the figure, the vertical green line denotes the shock ahead of the CME, the magenta lines identify the main CME body, the solid blue line show the extended boundary correlating to elevated Fe charge states, and dashed blue line is the extended boundary of elevated O and Si charge states.

Early studies of the interplanetary magnetic field measurements revealed important features of the magnetic structure of ICMEs. Klein & Burlaga (1982) observed a systematic change in direction of the magnetic field components within the CME boundary. The rotation of the magnetic field was attributed to a helix-like magnetic field topology, as observed in the shaded gray region for panel (d) and (e). This suggested CMEs contained twisted magnetic field lines resembling a flux rope. The same study found the CMEs were associated with an initial enhancement of magnetic field strength that was followed by large magnetic field fluctuations observed within the turbulent sheath as a result of a shock formed ahead of the CME, as shown between the green and first magenta line in panels (c)-(e). Subsequently, a decrease of magnetic field oscillations and strength follow the shock as the spacecraft entered the CME boundary. These features suggest CMEs often form a shock that compresses and heats the plasma as it travels into the heliosphere which appears as the CME front in coronagraph images.

The study of magnetic clouds in Klein & Burlaga (1982) also suggested ICME plasma appeared cooler and less dense compared to the ambient solar wind. Solar wind data find the ICME front and tail travel at $v_{ICME} + v_{Exp}$ and $v_{ICME} - v_{Exp}$, respectively, and the expansion velocity, v_{Exp}, is typically half the Alfven speed (Zurbuchen & Richardson, 2006). The gradual decrease in the cloud plasma velocity and density between the leading and trailing edge of the ICME is indicative of expansion (shown in panel (g) and (c), respectively). Compared to the empirical relationship between the temperature and velocity (T-V) established for the solar wind (Lopez & Freeman, 1986), Richardson & Cane (1995) found ICME ejecta had consistently lower ion temperature than predicted by ordinary solar wind expansion concluding that ICME expansion occurs more rapidly than solar wind (displayed in panel (f) with expected proton temperature in red).

Initial solar plasma ion measurements were mainly of H and He ions, e.g. the Mariner and Pioneer missions. Subsequent studies with the International Sun-Earth Explorer (ISEE) measured distributions of C, N, O, and Fe (Ipavich et al., 1986) while later studies extended the number of minor ion detected in the solar wind by using time-of-flight mass spectrometer instruments, such as Solar Wind Ion Composition Spectrometer (SWICS) on Ulysses(Gloeckler & Geiss, 1992) and the Advanced Composition Explorer (Gloeckler et al., 1998), the Charge-Time-Of-Flight sensor (CTOF; Hovestadt et al. 1995) on SOHO, and Plasma and Suprathermal Ion Composition (PLASTIC; Galvin et al. 2008) on the twin STEREO spacecrafts beginning in the 1990s. The SWICS instruments on Ulysses and ACE allow for the identification of individual ions for species $Z = 1 - 30$ with an energy-per-charge, E/Q, between $0.49 - 100$ keV e^{-1} which can reliably identify several ions of C, O, Mg, Si, and Fe.

Some of the first studies found that ICMEs were characterized by an enhanced He^{2+} density, where He/p $> 8\%$, increasing to almost twice the amount found in the ambient solar wind density (enhancement displayed in panel (o)) (Hirshberg, 1971). Later studies, which included heavier ions, established additional signatures in the ejecta. In general, it was found that ICMEs contained higher ionized charge states compared to the surrounding solar wind plasma. In a study of 50 CMEs, Neukomm (1998) consistently found elevated O^{7+}/O^{6+} ratios during CMEs. This is shown in panel (i) which compares O^{7+}/O^{6+} between the expected solar wind observations (red) to the enhanced values observed in the ICME (black). Furthermore, a survey by Lepri et al. (2001) between $1998-2000$ found that 90% of periods with enhanced highly ionized Fe charge states, $Fe^{\geq 16+}$, were associated with ICME events, as shown in panel (n). These features were an indication that CMEs experienced significant ionization near the Sun that was unlike the typical solar wind evolution.

However, the prominence core of CMEs suggest that low ionized material should also be present along with highly ionized material. Statistical studies find that roughly 70% of CMEs are observed to contain a cool, partially ionized prominence core when leaving the Sun (Webb & Howard, 2012). However, despite its nearly ubiquitous appearance at the Sun, low charge states are seldom detected in situ within ICMEs. A survey by Lepri & Zurbuchen (2010) found only roughly 4% of filament related CME eruptions contained a significant contribution of low ionized material. This discrepancy remains an open question. Some observations suggest the heating observed during the eruption could potentially erase the presence of low ionized material before reaching 1AU (Kucera & Landi, 2006; Lee et al., 2017). Alternatively, the low density filling factor of prominence plasma could make it difficult to detect filaments in the heliosphere (Lee & Raymond, 2012). Beyond that, the spacecraft itself poses limitations to the data collected simply due to the orientation and size of the instrument compared to the ICME. This limits measurements to only a small sample of the ICME that can miss detecting prominence material altogether.

1.3.3 CME Heating

It is well established that CMEs undergo rapid heating at the Sun as indicated by spectroscopic measurements of the eruption and highly ionized minor ions measured in the heliosphere. In particular, the thermal energy of cool prominence material is shown to increase during and following the eruption, suggesting rapid ionization of some neutral and low-ionized material is taking place (Kucera et al., 1998; Lee et al., 2009; Landi et al., 2010; Lee et al., 2015, 2017; Kocher et al., 2018). However, there are limited spectral observations of CMEs available due to their sudden and unpredictable release, rapid acceleration, and expansion that weakens their emission, making the plasma difficult to track and observed far above the surface. Therefore, it remains unclear what level of heating is experienced by the plasma, which is central to understanding the fate of prominence material. Addressing this question will also shed light on an important overarching question in CME science; what mechanism supplies the energy that heats the CME? There are several mechanisms discussed as possible sources; large-scale and local reconnection, current sheet dissipation, wave heating, compression from shocks and others however it remains difficult to identify which mechanism(s) effectively convert(s) magnetic energy into energy used to accelerate and heat CME plasma (Murphy et al., 2011). Therefore, charge states within the ejecta can also serve as an important constraint to the CME heating process, as further discussed in Section 1.4.

Moreover, ICME measurements made throughout the heliosphere suggest they undergo prolonged and continuous heating after they leave the Sun. A collection of measurements within CMEs taken with Helios 1 & 2, Ulysses, Voyager 1 & 2 between 0.3AU and 20 AU, shown in Figure 1.18, indicate that ICMEs expand faster and cool slower than adiabatic (Liu et al., 2006). Assuming the plasma behaves similar to an ideal gas, typical adiabatic expansion dictates that density and temperature should follow, $n \propto r^{-2}$ and $T \propto r^{-4/3} \propto r^{-1.33}$. Best fit power law values for the proton density and temperature, shown in panel 1 and 3 of Figure 1.18, find ICMEs show a steeper proton density profile, $n_{ICME} \propto r^{-2.23\pm0.04}$, and a shallower proton temperature profile, $T_{ICME} \propto r^{-0.72\pm0.03}$, as compared to predicted adiabatic values

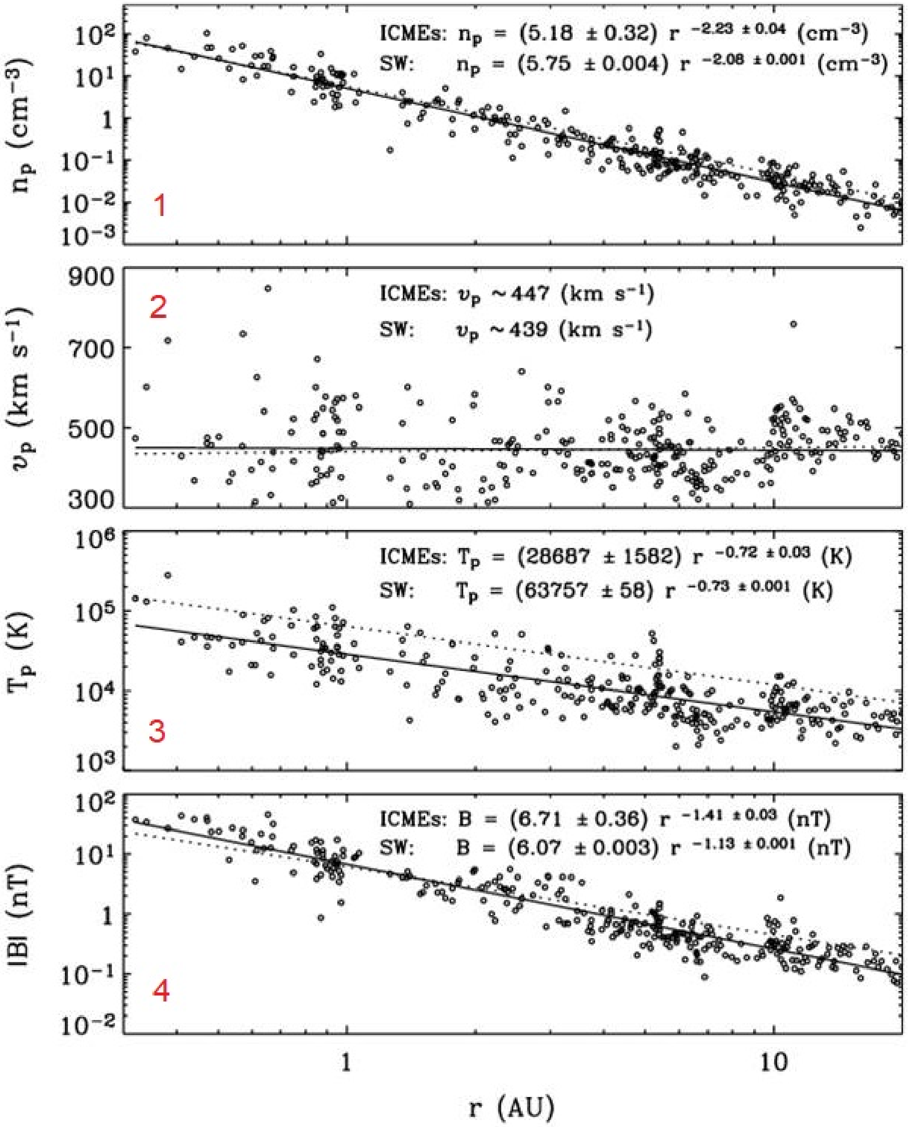

Figure 1.18: Fits to radial measurements of CMEs and the solar wind taken from Helios 1 & 2, Ulysses, and Voyager 1 & 2, taken from Liu et al. (2006).

and, for density, the solar wind profile. Density measurements suggest the magnetic field within CMEs is much larger compared to the ambient wind, contributing to the rapid expansion and lower proton density observed in situ, see panel (c) in 1.17. Measurements of the temperature suggest ICME plasma cools at a slower rate than a self-similar expanding parcel of plasma in a closed system, i.e. having no energy exchange with the surrounding environment. This indicates that the mechanism depositing thermal energy to the system is active well after the plasma leaves the eruption site suggesting there is a local energy source, and possible ongoing ionization and recombination processes taking place.

Despite heating occurring rapidly and continuously, several observations from eclipses, white-light coronagraphs, and heliospheric imagers still find low ionized charge states at large distances from the Sun (Habbal et al., 2010; Wood et al., 2016; Ding & Habbal, 2017). This suggests that prominence material can remain in a neutral and low ionized state well into the interplanetary medium. Numerical simulations and charge state ionization modeling indicate localized, spatially dependent heating within the multi-part CME, suggesting that adjacent structures may experience different levels of heating which can allow for part of the core neutrals and low ionzed material to remain (Reeves et al., 2010; Rakowski et al., 2011; Lynch et al., 2011; Gruesbeck et al., 2011, 2012; Lepri et al., 2012; Manchester et al., 2014). For instance, Reeves et al. (2010) tracks the energy flow within an MHD simulation of a CME between the surface and $20R_\odot$. The simulation follows the energy released from the current sheet that forms prior to reconnection. The study finds that throughout the eruption, the energy outflow is compartmentalized to regions surrounding the current sheet, suggesting that the deposition of energy depends on where the current sheet forms and how the magnetic field is oriented, which may not effectively reach the prominence material.

1.4 Ionization and Recombination Processes that Govern Ion Evolution During the Plasma's Radial Expansion

A method to study the evolution and eventual fate of the prominence plasma is by analyzing the ionization and recombination processes taking place during its radial propagation. These processes directly shape the charge state distributions measured by compositional instruments in the solar wind and transients. Ion densities are a product of the heating, cooling, and any other process, such as the interaction with solar radiation and charge exchange, experienced by the plasma as it is accelerated into the interplanetary medium. In turn, the ions within CMEs can be examined to retrieve the plasma's thermodynamic history to indirectly quantify the energy deposition throughout the eruption.

The dominating ionization and recombination processes occurring at typical coronal conditions include collisions with free electrons and interaction with the radiation field however charge exchange can be an important process in plasma below 25,000K (Arnaud & Newkirk, 1987). Photoionization and, its reverse process, radiative recombination as described in Phillips et al. (2008) is as follows,

$$X_i^{+m} + h\nu \leftrightarrow X_j^{+m+1} + e(E) \tag{1.2}$$

where X_i^{+m} is element X at ionization state $+m$ and energy level i, $h\nu$ is the photon energy from the radiation field, and $e(E)$ is the released electron of kinetic energy, E. This describes an incident photon with energy, $h\nu$, interacting with an electron in X_i^{+m} which provides it with enough energy to escape the atom. This produces an electron, e(E), and an atom with a higher level ionization, X^{+m+1}. Photoionization can take place if the photon energy is larger than the difference of the energy levels, as h$\nu > E_j - E_i$, such that the electron gains enough energy to become unbound.

Collisional ionization and its reverse reaction, three-body recombination, is described as,

$$X_i^{+m} + e_1(E_1) \leftrightarrow X_j^{+m+1} + e_1(E_2) + e_2(E_3). \tag{1.3}$$

Excitation-autoionization and its reverse reaction, dielectronic recombination, are described as,

$$X_l^{+m} + e(E_1) \rightarrow X_j^{+m} + e(E_2) \rightarrow X_i^{+m+1} + e(E_2) + e^{'}(E) \tag{1.4}$$

$$X_i^{+m+1} + e(E) \rightarrow X_j^{+m} \rightarrow X_l^{+m} + h\nu \tag{1.5}$$

where, in excitation-autoionization, $e(E_1)$ collides with X_l^{+m} which excites X^{+m} from level l to j, where level j is above the ionization threshold of the ion. The incoming electron leaves with energy, $e(E_2)$, and $e^{'}(E)$ is the electron released through autoionization. In the reverse reaction, $e(E)$ is captured by X_i^{+m+1} into a level above the ionization threshold, j, leaving the ion unstable. The ion can either release the captured electron, or radiatively decay to a level below its ionization threshold, for which the latter completes reaction 1.5.

The ion abundances can be simulated along the radial expansion of the solar wind by taking into account the cumulative effect of the described ionization and recombination processes. One example of such ionization code is the Michigan Ionization Code (MIC), fully described in Landi et al. (2012a), which is the primary code used in the numerical simulations throughout this thesis work. The MIC is a nonequilibrium ionization code that solves a system of differential equations using a Runge-Kutta method of order 4. The equations are given as,

$$\frac{dy_i}{dt} = n_e \left[y_{i-1} I_{i-1}(T_e) + y_{i+1} R_{i+1}(T_e)\right] + y_{i-1} P_{i-1} - y_i \left[n_e \left(I_i(T_e) + R_i(T_e)\right) + P_i\right] \tag{1.6}$$

where n_e is the electron density, y_i the relative abundance of ionization stage i, R and I are the recombination and ionization rate coefficients, respectively, and P is the photoioinzation rate. The rate coefficients are the total ionization and recombination processes included in reactions 1.2−1.5. The MIC generates relative abundances of individual elements governed by the ionization and recombination processes where each reaction is sensitive to the local electron temperature, electron density, and bulk speed of the parcel of plasma propagating radially from the Sun. Initial conditions include thermodynamic equilibrium at the beginning of the simulation, which is taken to be the inner boundary closest to the Sun, where we assume ionization equilibrium holds, that is $dy_i/dt = 0$. Also, the reaction coefficients are computed under the assumption the electrons remain in a Maxwellian velocity distribution.

1.4.1 Ion Freeze-in Process; the Diagnostic Potential of Minor Ions

The charge state densities observed in the heliosphere can serve as useful diagnostics of plasma dynamics near the Sun. This is a consequence of the expanding solar wind quickly becoming too tenuous for ionization and recombination processes to remain effective far from the Sun. Once ionization and recombination processes become ineffective, the ions become decoupled to thermodynamic changes in the plasma and are said to become 'frozen-in' to their present ionization state (Hundhausen et al., 1968). The result are ions which preserve ion densities that are representative of their evolution up to their freeze-in location.

Each ion's freeze-in distance is governed by the plasma's electron density, temperatures, and bulk speed, which can vary due to the distinct plasma properties between solar wind types and transients. For instance, denser plasma, e.g. streamer belt wind, with a similar expansion timescale to tenuous coronal hole wind, can undergo ionization and recombination processes longer, in turn, further from the Sun (Landi et al., 2012a). This is demonstrated in Figure 1.19, where the simulated evolution are plotted for several C, O, and Fe ions within two models of the solar wind: equatorial (slow) and coronal hole (fast) solar wind derived in Cranmer et al. (2007). The figure presents the simulated ion densities divided by their final freeze-in densities between its release at the solar surface to $5R_\odot$. As the figure illustrates, lighter ions, such as C and O, generally freeze-in closer to the Sun compared to heavier ions, like Fe charge states. Also, within different species, individual ion freeze-in distances can

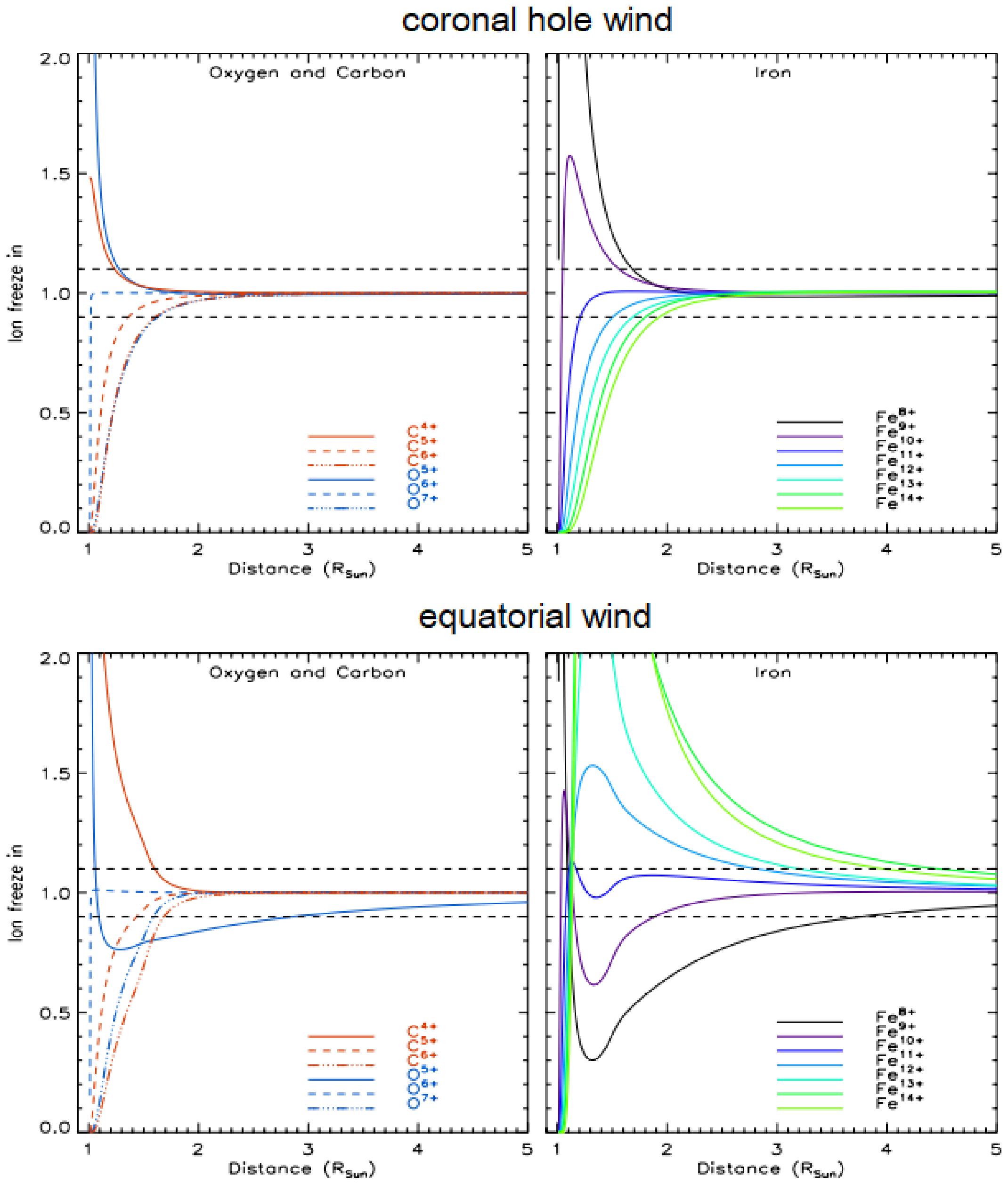

Figure 1.19: Simulated ion freeze-in distances for O, C, and Fe within the fast (top) and slow (bottom) solar wind taken from Landi et al. (2012a). The vertical axis is the ion relative abundance divided by its final freeze-in value. The dashed lines represent values at 0.95 to 1.05.

occur within a range of heights, such as is shown for Fe ions in the second column of Figure 1.19. This indicates that individual ions undergo a unique evolution governed by ionization and recombination processes up to their freeze-in point providing an indirect measure of the plasma properties along their evolution.

1.4.2 Necessity of Nonequilibrium Modeling

Departures from ionization equilibrium will occur for plasma that is rapidly changing, such as for explosive events like flares and CMEs. Ionization equilibrium refers to the balance between the creation and destruction among the different ionization levels such that,

$$N_i(R_{Tot} + I_{Tot}) = N_{i-1} I_{Tot} + N_{i+1} R_{Tot} \tag{1.7}$$

where N_i is the ion population density of ionization level i in cm^{-3}, R_{Tot} and I_{Tot} are the total recombination and ionization rate coefficients, respectively, in cm^3 s^{-1}. Deviation from ionization equilibrium occur when this equation is violated at any point during which the ion fractions do not represent the plasma temperature and density. Nonequilibrium may arise during impulsive heating and cooling phases, e.g. transients as well as the solar wind, where the timescale for these processes occur faster than the ionization and recombination processes causing unbalanced formation and creation of the corresponding ion. Given the ions may not be in ionization equilibrium, the freeze-in ion densities cannot be directly used to extract a freeze-in temperature. Instead, nonequilibrium modeling is necessary to interpret the evolution of charge state distributions in plasma, such as with the MIC.

Also, nonequilibrium occurs when velocity distributions deviate from Maxwellian, resulting in the reaction coefficients being different than those computed under the ionization assumption. It is typically assumed that plasma in the solar photosphere

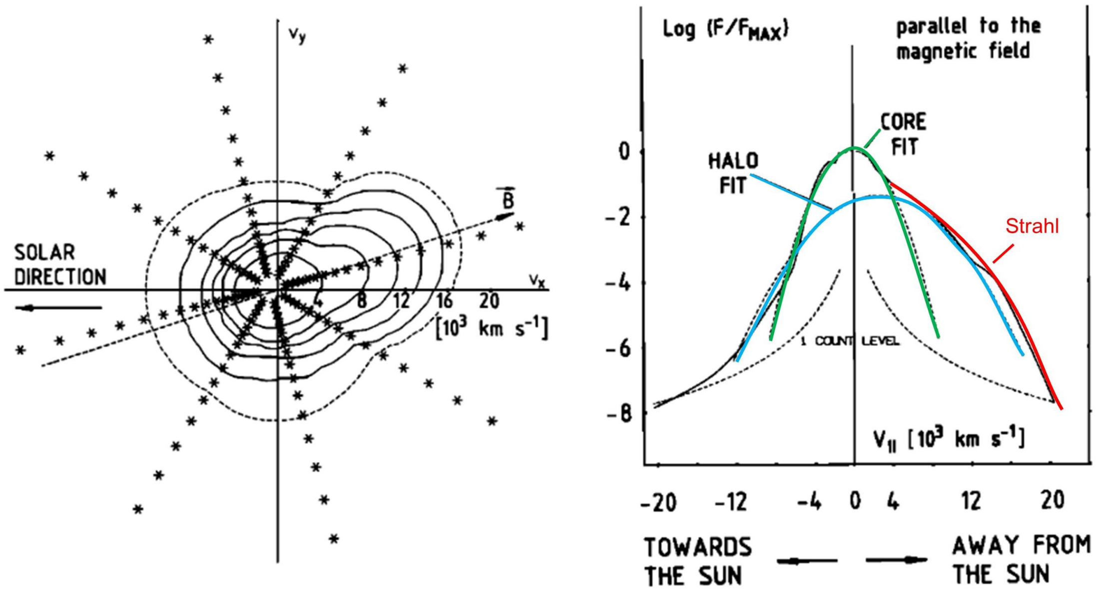

Figure 1.20: 2D (left) and 1D (right) electron velocity distribution function from Helios 2. Adapted from Pilipp et al. (1987a).

and chromosphere regions are in local thermodynamic equilibrium (LTE) and the electrons and ions are well represented by Maxwellian velocity distributions however this assumption becomes less valid farther from the Sun. Coulomb collision frequency, ν_C, between ions and electrons are governed by the plasma density and temperature as follows,

$$\nu_C = \frac{5 \times 10^{-11} n_e Z_i \ln(\Lambda)}{17 \cdot T_e^{3/2}} \propto \frac{n_e}{T_e^{3/2}} \ [\mathrm{s}^{-1}], \tag{1.8}$$

where n_e is the electron density, Z_i is the atomic number, $\ln(\Lambda)$ is the Coulomb logarithm, and T_e [eV] is the electron temperature. This relationship leads to a decrease in collision frequency as the plasma expands or heats up, both which occur rapidly at the transition region, as shown previously in Figure 1.2. The abrupt changes at the transition region result in the plasma quickly becoming collisionless in the corona. Given that the Maxwellian profile is governed by frequent collisions that redistribute energy and maintain LTE, a consequence to this is that deviations from Maxwellian velocity distributions may arise. The distribution function directly impacts the reaction rate coefficients used to compute the ion densities. The reaction rate coefficients are given as,

$$R(v) = \int \sigma(v) 4\pi v^2 f(v) dv \tag{1.9}$$

where $\sigma(v)$ is the reaction cross-section and $f(v)$ is the velocity distribution function (VDF), where a Maxwell-Boltzmann velocity distribution is given as,

$$f(v) = \left(\frac{m}{2\pi k_{\mathrm{B}} T} \right)^{3/2} e^{-\frac{mv^2}{2k_{\mathrm{B}}T}} \tag{1.10}$$

where m is particle mass, k_{B} is the Boltzmann constant, T is temperature, and v is the bulk plasma velocity. Non-Maxwellian VDFs are often exhibited by electrons, protons, and alpha particles in the solar wind and, ocassionally in CMEs (see summary of particle distributions in Marsch 2006). Figure 1.20 is a electron VFD in two (left) and one (right) dimensions within the solar wind, showing a highly structured distribution composed of a cool isotropic core, surrounding halo, and a magnetic field directed bulge, known as the electron strahl (Pilipp et al., 1987a). The electron strahl is composed of energetic electrons that can contribute to additional ionization in the plasma that is unaccounted for under the Maxwellian assumption. This can be a source of uncertainty in nonequilibrium modeling if VDFs deviate significantly from Maxwellian prior to the ion freeze-in distances.

In addition, nonequilibrium ionization is important to consider for the meaningful interpretation of plasma properties from spectroscopic measurements. Analysis of spectral lines from ions in nonequilibrium can potentially yield incorrect information about the ion and electron properties in the plasma, see Dudík et al. (2017) for a review of nonequilbrium processes in the corona, transition region, flares, and solar wind. This can occur when computing ion temperature from a spectral line, as well as for consecutive ion intensity ratios, which both assume ionization equilibrium. This

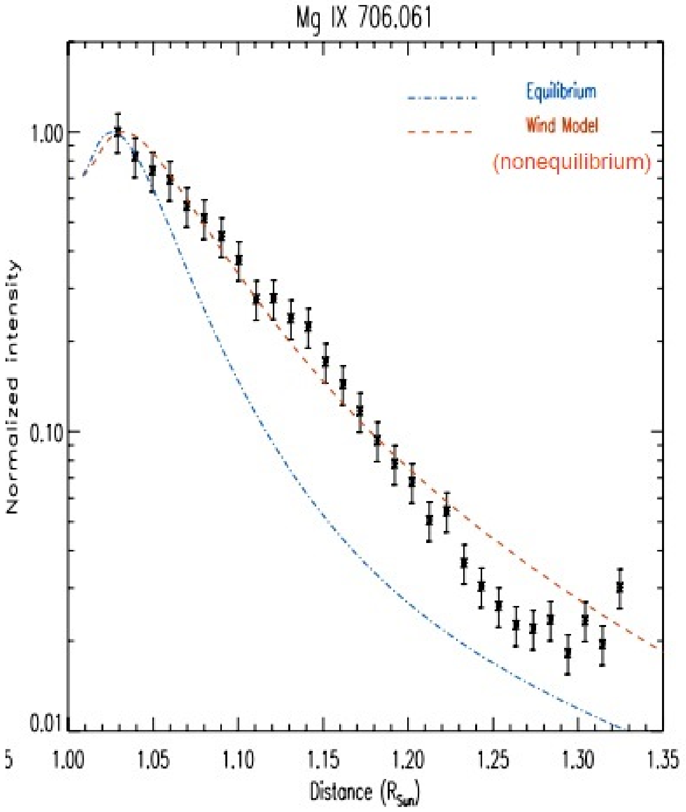

Figure 1.21: Plot of observations from the Mg XI 706 spectral line formed along an equatorial streamer, black stars, compared to by synthetic intensities formed within equatorial solar wind model for equilibrium (blue) and nonequilibrium (red) conditions, taken from Landi et al. (2012a).

is demostrated in Landi et al. (2012a), where intensities from the EUV Imaging Spectrometer (EIS; Culhane et al. 2007) slit spectrometer of coronal hole and equatorial streamer observations are compared to synthetic intensities generated for nonequilibrium and equilibrium ion densities using the Cranmer et al. (2007) coronal hole and equatorial wind profiles, as shown in Figure 1.21 for the equatorial streamer case. This study demonstrated that significant deviations from ionization equilibrium can occur for certain ions in the low corona, and due to this, the emission of selected spectral lines are affected. This study demonstrated the usefulness of nonequilibrium modeling as a tool for linking remote and in situ observations, as well as the necessity remote and in situ observations, to investigate dynamic processes along the plasma trajectory.

1.5 Interplanetary Dust and its Interaction with the Solar Wind

Along with the ionization and recombination processes governed by the interaction with the radiation field and electrons, the solar plasma ions can also interact with the interplanetary dust and other bodies present throughout the heliosphere. Small orbiting grains are distributed along the ecliptic and concentrated near the Sun which make up the interplanetary dust. Similar to a cometary environment, its thought that the dust grains are a source of neutral and low ionized material that interact with and feed into the normal solar wind.

1.5.1 Interplay with the Solar Wind

One of the first observations of the interaction between the solar wind and interplanetary dust was through the discovery of the inner source ions with the Ulysses spacecraft (Gloeckler & Geiss, 1998). The inner source ions are a subset of pick up ions (PUIs) which are suggested to originate from the interaction of the solar wind with interplanetary dust in the vicinity of the Sun. Traditionally, PUIs are neutrals of non-solar origin which are ionized through photoionization, charge exchange with solar wind ions, or through electron impact ionization as they travel closer to the Sun. Once ionized, the ions begin to gyrate around the interplanetary magnetic field and flow as part of the solar wind. PUIs are distinguished from solar material by their non-thermal VDFs, as shown in Figure 1.22. PUIs form VDFs that uniformly cover velocities up to twice the solar wind speed, that contrasts the narrowly peaked Maxwellian distribution formed by solar wind ions (Möbius et al., 1985; Chalov & Fahr, 1998; Gloeckler et al., 1993; Drews et al., 2016). Their velocity distribution is a result of newly formed PUIs that become accelerated by the field, forming a ring velocity distribution between zero to twice the solar wind speed in the reference frame of the spacecraft. Through subsequent fast pitch-angle scattering processes and continued adiabatic expansion of the solar wind, the ions form a shell distribution and continue to evolve towards thermodynamic equilibrium. Compared to the interstellar PUIs, the inner source ions appear to be more coupled to solar wind properties, such that the distributions begin to form a peak. This is a result of the ions being formed closer to the Sun which provides them with time to thermalize before their detection in the heliosphere.

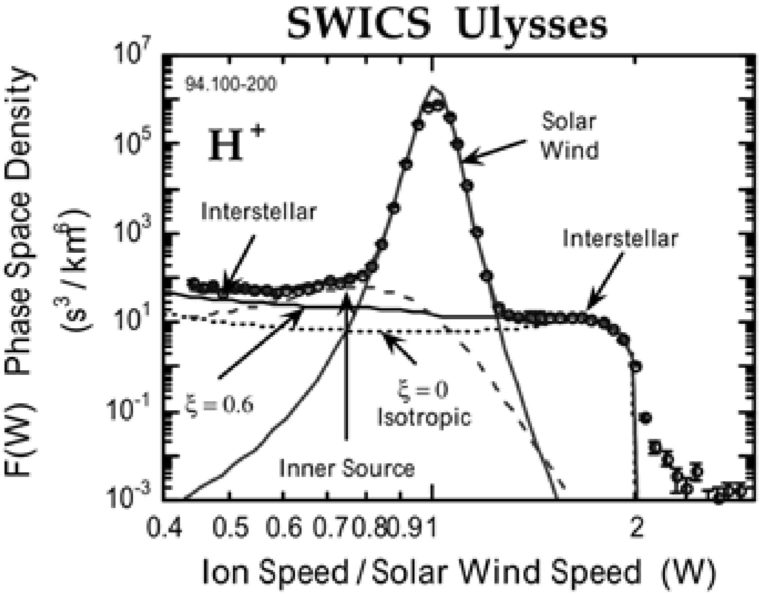

Figure 1.22: Velocity distribution function for H^+ measured by Ulysses taken from Gloeckler & Geiss (1998). The plot shows a contribution of ions from the solar wind, and both interstellar and inner source pick up ion populations.

The interstellar PUIs have a well constrained source however it is still unclear how the dust and solar wind interact to form the inner source ion population. The leading two models include; 1) recycling (Gloeckler et al., 2000), and 2) neutralization (Wimmer-Schweingruber & Bochsler, 2003) of the solar wind. In the recycling model, the solar wind ions are implanted on the dust and are released as neutrals, while in the neutralization model, the ions collide with dust grains immediately becoming neutralized. In both cases, the neutrals outgassed by the dust become ionized and picked up by the radially convecting solar wind.

However, it remains unclear how the interaction between the solar wind and dust alters ion densities in the solar wind. Once neutrals form through the models described above, several processes compete to ionize them; electron impact ionization, photoionization, and recombination through charge exchange with solar ions. These processes can become important at different distances from the Sun, however the net effect is undetermined. It is important to quantify this interaction to: 1) accurately simulate the evolution of solar charge states with ionization codes to rigorously constrain the ionization and recombination processes taking place, 2) to determine the formation of low ionized material in solar plasma from the presence of the dust, and 3) to constrain dust distribution and grain size that remains relatively unknown in the vicinity of the Sun.

Early studies of the interaction of neutrals from dust and the solar wind are not well constrained because of the lack of observations associated with this process, along with the uncertainty in the distribution of interplanetary dust density and grain size (Banks, 1971; Fahr et al., 1981; Gruntman, 1994, 1996), as will be discussed in Section 1.5.2. However, the studies predicted the importance of the formation of neutrals and singly ionized solar material due to charge exchange processes with interplanetary dust neutrals.

1.5.2 Brief overview of remote and in situ dust observations

The dust in the heliosphere can be seen illuminating the sky along the ecliptic plane during twilight, known as the zodiacal light, as seen from Earth shown in Figure

Figure 1.23: Taken at Teide National Park on Tenerife, in the Canary Islands

1.23[4]. The zodiacal light is just one of three parts that comprise light from the Sun's corona which include the E-corona, K-corona, and F-corona. The E-corona is the emission of the particles in the Sun's corona. The K-corona is produced through the scattering of photospheric light by free electrons in the corona, referred to as Thomson scattering. The F-corona is a result of photospheric light scattered by small particles of interplanetary dust surrounding the Sun which forms the zodiacal light that extends out into the heliosphere. In addition, the dust emits blackbody radiation that produces emission that peaks in the infrared corresponding to its temperature of $270 \cdot (R_E/r)^2$ (K) (Kaiser, 1970; Peterson, 1971; Kimura & Mann, 1998).

The F-corona, and therefore the dust, generally appears stable in shape across the solar cycle, indicating a continuous presence along the solar wind path (Leinert et al., 1983). However, one of the primary inhibitors to the progress in our understanding of

---

[4] `https://www.flickr.com/photos/starryearth/40034769572/`

the solar wind and dust interaction is due to large uncertainties in the distribution of grains that constitute the dust. The dust can be inferred from white light and infrared emission of the F-corona, as well as through in situ observations of dust and ions, however they generally disagree (Kimura & Mann, 1998). The grain size distribution is described by the geometric factor, Γ, which represents the dust cross-sectional area per unit volume as follows,

$$\Gamma(r) = \int_{s_{min}}^{s_{max}} \pi s^2 f(s,r) ds \tag{1.11}$$

where s is the radius of the grain, $f(s,r)$ is the distribution of grains with grain radius, s, and distance from the Sun, r. At 1AU, in situ measurements of He^+, assumed to originate from the ionization of dust released He, estimate Γ to be on the order of 10^{-17}, while observations in the optical and near-infrared, derive values that range between $10^{-21} - 10^{-18}$ (Banks, 1971). The discrepancy ranges 5 order of magnitude which has made it difficult to meaningfully quantify the dust's interaction with solar plasma. In addition, Γ is assumed to change with distance from the Sun which can mean the distribution of grain size may be significantly different at the Sun compared to where in situ measurements are made.

One method of constraining the interplanetary dust distribution, and its effect on the solar wind, is through in situ observations of the neutral density and dust in vicinity of the Sun where charge exchange processes are likely taking place. However, these measurements are unavailable with current and planned solar and heliospheric missions. Another method is by examining the solar wind for signatures of the solar wind-dust interactions, such as by investigating low ionized material present in the solar wind that are outside of cool prominences within CMEs. Analysis of the low ionized material in the normal solar wind can be used to characterize this interaction, along with the dust environment near the Sun (Mann et al., 2010). This interaction can indicate the role interplanetary dust plays in the formation of low charge states and the importance of charge exchange processes along the propagating of solar plasma to improve current ionization modeling.

1.6 Motivation for Thesis Work

The primary science questions addressed in this thesis are derived from understanding the origin and evolution of low ionized material observed at 1AU. The work throughout the thesis has been previously published in The Astrophysical Journal; Chapter II in Rivera et al. (2019b), Chapter III in Rivera et al. (2019a), and Chapter1.5 in Rivera et al. (2020).

The work in Chapter II addresses the following question,

1. What is the fate of neutral and low ionized material in prominences and how is the CME heated?

As described previously, there is much uncertainty surrounding the fate of neutral and low charge states of prominences in CMEs. In Chapter II, we simulate the ion evolution within the radial propagation of a CME using the MIC to determine the conditions in which CME structures evolve to reproduce in situ charge state measurements. We reconstructed the charge state distributions from a CME on the list of Lepri & Zurbuchen (2010), and further investigated in Gilbert et al. (2011), which contained a continuous signal of low ionized C, O, and Fe that is suggested to originate from prominence material measured together with typical highly ionized plasma. This work aimed to determine the thermodynamic evolution that would reproduce these observations to determine if the low ionized material originated from prominence plasma, or if the ions observed were a product of recombination processes of hot plasma. The plasma temperature, density, and velocity derived are used to compute CME energetics for the event which provides the power required during the eruption and subsequent evolution to heat and accelerate the CME. These results are important constraints for determining the contribution of and timescale in which energy is deposited to CME structures to identify the mechanism(s) at work.

To continue testing our modeling results, it is necessary to couple properties of CMEs at the Sun with nonequilibrium modeling and in situ observations. Chapter III addresses the following science question,

2. Which spectral lines will enable the comprehensive study of solar eruptions with upcoming solar observatories?

The structures derived in Chapter II, consisted of a mixture of plasma from the prominence, PCTR, and adjacent corona, each with distinct heating, cooling, and expansion rates. These results suggested that in order to capture the full extent of heating experienced by all CME components, it is necessary to analyze spectra of the prominence and adjacent structures together. Chapter III is motivated by a need for a comprehensive list of useful spectral lines formed by the multi-thermal CME structure. The study was designed for complementary ground-based observations with DKIST and UCoMP, and with space-based EUV spectrometer, SPICE, on Solar Orbiter. Combined, these instruments extend the spectral range and the FOV in which CME diagnostics can be carried out, which can often pose limitations to CME science. We include a list of the most observable lines formed within the prominence, and adjacent material, along with a discussion of their diagnostic potential for future observations.

Throughout Chapters II and III, low ionized material of solar origin was attributed to the presence of prominence material in the heliosphere. In Chapter IV, we study the manifestation of singly ionized He in the solar wind centered around the following science question,

3. What is the origin of singly ionized He outside of CME cores and how is it formed?

As mentioned in Section 1.5, the solar wind can interact with dust throughout the interplanetary medium and has been tied to the production of inner source ions. However, it remains unclear how the dust modifies and interacts with solar wind ions. In this work, we aim to determine the source of He^+, where and how He^+ is formed, and its potential connection to interplanetary dust. The modeling results provide a method of quantifying the interaction between dust and the solar wind. Also, it predicts the structure of dust in the vicinity of the Sun, which remains highly uncertain between remote and in situ observations. Apart from the immediate science addressed, constraints to the dust environment can be useful for current and future solar probes that are exposed to dust near the Sun.

CHAPTER II

Empirical Modeling of CME Evolution Constrained to ACE/SWICS Charge State Distributions

2.1 Background

Coronal mass ejections (CMEs) are eruptions that release enormous amounts of ionized material into the interplanetary medium (IM). Earth-bound CMEs are the main drivers of geomagnetic storms which can cause damage to satellites orbiting the Earth and electronics on the ground directly affecting modern society (Koskinen & Huttunen, 2006). They are traditionally observed near the Sun to be composed of a multi-part structure, with a compressed leading edge followed by a tenuous cavity, both at coronal temperatures ($> 10^6$K), and trailed by a denser core component, typically associated with a prominence, made up of cooler chromospheric plasma ($< 10^5$K) (Labrosse et al., 2010; Parenti, 2014). The cool prominence material can maintain neutral and singly ionized charge states that absorb extreme ultraviolet (EUV) radiation causing it to appear dark in EUV images while the neighboring structure contains significantly higher ionization states, as inferred from its emission of spectral lines from those ions (Giordano et al., 2013).

Once in the IM, the degree of ionization and composition of solar wind plasma is often used as an observational signature to link in-situ heliospheric phenomena to structures at the Sun. The ionization state of plasma is a powerful diagnostic, not only in the identification of Interplanetary CMEs (ICMEs) but also in the characterization of different structures within the CME boundary, such as prominence material or flare heated material (Lepri et al., 2001; Reinard, 2005; Lepri & Zurbuchen, 2010; Gilbert et al., 2012; Richardson & Cane, 2010). This is possible as a result of the freeze-in process which renders the charge states in the plasma fixed within some distance from the Sun effectively preserving information about the local environment. The process occurs as the expanding plasma reaches a distance where the density becomes too low for ionization and recombination processes to take place (Hundhausen et al., 1968). Beyond this freeze-in height, the ions are unchanged and remain imprinted with the plasma's thermodynamic history from below the transition point as they journey through the heliosphere.

However, below the freeze-in point, the plasma may experience some level of heating due to the energy released throughout the CME eruption process that may alter its ionization state. In fact, spectroscopic diagnostics applied to an erupting prominence in the lower corona using coupled Hinode/EIS (Culhane et al., 2007) and SOHO/UVCS (Kohl et al., 1995) high-resolution spectra measure a significant increase in thermal energy of the core between 1.1 and $1.9R_\odot$ (Landi et al., 2010). Similarly, other studies find evidence for continuous heating and a corresponding thermal energy that is significantly larger or comparable to the plasma's kinetic energy, making the heating process key to understanding the eruption (Akmal et al., 2001; Rakowski et al., 2007, 2011; Murphy et al., 2011; Lee et al., 2015, 2017; Kocher et al., 2018). Currently, the underlying mechanism for this heating process remains largely uncertain; however, ions within ICMEs may provide clues to the energy deposition close to the Sun.

To date, efforts aimed at identifying a potential mechanism remain inconclusive.

Landi et al. (2010) found that certain proposed mechanisms such as wave heating induced by photospheric motions, thermal conduction and internal shocks were unfeasible to maintain the thermal energy requirements for their observations. However, given the limited number and field of view of the observations available, their measurements were not able to capture the full heating process, missing much of the evolution. Similarly, in a parametric study using an ionization code to constrain plasma heating of different plasma structures for an eruptive event, Murphy et al. (2011) found many of the mechanisms considered (thermal conduction, energetic particles, wave heating, local small-scale reconnection events, current sheet dissipation) were not definitive sources for the heating, adding that further constraints were necessary.

This work sets out to quantify the heating beyond the current field of view of remote sensing observations to capture the full CME evolution. Our approach is to probe the thermal history of the plasma near the Sun by examining the heliospheric ion properties of the ejecta. As mentioned, the ion distributions, unlike other plasma properties, will retain information of heating and cooling experienced below their freeze-in distance as they travel through the heliosphere which provides indirect access to plasma temperature during the early stages of evolution. Through simulations of the freeze-in process of ion distributions, we can recreate compositional observations to empirically determine the thermodynamic properties of plasma. Previous work employing a similar approach targeted recreating the bi-modal peaks standard to Fe distributions, and in a later study additional features as well, within ICMEs to derive properties of their evolution (Gruesbeck et al., 2011, 2012). Their results indicate that rapid heating and subsequent adiabatic cooling and expansion generated ionic profiles compatible with some features of the C, O, Si and Fe distributions of their event. Here we test profiles outside of the adiabatic assumption to account for the transfer of energy between the plasma and the local environment. In addition, we aim to reproduce the entire distribution of C, O and Fe, including measurements of low-ionization charge states previously unavailable, providing more accurate results.

Then, we investigate the contribution to the total energy deposition and loss rates of several heating and cooling processes that can be estimated from the derived properties of the CME. These values will provide useful constraints to a future complementary study that will focus on evaluating the viability of proposed energy mechanisms through an extensive comparison with an magnetohydrodynamic (MHD) CME simulation.

2.2 ICME event

The ICME event we chose to reproduce was detected in-situ from a combination of Solar Wind Ion Composition Spectrometer (SWICS; Gloeckler et al. 1998) and Solar Wind Electron, Proton, and Alpha Monitor (SWEPAM; McComas et al. 1998) measurements on the Advanced Composition Explorer (ACE; Stone et al. 1998) spacecraft at the L1 Lagrange point between 2005 January 8 21:00UT - 2005 January 9 18:00UT as listed in the Richardson & Cane (R&C) ICME catalog[1] and displayed in a multi-panel plot in Gilbert et al. (2012) (Figure 3). This filament has also been the focus of another study investigating its geoeffectiveness at Earth (Sharma et al., 2013). The R&C catalog contains a list of events detected near 1 AU that are identified using a combination of plasma, magnetic field and compositional signatures as outlined in Cane & Richardson (2003) and Richardson & Cane (2010). Among the ICME boundaries, the comprehensive list often provides a date to the event's CME counterpart at the Sun. The ICME in the present study is linked to a prominence eruption that drives a halo CME on 2005 January 5 15:30UT as first observed by the solar coronagraphs from the Large Angle and Spectrometric Coronagraph (LASCO; Brueckner et al. 1995) aboard the Solar and Heliospheric Observatory satellite (SOHO; Domingo et al. 1995) and is associated with a weak B-class flare as observed from the soft X-

---

[1] `http://www.srl.caltech.edu/ACE/ASC/DATA/level3/icmetable2.htm`

ray flux detected by the Geostationary Operational Environmental Satellite (GOES) provided in the Coordinated Data Analysis Workshops (CDAW) catalog[2].

The ICME event was chosen from a list compiled by Lepri & Zurbuchen (2010) which was found to contain low ionization states e.g. C^{2-3+}, O^{4+} and Fe^{4-7+}, of filamentary origin, detected together with hotter ions spanning several hours within the CME cloud. Further investigation by Gilbert et al. (2012) reported that this event contained even lower ionization stages within the interval stated e.g. C^{+}, O^{+} and Fe^{2-3+}. This CME is of particular interest to this study because it contains ions with equilibrium ionization temperature between 10^{4-5}K which are believed to have evolved within the cooler parts of the CME at the same time but independent of highly ionized charge states (O^{7-8+}, C^{6+}, Fe^{16+}) that are typically found in solar ejecta (Lepri et al., 2001; Henke et al., 2001; Richardson & Cane, 2004). Together they provide a wider distribution of ions placing more stringent constraints to our modeling results.

The ion distributions used to constrain the plasma models are a combination of the low and singly charged states that are not part of the traditional SWICS dataset, along with the standard higher ionized charge states observed by the instrument. The standard ion detection method for SWICS uses the ion's selected energy-per-charge from the electrostatic analyzer's corresponding voltage step, speed from the time of flight (TOF) measured by the start and stop signals from the secondary electron detector, and the total energy recorded by a solid state detector. These three independent values identify the higher charge states whose energy per charge falls well within the instrument's range of $0.49 - 100$ keV e^{-1}. These are referred to *triple coincidence* events where the TOF start and stop signals, along with the total energy is measured in coincidence and follows the typical processing procedure (von Steiger et al., 2000; Shearer et al., 2014). Low and singly ionized charge states whose

---

[2] `https://cdaw.gsfc.nasa.gov/CME_list/`

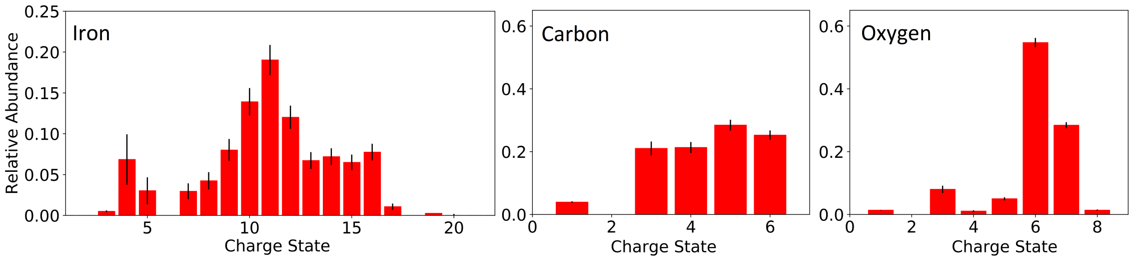

Figure 2.1: Relative abundance distributions with corresponding error bars of Fe, C and O collected by ACE/SWICS within a two hour window during the 2005 January 9 ICME event.

total energy cannot be recorded by the instrument because the ion's energy is usually lower than the energy threshold of the solid state detector, can still trigger the start and stop signals, leading to *double coincindence* events. Triple coincidence events allow for a straightforward determination of the ion's charge, mass, and energy while double coincidence events can only provide the mass-per-charge and speed of the particles. The double coincidence events are limited and require specific extraction from the SWICS raw dataset as detailed in Gilbert et al. (2012). This dataset provides measurements from C^{+}, O^{+} and Fe^{2-5+} that can be unambiguously extracted from the double coincidence events given small overlap in their distributions to other ions on the mass-per-charge spectrum. The advantage of combining double and triple coincidence ions in this study is that it provides measurements of cold plasma that would otherwise be invisible in the triple coincidence events.

To constrain our models, we use charge state distributions of C, O and Fe that are collected in a two hour window within the ejecta where the singly ionized charge states were observed, between 2005 January 9 09:00-11:00UT, as shown in Figure 2.1. We omit C^{2+} and O^{2+} charge states, taken from the double coincidence measurements, in our distributions due to their significant overlap with Fe^{7+} and Fe^{9+}, respectively, making their signal too convoluted to provide a reliable measurement.

2.3 Methodology

We derive the electron density, n_e, electron temperature, T_e, and bulk velocity, v_{bulk}, for a CME as it propagates between initiation at the Sun through the ion freeze-in range of several ion species by modeling the evolution of abundances using our in-house ionization code. Through a parametric search, we vary the n_e, T_e, and v_{bulk} profiles, each governed by a set of parameters, until a match between simulated frozen-in ions generated through the ionization code and the CME observations is reached. Once agreement between the charge state distributions is found, the n_e, T_e, and v_{bulk} derived will be used to determine the energy evolution and heating requirements for our event.

2.3.1 Michigan Ionization Code

To model the freeze-in process, we use the 1D Michigan Ionization Code (MIC) (Landi et al., 2012a), that solves a system of equations describing the ionization stages of each ion in the plasma to produce the element's charge state distribution as a function of radial distance from the Sun. The code solves the time-dependent ionization equation using recombination and ionization rates from the CHIANTI 8 atomic database (Dere et al., 1997; Del Zanna et al., 2015) and is given by,

$$\begin{aligned}\frac{dy_i}{dt} &= n_e \left[y_{i-1} I_{i-1}(T_e) + y_{i+1} R_{i+1}(T_e)\right] \\ &+ y_{i-1} P_{i-1} - y_i \left[n_e \left(I_i(T_e) + R_i(T_e)\right) + P_i\right] \end{aligned} \tag{2.1}$$

where y_i is the ion's relative abundance of the given element in charge state i, n_e is the electron density, T_e is the electron temperature, $R(T_e)$ and $I(T_e)$ are the recombination and ionization rates, respectively, and P is the photoionization term described as,

$$P_i = \int_{\nu_i}^{\infty} \frac{4\pi J(\nu)\sigma_i(\nu)}{h\nu} d\nu \qquad (2.2)$$

where $J(\nu)$ is the mean spectral radiance of the Sun, $\sigma(\nu)$ is the photoionization cross-section for ion i, h is the Planck constant and ν is the frequency for the ion's corresponding ionization energy. The model incorporates ionization and recombination mechanisms from the following processes that are relevant in the coronal plasma regime: excitation-autoionization, dielectric re-combination, collisional ionization, radiative recombination and includes the effects of EUV and X-ray photoionization. The photoionization term becomes increasingly important once collisional effects are reduced in the expanding plasma. In particular, photoionization has been shown to become a significant process for $\mathrm{Fe}^{\geq 16+}$ and $\mathrm{O}^{\geq 7+}$ prior to the plasma freeze-in height for models of the solar wind (Landi & Lepri, 2015). Those ions are common to ICME plasmas and can be found in our current event, making photoionization effects highly relevant to our present study.

The main MIC inputs are user-specified n_e, T_e, and v_{bulk} of the plasma as a function of radial distance from the Sun, as well as the daily averaged solar photoionization intensity from space observations. The calculation can be carried out for all elements between Hydrogen and Zinc to conveniently match any of the observations. MIC assumes that the plasma at the base of the solar wind, before being accelerated, is in thermodynamic equilibrium and that the plasma free electron velocity distribution can be described by a Maxwellian throughout its propagation. A thorough description of the MIC and of its strengths and approximations can be found in Landi et al. (2012a).

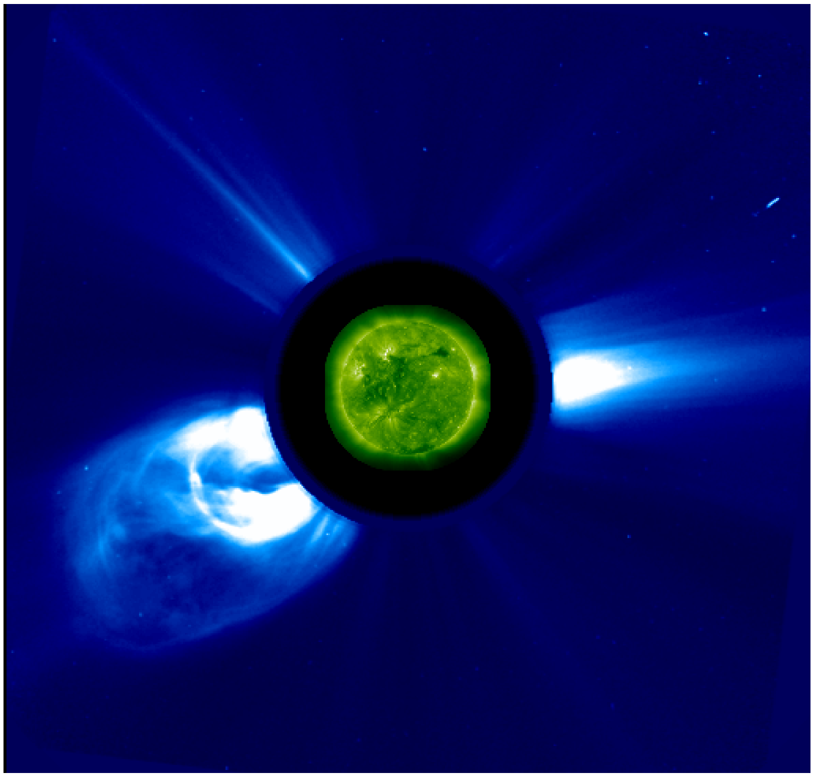

Figure 2.2: A composite image showing a classic CME three-part structure: dense leading front, central void, and trailing core. The center image is taken by SDO/AIA in the 193 Å waveband which is surrounded by a white light image from C2 SOHO/LASCO on 2010 December 6 20:24UT. The southeast limb event was used to construct the initial density and velocity profiles described in Section 2.3.2.

2.3.2 MIC Density, Temperature and Velocity Input Profiles

We construct approximated initial input profiles to run the ionization code from an ensemble of remote sensing observations. At this stage, the profiles are meant to be a crude estimate to the evolution which are then modified during the iteration process.

2.3.2.1 Remote Sensing Observations

Remote sensing observations in the lower corona are used to estimate the electron density and velocity of the plasma along its trajectory to construct the input profiles

Table 2.1: Initial parameter ranges to the Search Algorithm.

Plasma	c_1	c_2	c_3	c_4	c_5	c_6	c_7
Cool	$1 \times 10^{9-11}$	$0-2$	$1-8 \times 10^5$	$0.1-1$	$0.1-1$	0.5-1	2
Hot	$1 \times 10^{7-8}$	$0-2$	$1-8 \times 10^6$	$0.1-1$	$0.1-1$	0.5-1	2

for the MIC. The ICME in the present investigation, described in Section 2.2, is linked to a halo CME at the Sun. The halo CME is directed towards the solar imagers making it difficult to visually track along its trajectory. Therefore, for this step we substitute observations from a similar CME erupting close to the solar limb, shown in Figure 2.2, to follow its evolution more easily. The limb event reduces projection effects caused by motion outside of the plane of the sky, providing less ambiguity in measurements along the CME's trajectory. It is important to note that the results will be used only as a starting point for our work and not need to be accurate.

Using the CDAW database, the limb event was specifically selected to undergo similar acceleration to the halo CME, such that a compatible velocity profile was constructed. Furthermore, we searched for a limb eruption that contained the same order of magnitude mass and similar kinetic energy as determined by the CDAW analysis for further compatibility. The limb eruption chosen occurred on 2010 December 6 at approximately 14:33 UT on the southeast limb of the Sun as seen in the high cadence full disk images in the 193Å waveband taken by the Atmospheric Imaging Assembly (AIA) aboard the Solar Dynamics Observatory (SDO; Lemen et al. 2012). The event is associated with a filament eruption with no significant indication of an associated flare. The CME can be observed in the SDO/AIA FOV between 14:33UT-16:04UT capturing the CME between the solar surface and 1.3 solar radii ($R_\odot$). Beyond the SDO FOV, we use a sequence of white light observations from LASCO C2 & C3, with a combined FOV of $1.5-30R_\odot$, starting at 17:24UT until the plasma is out of view.

2.3.2.2 Constructing the profiles

For the purpose of constructing the electron density profile, we assumed the plasma to be a self-similar expanding sphere in the series of EUV and white light images which is more or less consistent with observations at this height (Wood et al., 2016). Within SDO/AIA's FOV, we calculated the radius of the cloud in 12 minute cadence as it moves away from the surface until the filament is no longer visible. The radius is estimated by taking half of the average diameter, which in turn is taken to be the mean of its radial and perpendicular-to-the-limb size at each frame. Similarly, we continue to record the radius of the cloud along the white light images out to $30R_{\odot}$ with SOHO/LASCO. We calculate the volume of the sphere, $V_{CME}(r)$, at each radial distance, r, along its expansion where we assume the mass remains constant. We estimate the changing number density to be related to the inverse of the volume of the expanding plasma as, $n_e(r) \propto 1/V_{CME}(r)$, where n_e is the electron density.

Equation 4.4 displays the density profile used in the iteration process,

$$n_e(r) = \frac{c_1}{V_{CME}(r)} \cdot \frac{1}{r^{c_2}} \tag{2.3}$$

where there are two parameters used to adjust the density profile; the first, c_1, is the initial boundary density. The second is the power to a decaying power law function multiplied to the original density profile to vary the plasma's expansion rate, given by $\propto 1/r^{c_2}$, where c_2 is the parameter that is varied in the search. This will test density profiles for plasma expanding slower or faster than adiabatic.

The velocity profile was generated by estimating the velocity of the CME between each frame at 24 minute cadence along the plane of the sky using a series of white light images from C2 & C3, while beyond this height we assume the plasma travels at a constant velocity. We also assume no differential flow between ions meaning all particles travel at the same velocity. We calculate the average velocity of the plasma structure at each snapshot by measuring the distance traveled by the leading edge between each frame and divide by the total travel time. Initially we constructed two profiles; the first traced the compressed leading edge and the second followed the dense core of the CME, which do not necessary travel together (Wood et al., 2016). In this case, we find that both have similar acceleration while traveling in the corona, leading to nearly parallel velocity profiles except that the leading edge has a larger velocity compared to the filament within the $30R_\odot$ FOV. As will be described further in the text, we plan to adjust the velocity to match our event's approximate transit time. This permits for the arbitrary selection of either profile as the main MIC input and therefore we utilized the profile determined for the CME core.

Unlike the density profile, the velocity profile is not governed by any parameters because it is not varied in the iterative search. To be consistent with the observed transit time of the event in the present study, the velocity profile is adjusted before the iteration process such that it propagates the simulated plasma to 1 AU with a matching propagation time to the event. The 2005 January 9 event has a transit time of 3.81 days based on an eruption time of approximately 2005 January 5 13:30UT as observed with the Extreme-Ultraviolet Imaging Telescope (EIT; Delaboudinière et al. 1995) on the Solar and Heliospheric Observatory (SOHO) and arrival time of 9:00UT on 2005 January 9 from the ACE/SWICS measurements. We determine a single velocity profile to match the propagation time which remains unchanged throughout the search to restrict the plasma arrival to within the two hour window observed in-situ.

Lastly, the temperature profile is generated using a function composed of several variables we use to alter its shape in the iteration process. It can be adjusted using four main parameters that serve to increase the peak temperature, c_3, control the spread of the function producing prolonged or more rapid heating and cooling, c_4, that shift the peak temperature in the radial direction, c_5, and adjust the cooling rate, c_6, described by the following equation,

$$T_e(r) = c_3 \frac{(c_4 \cdot r)^{c_6}}{r - c_5} \exp(\frac{-c_4}{r - c_5})^3 \tag{2.4}$$

where r is the heliocentric distance. Gruesbeck et al. (2011, 2012) results demonstrate that a temperature profile with rapid heating and subsequent adiabatic cooling produced a reasonable match to many of the peaks found in the C, O, Si, and Fe distributions they aimed to reproduce. We expand on this in the present work with the function in Equation 2.4 that will allow us to test a broad range of scenarios, not limited to the adiabatic process, to account for heating from processes beyond plasma compression. This includes plasma that is significantly heated as it travels through the corona, whose peak temperature is reached along its propagation, as well as plasma that experiences no increase in temperature as it propagates away, both whose cooling patterns can be faster or slower than adiabatic.

Both the velocity and density are constructed using 65 data points from observations between $1.1 - 30R_\odot$. We perform a spline interpolation between the sparse values, using IDL program INTERPOL.PRO, for smoother transitions between timesteps (or spatial steps) in the n_e, T_e, and v_{bulk} along the propagation path.

Each set of MIC profiles are associated with a set of 6 parameters, $c_1 - c_6$ where each combination of parameters form the n_e, T_e, and v_{bulk} profiles that govern the distinct evolution of each plasma component (PC) determined. In addition, we include one additional parameter, c_7, representing the total number of independently modeled PCs whose simulated ions are combined to form a single distribution. This parameter permits the resulting distribution to be composed of ions generated by several PCs with distinct thermal histories.

2.3.3 Search Algorithm

We empirically determine the CME properties through a heuristic process by varying the input profiles of the MIC to find agreement between the modeled frozen-in values and observations. To make our search more efficient and systematic, we constructed a Search Algorithm (SA) that executes the MIC through a series of pre-defined iteratively adjusted n_e, T_e, v_{bulk} profiles where each set simulates the distinct evolution of the selected ion species.

The main inputs to the SA are the following:

1. A set of initial profiles to run the MIC;
2. A range and step size for all parameters to vary the input profiles;
3. The measured relative abundance of each ion, to be compared with the simulated value.

We employ the chi-square test to quantify the deviation between the observed and predicted frozen-in ions, e.g. all ions for C, O and Fe. For each run, the SA calculates and tracks the lowest chi-squared value, defined as $\chi^2 = \sum_{i=1}^{N}(P_i - O_i)^2/O_i$ where N are the number of available ions, P and O are the predicted and observed relative abundances, respectively. We aimed to meet a significance level of 90% which corresponds to a critical χ^2 of 0.584, 0.211, 0.016 for 3, 2, 1 degrees of freedom (DOF), respectively, where the DOF here is $\mathrm{c}_7 - 1$.

After searching the parameter space specified, the SA returns the set of parameters associated with the profiles that produced the lowest χ^2 value from the entire search. This process is refined by repeating the SA with parameter ranges honed in to the results from the previous search and accompanied by a reduction of the increment size. The SA was repeated until the χ^2 result converged to a value below the critical χ^2 with a minimum number of DOFs.

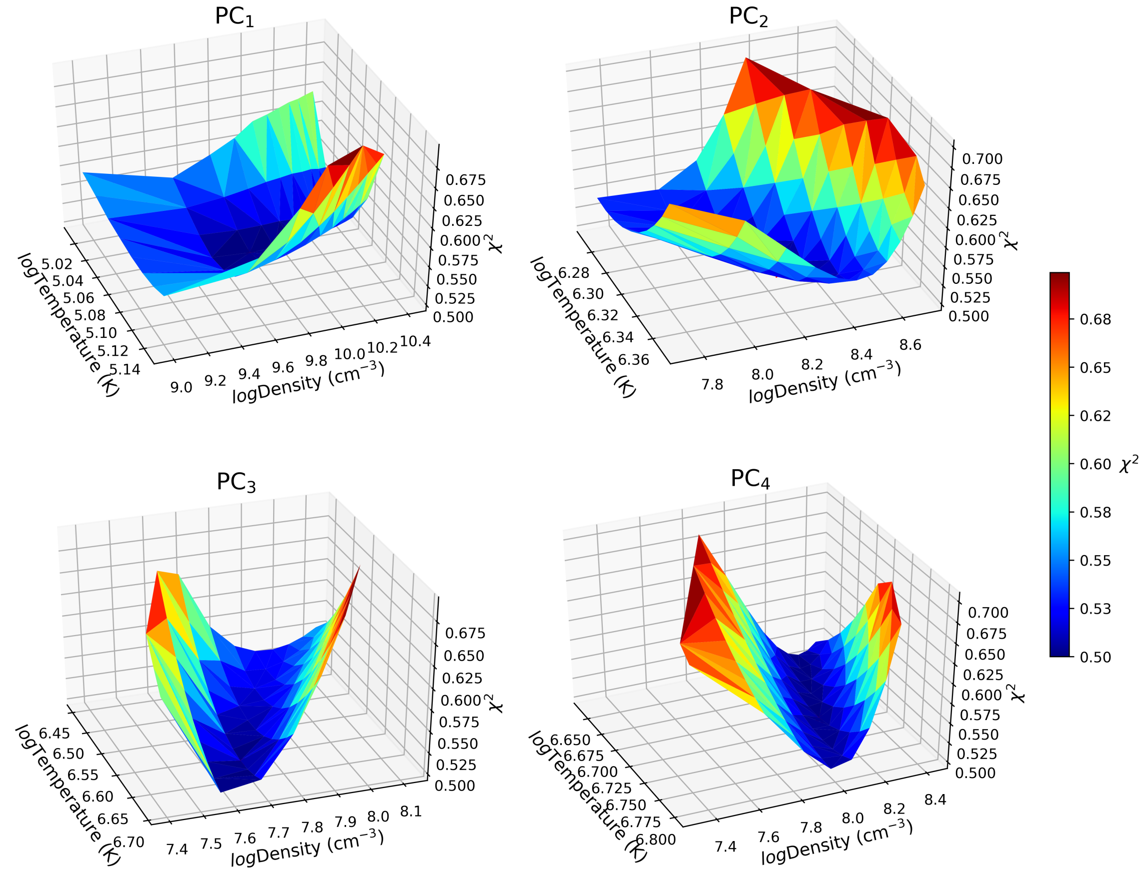

Figure 2.3: Surface χ^2 plots for each PC from our results (the triangular shapes are an artifact of the plotting procedure and are not meaningful). Vertical axis is the χ^2 value, horizontal axes are a range of initial density and peak temperature. The plots were generated by varying the initial density and peak temperature of the corresponding PC while holding the remaining PCs constant.

2.4 Charge State Modeling Results

2.4.1 Search Procedure

All together there are 7 free parameters that are varied in the SA; $c_1 - c_6$, associated with the input density and temperature profiles for each PC, plus an additional parameter for the number of PCs added together, c_7.

The process began with two PCs, a cool and hot plasma, intended to cover the scope of frozen-in temperatures from the observations. This is motivated by results from Gruesbeck et al. (2012) which utilized a two plasma model to recreate the ion distribution from a period containing prominence material. Table 2.1 lists the parameters chosen for the initial guesses. We have assumed the majority of the plasma is of coronal origin as previously found in comprehensive studies of the compositional makeup of CMEs therefore the PCs initially contain coronal composition (Reisenfeld et al., 2007; Zurbuchen et al., 2016).

We considered initial density and temperature whose boundary values range between those found in typical CME structures. We searched for erupting prominence material by using initial values typical of prominence material: log $n_e = 9 - 11$ and log $T_e = 4 - 5$ (Labrosse et al., 2010). Furthermore, we also analyzed values covering the properties of the warmer leading edge and cavity plasma, log $n_e = 7 - 8$ and log $T_e > 6$ (Chen, 2011).

We proceeded to find the minimum number of combined PCs that would meet the χ^2 criteria stated previously. Through extensive trial/error and the intended purpose of minimizing the total χ^2 value, we subsequently refined and incorporated additional PCs in subsequent searches until our threshold value was reached. For the additional PCs, we extended our search to testing values from the adjacent Prominence-Coronal Transition Region (PCTR) which is an interface layer acting as the main separation between the prominence and the coronal plasma. The PCTR layer is cooler than typical coronal plasma though warmer than the main core of the prominence, with a temperature that ranges between 10^{4-6}K (Labrosse et al., 2010). Its density is found to be much lower than prominence material, and can range several orders of magnitude between 10^{6-8} cm^{-3}.

Furthermore, after the search, through a simple algorithm that adjusted each PC's final weight in the full distribution, we obtain the optimal ratio between all PCs to produce the final χ^2 value.

Table 2.2: Final parameter for the Search Algorithm.

PC	c_1	c_2	c_3	c_4	c_5	c_6	c_7
1	8.79×10^9	0.92	1.10×10^5	0.90	0.52	0.93	4
2	2.57×10^8	0.00	4.20×10^6	0.10	0.40	0.50	4
3	6.61×10^7	0.25	6.10×10^6	0.90	0.90	0.70	4
4	1.97×10^8	0.25	8.00×10^6	0.60	0.90	0.73	4

2.4.2 Charge State Distributions

Based on the final χ^2 results, we find that a minimum of 4 PCs were required to reach the desired significance level corresponding to a threshold χ^2 value of 0.584 with a minimum of 3 DOF. The final parameters for each PC are listed in Table 2.2 which result in a final χ^2 of 0.505

Figure 2.3 displays a surface plot for each PC showing the χ^2 plotted on the vertical axis, and initial density and peak temperature are on the horizontal axes in log scale. For each plot we vary the initial density and maximum temperature of the single PC while maintaining the remaining PC parameters constant to demonstrate the χ^2 sensitivity of the surrounding parameter space. For PC_1, the final plot exhibits a valley-type shape with a base nearly parallel to the density axis. This shows PC_1 has a stronger dependence of the peak temperature as compared to the initial density of that plasma in this regime. PC_2 displays a bowl feature with a base that is not visibly aligned with either axes instead appears correlated such that the χ^2 remains low as both the peak temperature and initial density of the plasma increase. While the χ^2 values for $PC_{3,4}$ show slight anti-correlated behavior where an increase in the peak temperature favors a decrease in the initial density of the PC.

Initially all PCs are added together with equal 25% contribution. We proceeded to further optimize the distributions by adjusting the weights. Prior to running this optimization, we noticed that the Fe^{3-6+} states, which are entirely due to PC_1, were systematically higher than the observations, while C^{3+} and O^{3+}, also entirely due to PC_1, were well reproduced. For this reason, we explored the possibility that the composition of PC_1 may not be the same to the rest as a result of the First Ionization Potential (FIP) effect which can produce elemental fractionation among different solar structures (Laming 2015 and references therein). This compositional variation also manifests in the heliosphere as elemental abundance ratios can differ within solar wind types and periods containing CMEs (Pilleri et al., 2015). With this in mind, we adjust the contribution from PC_1 in the Fe distribution separately to the PC_1's contribution in C and O in this step.

Similarly, a distinct mixing ratio between C, O, Fe is found in results for the two plasma model in the Gruesbeck et al. (2012) prominence study. The treatment of adjusting the Fe/C/O contributions within the plasma hinted to compositional variation between the cool/hot plasma components. We further expand upon the implications of changing the Fe/C and Fe/O in terms of FIP effect in Section 2.5.4.

The final normalized ratios for each component are shown for Fe, in Equation 2.5, and for C and O, in Equation 2.6.

$$\text{Fe} : 0.10PC_1 + 0.33PC_2 + 0.33PC_3 + 0.24PC_4 \tag{2.5}$$

$$\text{C-O} : 0.28PC_1 + 0.26PC_2 + 0.26PC_3 + 0.20PC_4 \tag{2.6}$$

This final mixture of components reduces the total χ^2 value by 47.5%, producing a final $\chi^2 = 0.259$ which is a sum of the individual χ^2 of 0.128, 0.097 and 0.035 for the C, O and Fe distributions, respectively. Our final value is well below our original threshold value of 0.584 (3 DOF) for 90% significance level, in fact we reached a value below 0.352 (3 DOF) which corresponds to 95% significance level.

The final distributions from these results are presented in Figure 2.4 where the bars outlined by dashed red lines show the observed values with corresponding error

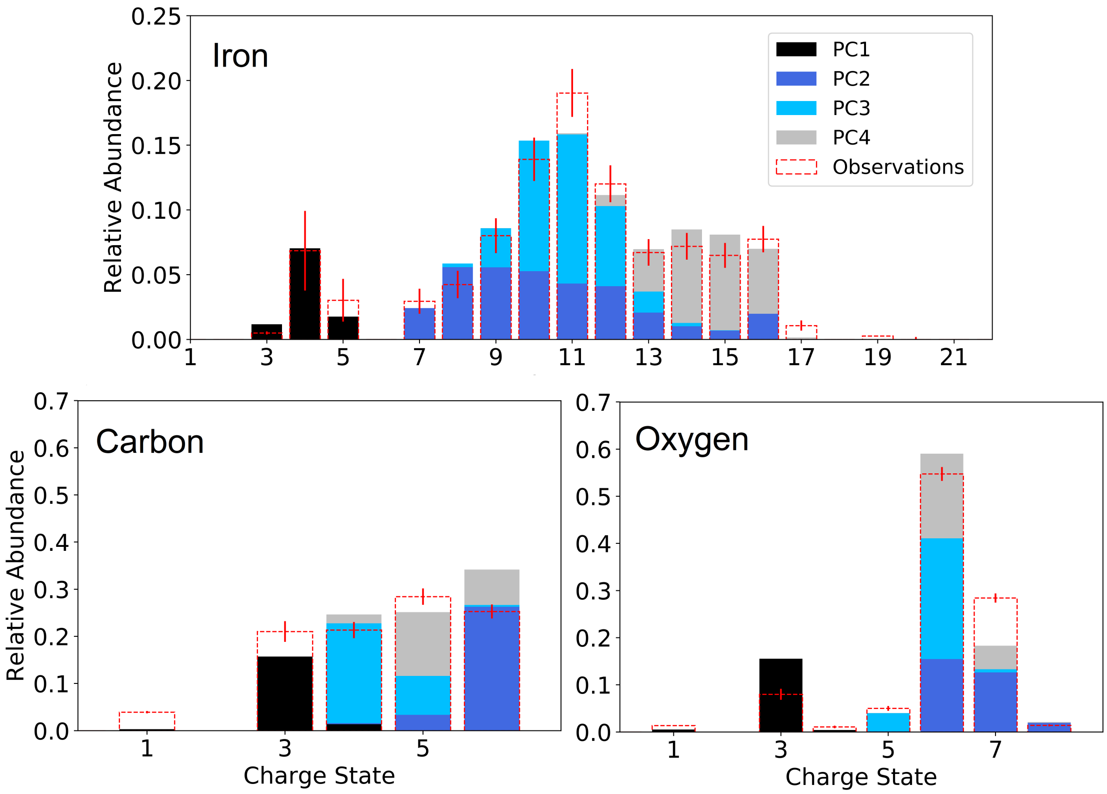

Figure 2.4: The relative abundance of the final distributions for modeled Carbon, Oxygen and Iron ions along with the observations. Each PC is denoted in its own color and the in-situ observations are plotted in empty, dashed red bars with corresponding error bars.

bars. The bar plot is composed of the sum of all four PCs in their own color to display their proportion to the full distribution. We define the simulated final charge state values in the plot as the relative abundance each ion reaches which no longer changes after a given heliocentric distance.

2.4.3 Density, Temperature and Velocity profiles

The final profiles between $1.13 - 15R_{\odot}$ for all four PCs are presented in Figure 2.5, with the corresponding color from the bar plot distributions in Figure 2.4. The top panel displays the density, the middle panel is the temperature, of each PC, while the bottom panel is the velocity profile used for all PCs. Table 2.3 lists the initial density

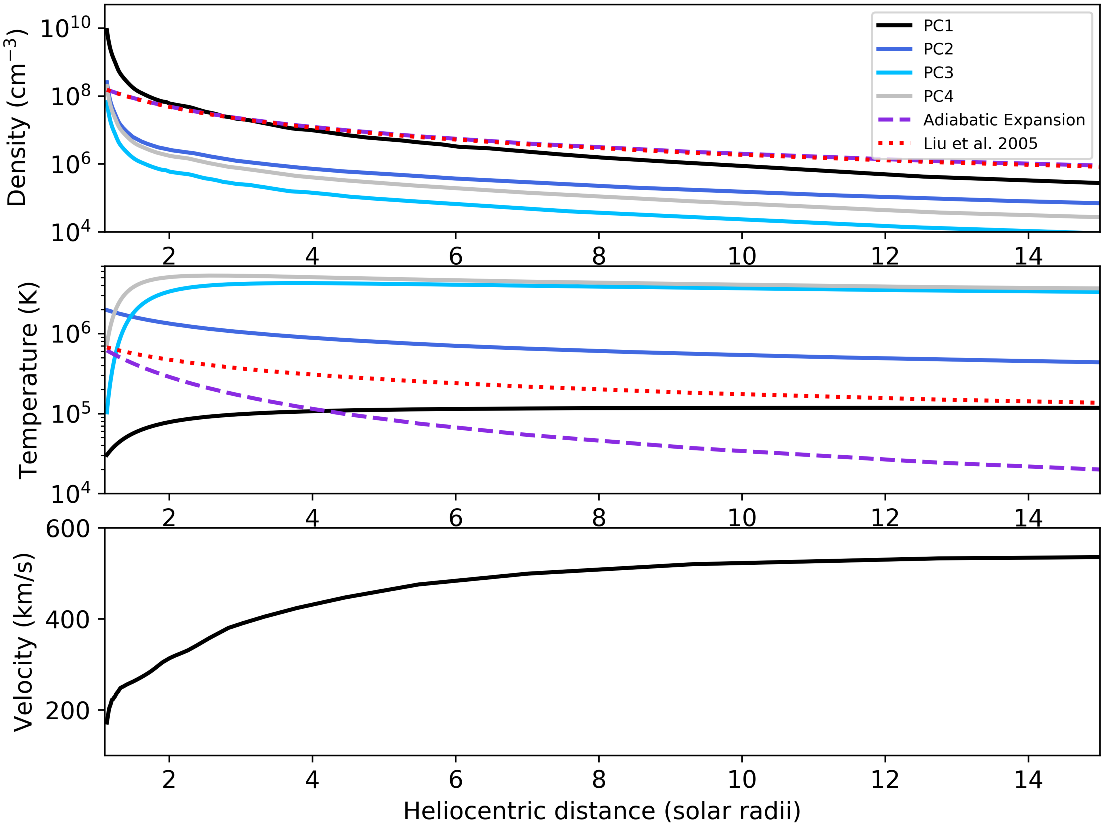

Figure 2.5: The final density (top), temperature (middle), and velocity (bottom) profiles for each PC plotted as a function of radial distance. Also plotted are the adiabatic expansion profiles and a heliospheric fit of electron density and temperature found in ICMEs from Liu et al. (2005).

and temperature, along with the peak temperature reached for each component and its heliocentric location. For comparison to our results, we include the density and temperature profiles as predicted by adiabatic expansion. The temperature and density evolution through adiabatic expansion are plotted in the dashed purple line and given as $T_e \propto 1/r^{4/3}$ and $n_e \propto 1/r^2$, respectively. We also include fits to the average electron density and temperature collected within the ICME boundary found in Liu et al. (2005). The Liu et al. (2005) profiles describe ICME behavior between $1-5$ AU from data collected by the Ulysses spacecraft. The ICMEs were identified based on an enhancement of alpha-to-proton ratio (≥ 0.08) and/or a depression of proton temperature as described in Richardson & Cane (1995). Liu et al. (2005) found the best fits to the ICME density to be adiabatic, $n_e \propto 1/r^{2.03\pm0.21}$, and the temperature fit is found to decrease much slower compared to adiabatic cooling, $T_e \propto 1/r^{0.64\pm12}$, both plotted with the dashed red line. Both profiles are extrapolated to the Sun and assume an initial value to be the same as PC_4. The theoretical fits from Lui et al. are not intended to be accurate representations of CME evolution below 1 AU but rather a point of comparison of between our results and observed electron behavior in ICMEs.

In most cases, the profiles appear to have two main regimes; an impulsive phase near the surface where the plasma properties and speed are rapidly changing, and a subsequent coasting phase where the profiles change more gradually. This can be seen in the density profiles which rapidly decrease near the surface, within $0.5\mathrm{R}_\odot$ from the boundary, and subsequently settles to an expansion rate similar to adiabatic and that found in Liu et al. (2005) for $\mathrm{PC}_{2,4}$ while $\mathrm{PC}_{1,3}$ decrease at an accelerated rate. For the temperature, our results show $\mathrm{PC}_{1,3,4}$ rapidly increase in temperature as they propagate away while PC_2 simply cools after its release. Furthermore, all temperature profiles follow a slower cooling pattern compared to adiabatic cooling and the Liu et al. (2005) heliospheric temperature profile, with the exception being PC_2 that matches well with the cooling behavior found in Liu et al. (2005). Lastly, the velocity profile exhibits a sudden acceleration phase just after the explosive release of the plasma, followed by a velocity that gradually reaches an asymptotic value, just below 500 km s^{-1}, following typical CME kinematics observed by solar imagers (Bein et al. 2011; Gopalswamy et al. 2009). Furthermore, assuming the CME continues to evolve in a similar manner, when extrapolated out to 1 AU the final profiles provide temperature and density well within in-situ measurements of ICMEs.

Table 2.3: Properties of the final profiles.

PC	Initial n$_e$ (cm^{-3})†	Initial T$_e$ (K)†	Peak T$_e$ (K)†	Peak T$_e$ Location (R$_\odot$)
1	9.94	4.48	5.08	12.7
2	8.41	6.29	6.29	1.13
3	7.82	5.02	6.63	3.83
4	8.29	5.86	6.73	2.50

†Values are in $\log_{10}$.

2.4.4 Energy Calculations

Utilizing the data-constrained n_e, T_e, and v_{bulk} profiles derived in our results, we estimate the evolution of several energy terms and their contribution to the total energy rate of each PC. We include the contribution from thermal energy, potential energy, kinetic energy, radiative cooling, thermal conduction and adiabatic cooling rates. The energy release and heating rates of different plasma structures within the CME that we include here may be useful to determine the spatial distribution of energy released, improving our understanding of the flow of energy during the eruption process. Furthermore, the energy rates can also provide important constraints to the energy mechanism(s) necessary to power the eruption and sustain the post-eruption heating throughout its evolution in the lower corona (Akmal et al., 2001; Rakowski et al., 2007).

We computed the rates in units of ergs cm^{-3} s^{-1}. The kinetic energy is calculated as,

$$KE\ [\text{ergs cm}^{-3}] = \frac{1}{2}(n_e m_e + m_i n_i) v_{bulk}^2 \tag{2.7}$$

where m_e is the electron mass and $m_i n_i$ is the ion mass and ion number density,

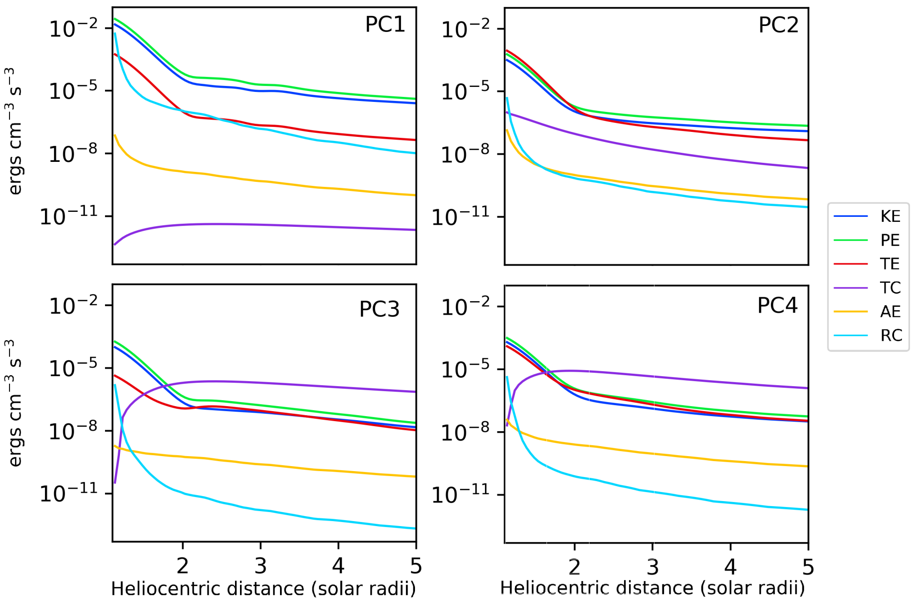

Figure 2.6: A plot of the evolution of the individual energy rates vs. heliocentric distance for each PC. These include Kinetic Energy, KE, Potential Energy, PE, Thermal Energy, TE, Thermal Conduction, TC, Adiabatic Expansion, AE, and Radiative Cooling, RC. The energy rates are each plotted as positive showing their magnitude.

respectively. We assume the plasma to be made up of free electrons, Hydrogen, and Helium. We define $m_i n_i = m_H n_H + m_{He} n_{He}$.

We rearrange Equation 2.7 to,

$$KE = \frac{1}{2} n_p \left(m_e \frac{n_e}{n_p} + m_p + m_{He} \frac{n_{He}}{n_p}\right) v_{bulk}^2 \tag{2.8}$$

where for the warmer plasma, PC_{2-4}, we can assume H and He are fully ionized and take $n_p/n_e \approx 0.83$ (assuming 10% He abundance) while for the cooler PC_1 we compute the ratio using PROTON_DENS.PRO from the SolarSoft suite. The PROTON_DENS.PRO IDL routine calculates the proton to electron density ratio taking into account the elemental abundance and the ion fractions calculated from the input plasma temperature. Furthermore, for simplicity, we assume a constant value of $n_{He}/n_p = 0.08$, although this value can vary between the Sun and in the he-

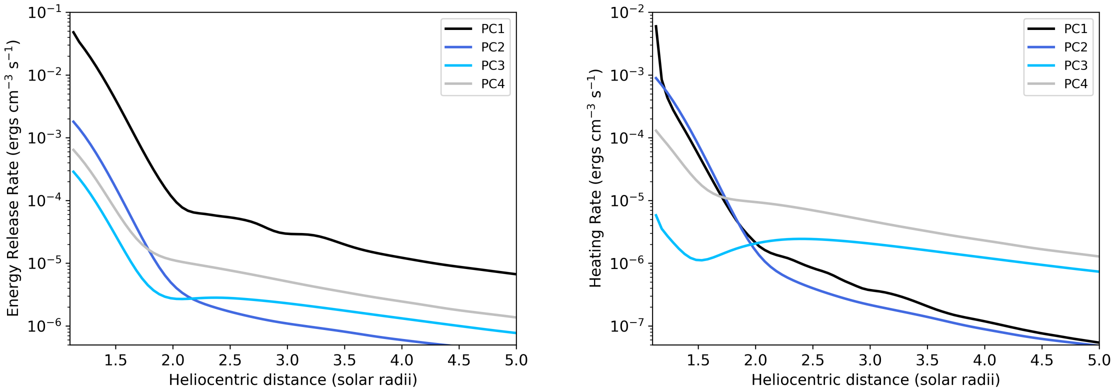

Figure 2.7: The energy release rate, including a sum all of energy terms from Section 4.4, (left) and heating rate, which excludes the KE and PE energy terms, (right) for each PC as a function of distance from the Sun.

liosphere, in different plasma structures, and has a solar cycle dependence (Hirayama, 1971; Borrini et al., 1982; Kasper et al., 2007). Lastly, we calculate the n_p profile using the aforementioned PROTON_DENS.PRO, and n_e derived from our modeling results. The kinetic energy rate is calculated as, $\Delta KE/\Delta t$ [ergs s^{-1} cm^{-3}], where ΔKE is the variation of kinetic energy between two steps and Δt is the simulation time step.

The potential energy is given as,

$$PE \text{ [ergs cm}^{-3}] = (n_e m_e + m_i n_i) G M_\odot \left(\frac{1}{R_\odot} - \frac{1}{r} \right) \tag{2.9}$$

where the gravitational constant is $G = 6.67 \times 10^{-11}$ m^3 kg^{-1} s^{-2}, the mass of the Sun is $\mathrm{M}_\odot = 1.99 \times 10^{30}$ kg, the radius of the Sun is $R_\odot = 6.96 \times 10^8$ m, and the rate is calculated as $\Delta PE/\Delta t$ [ergs s^{-1} cm^{-3}].

The thermal energy is given as,

$$TE \text{ [ergs cm}^{-3}] = \frac{3k_B}{2}(n_e T_e + n_i T_i) \tag{2.10}$$

where $k_B = 1.38 \times 10^{-23}$ m^2 kg s^{-2} K^{-1} is the Boltzmann constant and T_i is the ion temperature. We can rearrange to,

$$TE = \frac{3k_B}{2} n_e T_e \left(1 + \left(\frac{n_p}{n_e}\frac{T_p}{T_e}\right) + \left(\frac{n_{He}}{n_e}\frac{T_{He}}{T_e}\right)\right) \tag{2.11}$$

where we approximate $T_p/T_e = 4$, taken to be an average from the range found in in-situ observations (Sittler & Burlaga, 1998; Richardson et al., 1997). Also, we assume the ion temperature is approximately mass proportional, where $T_{He}/T_H \approx m_{He}/m_H = 4$ (Bochsler et al., 1985). Both are kept constant for simplicity. We calculate the rate as $\Delta TE/\Delta t$ [ergs s^{-1} cm^{-3}].

The radiative cooling rate is given as,

$$\frac{dRC}{dt}\ [\text{ergs s}^{-1}\text{cm}^{-3}] = 0.83 n_e^2 P(T) \tag{2.12}$$

where P(T) is the radiative loss function taken from CHIANTI.

Adapted from Lee et al. (2015), the thermal conduction rate is given as,

$$\frac{dTC}{dt}\ [\text{ergs s}^{-1}\text{cm}^{-3}] = \frac{\kappa T_e^{7/2}}{l^2} \tag{2.13}$$

where l is the length from the leading edge of the flux rope structure and $\kappa = 7 \times 10^{-7}$ ergs cm^{-1} K$^{-7/2}$ s^{-1}. Previously we assumed a self-similar expanding sphere to construct an initial density profile however for the purposes of this calculation, we estimate the geometry as a semi-circular loop rooted at the Sun. The loop length from the flux rope apex is $l = \pi h/2$ where h is the radius of the semi-circle made up by the loop as well as the radial distance from the solar surface given as $h = r - R_\odot$ where r is the heliocentric distance.

The Adiabatic Expansion rate is given as,

$$\frac{dAE}{dt}\ [\text{ergs s}^{-1}\text{cm}^{-3}] = \frac{5}{2}\left(n_e + n_p\right) k_B \left(2T\frac{v_{bulk}}{r}\right) \tag{2.14}$$

taken from Lee et al. (2015) which assumes a monotomic ideal gas. This is due to cooling from expansion of the plasma.

The energy release rate is then a sum all the rates listed while the heating rate includes all but the kinetic and potential rates. We did not include the ionization energy rate because we found it to be negligible in our calculations.

To evaluate the energy release rate sensitivity of different n_{He}/n_p and temperature ratios, which are held constant in our calculations, we calculated the energy release rate using a range of possible values. For $0.06 \leq n_{He}/n_p \leq 0.1$ we found a maximum change in energy release rate results to be approximately 10% for each PC. For T_p/T_e and T_{He}/T_H, we vary their values between $1 - 10$. We find for PC_1, the change in both ratios has nearly no effect to the final energy release rate. For PC_{2-4}, between the minimum and maximum value, T_{He}/T_H can vary the energy release rate $\leq 5\%$ while T_p/T_e causes a $5 - 25\%$ change, where the largest changes occur near peak temperatures.

We plot the individual energy rates for each PC in the four panels of Figure 2.6 and the energy release and heating rates are plotted in Figure 2.7, left and right panels respectively. The rates of energy losses, such as radiative cooling, are plotted as positive values because we are only interested in their magnitude to determine the energy release and heating rates. From the individual energy rates, we find that the energy release rate for PC_1 is dominated by the potential/kinetic terms and has the largest value throughout its evolution within $5R_\odot$ compared to the other PCs. For PC_2, the thermal energy rate has the largest value near the Sun and quickly decreases to a rate below the kinetic and potential values as it continuously expands and cools.

We find PC_2's energy release rate is over an order of magnitude smaller at the Sun compared to PC_1 and decreases rapidly below PC_{3-4} just prior to reaching $2R_\odot$. Moreover, $PC_{3,4}$'s energy release rate is driven by their kinetic and potential energy terms below $2R_\odot$ after which thermal conduction rate becomes significant as their electron temperature rises to multi-million Kelvin values. Also, we find the thermal energy rate is significantly higher for PC_4 as compared to PC_3 below $2R_\odot$ due to its much larger density.

From the heating rate results, displayed on the right panel of Figure 2.7, we find PC_1 has the largest heating rate closest to the Sun which quickly decreases to a rate similar to PC_2. PC_1's heating rate is driven by radiative cooling and thermal energy terms while the radiative cooling is significantly less important to PC_2 due to its much higher temperature. $PC_{3,4}$ are multiple of orders of magnitude smaller compared to PC_1 near the Sun however maintain a heating rate comparable to its initial value farther from the solar boundary. This is a result of the heating rate counteracting the cooling from thermal conduction while the temperature for $PC_{3,4}$ continues to rapidly increase out to 2.5 and $3.83R_\odot$, respectively.

Lastly, we find the heating rate results at the beginning of our simulation, $1.13R_\odot$, are smaller compared to the level of heating reported for two prominences near $1.1R_\odot$ calculated from spectroscopic measurements (Lee et al., 2017). Final heating rates from Lee et al. (2017) were found to be between $5 - 14 \times 10^{-2}$ ergs cm^{-3} s^{-1} for the CME core which are an order of magnitude larger than the values for the prominence plasma in our results, PC_1, just beyond the height in their calculations.

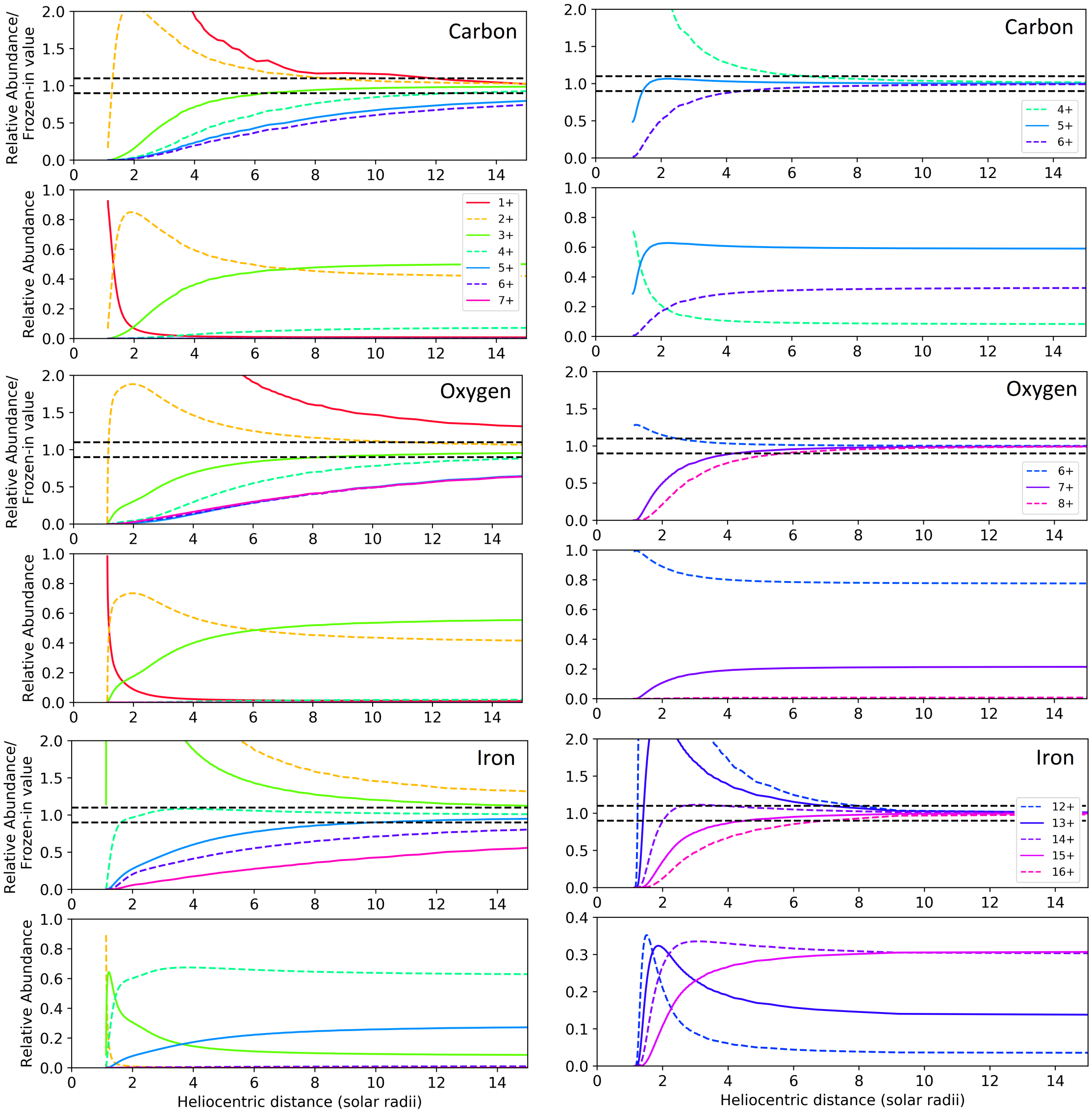

Figure 2.8: Vertical two-panel plots for each element showing the simulated relative abundance/final frozen-in value (top panel) and relative abundance (bottom panel) for the relevant ions of Carbon, Oxygen and Iron (top to bottom). Results for PC$_1$ are in the left column, with a single corresponding legend, and for PC$_4$ on the right column, with a legend for each element. The horizontal black dashed lines on the top plots of each species show where the ion reaches within 10% of its final frozen-in value.

2.5 Discussion

2.5.1 Modeled Ionic Distributions

The final modeled ionic distributions reached the threshold χ^2 value desired. Results show that the largest differences in ion evolution occur between PC_1 and PC_{2-4} while the freeze-in distances within PC_{2-4} are similar. Therefore we present results for the ion evolution of PC_1 along with PC_4, which serves as a representation of PC_{2-4}. Furthermore, PC_4 is chosen because it is also the focus of further discussion in this section. Figure 2.8, displays the ion evolution in PC_1 (left column) and PC_4 (right column). The figure includes a set of vertical plots for each element where the top panel displays the evolution of each ion's relative abundance compared to its final frozen-in value, and the bottom panel displays the evolution of each ion's relative abundance, both as a function of distance from the Sun. The horizontal dashed lines in black on the top panels of each set represent where the ion reaches a relative abundance within 10% of its final freeze-in value.

We find that most ions within PC_{2-4} freeze-in between $2-10R_\odot$ as seen for PC_4 in the right panels of Figure 2.8 while for PC_1, densest and coolest component, the ions continue to evolve much farther from the Sun as shown in the left panels of the same figure. In general, the freeze-in distance for many ions in PC_1 occur within $15R_\odot$ however a few ions with very low relative abundances (O^{1+}, O^{7+}, Fe^{2+}, and Fe^{7+}) reach out to $25R_\odot$. These distances are well within the planned Parker Solar Probe trajectory. A fortuitous encounter with a CME at this height will provide valuable plasma measurements during a period where we predict many ions in the prominence material to still be evolving.

The freeze-in distances in our results are significantly farther from the Sun compared to ions in the solar wind which are expected to reach between $2-5$ $R_\odot$ (Landi et al., 2012a). However, there have been observations which indicate that ionization within filaments is taking place farther from the Sun. A study of an erupting prominence found evidence for ionization of neutral Hydrogen occurring as far as $9R_\odot$ (Howard, 2015). In the Howard (2015) study, measurements of the ratio of polarized brightness to total brightness ($\mathrm{pB}/\mathrm{B}_{Total}$) of a filament were taken using STEREO COR1 & COR2 where it was assumed that the excess brightness was Hα emission. They found an increasing pB ratio with increasing distance from the Sun suggesting a transition of Hα emission to an enhancement of Thomson scattered light. This result was a strong indicating that ionization was taking place at least up to that height which is comparable to distances for many ions within PC_1.

In addition, final ion distributions match well with the ionic trend found in the observations but we find significant discrepancies in some ions. PC_1 simulated the Fe^{3+} to Fe^{5+} population fairly successfully, but missed the singly ionized charge states of C and O almost entirely. As displayed in the top panel for C, O, Fe in the left column of Figure 2.8, C^{1+} to C^{4+} and O^{1+} to O^{4+} freeze-in much farther, at $> 15R_\odot$, as compared to Fe^{3+} to Fe^{5+} where the freeze-in distance of Fe^{4+} occurs at $< 5R_\odot$ and, for Fe^{3+} and Fe^{5+} occurs at $< 15R_\odot$. This means that these particular C and O ions spend more time undergoing ionization and recombination processes which provide enough time to deplete the C^{+} and O^{+} charge state almost entirely well before freezing-in. This suggests that the plasma temperature may reach a value which is too high too early, causing the 1+ charge state to ionize much faster than desired. Moreover, this can also arise if the electron density is too large during the evolution of these ions, causing a delay to the freeze-in location. However, despite underestimating the singly charge state, the PC_1 profiles provided the least discrepancy between C^{3+} to C^{4+}. Conversely, the profiles generate an overabundance of O^{3+}. The discrepancy in the O^{3+} ion arises from an effort to enhance the C^{3+} that is too low. We find that because the C^{2+} freezes-in just prior to O^{2+} state, the O^{2+} continues to be ionized, increasing O^{3+}, while C^{3+} ceases its evolution, preventing any further enhancement.

Furthermore, the simulated distribution predicts a lower O^{7+}/O^{6+} ratio when compared to observations. The O^{7+}/O^{6+} ratio is one of the primary signatures used to identify slow/fast solar wind streams, as well as ICMEs embedded in the solar wind (Zhao et al., 2009; von Steiger et al., 2000; von Steiger & Zurbuchen, 2003). For ICMEs, this value is generally found to be > 1 however in our particular dataset the ratio is lower. Nevertheless, the combined simulated 6+ ions, from PC_{2-4}, are overestimated approximately by as much as we underestimate the 7+ charge state. It appears that PC_4 could be further ionized to adjust this discrepancy however, even though an increase to the temperature could improve O, and possibly Fe as well, it would increase the C^{6+} state further out of proportion. This arises from the fact that the freeze-in altitude for $C^{5,6+}$ is slightly larger than $O^{6,7+}$ which allows the C^{5+} to continue to ionize at this temperature while O^{6+} no longer evolves, as shown in the C, O freeze-in and relative abundance plots for PC_4 in the right column of Figure 2.8. Overall, we find each ion's evolution is highly sensitive to the MIC profiles making their final freeze-in altitude, ergo the final distributions, strongly interdependent. In other words, finding agreement between all ions required very specific combination of plasma temperature and density evolution.

In addition, the freeze-in evolution of ions within the prominence material provide some insight on the rarity of low and singly charges states detected in-situ. From a survey of cataloged ICMEs between 1998-2007, Lepri & Zurbuchen (2010) found only 4% of ICMEs associated with a filament eruption were found to contain low ionized states from prominence material; our present event is 1 of 11 events found in their study. Their infrequent occurrence in-situ remains an open question in heliophysics. It has long been speculated that ionization below the frozen-in altitude of these ions may be the cause. However our results show ions specific to the filament search criteria of Lepri & Zurbuchen (2010), C^{2-3+}, O^{4+}, Fe^{4-7+}, in our case can survive the level of heating experienced by the modeled prominence material even though they remain active beyond $10R_\odot$. This result suggests the limited filament observations at 1 AU is likely due to additional factors as well. This can include the filament's filling factor where studies suggest that cool, small-scale threadlike structures makeup only a small portion of the filament volume making cool ions highly sparse. Furthermore, another main cause may be the due to the limited spatial sampling by ACE/SWICS itself.

Nevertheless, we do find that the coldest ions, C^{1+}, O^{1+} and Fe^{2-3+}, from the extended double coincidence measurements are almost entirely destroyed during the early stages of propagation and continue to evolve throughout the heating stage of that plasma. Therefore, we do not anticipate a significant presence of the coolest ions from prominence material at large distances from the Sun.

2.5.2 Technique Approximations

We note here some approximations in our modeling approach that may contribute to some of the discrepancies between the simulated and observed distributions. For example, we find the freeze-in altitude for many ions in our modeled CME components to be several solar radii from the solar surface. This is important to note given that one of the main assumptions we prescribe for the MIC is that the free electrons maintain a Maxwellian velocity distribution throughout the plasma evolution. However, the Coulomb collision frequency ($\nu_{Coulomb} \propto n/T^{3/2}$), that acts to maintain the Maxwellian profile during its radial evolution, quickly decreases as the Coulomb collision timescale ($\tau_{Coulomb} = 1/\nu_{Coulomb}$) overcomes the expansion timescale, as shown for each PC in Figure 2.9. This means that while the plasma continues to be heated, this assumption may likely fail prior to the freeze-in altitude of the majority of ions. This effect can be seen in-situ, as non-Maxwellian distributions are often encountered in proton and electron velocity distribution functions of the solar wind and ICMEs in the heliosphere (Marsch, 1983; Pilipp et al., 1987a,b; Marsch et al., 2009). Given the

CHIANTI reaction rates we used are computed under the Maxwellian assumption, deviations from it have implications to the evolution of each ion in our simulations, particularly those with the furthest freeze-in altitudes. Future Parker Solar Probe measurements taken within the ion frozen-in distance will provide a better indication the level of accuracy of this approximation.

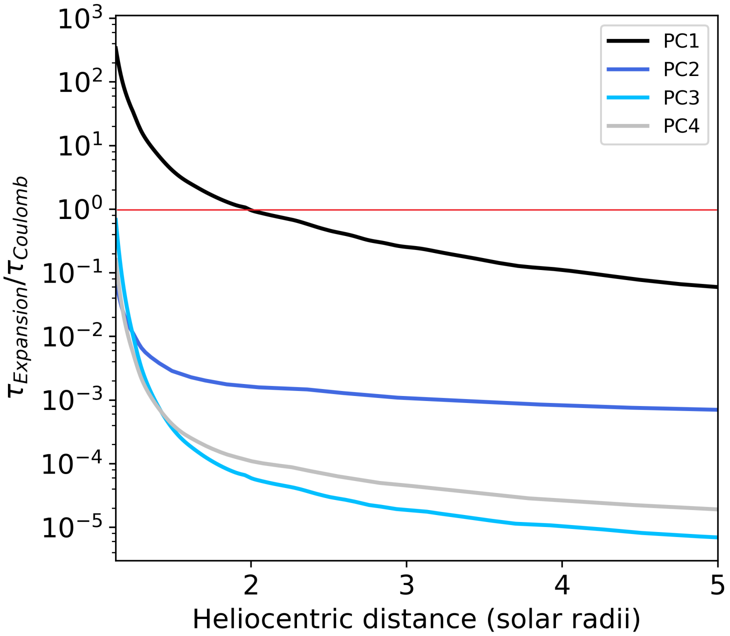

Figure 2.9: A ratio of the expansion to Coulomb collision timescale as a function of distance from the Sun for PC_{1-4}. The horizontal red line denotes the location where the Coulomb collision timescale overcomes the expansion timescale.

Moreover, the ionization and recombination cross-sections used in the calculation of the reactions rates that produce the ion population in the MIC can also be a source of uncertainty. These values are taken from laboratory experiments and theoretical calculations, both of which inherently have a level of inaccuracy. For this reason, there have been efforts in the atomic physics community to determine error to these values, that can be propagated through to excited ion populations and the ionization/recombination reaction rates. This may be useful to incorporate in future work,

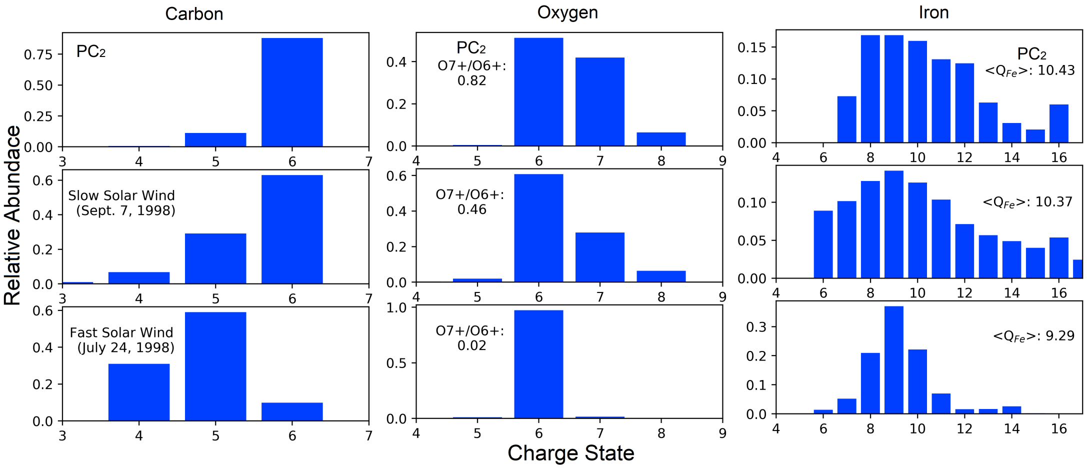

Figure 2.10: Comparison of PC$_2$ (top row) to typical slow (middle row) and fast (bottom row) solar wind composition of Carbon (left), Oxygen (middle), and Iron (right) from two periods taken from Lepri et al. (2001).

as it has been shown that the these uncertainties can vary between ions and are highly dependent on the temperature and density regime of the plasma that can be relevant to the different CME structures (Loch et al., 2013).

2.5.3 Plasma Evolution

In our investigation we find four main constituents that make up the full distribution range of the observations. The values for the temperature and density for PC$_{1,3,4}$ near the solar boundary, as shown in Table 2.3, suggest they originate from the prominence and the surrounding PCTR. For PC$_1$, the boundary density, log n$_e$ = 9.94, and temperature, log T$_e$ = 4.48, are within the density and temperature ranges of spectrosopic values for the prominence's main core, log n$_e = 9 - 11$ and log T$_e = 4 - 5$ (Labrosse et al., 2010). This component also generates the lowest charge states in the distributions, which are assumed to originate from the filament in the in-situ observations (Lepri & Zurbuchen, 2010). PC$_3$ and PC$_4$ are warmer (log T$_e$ = 5.02 and 5.86, respectively) and more tenuous (log n$_e$ = 7.82 and 8.29, respectively) compared to PC$_1$, with properties at the Sun most analogous to the PCTR that ranges between log $n_e = 6-8$ and log $T_e = 4-6$ (Labrosse et al., 2010). Our results indicate that the prominence and PCTR originate together at the Sun and remain in close proximity to one another as they travel in the heliosphere.

The PC_2 component has a much higher temperature at the boundary compared to the others, nearly 2 million Kelvin, which gradually decreases with radial distance. Its warmer initial temperature and tenuous state, log $n_e = 8.41$, at the Sun are akin to the properties of ambient coronal plasma. Its presence as a main component in the modeling results may indicate that part of the corona surrounding the prominence was possibly carried away during the eruption and traveled alongside the prominence material, eventually detected together near the Earth.

When compared to the typical composition of slow and fast solar wind, we find that PC_2 has similar C, O and Fe distributions to those found in slow solar wind streams. This is evident in Figure 2.10 where we plot the C, O and Fe distributions of PC_2 (top row), and two-hour periods of slow (middle row) and fast (bottom row) solar wind, that were identified in Lepri et al. (2001). In the first column, the modeled C^{4-6+} have a similar profile to the slow solar wind as compared to the fast. Similarly, the O distributions, plotted in the second column, match well with the slow solar wind. In addition, we find the modeled O^{7+}/O^{6+} ratio to be well within the range found in slow solar wind, $0.1 < O^{7+}/O^{6+} < 1$ (Zhao et al., 2009). Lastly, the modeled Fe distribution spans a similar range of ions found in the slow solar wind and similar average Fe charge state. The resemblance here suggests the distribution is possibly made up of prominence and the surrounding ambient plasma.

The variation of the thermodynamic properties in the different components from our modeling results are in agreement with spectroscopic observations of CME cores in the low corona. A Differential Emission Measure (DEM) analysis of prominence material during an eruption identified two main plasma structures along with the ambient plasma traveling together within the corona. The study finds a cool, dense component, log $n_e \sim 10-11$ and log $T_e \sim 5.1$, and a warmer, tenuous component log $n_e \sim 8.7$, log $T_e(K) \sim 5.7$ and the background corona at log $n_e \sim 7.6$, log $T_e \sim 6.1$ (Landi et al., 2010). This co-spatial contrast is most evident when comparing the boundary temperature and density between PC_1 and $PC_{2,3,4}$ near $1.1R_\odot$ where the Landi et al. (2010) measurements were taken.

In addition, Kucera & Landi (2008) found prominent spatial variation in the absorption properties of the main core and filament edge during the eruption showing non-uniform heating between neighboring structures. $PC_{1,3,4}$, that model the prominence and adjacent structure, also exhibit this variation, albeit to a larger extent, where each component experiences a level of heating between $1-2$ orders of magnitude apart, as shown by the heating rate in Figure 2.7.

Furthermore, MHD simulations also suggest uneven heating and thermally heterogeneous substructure within CMEs. An MHD simulation following the energy flow during a solar filament eruption shows current sheet energy release can vary spatially (Reeves et al., 2010). Their study finds a net flow of energy into the radial current sheet boundaries while a net outflow in the CME and Sun-ward directions. This suggests energy is transported to specific regions which can vary for nearby structures. In another study, two MHD CME simulations, governed by different eruption drivers and coronal heating terms, investigated the ionic structure within the multi-part ejecta throughout its freeze-in process (Lynch et al., 2011). The study finds localized enhancements of elevated ionization states within the ICME demonstrating that thermally distinct pockets of neighboring plasma can generate separate ionization levels. This directly supports the present results that find the distributions to be a collection of ions from multi-thermal plasma constituents.

2.5.4 Plasma Composition

Furthermore, as mentioned in Section 2.4.2, final results have been adjusted such that the Fe contribution of PC_1 is optimized independently from the C and O distributions resulting in the depletion of Fe in PC_1, due to its final contribution being much lower (shown in Equation 2.5), as compared to the other three components. A reduction of Fe in PC_1 that is favored to match observational abundances may be an indication of fractionation caused by the FIP effect. As a result of the FIP effect, the composition of the corona is observed to be enhanced of low, < 10eV, FIP elements e.g. Mg, Si and Fe, as compared to photospheric values (Laming 2015 and references therein). The variation among the PCs in our results suggest that PC_1 is compositionally distinct from $PC_{2,3,4}$.

To investigate this, we computed the absolute abundances, i.e. abundances relative to H, for individual elements (Fe, O, C) to determine each PC's composition. The absolute abundances are calculated using the average Fe, O, C and H densities from SWICS within the two hour period of the observations. The average density of each element is the sum of the density of each ion which is calculated as $\sum_{i=1}^{N} \mathrm{n}X^{i+}$ where i is the charge state, N is the atomic number of the element, $\mathrm{n}X^{i+}$ is the density of the charge state of element X.

The error for each absolute abundance was computed as the difference between the absolute abundances calculated using proton density data from two instruments on ACE; SWICS and SWEPAM. This incorporates the error due to variation in these measurements which produces roughly a 15% difference between the absolute abundance values. In addition, since we do not know the H densities of each PC, we compute the absolute abundance two ways and add the difference between the methods to the error calculation. The two methods include the distribution of H: 1) evenly between PCs (25% each), and 2) using the C-O distributions weights found in our results (Equation 2.6) as PC_1 (28%), $PC_{2,3}$ (26%), PC_4 (20%).

Table 2.4: Ratio of absolute abundances to photospheric values in each PC.

PC	Fe	C	O
1	1.08±0.25	0.91±0.35	1.28±0.21
2 & 3	3.56±0.84	0.85±0.32	1.19±0.20
4	2.59±0.61	0.65±0.25	0.92±0.15

Final ratios of the absolute abundances to photospheric values with corresponding error are shown in Table 2.4. The ratio is computed as $(X/H)/(X/H)_{\mathrm{phot}}$ where the absolute abundances, (X/H), are evaluated using the evenly distributed H densities and $(X/H)_{\mathrm{phot}}$ is taken from Asplund et al. (2009). Following the typical convention, the absolute abundances are computed as Fe/H = log(nFe/nH) + 12 = 7.53, C/H = log(nC/nH) + 12 = 8.39, and O/H = log(nO/nH) + 12 = 8.80. The photospheric absolute abundances used are $(\mathrm{Fe/H})_{\mathrm{phot}} = 7.5$, $(\mathrm{C/H})_{\mathrm{phot}} = 8.43$, and $(\mathrm{O/H})_{\mathrm{phot}} = 8.69$.

We find no significant enhancement in the absolute abundances in PC_1, the filament component, suggesting it resembles photospheric composition. While PC_2, the coronal component, and $\mathrm{PC}_{3,4}$, the PCTR plasma, contain 2−4 times more low FIP Fe compared to the photospheric value suggesting a coronal composition. This result is consistent with the prominence material originating from photospheric plasma while suggesting that the PCTR interface is more similar to the corona. This may be an indication of variation of the FIP effect experienced by these adjacent structures as they evolve.

2.6 Conclusions

In the present study, we modeled the evolution of the charge state distribution of C, O and Fe in an Earth-bound CME associated with a filament eruption from launch to freeze-in. The plasma evolution was constrained by in-situ charge states of C, O and Fe detected during the 2005 January 9 ICME passage at ACE/SWICS. We find that a collection of ions generated from four plasma components (PC) with distinct thermodynamic histories were necessary to reconstruct the full range of charge states found within the ejecta to within the threshold χ^2 we specified.

Results show the properties of three plasma components, $PC_{1,3,4}$, at the Sun suggest the ions originate from prominence and prominence-corona transition region plasma. In addition, we find a fourth plasma, PC_2, with a boundary density and temperature similar to values of coronal plasma. When comparing the simulated ions from PC_2 to the solar wind, we find they resemble typical ionic distributions found in slow solar wind at 1 AU. This suggests the PC_2 ions may have been swept along during the release prominence structure, originating from the surrounding corona.

We also find non-uniform elemental abundances between the different PCs in our results. The densest, coolest component (PC_1) with properties analogous to prominence material has photospheric abundances while the warmer PC_2 and PCTR plasma, $PC_{3,4}$, contain coronal abundances. This further supports PC_2's coronal origin. Also, it suggests that the prominence material may differ compositionally from the rest of the CME. Compositional studies specific to prominences and the PCTR are limited however both remote sensing and in-situ studies suggest variation within CME structures (Widing et al., 1986; Spicer et al., 1998; Song et al., 2017).

In addition, each plasma is found to undergo a different level of heating and expansion as it propagates from the eruption site. The distinct thermal history and properties of each component may indicate isolated evolution between neighboring structures. This would also be in accordance with CME observations that find multi-thermal plasma traveling together in the inner corona during a CME (Landi et al., 2010; Ding & Habbal, 2017).

The thermal, kinetic, potential energy rates along with the adiabatic cooling, thermal conduction, and radiative cooling rates were computed for each PC. The energy release rate, which is a sum of all terms listed, is largest near the solar boundary and rapidly decreases after leaving the Sun. The prominence material, PC_1, maintains the highest energy release rate out to $5R_\odot$, and is approximately an order of magnitude or higher compared to the other components. The heating rate, which is a sum of all terms excluding the kinetic and potential rates, is highest for PC_1 near the solar surface and driven by the thermal energy and radiative cooling rate. For PC_{2-4}, the radiative cooling becomes less important compared to the thermal energy. Furthermore, for PC_{3-4}, the thermal conduction term becomes increasingly significant above $1R_\odot$ from the surface just after the plasma is heated to over a million Kelvin.

Furthermore, we find that for most ions, the temperature and density in the PCs maintain an environment suitable for ionization and recombination processes to remain active farther from the Sun compared to what is predicted for ions in the solar wind ($2-5R_\odot$) (Landi et al., 2012a,b). Freeze-in distances for ions in the dense prominence, PC_1, occur between $2{-}25R_\odot$ while in the more tenuous components, $PC_{2,3,4}$, occur between $2{-}10R_\odot$. CME observations of particle distributions from Parker Solar Probe within these distances can provide a better indication to the reliability of approximating the free electrons as Maxwellian out to those heights, as has been assumed with the Michigan Ionization Code. The measurements will also be valuable to further constrain ion evolution below their freeze-in distances to improve our results.

Lastly, in a future study, we plan to use the energy results derived from this work to perform a detailed comparison with an MHD CME simulation. Our plasma heating requirements will be compared to the energy evolution of the CME by tracking specific plasma structures as they travel through the corona and calculating the individual contributions from different heating sources to measure their potential viability.

CHAPTER III

Identifying Spectral Lines to Study Coronal Mass Ejection Evolution in the Lower Corona

3.1 Background

Solar prominences, as referred to while appearing on the limb or filaments when observed on the solar disk, are made up of relatively cool, dense plasma, magnetically suspended within a million Kelvin corona. There exists an interface separating the prominence plasma from the coronal plasma referred to as the prominence-corona transition region (PCTR) (Engvold, 1988; Parenti et al., 2012). Just as the solar transition region marks a region where temperatures in the chromosphere transition from $10^4 - 10^5$ K up to 10^6 in the solar corona, the PCTR is a region where plasma temperatures transition from 10^6 down to as low as 10^4 K.

Despite being surrounded by coronal plasma with properties up to several orders of magnitude warmer and more tenuous, prominences can persist in a cool, dense state for up to several weeks in the low corona (or above the solar surface) (Gibson et al., 2006; Stellmacher & Wiehr, 2017; Wiehr et al., 2019).

Through the destabilization of the magnetic field configuration, prominences are released into interplanetary space as eruptions associated with a coronal mass ejections (CMEs). They are frequently observed as the brightest feature embedded in the multi-component CME structure leaving the Sun in white light coronagraph images. Furthermore, during the eruption, parts of the prominence are rapidly heated. This can be seen in extreme ultraviolet (EUV) images where the strong absorption features that are commonly observed prior to its release begin to disappear en route (Filippov & Koutchmy, 2002; Landi et al., 2010; Lee et al., 2017). As the plasma heats up, the cool ions in the plasma ionize and begin to emit radiation associated with the increasing plasma temperature. This transition causes the prominence to disappear from images made from the emission of cooler ions as it begins to heat up to higher temperatures. However, not all the cool material is entirely destroyed. Schmahl & Hildner (1977) and Ding & Habbal (2017) find that part of the cool structure can survive out to long distances from the Sun as observed during a prominence eruption captured by Skylab in 1973 and during the 2015 total solar eclipse, respectively. Ultimately, this cool material is detected in the form of low ionized charge states with mass spectrometers in the heliosphere (Lepri & Zurbuchen, 2010; Sharma & Srivastava, 2012; Song et al., 2017).

Furthermore, studying solar filament eruptions may hold clues that can help identify the heating mechanism supplying the energy to the system. This mechanism is presently unknown and treated empirically (Merkin et al., 2016) or derived from theoretical work in large scale magnetohydrodynamic (MHD) simulations (Oran et al., 2013; van der Holst et al., 2014) for the solar wind. Furthermore, the injection of energy is thought to be somewhat irregular as found in studies that suggest the energy supplied to different structures within the CME, including the prominence and adjacent PCTR, can vary during its release (Kucera & Landi, 2008; Reeves et al., 2010; Rivera et al., 2019b). These studies demonstrate that in order to fully capture the spatial and temporal energy evolution, simultaneous observations of the cool and hot components of the CME are necessary.

Prominence structures at the Sun are traditionally observed in Hα from ground observations and in the He II 304Å line with space based instruments. However, the complex multi-thermal nature of the eruption makes it challenging to study the temporal evolution once it leaves the solar surface. Therefore in this work, we aim to identify spectral lines between the EUV to visible and infrared range that are important to carryout measurements of CME substructure within 2 solar radii ($R_\odot$) field of view (FOV). We target spectral lines within the range of planned instrumentation that include two future ground based telescopes; Daniel K. Inouye Solar Telescope (DKIST; Keil et al. 2009; Tritschler et al. 2016) and Upgraded Coronal Multi-channel Polarimeter (UCoMP; Landi et al. 2016) set to begin operations early 2020 and late 2019, respectively. Also, we include lines within the range of the space-based Spectral Imaging of the Coronal Environment (SPICE) instrument onboard the Solar Orbiter mission (Fludra et al., 2013). DKIST is a five-instrument telescope with a planned collective viewing range of $3900 - 50000$Å focusing on solar disk and off the limb phenomena. UCoMP is a coronagraph with multi-wavelength capability in the visible able to observe a few spectrally resolved coronal lines near-simultaneously over the entire corona out to $2R_\odot$. SPICE is a space based EUV imaging spectrograph observing in two wavelength bands, $704 - 790$Å and $973 - 1049$Å, that contain lines from several ions covering a range of temperatures to investigate plasma state and composition. Coordinated efforts between these instruments can provide CME coverage between initiation and early stages of propagation to study the heating and evolution. The lines studied in the present work can be used to develop observing sequences in each of these instruments, aimed at addressing the open problems of CME physics. Furthermore, we also explore lines that may be useful to incorporate for the planning of future spectrometers and solar imagers.

The paper is organized as follows: Section 3.2 describes the method of computing synthetic intensities we analyze and includes the properties of the prominence and adjacent structures we utilized for the analysis. Section 3.3 describes the intensity results for each structure. Section 3.4 is a brief discussion of the useful lines that we identified and applicable diagnostic techniques. Section 3.5 is a summary of our work.

3.2 Methodology

3.2.1 Generating Synthetic Intensities

We compute synthetic line of sight intensities emitted by each emission line specified driven by collisional excitation and photoexcitation which are the most important processes in the corona (Phillips et al., 2008). The total intensity is a sum of the collisional and radiative scattering intensities, I = I_{coll} + I_{rad}, where intensity is in units of phot cm^{-2} s^{-1} $arcsec^{-2}$. The intensity governed by collisional excitation is given as,

$$I_{coll} = \frac{1}{4\pi} \int_{-\infty}^{\infty} G(T, n_e)\varphi(T)dT \tag{3.1}$$

where T and n_e are the electron temperature and density, respectively. The Contribution Function in units cm^3 s^{-1} and the Differential Emission Measure (DEM) in units of cm^{-5} K^{-1}, $G(T, n_e)$, $\varphi(T)$, respectively, are given as follows:

$$G(T, n_e) = \frac{n_j(X^{+q})}{n(X^{+q})} \frac{n(X^{+q})}{n(X)} \frac{n(X)}{n(H)} \frac{n(H)}{n_e} \frac{A_{ji}}{n_e} \tag{3.2}$$

$$\varphi(T) = n_e^2 \frac{dx}{dT} \tag{3.3}$$

where $n_j(X^{+q})/n(X^{+q})$ is the level population of the +q ion, $n(X^{+q})/n(X)$ is the relative abundance of the +q state, $n(X)/n(H)$ is the absolute abundance, $n(H)/n_e$ is the Hydrogen to electron ratio and A_{ij} is the Einstein coefficient for spontaneous emission. The DEM is a function of the electron density and temperature along the line of sight (LOS).

Intensity from radiative scattering is given as,

$$I_{rad} = \frac{BA_{ij}}{4\pi A_{tot}} \int_{-\infty}^{\infty} W(r) N_{abs} p(\varphi) F_{inc} D(v) dr \tag{3.4}$$

where $W(r) = 0.5(1 - \sqrt{1 - R_\odot/r})$ is the dilution factor that accounts for the weakening radiation field with increasing distance from the source and r is the heliocentric distance, B is the spontaneous absorption coefficient, A_{tot} is the total decay rate by spontaneous emission, $p(\varphi)$ is the scattering coefficient, N_{abs} (cm^{-3}) is the number of absorbers given as,

$$N_{abs} = \frac{n(X^{+q})}{n(X)} \frac{n(X)}{n(H)} \frac{n(H)}{n_e} n_e, \tag{3.5}$$

and $D(v)$ is the Doppler dimming term, expressed as,

$$D(v) = \int_{0}^{\infty} \phi(\nu_i) \psi(\nu_1, \nu) d\nu_1 \tag{3.6}$$

where ν_i and $\phi(\nu_i)$ is the incident radiation frequency and profile, respectively, and $\psi(\nu_1, \nu)$ is the absorption profile (Phillips et al., 2008).

Due to the dynamic nature of the eruption, we account for nonequilibrium ionization (NEI) conditions in the plasma by using relative ion abundances calculated by the Michigan Ionization Code (MIC; Landi et al. 2010) at all places along the CME trajectory (see Section 3.2.3). The nonequilibrium ion fractions are then used to evaluate $G(T, n_e)$ and N_{abs}. The MIC is a time-dependent ionization code that simulates charge state evolution of plasma as it propagates away from the Sun. The time-dependent ion fractions (cm^{-3} s^{-1}) are computed solving the following system of equations along the whole CME trajectory,

$$\begin{aligned} \frac{dy_i}{dt} &= n_e \left[y_{i-1} I_{i-1}(T_e) + y_{i+1} R_{i+1}(T_e) \right] \\ &+ y_{i-1} P_{i-1} - y_i \left[n_e \left(I_i(T_e) + R_i(T_e) \right) + P_i \right] \end{aligned} \tag{3.7}$$

where y_i is the ion's relative abundance of the given element in charge state i, n_e is the electron density, T_e is the electron temperature, $R(T_e)$ and $I(T_e)$ are the recombination and ionization rates, respectively, and P (s^{-1}) is the photoionization term described as,

$$P_i = \int_{\nu_i}^{\infty} \frac{4\pi J(\nu) \sigma_i(\nu)}{h\nu} d\nu \tag{3.8}$$

where ν is frequency, $J(\nu)$ is the mean spectral solar radiance, $\sigma(\nu)$ is the photoionization cross-section of the level i, and h is the Planck constant. We assume local thermal dynamic equilibrium at the initial height and Maxwellian electron velocity distribution at all points along the CME trajectory.

The code computes charge state distributions along its path from user-specified inputs of electron temperature, electron density, and bulk plasma velocity as a function of radial distance describing the plasma evolution as it propagates through the corona.

The atomic data required to carryout the intensity calculation are taken from the CHIANTI 8 atomic database (Dere et al., 1997; Del Zanna et al., 2015). In addition, we assume photospheric composition for the prominence from Asplund et al. (2009) which is often encountered at the Sun and in-situ observations (Widing et al., 1986; Spicer et al., 1998; Song et al., 2017; Parenti et al., 2019) as well as a main result in Rivera et al. (2019b). Furthermore, we use coronal abundances for the remaining

PCTR and warmer structures as concluded in Rivera et al. (2019b) are taken from Schmelz et al. (2012).

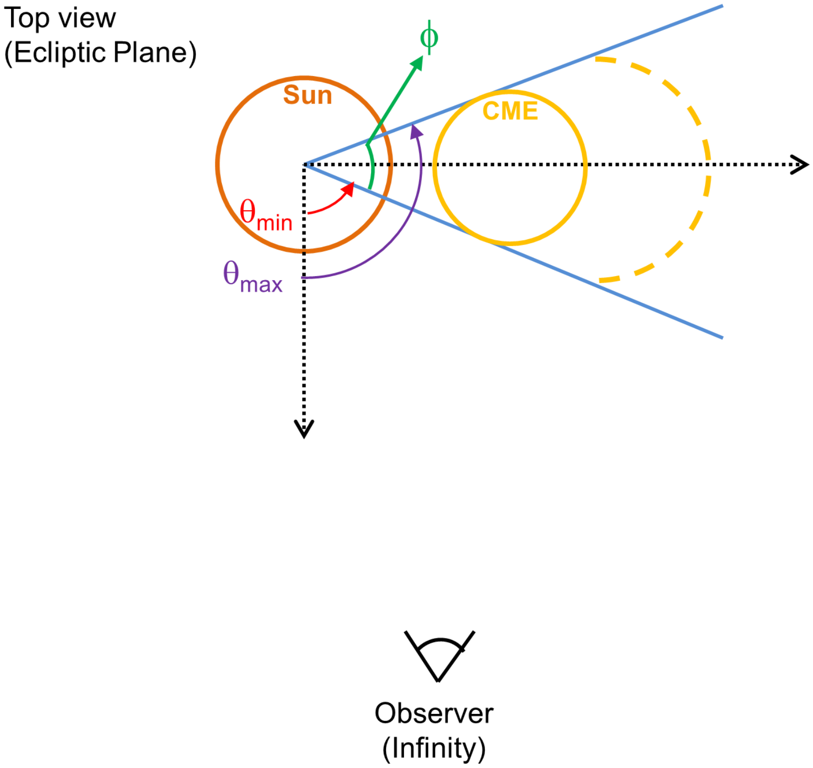

Figure 3.1: Geometry for the LOS integration.

Each line is integrated along the LOS as seen from an observer at infinity, illustrated in Figure 3.1. In the figure, the CME is released from the Sun and is assumed to subtend a constant angle, ϕ, along its propagation. The angular width, ϕ, spans the outer edges of the structure considered and is defined as $\phi = \theta_{max} - \theta_{min}$ where θ increases in the counterclockwise direction from the observer's LOS.

Furthermore, the plasma filling factor, which is defined as the fraction of the radiating volume, can also be specified for the plasma.

3.2.2 Candidate Spectral Lines

All lines that were tested are listed in Table 3.1 (100 – 1000 Å), Table 3.2 (1001 – 4000 Å), Table 3.3 (4001 – 14400 Å) where we include information of the emitting ion, spectral line, equilibrium formation temperature of the ion taken to be at the peak of the ion fraction curve assuming ionization equilibrium[1], the line transition, and the instrument range of the line where $\star$, $\diamond$, $\times$ denote the UCoMP, DKIST, and SPICE range, respectively. However in the main text, we only include a selection of lines recommended for consideration when planning for new instrumentation, to observe each CME component (Table 3.4 of the Results Section 3.3).

The candidate lines were selected using various sources. We first searched for lines from spectra generated with CHIANTI using a DEM of a previously studied CME core (Landi et al., 2010). The synthetic spectra are generated using all ions available in the database within a specified spectral range. Using the spectra formed from the DEM of the erupting prominence in Landi et al. (2010), we searched for prominent spectral lines from EUV to infrared (100 – 14400Å) for the analysis.

This included the spectral range of the future DKIST observations. DKIST is made up of a five instrument suite (Tritschler et al., 2016) with spectropolarimetric capabilities;

1. Visible Broadband Imager (VBI) red and blue, which is the only instrument without polarimetric capabilities, ranging between 3900 – 5500Å (blue) and 6000 – 8600Å (red);
2. Visible Spectro-Polarimeter (ViSP), ranging between 3800 – 9000Å;
3. Diffraction-Limited Near Infrared Spectro- Polarimeter (DL-NIRSP), ranging between 5000 – 9000Å, 9000 – 15000Å, and 15000 – 25000Å;
4. Visible Tunable Filter (VTF), covering 5200 – 8700Å;
5. Cryogenic Near Infrared Spectro-Polarimeter (Cryo-NIRSP), extending between 10000 – 50000Å;

---

[1] Generated with CHIANTI's plot_ioneq.pro

Each instrument can be used with or without spectropolarimetry and, other than ViSP, observe specific wavelengths in the range specified. For Table 3.3, we also include the goal range of ViSP[2], extending between 3900 – 16000Å, marked with †. DKIST observations are mainly focused over small portions of the solar disk; however, off-limb observations of the solar corona in the visible range out to $1.5R_\odot$ are also planned. Strategic tracking of filaments with full disk observation can facilitate in detecting potential eruptions that can be observed with DKIST at the limb to study initiation and lift off of the material (Forland et al., 2013).

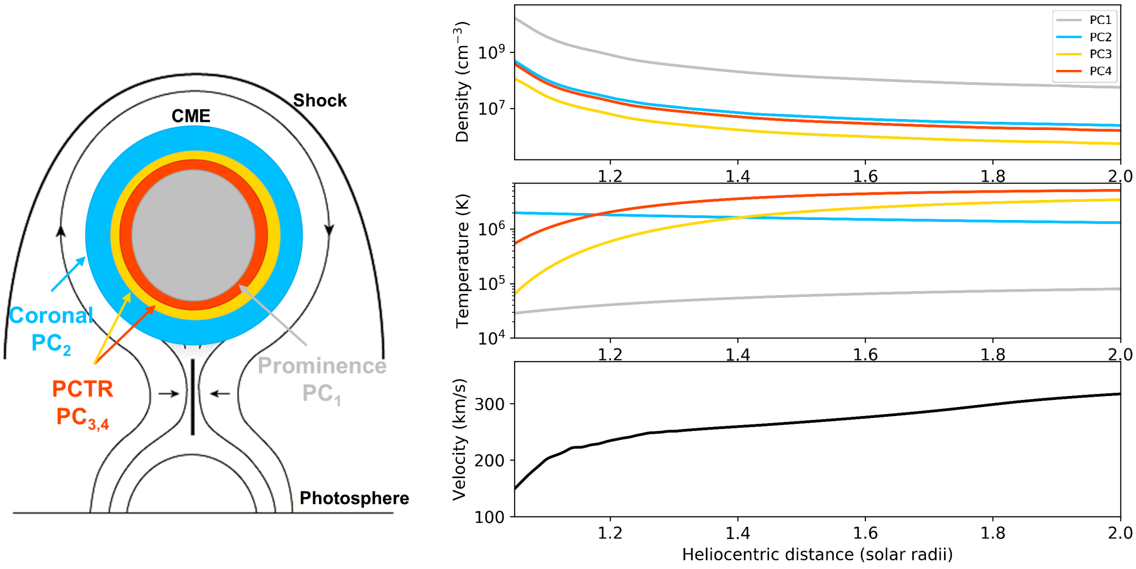

Figure 3.2: On the left, a picture of a CME lifting off the Sun displaying the geometry of the plasma components. The illustration is adapted from Martens & Kuin (1989). On the right, the thermodynamic evolution for PC_{1-4} shown on the left, taken from Rivera et al. (2019b) used in the MIC to compute relative abundance of ions that were used to generate the synthetic intensity along the plasma trajectory. The plot shows density (top), temperature (middle), and the same velocity profile for each case (bottom).

Also, we include lines specific to the UCoMP which is an upgraded version of the CoMP instrument (Tomczyk et al., 2008). UCoMP is a coronagraph that will

---

[2] `https://dkist.nso.edu/inst/ViSP`

be observing in nine visible wavelengths labeled with a $\star$ in Table 3.3 and further described in Landi et al. (2016). The list of spectral lines selected for the instrument allows UCoMP to observe the multi-thermal CME structure and heating of the prominence material, ranging between $\log T(K) = 4 - 6.68$. Furthermore, UCoMP will have the capability of capturing CME evolution well above the limb because its FOV encompasses the entire corona, from $1.05 - 2.0R_\odot$, simultaneously.

Additionally, we include lines highlighted in the description of SPICE. The future instrument is a high resolution spectrometer on Solar Orbiter that will observe in two wavelength bands in the EUV, $704 - 790$Å and $973 - 1049$Å (Fludra et al., 2013). A list of spectral lines ranging between $\log T(K) = 4.0 - 7.0$ in formation temperature are identified for addressing some of SPICE's science objectives aimed at probing the connection between the chromosphere and corona. We select lines from their list to test in our analysis.

3.2.3 CME substructure models

The lines generated for the present work utilize the electron temperature, density, and velocity profiles, derived from a previous study which reconstructed the thermodynamic evolution of all the components of a CME, including the erupting prominence (Rivera et al. (2019b) here after referred to as Rivera19). The Rivera19 study constrains the temperature, density, and velocity evolution of different plasma structures within the CME by iteratively looking for agreement between the simulated 'frozen-in' ion distributions and in-situ observations from the 2005 January 9 ICME ejecta detected near the Earth. That study finds that the observations can be effectively reproduced by combining ion populations formed within four plasma components with distinct thermal histories. The components found represent a structure with properties near the Sun that resemble prominence plasma (referred to as PC_1 in Rivera19 and in the present manuscript), two adjacent structures with prominence-

Table 3.1: A list of all the lines tested between 100−1000 Å

Ion	λ (Å)	Log T (K)	Transition	Instrument Range
S II	912.74	4.25	$3s^2\,3p^3\,{}^4S_{3/2}-3p^2\,(3P)\,4s\,{}^4P_{1/2}$	
O II	537.83	4.45	$2s^2\,2p^3\,{}^2D_{3/2}-2s\,2p^4\,{}^2P_{1/2}$	
O II	718.50	4.45	$2s^2\,2p^3\,{}^2D_{5/2}-2s\,2p^4\,{}^2D_{5/2}$	×
He II	256.32	4.70	$1s\,{}^2S_{1/2}-3p\,{}^2P_{3/2}$	
He II	303.78	4.70	$1s\,{}^2S_{1/2}-2p\,{}^2P_{3/2}$	
C III	977.02	4.85	$2s^2\,{}^1S_0-2s\,2p\,{}^1P_1$	×
N III	362.84	4.85	$2s\,2p^2\,{}^4P_{1/2}-2s\,2p\,3d\,{}^4D_{1/2}$	
N III	686.34	4.85	$2s^2\,2p\,{}^2P_{3/2}-2s\,2p^2\,{}^2P_{1/2}$	×
N III	991.58	4.85	$2s^2\,2p\,{}^2P_{3/2}-2s\,2p^2\,{}^2D_{5/2}$	×
O III	599.59	4.90	$2s^2\,2p^2\,{}^1D_2-2s\,2p^3\,{}^1D_2$	
O III	702.90	4.90	$2s^2\,2p^2\,{}^3P_1-2s\,2p^3\,{}^3P_2$	
S IV	744.90	5.00	$3s^2\,3p\,{}^2P_{1/2}-3s\,3p^2\,{}^2P_{3/2}$	×
S IV	750.22	5.00	$3s^2\,3p\,{}^2P_{3/2}-3s\,3p^2\,{}^2P_{3/2}$	×
N IV	765.15	5.15	$2s^2\,{}^1S_0-2s\,2p\,{}^1P_1$	×
N IV	923.68	5.15	$2s\,2p\,{}^3P_1-2p^2\,{}^3P_0$	×
O IV	553.33	5.15	$2s^2\,2p\,{}^2P_{1/2}-2s\,2p^2\,{}^2P_{3/2}$	
O IV	554.51	5.15	$2s^2\,2p\,{}^2P_{3/2}-2s\,2p^2\,{}^2P_{3/2}$	
O IV	609.83	5.15	$2s^2\,2p\,{}^2P_{3/2}-2s\,2p^2\,{}^2S_{1/2}$	
O IV	787.71	5.15	$2s^2\,2p\,{}^2P_{1/2}-2s\,2p^2\,{}^2D_{3/2}$	×
O IV	790.20	5.15	$2s^2\,2p\,{}^2P_{3/2}-2s\,2p^2\,{}^2D_{5/2}$	×
Ne IV	469.83	5.20	$2s^2\,2p^3\,{}^2D_{5/2}-2s\,2p^4\,{}^2D_{5/2}$	
S V	786.47	5.20	$3s^2\,{}^1S_0-3s\,3p\,{}^1P_1$	×
S VI	706.47	5.30	$3p\,{}^2P_{1/2}-3d\,{}^2D_{3/2}$	×
S VI	712.67	5.30	$3p\,{}^2P_{3/2}-3d\,{}^2D_{5/2}$	×
O V	629.73	5.35	$2s^2\,{}^1S_0-2s\,2p\,{}^1P_1$	
O V	760.45	5.35	$2s\,2p\,{}^3P_2-2p^2\,{}^3P_2$	×
Ne V	359.38	5.41	$2s^2\,2p^2\,{}^3P_2-2s\,2p^3\,{}^3S_1$	×
Fe VIII	168.17	5.65	$3s^2\,3p^6\,3d\,{}^2D_{5/2}-3s^2\,3p^5\,3d^2\,{}^2D_{5/2}$	
Mg VI	314.54	5.65	$2s^2\,2p^3\,{}^2P_{1/2}-2s\,2p^4\,{}^2S_{1/2}$	
Ne VII	973.33	5.70	$2s\,2p\,{}^1P_1-2p^2\,{}^1D_2$	×
Mg VII	319.03	5.77	$2s^2\,2p^2\,{}^1D_2-2s\,2p^3\,{}^1D_2$	
Ne VIII	770.43	5.80	$1s^2\,2s\,{}^2S_{1/2}-1s^2\,2p\,{}^2P_{3/2}$	×
Ne VIII	780.39	5.80	$1s^2\,2s\,{}^2S_{1/2}-1s^2\,2p\,{}^2P_{1/2}$	×
Fe IX	171.07	5.85	$3s^2\,3p^6\,{}^1S_0-3s^2\,3p^5\,3d\,{}^1P_1$	
Mg VIII	430.45	5.90	$2s^2\,2p\,{}^2P_{1/2}-2s\,2p^2\,{}^2D_{3/2}$	
Mg VIII	782.36	5.90	$2s^2\,2p\,{}^2P_{3/2}-2s\,2p^2\,{}^4P_{3/2}$	×
Si VIII	276.85	5.92	$2s^2\,2p^3\,{}^2D_{3/2}-2s\,2p^4\,{}^2D_{3/2}$	
Mg IX	706.06	6.00	$2s^2\,{}^1S_0-2s\,2p\,{}^3P_1$	×
Mg IX	749.55	6.00	$2s\,2p\,{}^1P_1-2p^2\,{}^1D_2$	×
Si IX	349.86	6.02	$2s^2\,2p^2\,{}^3P_2-2s\,2p^3\,{}^3D_3$	
Ne IX	510.15	6.15	$1s\,4p\,{}^1P_1-1s\,5s\,{}^1S_0$	
S X	776.37	6.17	$2s^2\,2p^3\,{}^4S_{3/2}-2s^2\,2p^3\,{}^2P_{3/2}$	×
Fe XII	186.89	6.20	$3s^2\,3p^3\,{}^2D_{5/2}-3s^2\,3p^2\,3d\,{}^2F_{7/2}$	
Fe XII	195.12	6.20	$3s^2\,3p^3\,{}^4S_{3/2}-3s^2\,3p^2\,3d\,{}^4P_{5/2}$	

× Planned SO/SPICE range.

Table 3.2: A list of all the lines tested between 1001−4000 Å

Ion	λ (Å)	Log T (K)	Transition	Instrument Range
H I (Ly-β)	1025.72	–	1s ^{2}S$_{1/2}$−3p ^{2}P$_{1/2}$	×
H I (Ly-α)	1215.67	–	1s ^{2}S$_{1/2}$−2p ^{2}P$_{1/2}$	
Ca II	3934.78	4.05	3p^6 4s ^{2}S$_{1/2}$−3p^6 4p ^{2}P$_{3/2}$	◇ (VBI blue)
S II	1259.52	4.25	3s^2 3p^3 ^{4}S$_{3/2}$−3s 3p^4 ^{4}P$_{5/2}$	
C II	1036.34	4.40	2s^2 2p ^{2}P$_{1/2}$−2s 2p^2 ^{2}S$_{1/2}$	×
C II	2748.09	4.40	2s^2 3p ^{2}P$_{3/2}$−2s^2 4d ^{2}D$_{5/2}$	
N II	1083.99	4.45	2s^2 2p^2 ^{3}P$_0$−2s 2p^3 ^{3}D$_1$	
O II	1128.07	4.45	2s 2p^4 ^{4}P$_{5/2}$−2s^2 2p^2 (3P) 3p ^{4}P$_{5/2}$	
Mg III	3354.70	4.55	2s^2 2p^5 3d ^{3}P$_0$−2s^2 2p^5 4p ^{3}S$_1$	
Ne II	3345.36	4.55	2s^2 2p^4 3s ^{4}P$_{1/2}$−2s^2 2p^4 3p ^{4}D$_{1/2}$	
S III	1190.20	4.70	3s^2 3p^2 ^{3}P$_0$−3s 3p^3 ^{3}D$_1$	
Si III	1206.50	4.70	3s^2 ^{1}S$_0$−3s 3p ^{1}P$_1$	
Si III	1301.15	4.70	3s 3p ^{3}P$_1$−3p^2 ^{3}P$_0$	
Si III	1312.59	4.70	3s 3p ^{1}P$_1$−3s 4s ^{1}S$_0$	
C III	1176.37	4.85	2s 2p ^{3}P$_2$−2p^2 ^{3}P$_1$	
N III	2248.65	4.85	2s^2 3d ^{2}D$_{5/2}$−2s^2 4p ^{2}P$_{3/2}$	
N III	3366.77	4.85	2s 2p 3s ^{4}P$_{3/2}$−2s 2p 3p ^{4}P$_{1/2}$	
O III	1153.78	4.90	2s 2p^3 ^{3}S$_1$−2p^4 ^{3}P$_2$	
Fe V	3076.54	4.95	3d^4 ^{3}G$_3$−3d^4 (1) ^{3}F$_2$	
Fe V	3143.86	4.95	3d^4 ^{3}G$_5$−3d^4 (1) ^{3}F$_4$	
Fe V	3892.38	4.95	3d^4 ^{5}D$_4$−3d^4 (2) ^{3}F$_4$	◇ (ViSP)
O IV	1338.62	5.15	2s 2p^2 ^{2}P$_{1/2}$−2p^3 ^{2}D$_{3/2}$	
O IV	1399.78	5.15	2s^2 2p ^{2}P$_{1/2}$−2s 2p^2 ^{4}P$_{1/2}$	
O IV	1401.16	5.15	2s^2 2p ^{2}P$_{3/2}$−2s 2p^2 ^{4}D$_{5/2}$	
Fe VI	3814.63	5.20	3p^6 3d^3 ^{4}F$_{3/2}$−3p^6 3d^3 ^{2}P$_{3/2}$	◇ (ViSP)
Fe VI	3890.51	5.20	3p^6 3d^3 ^{4}F$_{5/2}$−3p^6 3d^3 ^{2}P$_{3/2}$	◇ (ViSP)
Fe VI	3983.44	5.20	3p^6 3d^3 ^{2}F$_{5/2}$−3p^6 3d^3 ^{2}D$_{5/2}$	◇ (ViSP)
O V	2790.67	5.35	2s 3s ^{3}S$_1$−2s 3p ^{3}P$_0$	
Mg V	2783.58	5.45	2s^2 2p^4 ^{3}P$_2$−2s^2 2p^4 ^{1}D$_2$	
O VI	1031.91	5.45	1s^2 2s ^{2}S$_{1/2}$−1s^2 2p ^{2}P$_{3/2}$	×
O VI	1037.61	5.45	1s^2 2s ^{2}S$_{1/2}$−1s^2 2p ^{2}P$_{1/2}$	×
Ne VI	1005.73	5.60	2s^2 2p ^{2}P$_{3/2}$−2s 2p^2 ^{4}P$_{3/2}$	×
Mg VI	1190.12	5.65	2s^2 2p^3 ^{4}S$_{3/2}$−2s^2 2p^3 ^{2}P$_{3/2}$	
Si VII	1049.15	5.79	2s^2 2p^4 ^{3}P$_1$−2s^2 2p^4 ^{1}S$_0$	
Mg VIII	1075.81	5.90	2s 2p^2 ^{2}P$_{3/2}$−2p^3 ^{4}S$_{3/2}$	
Fe X	1028.02	6.05	3s2 3p^4 3d ^{4}D$_{7/2}$−3s^2 3p^4 3d ^{2}F$_{7/2}$	×
Fe XIII	3388.91	6.25	3s^2 3p^2 ^{3}P$_2$−3s^2 3p^2 ^{1}D$_2$	

◇ Planned DKIST range.

× Planned SO/SPICE range.

Table 3.3: A list of all the lines tested between 4001−14400 Å.

Ion	λ (Å)	Log T (K)	Transition	Instrument Range
H I (Hβ)	4862.73	–	2p ^{2}P$_{3/2}$–4d ^{2}D$_{5/2}$	◇ (VBI blue, ViSP)
H I (Hα)	6564.72	–	2p ^{2}P$_{3/2}$–3s ^{2}S$_{1/2}$	⋆, ◇ (VTF, VBI red, ViSP)
He I	10833.31	–	1s 2s 3S$_1$–1s 2p ^{3}P$_2$	⋆, ◇† (DL-NIRSP, Cryo-NIRSP)
He I	4472.73	–	1s 2p ^{3}P$_2$–1s 4d ^{3}D$_3$	◇ (ViSP)
He I	5877.25	–	1s 2p ^{3}P$_1$–1s 3d ^{3}D$_1$	◇ (DL-NIRSP, ViSP)
He I	7067.14	–	1s 2p ^{3}P$_2$–1s 3s ^{3}S$_1$	◇ (ViSP)
Ca II	8544.44	4.05	3p^6 3d ^{2}D$_{5/2}$–3p^6 4p ^{2}P$_{3/2}$	◇ (VTF, ViSP, DL-NIRSP)
Mg II	9246.76	4.15	4s ^{2}S$_{1/2}$–4p ^{2}P$_{1/2}$	◇†
Mg II	10917.27	4.15	3d ^{2}D$_{5/2}$–4p ^{2}P$_{3/2}$	◇†
Mg II	10918.34	4.15	3d ^{2}D$_{3/2}$–4p ^{2}P$_{3/2}$	◇†
C II	4268.46	4.40	2s^2 3d ^{2}D$_{5/2}$–2s^2 4f ^{2}F$_{5/2}$	◇ (ViSP)
C II	6579.87	4.40	2s^2 3s ^{2}S$_{1/2}$–2s^2 3p ^{2}P$_{3/2}$	◇ (ViSP)
C II	6584.70	4.40	2s^2 3s ^{2}S$_{1/2}$–2s^2 3p ^{2}P$_{1/2}$	◇ (ViSP)
O II	7320.94	4.45	2s^2 2p^3 ^{2}D$_{5/2}$–2s^2 2p^3 ^{2}P$_{1/2}$	◇ (ViSP)
O II	7332.76	4.45	2s^2 2p^3 ^{2}D$_{3/2}$–2s^2 2p^3 ^{2}P$_{3/2}$	◇ (ViSP)
Mg III	7058.75	4.55	2s^2 2p^5 4s ^{3}P$_2$–2s^2 2p^5 4p ^{3}S$_1$	◇ (ViSP)
He II	4687.12	4.70	3d ^{2}D$_{5/2}$–4f ^{2}F$_{7/2}$	◇ (ViSP)
C III	4648.72	4.85	2s 3s ^{3}S$_1$–2s 3p ^{3}P$_2$	◇ (ViSP)
C III	4651.55	4.85	2s 3s ^{3}S$_1$–2s 3p ^{3}P$_1$	◇ (ViSP)
N III	9405.04	4.85	2s^2 4s ^{2}S$_{1/2}$–2s^2 4p ^{2}P$_{3/2}$	◇†
O III	5008.24	4.90	2s^2 2p^2 ^{3}P$_2$–2s^2 2p^2 ^{1}D$_2$	◇ (ViSP)
Fe VI	4015.69	5.20	3p^6 3d^3 ^{2}G$_{9/2}$–3p^6 3d^3 ^{2}F$_{7/2}$	◇ (ViSP)
Fe VI	5177.48	5.20	3p^6 3d^3 ^{4}F$_{9/2}$–3p^6 3d^3 ^{2}G$_{9/2}$	◇ (ViSP)
O V	5115.48	5.35	2s 3s ^{1}S$_0$–2s 3p ^{1}P$_1$	◇ (ViSP)
Fe VIII	4146.63	5.65	3s^2 3p^6 4s ^{2}S$_{1/2}$–3s^2 3p^5 3d^2 ^{2}P$_{3/2}$	◇ (ViSP)
Fe VIII	5414.19	5.65	3s^2 3p^6 4s ^{2}S$_{1/2}$–3s^2 3p^5 3d^2 ^{2}P$_{1/2}$	◇ (ViSP)
Fe IX	9788.36	5.85	3s^2 3p^5 3d ^{3}D$_3$–3s^2 3p^5 3d ^{1}F$_3$	◇†
S XIII	9916.70	5.91	2s^2 2p^5 ^{2}P$_{3/2}$–2s^2 2p^5 ^{2}P$_{1/2}$	◇†
Fe X	6376.29	6.05	3s^2 3p^5 ^{2}P$_{3/2}$–3s^2 3p^5 ^{2}P$_{1/2}$	⋆, ◇ (ViSP)
S IX	12523.48	6.05	2s^2 2p^4 ^{3}P$_2$–2s^2 2p^4 ^{3}P$_1$	◇†
Fe XI	7894.03	6.12	3s^2 3p^4 ^{3}P$_2$–3s^2 3p^4 ^{3}P$_1$	⋆, ◇ (VBI red, DL-NIRSP, ViSP)
Si X	14304.72	6.15	2s^2 2p ^{2}P$_{1/2}$–2s^2 2p ^{2}P$_{3/2}$	◇† (DL-NIRSP, Cryo-NIRSP)
Fe XIII	10749.11	6.25	3s^2 3p2 ^{3}P$_0$–3s^2 3p^2 ^{3}P$_1$	⋆, ◇† (DL-NIRSP, Cryo-NIRSP)
Fe XIII	10800.77	6.25	3s^2 3p2 ^{3}P$_1$–3s^2 3p^2 ^{3}P$_2$	⋆, ◇† (Cryo-NIRSP)
Fe XIV	5304.48	6.30	3s^2 3p ^{2}P$_{1/2}$–3s^2 3p ^{2}P$_{3/2}$	⋆, ◇ (DL-NIRSP, ViSP)
Fe XV	7062.15	6.35	3s 3p ^{3}P$_1$–3s 3p ^{3}P$_2$	⋆, ◇ (ViSP)
Ar XI	6918.02	6.68	2s^2 2p^4 ^{3}P$_2$–2s^2 2p^4 ^{3}P$_1$	⋆, ◇ (ViSP)

† Values are within the spectral goal of DKIST/ViSP
⋆ UCoMP line
◇ Planned DKIST range

corona transition region (PCTR) properties ($PC_{3,4}$) with markedly different thermal evolution, and a fourth with properties of the nearby corona (PC_2). Our present study utilizes the ion fractions computed at each point along the propagation of these four structures to generate the intensity of each line along the CME path.

The thermodynamic evolution of the prominence (PC_1) and adjacent material ($PC_{2,3,4}$) from the Rivera19 study is shown on the right panel of Figure 3.2. The profiles are used to calculate the evolution of the charge states between $1.05-2R_\odot$ for each of the different components that are used to compute intensities. In this study, we consider all four CME components identified by Rivera19, in order to investigate lines generated by a multi-thermal CME structure that is often observed at these distances (Filippov & Koutchmy, 2002; Landi et al., 2010).

Since we are following particular structures within the CME, we specify a smaller angular width compared to the span of the entire CME for each component. We set the angular width of the prominence, PC_1, to 30 degrees, which is estimated to be approximately 75% of the average angular width recorded for CMEs observed by the Large Angle and Spectrometric Coronagraph Experiment (LASCO; Brueckner et al. 1995) on board SOHO, which was found to be approximately 41 degrees (Webb & Howard, 2012). In addition, we assume a simple model for the remaining PCs where the coronal plasma, PC_2, and PCTR, $PC_{3,4}$, material are concentric layers surrounding the filament channel described by a small angle, $\phi = 5^\circ$ for PC_2 and 3° for each $PC_{3,4}$. These are estimates, not precise predictions, so the filamentary and sheath-like structure of PCTR allows the use of small angles. The geometry of the prominence and enveloping layers is illustrated on the left panel of Figure 3.2.

In prominences and PCTR plasma, the filling factor is still fairly unknown; however, from previous studies this value has been determined to be well below 1 (Cirigliano et al., 2004; Lee & Raymond, 2012). The range in prominences is summarized in Labrosse et al. (2010) to be approximately between 0.1-0.001. Therefore, in the

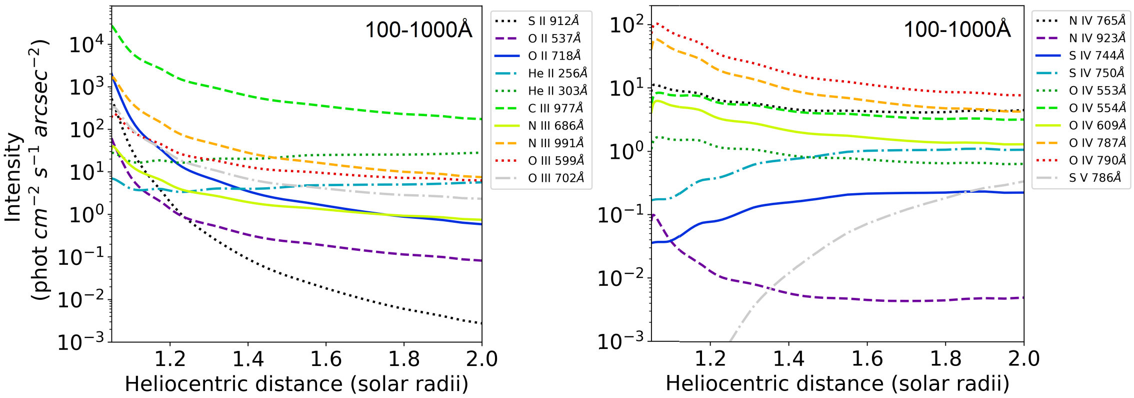

Figure 3.3: EUV intensities for all the lines between 1.05-2$R_\odot$ for PC_1.

present study, we estimate a value of 0.1 for $\mathrm{PC}_{1,3,4}$ while assuming a filling factor of 1 for PC_2. In actuality, the filling factor for the coronal plasma is likely < 1 given that not all the plasma along the LOS is radiating; however, this value is unknown for this plasma therefore we assume a value of unity in the present work. The intensity is proportional to the filling factor therefore any intensity result will scale linearly and can be easily deduced for a different filling factor. For filling factors less than one, we assume the emitting plasma is homogeneous and that the remaining volume is empty space that is not radiating.

3.3 Results

We generated the intensity of all lines listed in Table 3.1, 3.2, and 3.3 formed by the prominence and adjacent structures described. We reference selected intensities in the main text but include all computed intensities in Appendix Section A.1.1 in Figure A1−A3 for the prominence material (PC_1), Figure A4 and A5 for the coronal plasma (PC_2), Figure A6 and A7 for the PCTR material (PC_3) and Figure A8−A10 for the PCTR material (PC_4). We include only the most prominent lines for each component above 10^{-3} phot cm^{-2} s^{-1} arcsec^{-1}.

We also include a list of recommended lines, Table 3.4, which are lines with in-

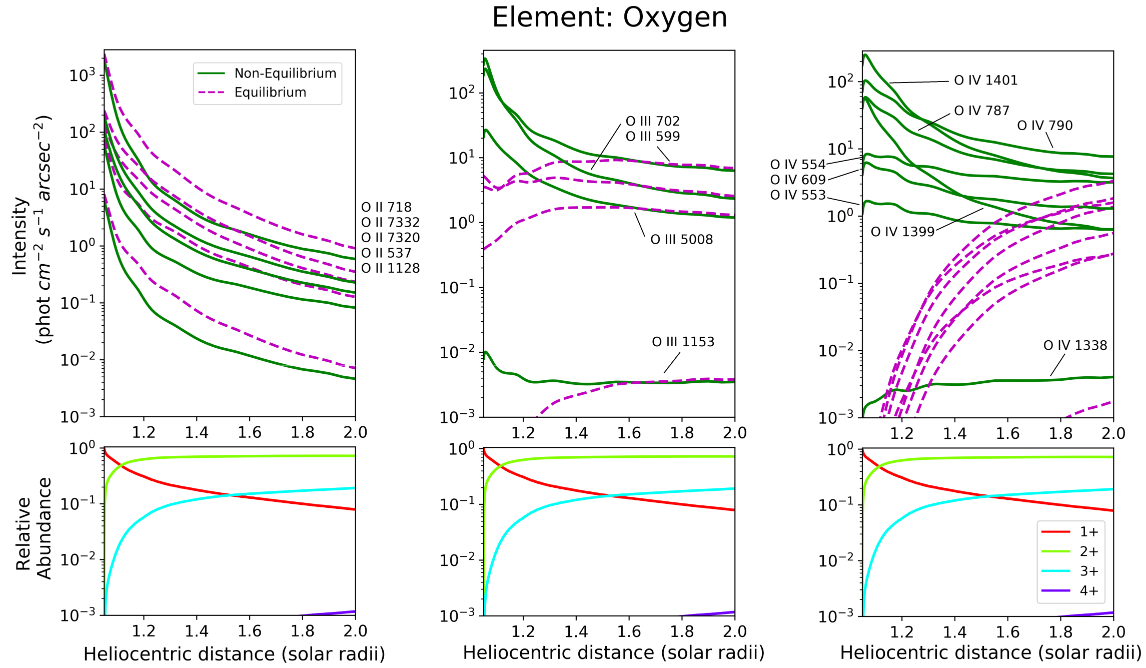

Figure 3.4: Results for PC_1; a vertical two panel plot for each element displaying the nonequilibrium (green) and Equilibrium (magenta) intensity for each line (top), and the relative abundance of each ion (bottom). For plots with a list of lines appearing adjacent on the right, the lines are organized in descending order by each line's initial nonequilibrium intensity value. In addition, as a note, the spectral lines include the common roman numeral convention describing the emitting ion while the relative abundance plots describe the charge states by the number of missing electrons which is typical heliospheric nomenclature. This results in mismatch of numbers such that Fe V is the Fe^{4+} charge state and so on.

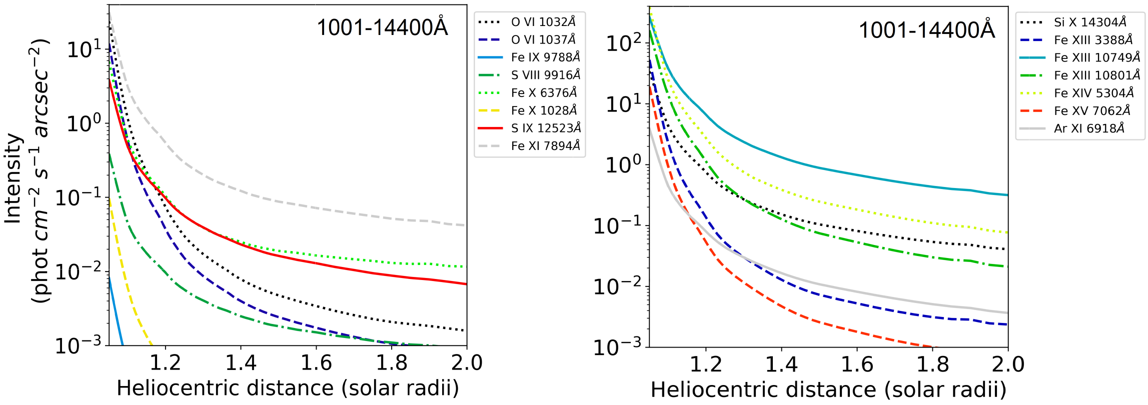

Figure 3.5: UV, visible, and infrared intensities for all the lines between 1.05-2$R_{\odot}$ for PC$_2$.

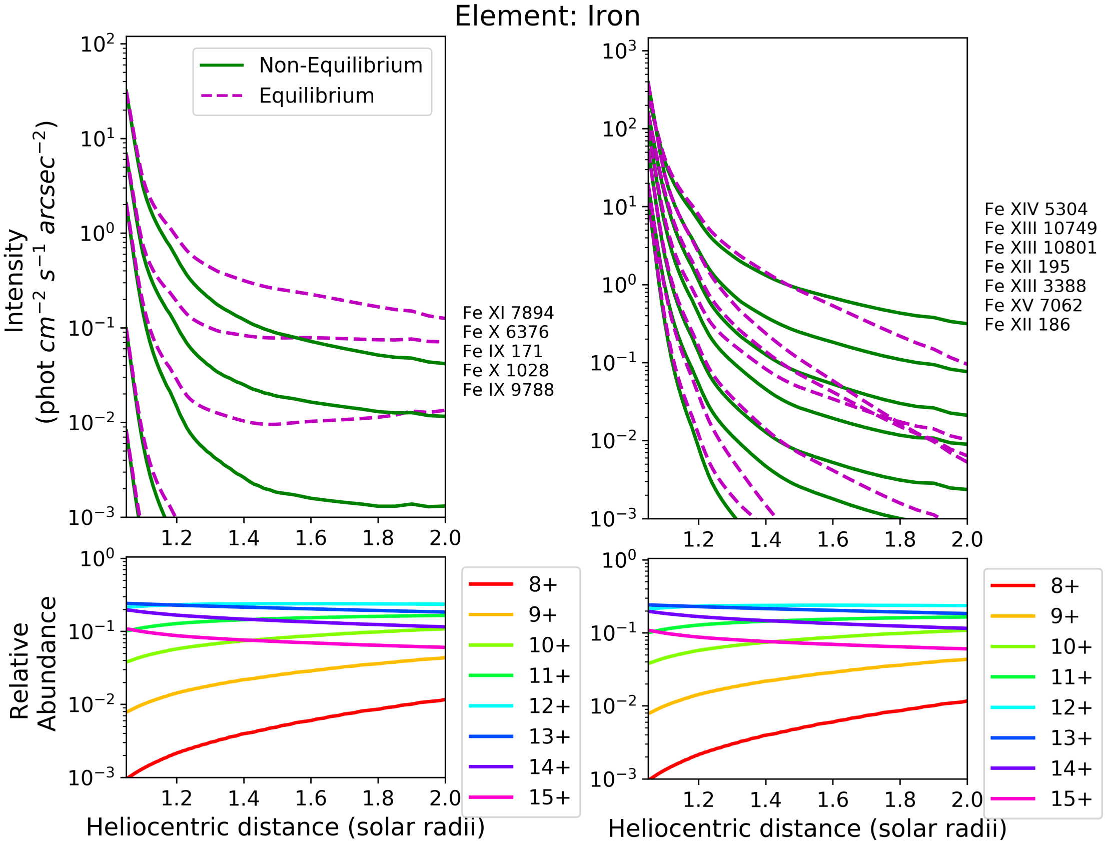

Figure 3.6: Same placement as Figure 3.4 for the coronal plasma, PC$_2$.

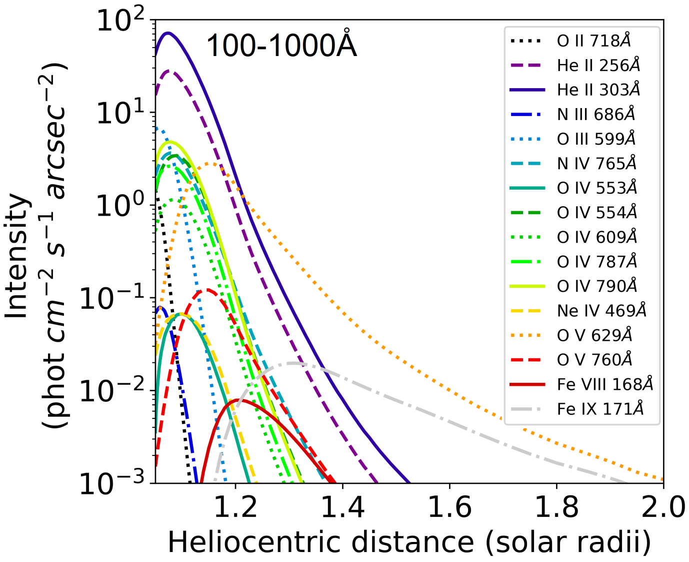

Figure 3.7: EUV intensities for all the lines between 1.05-2$R_\odot$ for PC$_3$.

tensities that reach a value above 1 phot cm^{-2} s^{-1} arcsec^{-1} at any point along the evolution. These are the lines that can be most easily observed by future instruments. The list includes the ion, wavelength, formation temperature under ionization equilibrium, and the plasma structure in which the lines are predicted to appear. The plasma structures are noted as prominence (P), PCTR (PC$_3$ or PC$_4$), and Coronal (C).

In addition, we include additional figures for each plasma, for example Figure 3.4, as two panels comparing the nonequilibrium versus the equilibrium intensity for each line (top), and the NEI ion fractions of the corresponding ions (bottom) as a function of distance. We reference selected plots as examples in the text; however, include all plots for each plasma and element in Appendix Section A.1.2 in Figure A11−A20. The equilibrium intensity plotted in the dashed magenta line is the intensity emitted by the plasma using the ion fractions computed under ionization equilibrium. Deviations from this value at any point along the plasma trajectory indicate how much the emitting ion is out of equilibrium.

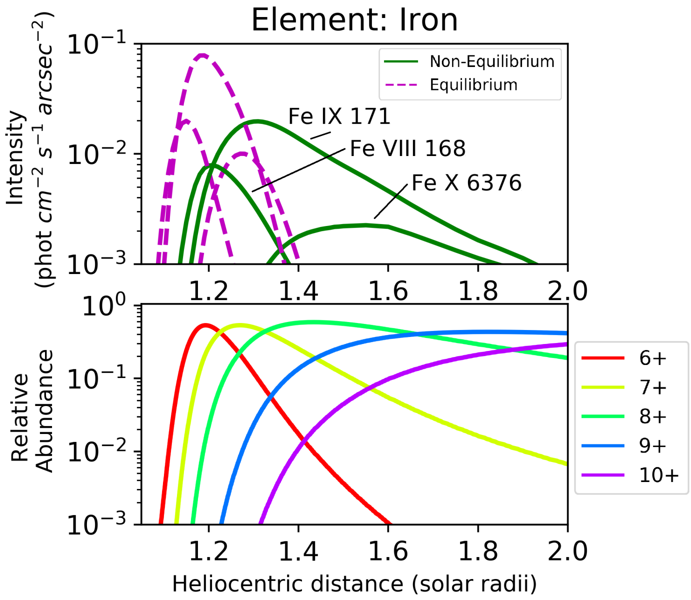

Figure 3.8: Same placement as Figure 3.4 for the PCTR plasma, PC_3.

3.3.1 Prominence Material

For the prominence material, we set the angular width, $\phi = 30°$, and filling factor of 0.1. We find that, in general, the prominence material has the strongest intensities compared to the other components in our analysis, as shown in Figure 3.3 for EUV. Many of the lines decrease sharply in intensity as the plasma propagates through the corona; however, they can maintain a comparable signal out to $2R_{\odot}$. Furthermore, we find that several lines, such as the S IV/V, He II, and Fe VI lines, peak at a point beyond the surface or remain in an upward trend becoming most visible somewhere along the plasma trajectory.

When comparing the nonequilibrium intensity to the equilibrium value, as shown in the top plots for each element, we find that most lines in the prominence material follow closely to their equilibrium intensity with the exception of the O lines tested, shown in Figure 3.4, as well as the Fe lines and certain locations of N III 991/2248, N IV 765 lines and the Ne II 3345 in Appendix Figure A11. For the O IV lines, we find the emission is orders of magnitude larger compared to its equilibrium value

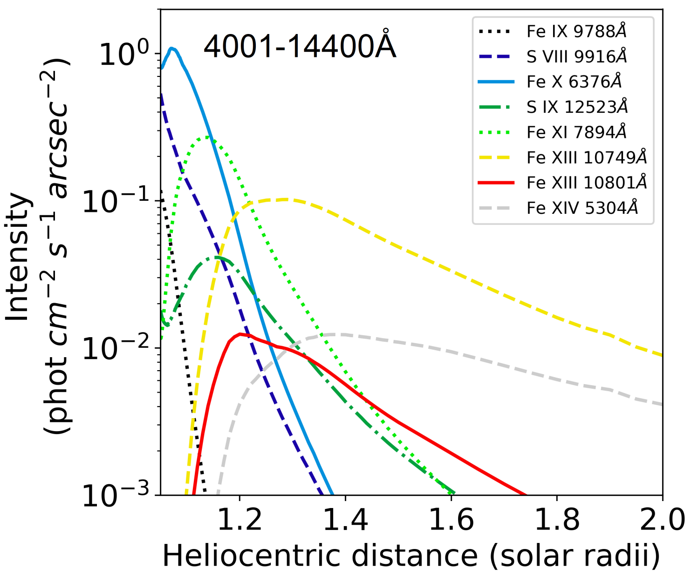

Figure 3.9: Visible and infrared intensities for all the lines between 1.05-2$R_\odot$ for PC_4.

during the early propagation of the plasma; however, the lines begin to converge to their equilibrium value as the material reaches 2$R_\odot$. This is a LOS integration effect further discussed in Section 3.4.1.

3.3.2 Coronal Material

In the coronal plasma, PC_2, we set the angular width, $\phi = 5°$, and filling factor to 1. Results for all prominent PC_2 lines are plotted in Figure 3.5 for the visible and infrared. We find a similar behavior as seen for the prominence lines where all intensities significantly decrease along the plasma path. Nevertheless, each line shows variation in the rate at which the intensity fades as the plasma moves away from the surface, providing insight to the range of its visibility.

When comparing the nonequilibrium to equilibrium intensities, we find the all ions remain closely tied to equilibrium during the early stages of evolution; however, they begin to deviate as the plasma cools and becomes more tenuous. This can be seen early along with some of the Fe ions, as shown in Figure 3.6, as well as, O and

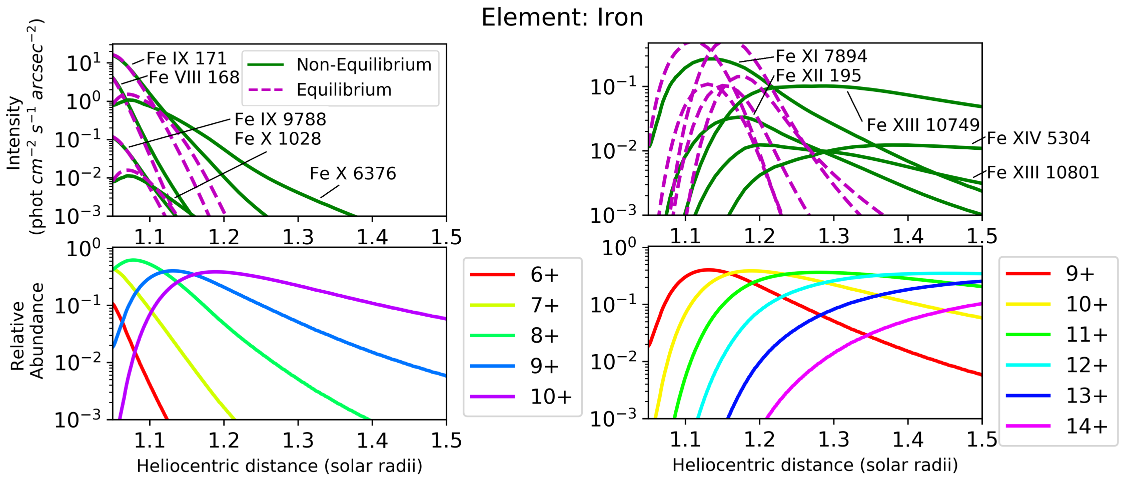

Figure 3.10: Same placement as Figure 3.4 for the PCTR plasma, PC_4.

the Mg, Si, S lines just past $1.2R_\odot$ and for Ar, Ne just beyond $1.5R_\odot$, in Appendix Figures A14 and A15. These heights are well within UCoMP's range, and also at the edge of DKIST; the ability to observe these deviations provides a powerful diagnostic tool for the plasma evolution.

3.3.3 PCTR Material

In the PCTR material, PC_3 and PC_4, we specify an angular width of, $\phi = 3°$, and a filling factor 0.1 which is the same as in the prominence material. The EUV intensities for PC_3 are presented in Figure 3.7 and visible to infrared for PC_4 in Figure 3.9. We find the intensities for the lines to be significantly more transient compared the lines formed within $PC_{1,2}$ where the intensity narrowly peaks and fades within the $2R_\odot$ FOV for many of the lines. This result predicts the sequence in which we expect specific lines to become the most visible during the plasma evolution.

Furthermore, for the Fe lines in PC_4 shown in Figure 3.10, the ions remain in equilibrium during the initial propagation of the plasma, especially the Fe IX, X, and XI lines that are formed first, after which they begin to depart from equilibrium and new lines are generated as the plasma struggles to keep pace with the increasing electron temperature. This is also seen in Si VII 1049, O V, VI and S V, VI lines below $1.1R_\odot$ while the remaining lines are entirely out of equilibrium found in Appendix Figure A19. Both He II 303 and 256 decrease below 10^{-3} phot cm^{-2} s^{-1} arcsec^{-1} just after $1.15R_\odot$ while remaining close to equilibrium up to that height. If observed, the PCTR lines will provide enormous insight to the evolution and potential heating experienced by the plasma.

For Fe lines formed in the more tenuous PC_3, the Fe VIII, XI and X intensities peak farther from the Sun, as compared to the Fe lines in PC_4, as shown in Figure 3.8. This is a result of the charge states forming later in the plasma evolution given that PC_3 remains cooler compared to PC_4 out to $2R_\odot$. In addition, all lines are completely out of equilibrium with the exception of instances of Ca II 8544, Si III 1206, and S III 1190 during the initial release as shown in Appendix Figures A17 and A18.

3.4 Discussion

3.4.1 Intensity Evolution

As seen in the nonequilibrium intensities, many of the lines significantly decrease with distance from the Sun. This is anticipated given the intensity generated has a electron density dependence, collisonal (n_e^2) and radiative (n_e), therefore as the plasma structures rapidly expand and decrease in electron density, the intensity follows. Nevertheless, some of the brightest lines in the prominence material, e.g. Ca II 3934, He I 5877 and 7067, remain strong out to $2R_\odot$. This occurs because each line decreases at a significantly different rate which is strongly governed by the number of emitters that are able to survive in the plasma during its radial evolution. This is evident between the H I 4862, 6564 lines compared to the He I 5877, 7067 lines which have initial intensities that are approximately an order of magnitude apart but descend to values which are multiple orders of magnitude apart as they reach $2R_\odot$,

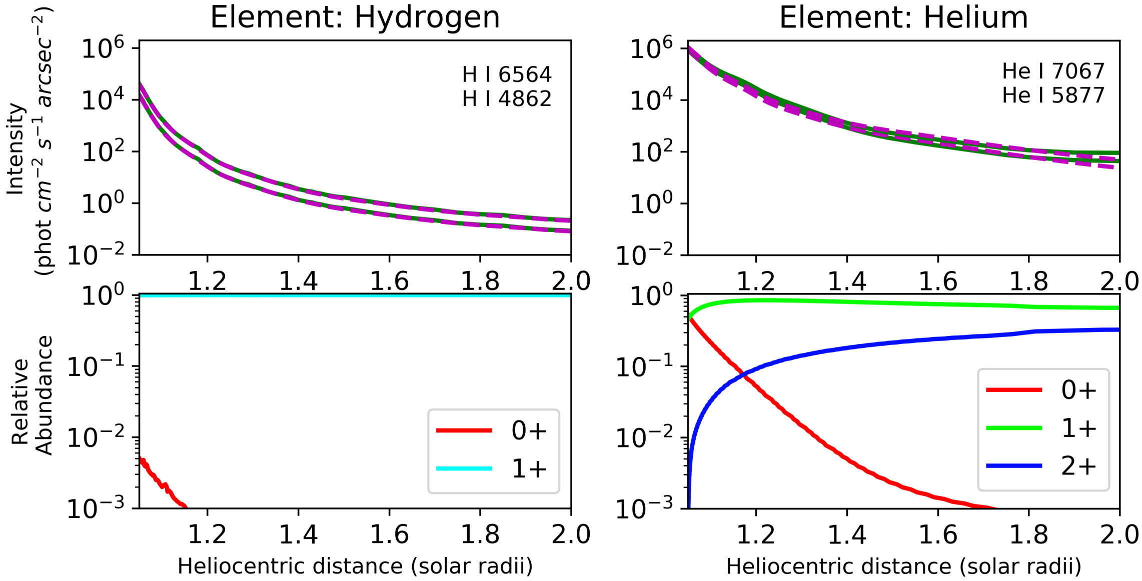

Figure 3.11: Same placement as Figure 3.4 for the prominence plasma, PC_1.

as shown in the top plots for each element in Figure 3.11. In this case, neutral He is able to survive within the plasma much farther from the Sun compared to neutral H which is almost entirely depleted below $1.2R_\odot$ under these conditions, as shown in the relative abundance plots below. This can be attributed to neutral He's larger ionization threshold compared to neutral H: 24.6eV compared to 13.4eV, respectively.

Furthermore, some lines exhibit an enhancement after the release of the plasma. This can be explained by the fact that the emitting ion is absent in the plasma at the beginning of the eruption, but forms later by ionization as the plasma gets strongly heated. This can be seen in the Fe XI, XIII lines of Figure 3.10 that begin to increase following the significant creation of the Fe^{10+} and Fe^{12+} charge states. This is the primary reason for the persistent enhancement and dimming of lines from sequential Fe ions within $PC_{3,4}$ which can be seen to follow the creation and immediate destruction of the corresponding ion.

We also find that the peak intensity does not coincide with location of the peak ion fraction in many of the lines, e.g. the Fe IX 171 intensity compared to Fe^{8+}

abundance in Figure 3.8. This occurs due to the geometry of the integration path where the LOS intensity computed intersects plasma at different radial distances from the surface, as shown in Figure 3.12. The distance in the plasma's outer edge, r_e, is larger compared to the distance to the center, r_c, and the ion distributions correspond to plasma properties at those distances. Because of projection effects, the plasma at the edges begins to form new ions that radiate lines that are not yet formed and emitted by plasma at the height r_c, given by the projection of r_e on the plane of the sky. However, in Figure 3.8 and in all other similar figures, the same coordinate is used for both the line intensity and the ion fractions, leading to an artificial mismatch.

Additionally, as a consequence of both PCTR components experiencing rapid heating with a few solar radii that increases the plasma temperature by over an order of magnitude, the plasma undergoes fast and continuous ionization while accelerating through the corona. This prevents most ions from reaching equilibrium which is most evident in the Fe lines plotted in Figure 3.8 and 3.10 for PC_3 and PC_4, respectively. For PC_3, we find that the lines for Fe are created well after the plasma is released during rapid ionization conditions where the ions perpetually fall behind equilibrium. In PC_4, the Fe lines are formed closer to the Sun at conditions where the ions can maintain equilibrium for a short distance from the surface. This can be seen for the Fe IX, X, XI lines which are generated within $1.1R_\odot$ but fail to maintain equilibrium beyond that point. Similarly, the lines whose ions are created after that distance never reach equilibrium.

3.4.2 Diagnostic Potential

In the prominence and coronal plasma, there are many lines from our analysis that can be used for diagnostic purposes given that nearly all ions remain close to equilibrium and many lines maintain a significant signal along the plasma trajectory. Some of the coolest lines, below $\log T$ (K) $= 5$, can be optically thick in prominences

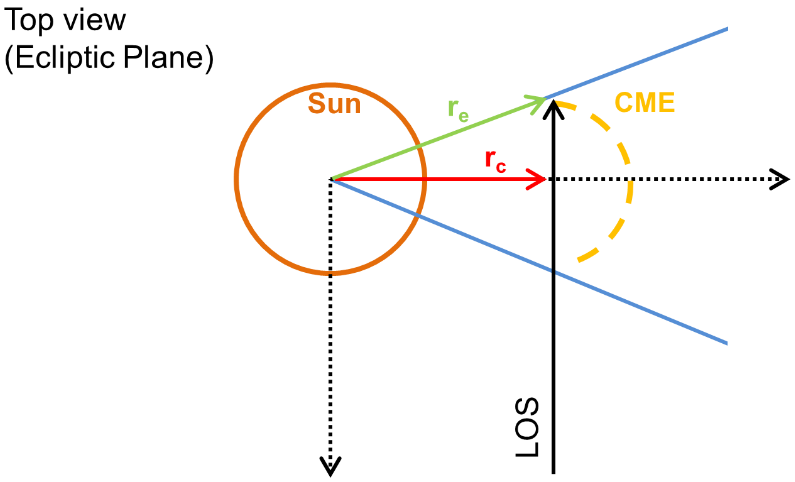

Figure 3.12: LOS geometry, see Section 3.4.1 for details.

observed on the disk; however, the optical thickness effects may become less important as the plasma decreases in density during its expansion after its release (Susino et al., 2018). Therefore, spectral lines emitted from the prominence material should be tested for effects of optical thickness in observations. If the lines are not optically thin, they can still be investigated with the appropriate radiative transfer conditions to gain insight on the properties of the plasma (Labrosse et al. 2010 and references therein). If radiative transfer effects are negligible, many of the lines can be used for straightforward line ratio temperature and density diagnostics as well as DEM diagnostics.

Based on our results, many of the prominence lines are predicted to be visible in observations and, with the exception of the Fe and O lines, remain within equilibrium throughout the most dynamic stage of the evolution. For example, the Ca II 8544 and Hβ (H I 4862) lines are some of the strongest lines in the prominence material. In previous work, the ratio of the Ca II to Hβ have been useful for pressure diagnostics of prominences (Heasley & Milkey, 1978; Gouttebroze et al., 2002). In addition, the O III 599 and 702 are also visible in the prominence plasma. The line ratio has been shown to be a temperature sensitive pair in solar observations (Keenan & Aggarwal, 1989). Furthermore, the H I Ly-α and He I 10830 which become linearly polarized through scattering in the corona, have been previously used to explore the coronal magnetic field direction through line depolarization as a result of the Hanle effect (Hanle, 1924; Raouafi et al., 2016). Through spectropolarimetric measurements with DKIST and UCoMP, He I 10830 may provide insight to the magnetic field evolution of prominences to investigate CME geoeffectiveness and connection to space weather at Earth. Additionally, the He I 10830 and 5877 have provided magnetic field diagnostics of prominences at the solar surface through the inversion of the Stokes profiles (Casini et al. 2009 and references therein). Inversion techniques are typically not applied to dynamic eruptions but they can provide important pre-eruptive magnetic topology of the prominence structures.

In addition, there are a few lines that have been identified as sensitive to electron density or temperature; C III 1175/977, N IV 923/765, and Si III 1312/1301 while O IV 790/553 and N III 991/686 can provide temperature diagnostics (Wilhelm et al. 1995; Harrison et al. 1995 and references therein).

The relatively low plasma density suggests that lines emitted in the coronal, as well as PCTR plasmas, are optically thin (Parenti, 2015). There are several lines emitted by the same ion that are formed within the coronal component (PC_2) and the PCTR (PC_4) from Fe, Ar, S that can be used for temperature and density diagnostics. The intensities can be useful for straightforward line ratio analysis which can be carried out for spectral lines emitted by the same or consecutive ions. For example, the Fe XIII 10749/10801 line pair can provide density diagnostics (Eddy & McKim Malville, 1967). They are also sensitive to the Zeeman and Hanle effect which make them ideal probes to the coronal magnetic field (Arnaud & Newkirk, 1987; Lin et al., 2000, 2004; Gibson et al., 2017). These emission lines are common in eclipse observations of the corona (Bao et al., 2009; Habbal et al., 2011b; Dima et al., 2018), and during

CMEs (Habbal et al., 2010, 2011a). From this analysis, we also predict the Fe lines to be particularly valuable to study the coronal plasma within the CME out to $2R_\odot$. Similarly, the Fe IX, X, XI, XIV, XV, which range in formation temperature between 1-5 million Kelvin, can be useful to investigate heating throughout the plasma's 2R$_\odot$ evolution.

Based on a comparison to equilibrium intensity, the diagnostic techniques can be confidently applied close to the Sun where the signal is largest and where lines are anticipated to remain at equilibrium. Specifically, in the coronal component, below $1.2R_\odot$ for Fe and S lines, while as far as $1.5R_\odot$ for the Ar line. While for PC$_4$, there is only a short window within $1.15R_\odot$ from the surface where the Fe IX-XI lines are predicted to be in equilibrium. In addition, S VIII is useful below $1.05R_\odot$, mainly on the surface and initiation of the eruption, while the Ar XI line, which is formed farthest from the Sun in this component, remains out of equilibrium.

However, neglecting recombination to excited levels, line intensity ratios can be applied to spectral lines from the same ion even under NEI conditions as the ratio is independent of both ion and elemental abundances. For some ions such as H I, however, recombination effects can alter line ratios.

An extended review of UV and EUV line diagnostics can be found in the recent summary by Del Zanna & Mason (2018) which discussed many of the lines presented here. Additionally, useful density and temperature sensitive EUV line pairs are listed for the Coronal Diagnostic Spectrometer (CDS) on Solar and Heliospheric Observatory (SOHO) in Harrison et al. (1995) and for Solar Ultraviolet Measurements of Emitted Radiation (SUMER) in Wilhelm et al. (1995).

3.5 Summary

One of the main ways of probing astrophysical plasma is by studying its radiative properties. Spectral lines and their polarization properties are a powerful diagnostic to measure plasma temperature, density, composition, and magnetic field. In this work, we identified lines that can be used to study the properties of an erupting prominence and adjacent structures within a $2R_\odot$ FOV. We test the intensities generated by lines between $\log(T_e) = 4 - 6.68$ mainly in the EUV to visible and infrared range, $\lambda = 100 - 14400$Å, to gain insight on how the lines are affected by the thermodynamic evolution of the plasma. We also provide a list of the brightest lines that are expected to be emitted by all CME plasmas, and discuss their diagnostic potential.

This work will be useful for planning observations to investigate the CME's multi-thermal components with future instruments; UCoMP, DKIST, and SPICE. These instruments cover the entire range of spectral lines tested in this work and can provide a powerful multi-messenger view of solar activity.

Table 3.4: Recommended lines above 1 phot cm^{-2} s^{-1} arcsec^{-2}.

Ion	λ (Å)	Log T (K)	Plasma Structure
H I (Ly-β)	1025.72	–	P (PC$_1$)
H I (Ly-α)	1215.67	–	P (PC$_1$)
H I (Hβ)	4862.73	–	P (PC$_1$)
H I (Hα)	6564.72	–	P (PC$_1$)
He I	4472.73	–	P (PC$_1$)
He I	5877.25	–	P (PC$_1$)
He I	7067.14	–	P (PC$_1$)
He I	10833.31	–	P (PC$_1$)
Ca II	3934.78	4.05	P (PC$_1$)
Ca II	8544.44	4.05	P (PC$_1$), PCTR (PC$_3$)
Mg II	9246.76	4.15	P (PC$_1$)
Mg II	10917.27	4.15	P (PC$_1$)
Mg II	10918.34	4.15	P (PC$_1$)
S II	912.74	4.25	P (PC$_1$)
S II	1259.52	4.25	P (PC$_1$)
C II	1036.34	4.40	P (PC$_1$)
C II	2748.09	4.40	P (PC$_1$)
C II	4268.46	4.40	P (PC$_1$)
C II	6579.87	4.40	P (PC$_1$)
C II	6584.70	4.40	P (PC$_1$)
O II	537.83	4.45	P (PC$_1$)
O II	718.50	4.45	P (PC$_1$), PCTR (PC$_3$)
O II	1128.07	4.45	P (PC$_1$)
O II	7320.94	4.45	P (PC$_1$)
O II	7332.76	4.45	P (PC$_1$)
N II	1083.99	4.45	P (PC$_1$)
He II	256.32	4.70	P (PC$_1$), C (PC$_2$), PCTR (PC$_3$)
He II	303.78	4.70	P (PC$_1$), C (PC$_2$), PCTR (PC$_3$)
S III	1190.20	4.70	P (PC$_1$)
Si III	1206.50	4.70	P (PC$_1$)
Si III	1301.15	4.70	P (PC$_1$)
Si III	1312.59	4.70	P (PC$_1$)
C III	977.02	4.85	P (PC$_1$)
N III	686.34	4.85	P (PC$_1$)
N III	991.58	4.85	P (PC$_1$)

Ion	λ (Å)	Log T (K)	Plasma Structure
C III	4648.72	4.85	P (PC_1)
C III	4651.55	4.85	P (PC_1)
O III	599.59	4.90	P (PC_1), PCTR (PC_3)
O III	5008.24	4.90	P (PC_1)
O III	702.90	4.90	P (PC_1)
Fe V	3892.38	4.95	P (PC_1)
S IV	750.22	5.00	P (PC_1)
N IV	765.15	5.15	P (PC_1), PCTR (PC_3)
O IV	553.33	5.15	P (PC_1)
O IV	554.51	5.15	P (PC_1), PCTR (PC_3)
O IV	609.83	5.15	P (PC_1)
O IV	787.71	5.15	P (PC_1)
O IV	790.20	5.15	P (PC_1)
O IV	1399.78	5.15	P (PC_1)
O IV	1401.16	5.15	P (PC_1)
O V	629.73	5.35	PCTR (PC_4)
O VI	1031.91	5.45	C (PC_2), PCTR (PC_4)
O VI	1037.61	5.45	C (PC_2), PCTR (PC_4)
Fe VIII	168.17	5.65	PCTR (PC_4)
Mg VI	1190.12	5.65	PCTR (PC_4)
Ne VIII	770.43	5.80	C (PC_2), PCTR (PC_4)
Ne VIII	780.39	5.80	C (PC_2), PCTR (PC_4)
Fe IX	171.07	5.85	C (PC_2), PCTR (PC_4)
Fe X	6376.29	6.05	C (PC_2), PCTR (PC_4)
S IX	12523.48	6.05	C (PC_2)
Fe XI	7894.03	6.12	C (PC_2)
Si X	14304.72	6.15	C (PC_2)
Fe XII	186.89	6.20	C (PC_2)
Fe XII	195.12	6.20	C (PC_2)
Fe XIII	3388.91	6.25	C (PC_2)
Fe XIII	10749.11	6.25	C (PC_2)
Fe XIII	10800.77	6.25	C (PC_2)
Fe XIV	5304.48	6.30	C (PC_2)
Fe XV	7062.15	6.35	C (PC_2)
Ar XI	6918.02	6.68	C (PC_2)

CHAPTER IV

On the Production of He$^+$ of Solar Origin in the Solar Wind

4.1 Background

As solar material is released from the photosphere into the solar wind, it simultaneously experiences a rapid rise in temperature and decrease in density as it travels through the chromosphere and transition region layers and then enters the multi-million degree corona. As it travels through the corona, the density continues to steadily decrease as the temperature evolves more slowly. Once density has decreased enough to effectively stop ionization and recombination processes, the solar wind ionization status remains constant (e.g. "frozen-in") in the heliosphere. Given the high temperature of the corona, the solar wind ionization state consists of fully ionized H and He along with highly ionized minor ions. Therefore, it is predicted that the solar wind includes very few neutrals or low ionized material as it travels through the interplanetary medium.

Consequently, low-ionized plasma detected by in-situ instruments is not ordinarily attributed to the solar wind, but rather associated with pick-up ions (PUIs; Möbius et al. 1985; Gloeckler et al. 1993) of interstellar origin or inner source PUIs which are predicted to be formed through the interaction with interplanetary dust (Geiss et al., 1994, 1995). PUIs are usually singly ionized particles that originate as neutrals of non-solar origin such as interstellar neutrals, cometary material (Nordholt et al., 2003; Gilbert et al., 2015), interplanetary dust (Gloeckler et al., 2000; Grün & Landgraf, 2001), or planetary wakes (Russell & Neugebauer, 1981; Grünwaldt et al., 1997) that enter or exist in the heliosphere. Once in the heliosphere, the neutrals can be ionized through photoionization or electron impact ionization, and can also undergo charge exchange with solar wind ions. Once ionized, the charged particles are then swept up by the interplanetary electromagnetic field and travel alongside the ambient solar wind.

Additionally, low ionized ions can be found to originate from prominence material within coronal mass ejections (CMEs; Lepri & Zurbuchen 2010; Gilbert et al. 2012). Prominences, or filaments while observed on the solar disk, are photospheric or chromospheric temperature ($\sim 10^4$K) plasma that can be seen as cloud-like structures hovering over the limb of the Sun (see recent reviews by Labrosse et al. 2010 and Parenti 2014). Despite being immersed within the coronal environment, prominences can sustain a low temperature throughout their lifetime where neutral or low ionized material is often observed. Prominences are thought to form within a twisted magnetic field that anchors them to the Sun. However, the magnetic field can become unstable, leading to a large scale eruption that releases the prominence plasma into interplanetary space forming a CME. Low ionized plasma that is able to escape without being further ionized during the eruption, can be observed in the extended solar corona as it travels into the heliosphere (Howard, 2015; Wood et al., 2016; Ding & Habbal, 2017). Therefore, prominence material can periodically contribute to the low ionized charge states observed near the Earth.

One manner in which PUIs can be differentiated from solar material such as prominence plasma is by examining their velocity distribution functions (VDFs) in phase space. PUI VDFs measured at 1AU do not exhibit a Maxwellian profile typical of the solar wind, but instead are amid thermalization governed by wave-particle interaction (Möbius et al., 1985; Gloeckler et al., 1993; Drews et al., 2016). The newly ionized neutrals, which now respond to electromagnetic forces, begin to gyrate around the solar wind's magnetic field. In phase space, freshly formed PUIs form a ring distribution surrounding the solar wind ion population with a radius of the solar wind speed. Subsequently, as they evolve as part of the solar wind, the PUIs experience strong pitch angle scattering processes arising from plasma instabilities. This transforms their ring distribution to a spherical shell as the particles converge towards the thermodynamic state of the solar wind.

This is illustrated in measurements of H^+ from the Solar Wind Ion Composition Spectrometer (SWICS) on Ulysses shown in Figure 4.1. The figure compares VDFs of the two main PUI populations, the interstellar and inner source PUI, to a typical solar wind distribution. The interstellar PUI VDF uniformly covers velocities below and above the proton VDF, with a sharp drop off at twice the solar wind speed. The inner source PUI VDF, formed closer to the Sun, are farther along the thermalization process as they have had more time to couple to solar wind properties. This distinction in the VDF profiles has become one of the main signatures used in the identification of non-solar material in the heliosphere.

The helium focusing cone is an example of known interstellar PUIs routinely observed at the distance of the Earth's orbit (Gloeckler et al., 2004). The helium focusing cone is formed from neutral interstellar He that enters the heliosphere in the direction of the interstellar flow. The neutrals penetrate the heliosphere, are gravitationally attracted to the Sun, and subsequently photoionized along their path. This process produces a focused stream of He^+ PUIs downstream of the Sun. At L1, instruments enter the interstellar He^+ flow from the helium focusing cone annually during the months of November and December. These PUI measurements have been useful in the characterization of the interstellar medium, in the study of PUI processes in the heliosphere, and in the identification of non-solar material in the solar wind (Gloeckler & Geiss, 1998; Möbius et al., 2004).

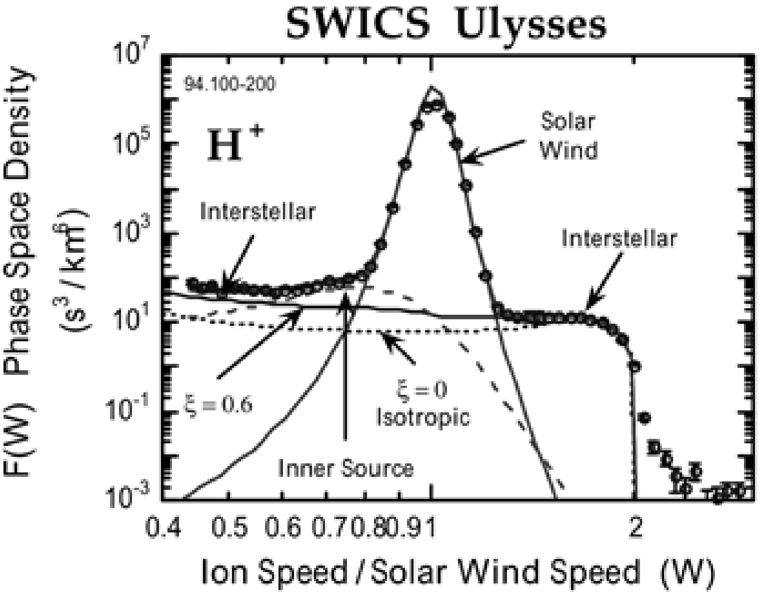

Figure 4.1: Taken from Gloeckler & Geiss (1998), this figure shows the superposition of the velocity distribution functions of interstellar pick up ions, inner source ions, and solar wind ions in phase space. ξ is the degree of anisotropy in pitch angle scattering from modeling results, see Vasyliunas & Siscoe (1976) and Thomas (1978) for details.

The production of the inner source ions is still debated (Gloeckler & Geiss, 1998; Allegrini et al., 2005); however, many studies propose a connection to the interplanetary dust and, possibly, sungrazing comets (Schwadron, 1998; Gloeckler et al., 2000; Wimmer-Schweingruber & Bochsler, 2003; Bzowski & Królikowska, 2005; Mann et al., 2010). Apart from their characteristic non-Maxwellian VDFs, the inner source ion origin is hinted at through studies of their chemical composition. Some studies find agreement between the inner source ion and the solar wind composition suggesting the inner source PUIs originate as part of the solar wind and subsequently formed as result of interaction with interplanetary dust (Brownlee, 1996; Gloeckler et al., 2000; Berger et al., 2015). Conversely, other studies find the elemental composition to differ from solar values (Taut et al., 2015). These discrepancies may be an indication that several processes could be taking part in forming the inner source ion population.

Earlier studies propose that neutrals (H, H_2, He) outgassed from the interplanetary dust grains can charge exchange with solar wind ions (Banks, 1971; Fahr et al., 1981; Gruntman, 1996). In this scenario, the dust neutrals encountered by the solar wind alphas and protons can charge exchange resulting in ionized dust material along with singly ionized and neutral solar material. This is akin to charge exchange in cometary environments (Cravens, 1997; Bodewits et al., 2004, 2006; Simon Wedlund et al., 2019). For the reactions, $\alpha + \mathrm{H_2} \rightarrow \mathrm{He^+} + \mathrm{H_2^+}$ and $\alpha + \mathrm{H} \rightarrow \mathrm{He^+} + \mathrm{H^+}$ where α and $\mathrm{He^+}$ originate as part of the solar wind, studies find that charge exchange can produce a non-negligible amount of solar $\mathrm{He^+}$ ions. This process would produce a singly ionized outgassed dust ion along with singly ionized He, from solar alphas, consistent with solar wind properties e.g. a Maxwellian profile narrowly peaked around the proton speed that is characterized by solar wind temperature.

Previous studies of $\mathrm{He^+}$ from SWICS on the Advanced Composition Explorer (ACE) investigate the interstellar component of the VDF; however, also find a distribution that peaks at the solar wind speed often attributed to inner source ions (Chen et al., 2013). Our present work systematically analyses $\mathrm{He^+}$ VDFs measured by ACE/SWICS between 1998 − 2011 to understand their source. Our analysis identifies several periods where $\mathrm{He^+}$ VDFs suggest a solar origin. However, we find current ionization models fail at reproducing the amount of solar wind $\mathrm{He^+}$ that is measured, therefore we test the effectiveness of charge exchange with interplanetary dust neutrals as a possible mechanism in the formation of $\mathrm{He^+}$.

Results from this study have important implications to our current interpretation of the thermal properties of the plasma which can be derived from ion composition measurements made in the heliosphere through nonequilibrium ionization modeling (Ko et al., 1997; Rakowski et al., 2007, 2011; Gruesbeck et al., 2011, 2012; Rivera

Table 4.1: Summary of VDF properties from Figure 4.4.

VDF	$T_p(10^5$ K)	$T_{He^+}(10^5$ K)	V_p (km s^{-1})	V_{He^+} (km s^{-1})	He^+/He^{2+}
1	1.08	6.77 ± 0.04	464	454	0.03
2	1.60	5.08 ± 0.30	573	626	0.01
3	1.85	5.57 ± 0.13	505	543	0.02
4	1.68	8.70 ± 0.02	718	720	0.06

et al., 2019b). In these studies, the charge state distributions are reconstructed from the known ionization and recombination processes that are accounted for in the ionization code, as well as the evolution of the wind plasmas's thermodynamic properties. However, if charge exchange does play a role during the solar wind's radial evolution it may be an important process taking part in shaping the charge state distributions observed in situ.

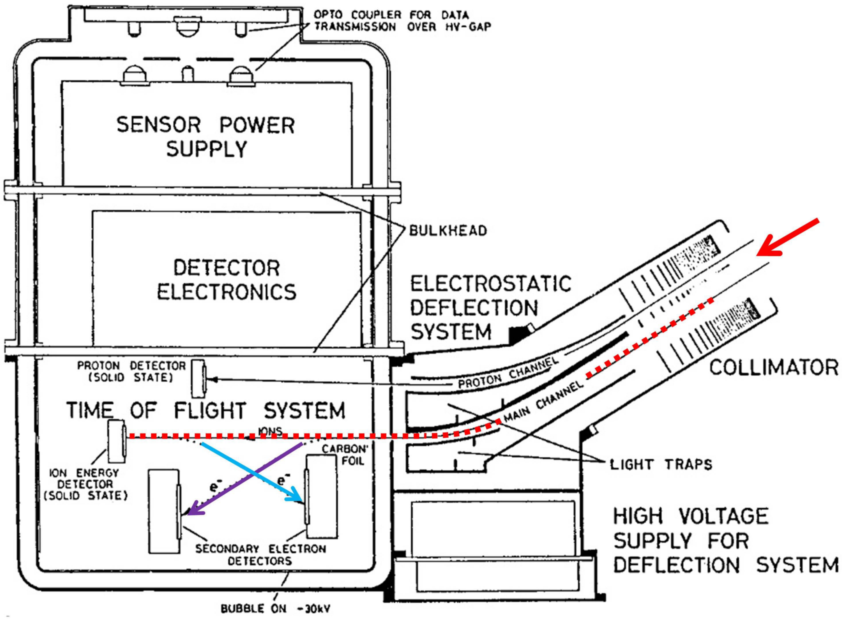

Figure 4.2: Schematic of the internal compartments of the ACE/SWICS instrument adapted from Gloeckler et al. (1998).

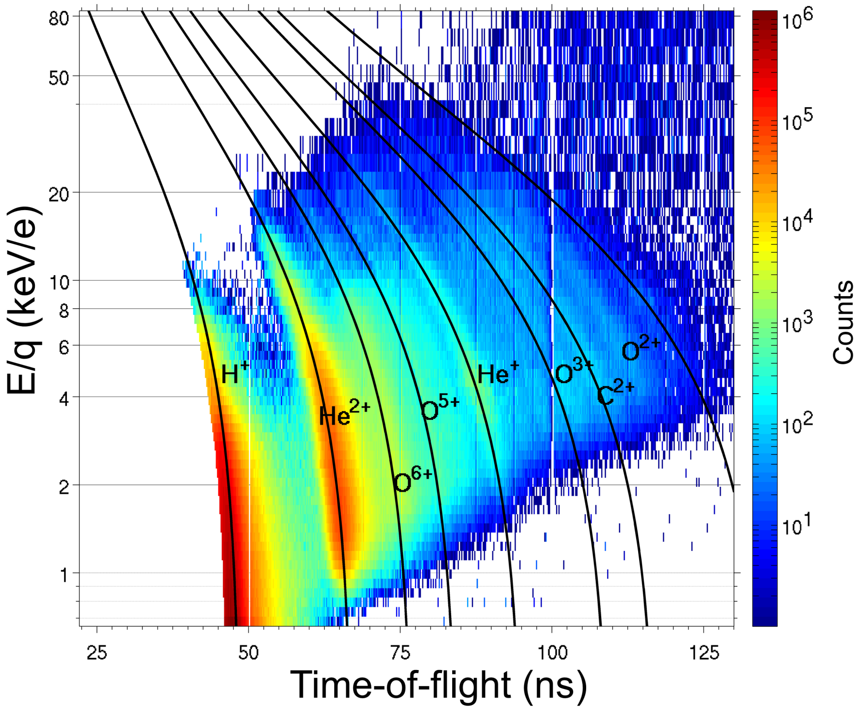

Figure 4.3: Time-of-flight versus energy-per-charge of ion counts from ACE/SWICS for an accumulation period of 1 January to 31 October 2005.

4.2 Observations

4.2.1 Observations from ACE/SWICS

He^+ measurements analyzed are taken from the time-of-flight mass spectrometer, SWICS, aboard ACE between 1998 – 2011. The identification of ions with SWICS is determined through a combination of measurements, as fully described in (Gloeckler et al., 1994). The SWICS instrument is shown in Figure 4.2, where the track in dashed red demonstrates the particle's trajectory.

Initially, the particle enters the instrument through the collimator, immediately deflected by the electrostatic analyzer plates such that only ions of a specific energy-per-charge, E/Q, reach the chamber entrance. The selected ions undergo a post-acceleration prior to entering the time-of-flight (TOF) system that increases their energy to exceed the energy threshold of the solid state detector that will measure

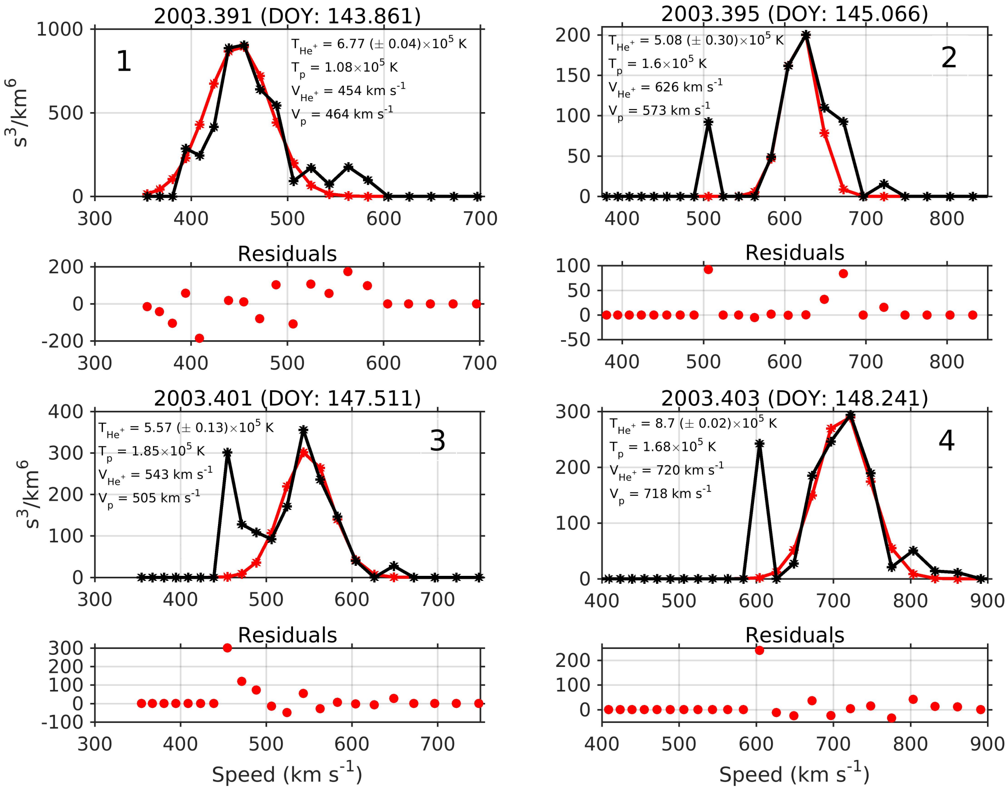

Figure 4.4: Two panel vertical plots for VDFs of 1 hour accumulation periods (top) and residuals (bottom) in 2003. The black curve are He$^+$ measurements and the red curve are Maxwellian fits. We include V$_p$, proton speed, V$_{He^+}$, He$^+$ speed, T$_p$, proton temperature, and T$_{He^+}$, He$^+$ temperature where V$_p$ and T$_p$ are 1 hour averages from ACE/SWEPAM and V$_{He^+}$ and T$_{He^+}$ are computed from the Maxwellian fit.

its energy. Once in the TOF chamber, ions pass through a carbon foil that releases a secondary electron to trigger the start detector, as shown in purple in Figure 4.2. The ion reaches the solid state detector at the end of the compartment which records the ion energy, E_{meas}, and releases a second electron to trigger the stop detector, as shown in blue.

From these independent measurements of the TOF, t, ion energy, E_{meas}, E/Q from the electric static analyzer, and the post-acceleration voltage, V, ions can be unambiguously identified through the following relationships taken from Gloeckler

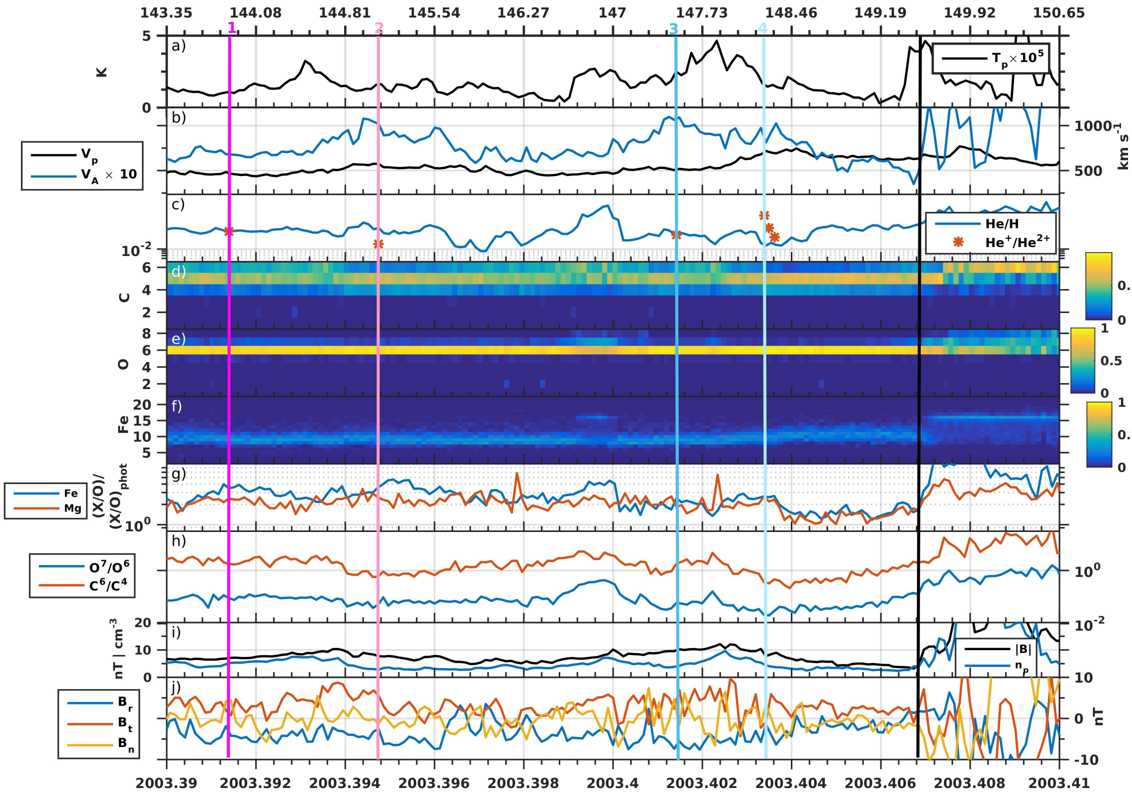

Figure 4.5: Solar wind properties of the period in 2003 day 143 to 150 from SWEPAM, SWICS, and MAG on ACE. Date in year fraction at the bottom and day fraction at the top. Top to bottom, a) proton temperature, T_p, b) proton speed, V_p, and Alfven speed, V_A, multiplied by 10, c) ratios of He/H and He^+/He^{2+} densities, d)-f) relative abundances of C, O, Fe charge states, respectively, g) ratio of Fe/O to photospheric $(Fe/O)_{phot}$ and Mg/O to photospheric $(Mg/O)_{phot}$ using photospheric values from Asplund et al. (2009), h) O^{7+}/O^{6+} and C^{6+}/C^{4+}, i) magnetic field magnitude, B, and proton density, n_p, j) radial, B_r, tangential, B_t, and normal, B_n, components of the magnetic field. The colored vertical bars labeled 1-4 correspond to the 1 hour periods from Figure 4.4. The black vertical solid correspond to beginning of a CME from Richardson & Cane (2010).

et al. (1998),

$$M = 2(t/d)^2(E_{\text{meas}}/\alpha) \tag{4.1}$$

$$Q = \frac{E_{\text{meas}}/\alpha}{V+E/Q-E_{\text{loss}}/Q} \tag{4.2}$$

$$M/Q = 2(t/d)^2(V+E/Q-E_{\text{loss}}/Q) \tag{4.3}$$

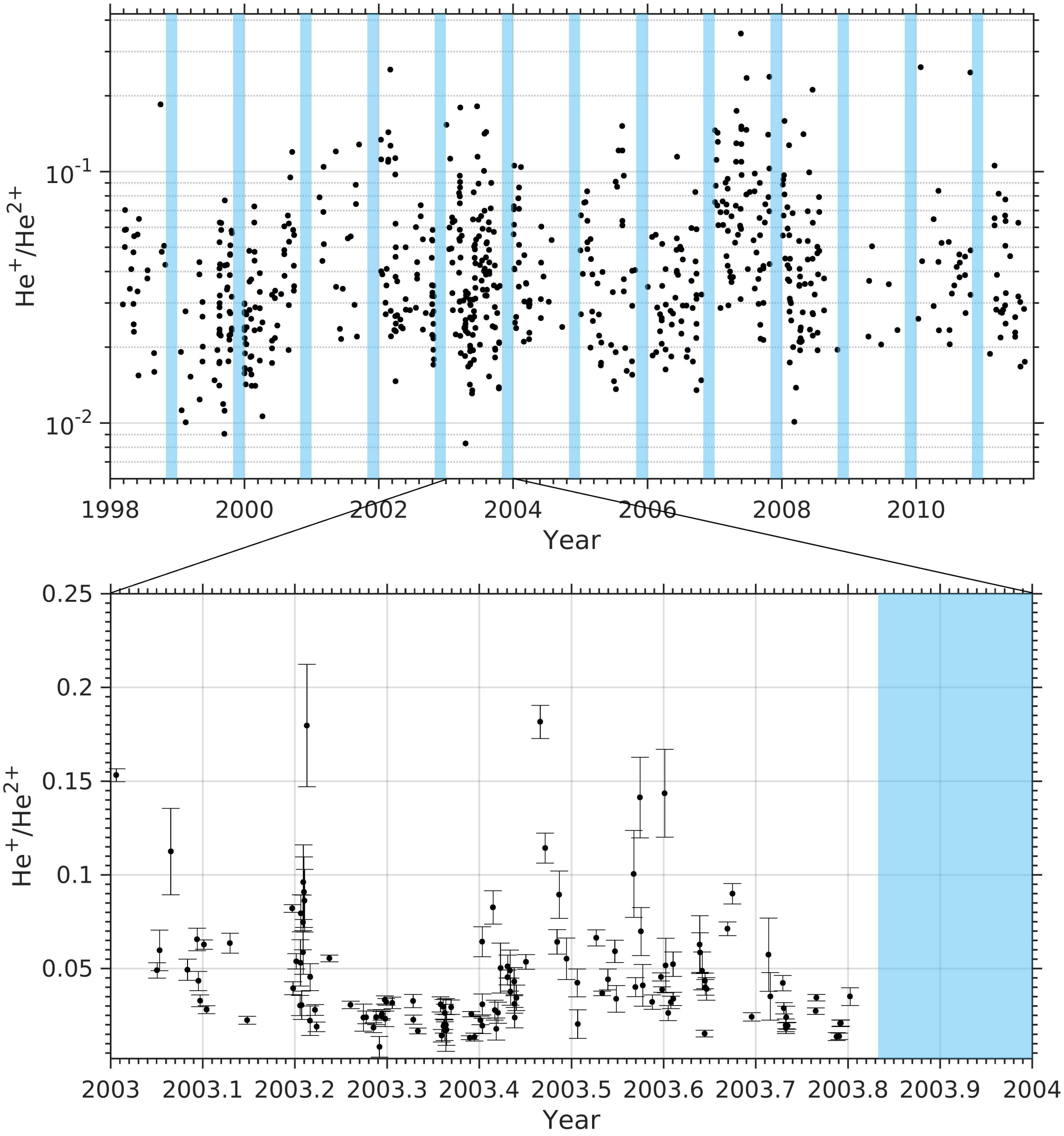

Figure 4.6: One hour average density ratio of He$^+$/He^{2+} from ACE/SWICS for the period between $1998.1 - 2011.6$ (top) and zoomed into the period of 2003 with corresponding errorbars (bottom). The timeframe highlighted in blue is the Helium focusing cone period, predicted to be between November and December.

$$E_{\text{ion}} = \frac{Q}{(Q/E)} \tag{4.4}$$

$$v_{\text{ion}} = 438 \cdot [(E/Q)/(M/Q)]^{1/2} \tag{4.5}$$

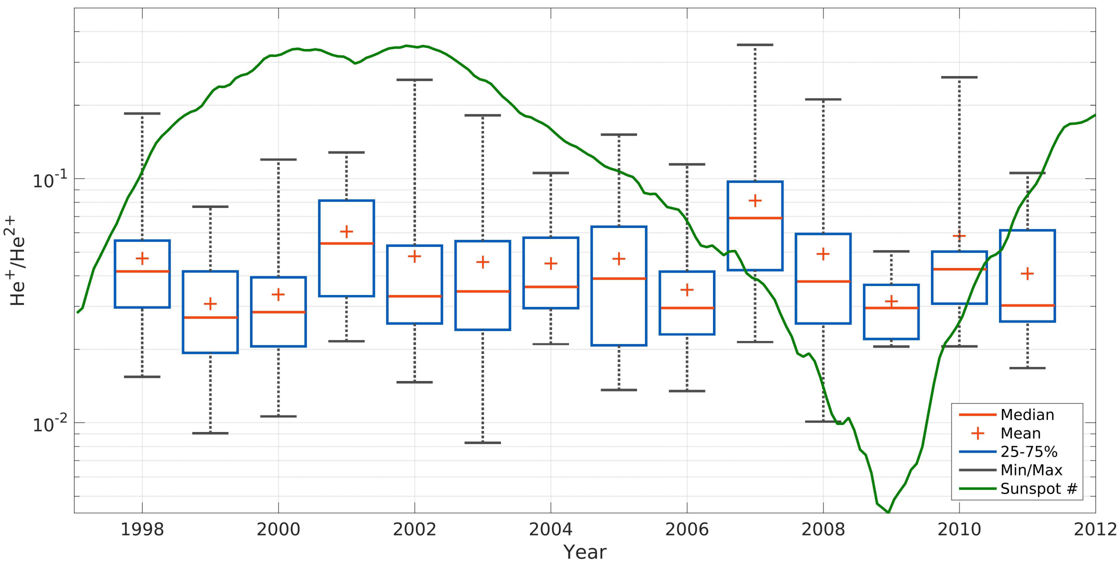

Figure 4.7: Box plot showing the annual median of He$^+$/He^{2+} represented by the red horizontal bar, annual mean values as a red '+', the blue box shows the range of values within $25 - 75\%$, and gray whiskers show the range of minimum and maximum annual values. The smoothed sunspot number, normalized to 0.35 for comparison, in plotted in green.

where d is the flight path distance, V is the post-acceleration voltage, E_{loss} is the energy lost by the ion as it passes through the carbon foil, α is the energy loss due to the solid state detector (Ipavich et al., 1978), and v_{ion} is the ion speed in km s^{-1}.

The particles that produce a concurrent TOF (1) start and (2) stop signal along with the (3) particle's energy measurement are said to produce *triple coincidence measurements*. However, not all ions can meet the minimum energy requirement to trigger the solid state detector. There are a subset of particles that only log a start and stop TOF signal which are known as *double coincidence* counts. This occurs for many singly and low ionized charge states such as the He$^+$ measurements which are of interest in present analysis. These ions are rare in triple coincidence counts except for those with high enough energy. Therefore, the double coincidence analysis enables the detailed study of He$^+$ that would otherwise be largely unseen through the triple coincidence measurements.

In the double coincidence counts, the instrument records the TOF, t, while the E/Q is known from the electrostatic analyzer. Since E_{meas} is not recorded, we cannot determine Equation 4.1, 4.2, and 4.4, however we can still retrieve M/Q and v_{ion} from Equation 4.3 and 4.5. These two quantities allow us to determine the wind speed and identify the particle, although particles with the same M/Q ratio are blended together making their interpretation difficult.

Figure 4.3 shows a histogram of double coincidence counts collected between January 1 through October 31 of 2005 plotted as a function of TOF and E/Q. We include a selection of modeled tracks (including He^+) calculated using Equation 4.3 where individual ions are expected to be found along these tracks. Spurious background counts have been removed from the data set using a solar wind speed threshold as discussed in Gilbert et al. (2014).

A consequence of not having a direct measurement of E_{meas}, is that ions with the same M/Q ratio overlap in the same track, and require specific analysis (Gilbert et al., 2012). Ions from some of the most abundant elements, such as C^{3+} and O^{4+} with $M/Q = 4$ are expected to mix with He^+ counts in the double coincidence analysis. To ensure the signal extracted from the data set is dominated by He^+, we determine the contribution from C^{3+} and O^{4+} during periods where He^+ is observed in the triple coincidence data set. These instances occur when higher energy He^+ ions manage to generate a signal in the solid state detector which allow for He^+, C^{3+}, and O^{4+} to be unambiguously identified. In these cases, we find $n_{He^+}/(n_{He^+} + n_{C^{3+}} + n_{O^{4+}})$ were $>$ 80% for over 95% of He^+ observations, suggesting that our signal is dominated by He^+ counts. Additionally, in the triple coincidence counts, C^{3+} and O^{4+} are well sampled while He^+ is periodically observed and less efficiently measured. Therefore, the He^+ counts in the triple coincidence data are likely still underrepresented compared to C^{3+} and O^{4+}. Given the He^+ counts are estimated to be a lower limit provides additional confidence that the He^+ measurements likely exceed C^{3+} and O^{4+} during the periods observed together.

As Figure 4.3 illustrates, the He^+ counts fall along the $M/Q = 4$ TOF track. The points included in this plot are those that fall within 20% of the proton speed. The He^+ counts cover a similar range and decrease at higher/lower E/Q values along the TOF track similar to common solar wind ions like He^{2+}, O^{6+}, O^{5+}.

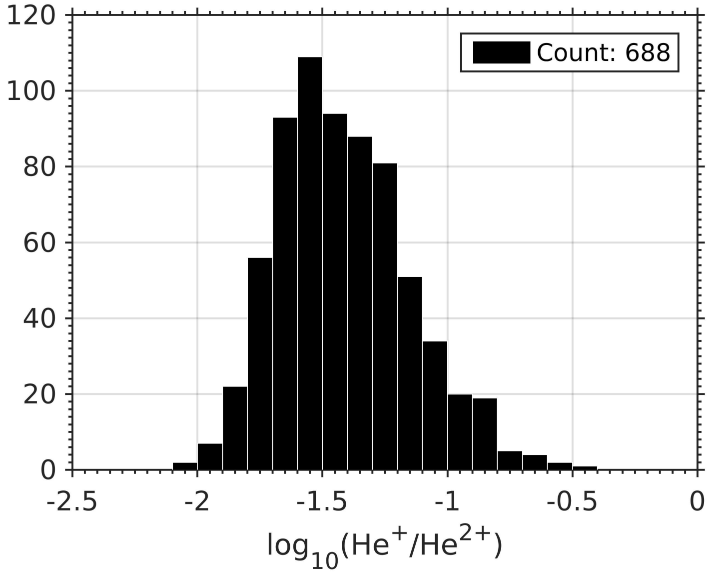

Figure 4.8: Distributions of $\mathrm{He}^+/\mathrm{He}^{2+}$ between $1998 - 2011$.

4.2.2 Solar He^+ measurements

We can determine the origin of heliospheric ions through an inspection of the profile formed by their VDFs. Ions of solar origin resemble Maxwellian distributions while non-solar PUIs are distinguished by their non-thermal profile.

Through inspection of He^+ VDFs, we identify several periods throughout $1998 - 2011$ where the He^+ VDFs peak within 20% of the solar wind speed and that are well modeled by a Maxwellian profile. We search the VDFs for a fit to the distribution made up of at least 5 points with relative errors below 30%. The measurements identified through this criteria were also manually inspected to ensure the VDFs were well fitted.

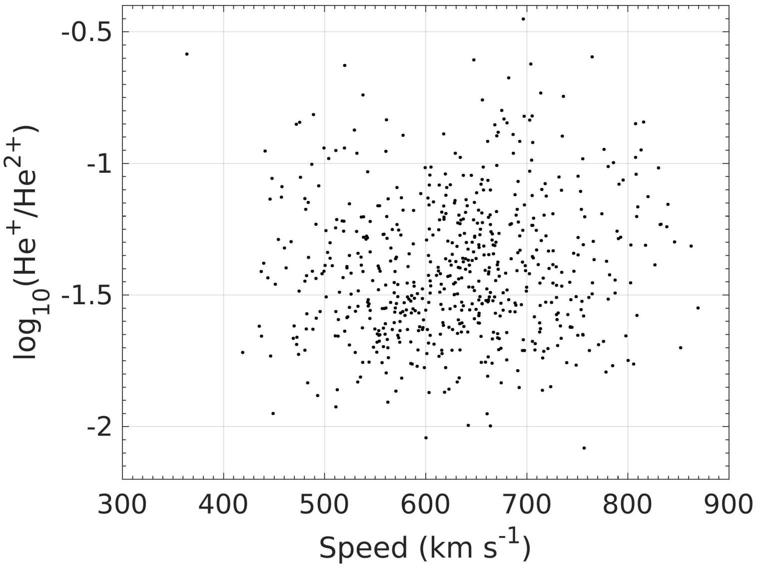

Figure 4.9: Scatter plot of He^+/He^{2+} against solar wind speed.

As examples, we present sample VDFs in units of s^3 km^{-6} for several 1 hr accumulation periods in 2003, shown in Figure 4.4. The figure includes a top plot where measurements are in black and a Maxwellian fit is in red, along with a plot of residuals between the fit and measurements plotted below. The counts in panels 2, 3, 4 outside of the Maxwellian fits that produce large residuals, such as at 500 km s^{-1} in panel 2, are counts that are not part of the solar He^+ distribution and possibly associated with the PUI distribution as shown in Figure 4.1. Additionally, we include the solar wind properties during the four periods from Figure 4.4 in Figure 4.5. Figure 4.5 includes a multi-panel plot between day $\sim 143 - 150$ in 2003 where the four colored vertical lines labeled 1 through 4 correspond to the labels in the four 1 hour VDFs. The black solid line denotes the boundary of an interplanetary CME identified in Richardson & Cane (2010).

In addition, the solar wind properties for the four periods are summarized in Table 4.1. We include the proton temperature, T_p, He^+ temperature, T_{He^+}, mean proton speed, V_p, and He^+ speed, V_{He^+}. The proton speed and temperature are 1 hour averages from Solar Wind Electron, Proton, and Alpha Monitor (SWEPAM;

McComas et al. 1998) on ACE and the He^{+} speed and temperature are computed from the Maxwellian fit.

Figure 4.6 shows a time series of all measurements that meet the VDF criteria. The top plot is the $\mathrm{He}^{+}/\mathrm{He}^{2+}$ density ratios between $1998.1-2011.63$ and the bottom plot is zoomed into 2003 with associated errorbars. We note that values of $\mathrm{He}^{+}/\mathrm{He}^{2+}$ are used instead of an absolute abundance of He^{+} to illustrate enhancements in He^{+} densities compared to the alphas, as well as, to easily compare with the results from the ionization code discussed in Section 4.4. We have removed measurements within CMEs and the helium focusing cone to capture He^{+} in ambient solar wind. The measurements within CMEs and the focusing cone made up approximately 16% and 15% of the total points, respectively. We find that the remaining $\mathrm{He}^{+}/\mathrm{He}^{2+}$ measurements are observed throughout individual years and the solar cycle with values ranging an order of magnitude apart.

A summary of these values is shown in Figure 4.7. The figure includes the $\mathrm{He}^{+}/\mathrm{He}^{2+}$ annual median denoted as the red bar inside each box, annual mean as a red '+', a blue box showing values within $25-75\%$, and gray whiskers extending between the annual minimum and maximum values. We note that 1998 and 2011 were partially measured. We also include the 13-month smoothed monthly sunspot number[1] in green, normalized to 0.35 for a more convenient comparison with $\mathrm{He}^{+}/\mathrm{He}^{2+}$ values. Generally, we find the median values of the $\mathrm{He}^{+}/\mathrm{He}^{2+}$ ratio range between 0.02 and 0.06, with the exception of an elevated value during 2007; however, there is no clear solar cycle dependence observed.

Figure 4.8 shows the distribution for all $\mathrm{He}^{+}/\mathrm{He}^{2+}$ values. The distribution peaks between $2.5-3.2\times10^{-2}$ and range between 8.0×10^{-3} to 4.0×10^{-1}. These values are larger that those previously reported from in situ measurements of Vela which measured $\mathrm{He}^{+}/\mathrm{He}^{2+}$ to be on the order of $\sim10^{-3}$ (Hundhausen et al., 1968).

---

[1] `http://www.sidc.be/silso/datafiles`

When plotting the He^+/He^{2+} values against solar wind speed, as shown in Figure 4.9, the He^+/He^{2+} ratio is uncorrelated to speed, however appears predominantly in wind traveling faster than 400 km s^{-1}. This may indicate the process producing He^+ becomes effective for plasma accelerated to a solar wind speed above this value but has no strong dependence with increasing speed. In addition, once above 400 km s^{-1}, He^+ appears independent of speed suggesting the production of He^+ is not dependent on the mechanism accelerating the solar wind.

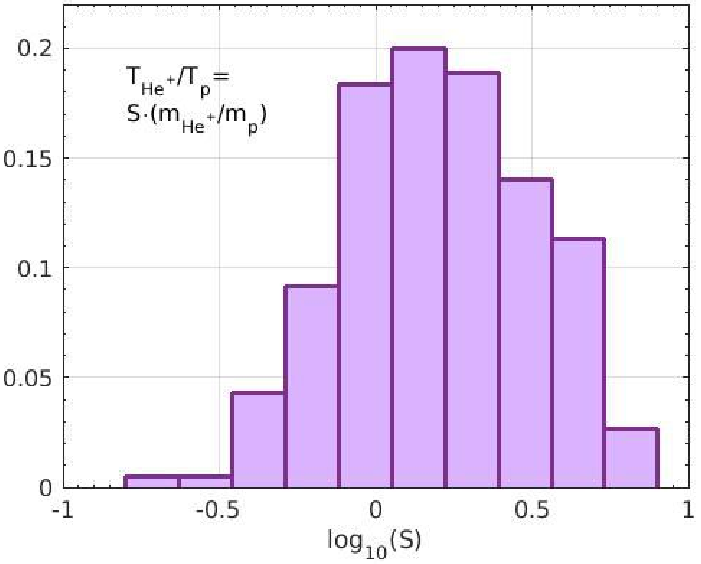

Figure 4.10: Normalized distribution of S, the proportionally constant in $T_{He^+}/T_p = S \cdot (m_{He^+}/m_p)$.

Furthermore, the temperature values computed for He^+ coincide with previous measurements from ACE/SWICS which find a mass proportional and super mass proportional relationship for a large number of minor ion temperatures in the solar wind (Tracy et al., 2015, 2016). Collectively for all ions, they find the following relationship, $T_{ion}/T_p = S \cdot (m_{ion}/m_p)$, for $S = 1.35 \pm 0.02$, where T_{ion} and T_p are the ion and proton temperature, respectively, and m_{ion} and m_p are the ion and proton mass, respectively. A value of $S = 1$ describes a mass proportional relationship while $S > 1$ would suggest a super mass proportional relationship. Although, the

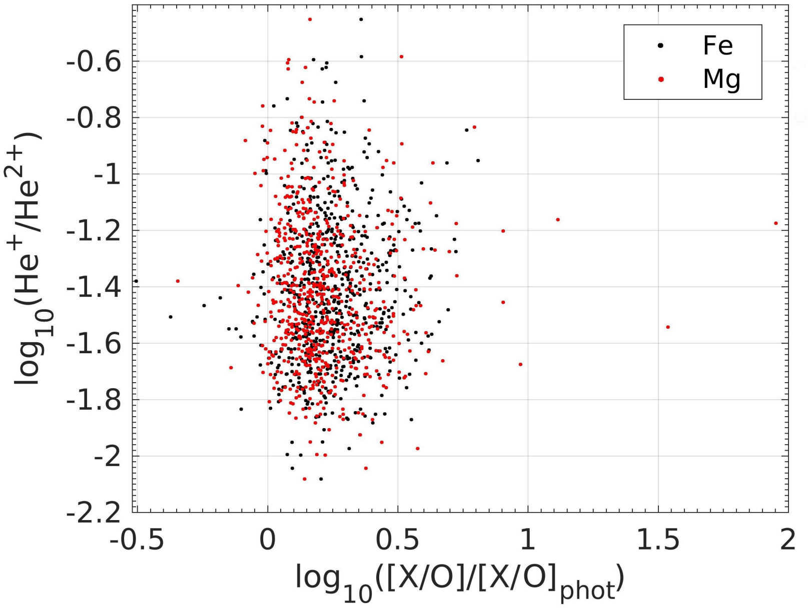

Figure 4.11: Scatter plot of He^{+}/He^{2+} versus $(X/O)/(X/O)_{phot}$ where X = Fe and Mg.

relationship is sensitive to the solar wind's collisional age, A_C, as described in Tracy et al. (2016). This proportionality describes ions within low A_C and is gradually erased for ions within plasma of higher A_C as ions become increasingly coupled to the proton temperature. For the VDFs in Figure 4.4, we compare the He^{+} temperatures within the different solar wind periods, 1) $T_{He^+}/T_p = 1.57\ m_{He^+}/m_p$, 2) $T_{He^+}/T_p = 0.8\ m_{He^+}/m_p$, 3) $T_{He^+}/Tp = 0.75\ m_{He^+}/m_p$, and 4) $T_{He^+}/T_p = 1.30\ m_{He^+}/m_p$. The normalized distribution of all values of S are presented in Figure 4.10. We find a relatively low A_C for the He^{+} values, between $8.1 \times 10^{-3} - 1.7 \times 10^{-2}$. The median ± median absolute deviation value, as was computed in Tracy et al. (2016), is $S = 1.5 \pm 0.5$ which is consistent with $S = 1.35 \pm 0.02$ from Tracy et al. (2016). T_{He^+} reflects ion temperatures typical at 1AU, further suggesting the He^{+} measurements undergo a similar thermal evolution to the solar wind, as well as, are independent of the mechanism heating the solar wind.

When examining the chemical composition of the plasma corresponding to He^{+}/He^{2+}

measurements, we find the solar He^+ is independent of solar wind type. The well known First Ionization Potential (FIP) effect has been shown to result in a range of elemental composition between different parts of the Sun, notably between the photosphere and other structures (Feldman & Widing, 1993; Feldman, 1998; Raymond et al., 1997; Raymond, 1999; Landi & Testa, 2015; Parenti et al., 2019). This makes the composition measured in the heliosphere a key indicator to the solar wind's origin at the Sun. Measurements of low FIP Fe and Mg to high FIP O compared to the ratio of its photospheric value, $(Fe/O)/(Fe/O)_{phot}$ and $(Mg/O)/(Mg/O)_{phot}$, are commonly used to characterize solar wind streams (Schwadron et al., 1999; von Steiger et al., 2000; Zurbuchen et al., 2012). Figure 4.11 shows a scatter plot of compositional values for all He^+/He^{2+} values. The compositional values are well distributed between photospheric, value of 1, to FIP enhanced solar wind, > 1, showing no preferred solar wind type. This further indicates that the He^+ is likely independent of the solar wind's birthplace, which is largely governed by the properties discussed, but rather a processes occurring after it leaves the Sun.

4.3 Genesis of Solar He^+ Ions

Previously, many non equilibrium ionization modeling studies have aimed to simulate the radial ion evolution of the solar plasma (Rakowski et al., 2007, 2011; Gruesbeck et al., 2012; Landi et al., 2012a; Rivera et al., 2019b). One example is a study using the Michigan Ionization Code (MIC), also used in the present study and further described in Section 4.4, to model the ionization and recombination processes governing the C, O, and Fe charge state evolution within coronal and equatorial solar wind streams (Landi et al., 2012a). We use the MIC to simulate the ion evolution of He within the same solar wind of Cranmer et al. (2007) as shown in Figure 4.12, and present the He evolution in Figure 4.13. The simulations predict a value of He^+/He^{2+} of 10^{-5} which is 3 orders of magnitude lower compared to the observations in the present study with a median value of $\sim 10^{-2}$. This suggests that either the radial profiles of the solar wind properties do not capture these observations or some other process, unaccounted for in the MIC, is active.

A comprehensive study comparing MIC results to measurements of C, N, O, Ne, Mg, Si, S, Fe in the solar wind found that, generally, the three leading solar wind models consistently underestimated the ionization level of all species (Landi et al., 2014). This indicated that the thermodynamic models of the solar wind needed to be adjusted such that it increased the ionization occurring in solar wind plasma. However, increasing the ionization of the plasma is the opposite to what would produce a higher He^{+}/He^{2+} necessary to meet observations. This suggests that the ionization codes, rather than the solar wind models, may be missing the necessary process generating the He^{+} that is measured.

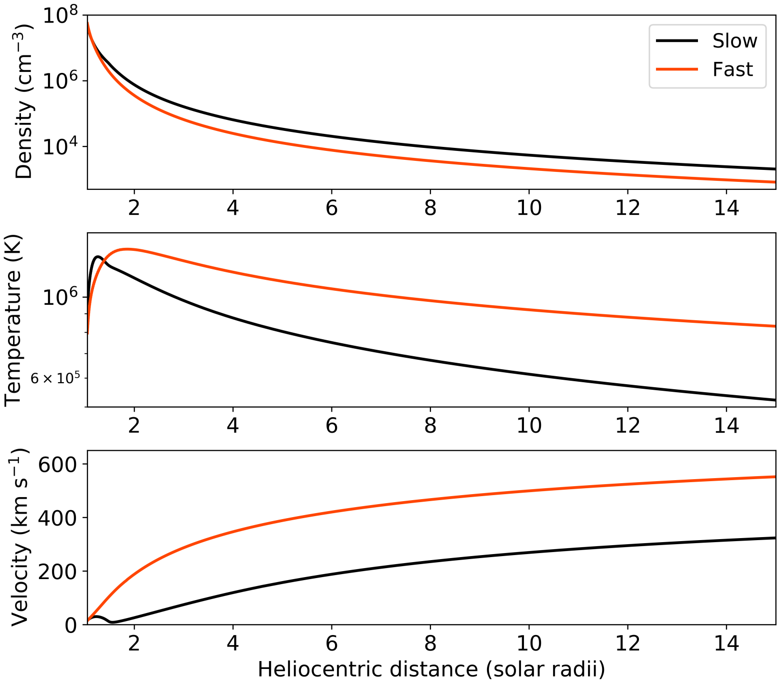

Figure 4.12: Solar wind thermodynamic evolution for slow and fast wind streams derived in Cranmer et al. (2007).

We find the He^{+} measurements in the present analysis are, 1) characterized by

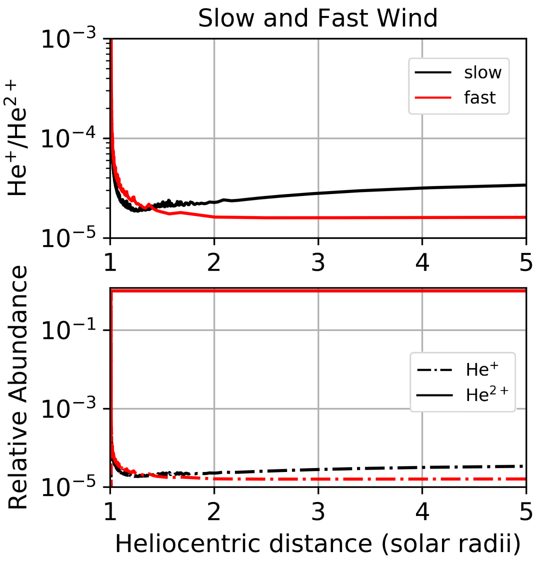

Figure 4.13: Simulated He evolution within the slow (black) and fast (red) solar wind derived in Cranmer et al. (2007). Top, density ratio He^+/He^{2+}, and bottom, relative abundance for each ion.

thermodynamic properties compatible with other solar wind ions, 2) independent of wind type and source region, and 3) do not appear to show a solar cycle dependence. This aligns well with the production of He^+ from charge exchanges processes that will largely preserve the ion's solar wind identity in phase space, assuming no significant transfer of energy, and are independent of solar wind type. Also, zodiacal light observations measured across the solar cycle are shown to remain stable suggesting the dust, and thus the charge exchange processes and He^+ densities, are not expected to exhibit a strong solar cycle dependence (Leinert et al., 1982).

We suggest that the He^+ observed is the solar wind is a signature of the charge exchange process that acts to transform small fraction of alpha particles to He^+ through this interaction. As mentioned previously, charge exchange between the solar wind and dust neutrals has been investigated in the past (see Banks 1971; Fahr et al. 1981; Gruntman 1996), however the studies did not include observations to constrain modeling results. In the present study, we test charge exchange from several reactions as a possible mechanism in the production of solar He^+ that is analyzed in Section 4.2.

Table 4.2: Charge exchange reactions included in the MIC.

Reaction #	Reaction
1	$\mathbf{He}^{2+} + H_2 \rightarrow \mathbf{He}^{+} + H_2^{+}$
2	$\mathbf{He}^{2+} + H_2 \rightarrow \mathbf{He}^{+} + H^{+} + H$
3	$\mathbf{He}^{2+} + H_2 \rightarrow \mathbf{He}^{+} + H^{+} + H^{+} + e$
4	$\mathbf{He}^{2+} + H \rightarrow \mathbf{He}^{+} + H^{+}$

Ions in bold originate from the solar wind.

4.4 Modeling of solar He^+ ions

To quantify the neutral population necessary to produce the He^+/He^{2+} observed through charge exchange processes, we simulate the radial evolution of He ions with an ionization code that includes the effects of charge exchange with outgassed dust neutrals on a parcel of plasma traveling from the Sun to 1AU. The background neutrals are test particles encountered by the solar wind and their radial distribution remain constant in time while the solar wind alpha particles recombine through charge exchange and thus decrease their abundance.

We have modified the MIC to simulate alpha particle evolution. The MIC solves a time-dependent set of equations at each step of the plasma's radial expansion using recombination and ionization rates from the CHIANTI 9 atomic database (Dere et al., 1997, 2019). The model incorporates the following processes: excitation-autoionization, dielectronic re-combination, collisional ionization, radiative recombination, photoionization, and it has been adapted in the present work to include specific charge exchange reactions from Table 4.2. Table 4.2 includes a collection of reactions previously investigated in the literature that are relevant to the present study (Banks, 1971; Gruntman, 1996). The cross-section values for each reaction are taken from Barnett (1990) and plotted as a function of speed in Figure 4.14.

The charge exchange reactions are included with a term denoted in the equation below as N_{CE},

$$\begin{aligned} \frac{dy_i}{dt} &= n_e \left[y_{i-1} I_{i-1}(T_e) + y_{i+1} R_{i+1}(T_e) \right] \\ &+ y_{i-1} P_{i-1} - y_i \left[n_e \left(I_i(T_e) + R_i(T_e) \right) + P_i \right] + N_{CE} \end{aligned} \tag{4.6}$$

where y_i is the ion's relative abundance of the given element in charge state i, n_e is the electron density, T_e is the electron temperature, $R(T_e)$ and $I(T_e)$ are the total recombination and total ionization rates, respectively, that include all mentioned processes except charge exchange. In Equation 4.6, simulations are for $i = 0, 1, 2$ corresponding to $\mathrm{He}^{0,1,2+}$, respectively. The P is the photoionization term described as,

$$P_i = \int_{\nu_i}^{\infty} \frac{4\pi J(\nu) \sigma_i(\nu)}{h\nu} d\nu \tag{4.7}$$

where $J(\nu)$ is the mean spectral radiance of the Sun, $\sigma_i(\nu)$ is the photoionization cross-section for ion i, h is the Planck constant, and ν_i is the frequency for the ion's corresponding ionization energy.

The term N_{CE} is defined as follows,

$$N_{CE} = \begin{cases} \Sigma_j (y_2 G_{2,j}^{CE} - y_1 L_{1,j}^{CE}) & \text{for He}^{+} \\ \Sigma_j (y_1 L_{1,j}^{CE} - y_2 G_{2,j}^{CE}) & \text{for He}^{2+} \end{cases} \tag{4.8}$$

where j reactions refer to reactions $1 - 4$ that are noted in Table 4.2. This incorporates the effect of concurrent charge exchange processes with neutrals below 1 AU. G^{CE} in s^{-1} are the charge exchange recombination process and L^{CE} in s^{-1} is the reverse process. For $L^{CE}_{i,j}$, we assume the principle of detail balance such that $L^{CE}_{i,j} = (y_{i-1}/y_i)G^{CE}_{i-1}$ for thermodynamic equilibrium conditions which is an approximation. The reaction rates are computed as a function of distance as $G^{CE}_i(r) = n_{H,H_2}(r)v(r)\sigma^{CE}_{i,j}(v)$ where $n_{H,H_2}(r)$ is the number density of H or H$_2$ with heliocentric distance, r, from the Sun. The $\sigma^{CE}_{i,j}(v)$ is the cross-section for each reaction j of ionization level i.

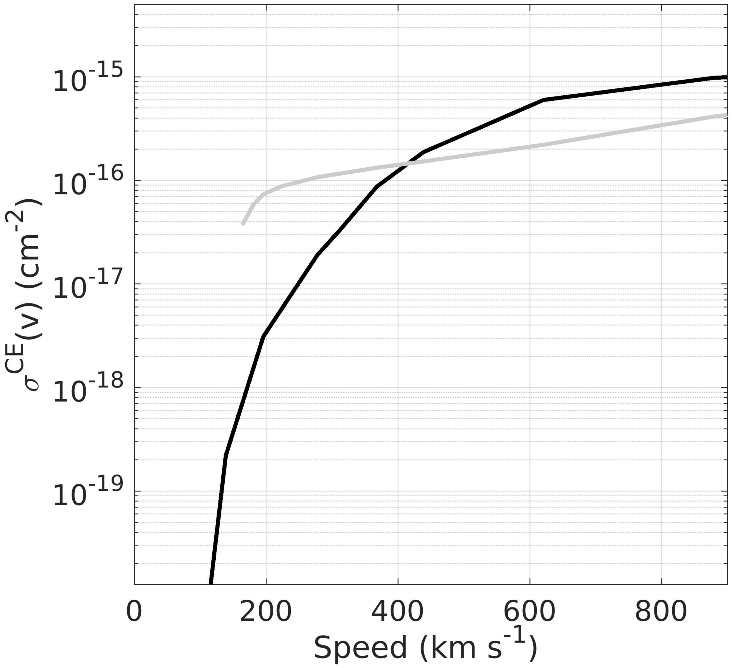

Figure 4.14: Cross-sections for reaction in Table 4.2. The gray curve describes the total cross-section for reaction $1-3$, and the black curve is the cross-section for reaction 4.

The dust neutrals within the interplanetary medium are test particles in the simulation. We assume a static profile for the population of outgassed H and H$_2$ originating from the circumsolar dust grains. The dust has been observed to be distributed symmetrically across the ecliptic plane with a large concentration in the vicinity of the Sun. The outgassed neutral profile in our simulations assumes a symmetric and

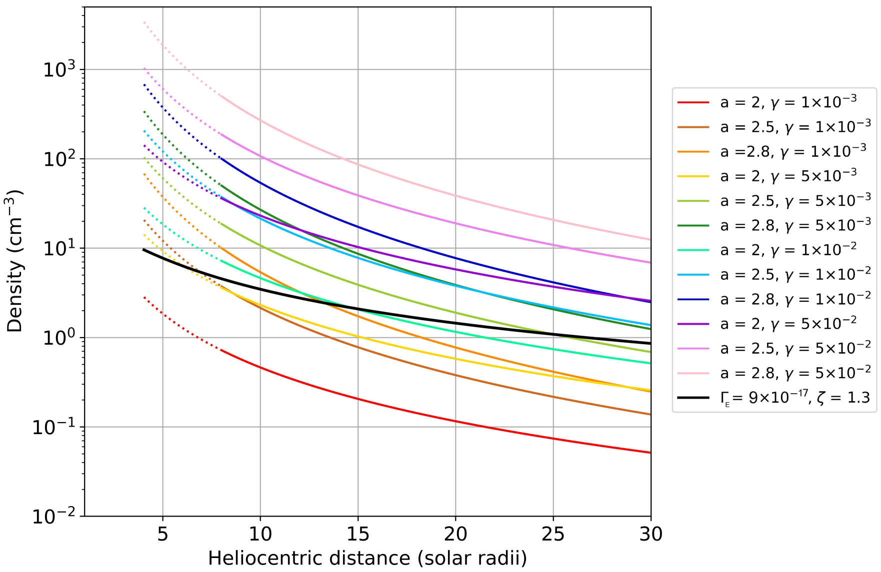

Figure 4.15: Empirical models of $\mathrm{H} + \mathrm{H}_2$ density profiles with an inner edge of $4R_\odot$ starting at the dotted line and $8R_\odot$ starting at the solid line. The solid line is the density of n_{H+H_2} predicted using the dust geometric factor, $\Gamma = \Gamma_E(r_E/r)^\zeta$, see description in Section 4.6.

constant distribution surrounding the Sun that coincides with the dust population. This assumption holds given that the dust structure is not observed to undergo large changes within the timeframe of the solar wind propagation to 1 AU, which is on the timescale of days.

The neutral dust profile, n (cm^{-3}), is taken to be in the form,

$$n_{H+H_2}(r) = \begin{cases} 0 & r < \text{Inner edge } (AU) \\ \gamma \cdot r^{-a} & r > \text{Inner edge } (AU) \end{cases} \tag{4.9}$$

where α and γ are free parameters that govern the density of neutral dust material available for charge exchange. The radial distance, r, is in AU. The density profiles and the corresponding parameters used are shown in Figure 4.15 where the neutral profiles are a sum of parts H and H_2 where $n_{H_2} = 8 \cdot n_H$ as is approximated to be outgassed by the dust in Gruntman (1996). In addition, the solid black curve is the

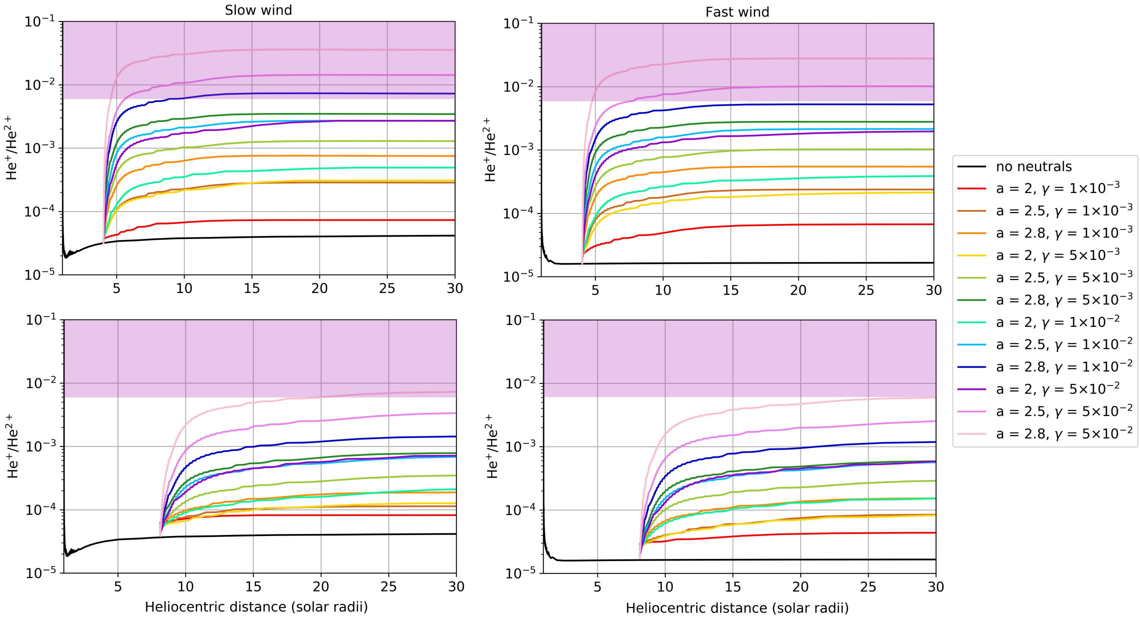

Figure 4.16: He charge state evolution generated using properties of slow (left column) and fast (right column) solar wind between 1 to $30R_\odot$. The plots show the radial evolution of $\text{He}^{+}/\text{He}^{2+}$ for a neutral profile with an inner boundary of $4R_\odot$ (top) and $8R_\odot$ (bottom). The shaded purple region covers the range of $\text{He}^{+}/\text{He}^{2+}$ values found in the observations.

n_{H+H_2} predicted by previous models, further discussed in Section 4.6.

Many different combinations of the free parameters have been used to test a range that may produce the observed $\text{He}^{+}/\text{He}^{2+}$ measured at 1 AU. Parameters are motivated by observations of the distribution of dust from zodiacal light and F-corona studies previously found in the literature (Kimura & Mann, 1998; Kimura et al., 1998; Mann et al., 2004). There is still a large variation between the distribution of interplanetary dust inferred through remote sensing measurements. Observations of the F-corona continuum in the near-infrared show a sharp drop off in brightness that scale between $\text{r}^{-1.9}$ to $\text{r}^{-2.5}$ for the equatorial and $\text{r}^{-2.3}$ to $\text{r}^{-2.8}$ for the polar solar regions below $10R_\odot$ which correspond to freeze-in distances in our simulations (Koutchmy & Lamy, 1985; MacQueen & Greeley, 1995; Leinert & Jackson, 1998). In Gruntman (1994, 1996), both n_H and n_{H_2} were estimated as $\propto r^{-1.15}$ below 1AU. However neutrals in the heliosphere are highly uncertain and remain relatively unknown in the vicinity of the Sun. For this reason, we explore a different range of values.

Furthermore, near-Infrared measurements observe an intensity enhancement at an elongation angle, ϵ, of 1°. The elongation angle is defined as the angle made between the line of sight of the observer and the Sun's center. The distance from the Sun along the plane of the sky for a corresponding ϵ is $r = \sin(\epsilon) \cdot 1(\mathrm{AU})$. For $\epsilon = 1^\circ$, this equates to approximately $r = 4R_\odot$ on the plane of the sky. An elevated intensity in remote measurements at this distance has long suggested a possible inner edge of the dust at that location (Kimura & Mann, 1998; Kimura et al., 1998; Mann et al., 2004). The empirical neutral profile we test assumes a theoretical inner edge that begins at $4R_\odot$. In addition, we investigate distributions peaking as far out as $8R_\odot$ to evaluate the sensitivity of the results to the location of the inner edge.

To simulate the solar wind ion evolution, we use models for the equatorial (slow) and coronal hole (fast) solar wind derived from Cranmer et al. (2007) shown in Figure 4.12.

4.5 Modeling Results

We simulated the charge state distribution of He as a function of distance using the modified MIC that includes charge exchange with the surrounding outgassed dust neutrals. For each neutral distribution in Figure 4.15, we present the corresponding simulated $\mathrm{He}^+/\mathrm{He}^{2+}$ radial evolution shown in the top plot of Figure 4.16, for the slow (left) and fast (right) solar wind. In addition, we include the solutions for a neutral inner edge of $8R_\odot$ in the bottom of Figure 4.16 where the simulated He charge states are presented in the same manner. Each plot includes the range of observed $\mathrm{He}^+/\mathrm{He}^{2+}$ observations denoted as the shaded purple region.

We test values between a power law exponent of $a = 2.0$ and $a = 2.8$ with increasing γ until the $\mathrm{He}^+/\mathrm{He}^{2+}$ value reaches the same order of magnitude as the mean $\mathrm{He}^{+}/\mathrm{He}^{2+}$ observed with ACE/SWICS, $\sim 10^{-2}$. The results show a sharp increase of $\mathrm{He}^{+}/\mathrm{He}^{2+}$ as the simulated plasma parcel encounters the dust. This is due to the step function used to describe the dust in the inner corona; however, the region below the inner edge we define could be decreasing to zero in a smoother way.

In both the slow and fast cases, we can begin to see a deviation between the He values with the presence of neutrals immediately at the inner edge of the dust. The slow and the fast solar wind values respond similarly to charge exchange processes even though their thermodynamic properties can differ significantly during the radial expansion. This is consistent with the $\mathrm{He}^{+}/\mathrm{He}^{2+}$ observations which are found to be largely independent of solar wind type e.g. solar wind speed and composition.

4.6 Discussion

We find the $\mathrm{He}^{+}/\mathrm{He}^{2+}$ simulated values are sensitive to the density for all the neutral profiles tested. The neutral profiles that generate a value of $\mathrm{He}^{+}/\mathrm{He}^{2+}$ within the range of the observations correspond to $a = 2.8$ and $\gamma > 1 \times 10^{-2}$, $a = 2.5$ and $\gamma > 5 \times 10^{-2}$, for an inner boundary of $4R_{\odot}$, shown at the top of Figure 4.16. For an inner boundary of $8R_{\odot}$, shown at the bottom of the same figure, the neutral profile within the observational range is $a = 2.8$ and $\gamma > 5 \times 10^{-2}$.

In addition, the He values are sensitive to the location of the inner edge along with the density of the dust profile. A distribution with an inner edge closer to the Sun produces an overall larger $\mathrm{He}^{+}/\mathrm{He}^{2+}$ heliospheric value when maintaining the same a and γ values. Comparing the rows of Slow and Fast wind, the profile with parameters, $a = 2.8$ and $\gamma = 5 \times 10^{-3}$, with an inner edge of $4R_{\odot}$ produced a $\mathrm{He}^{+}/\mathrm{He}^{2+}$ value roughly an order of magnitude higher compared to a profile with an inner edge of $8R_{\odot}$. This may be a result of charge exchange occurring earlier in the evolution, giving the alpha particles more time to recombine prior to the freeze-in height of He^{2+}. Alternatively, given that the reaction rates, L and G, depend on the neutral density, a higher density of neutral material can also contribute to a larger He^+/He^{2+} ratio overall.

Moreover, we expect the majority of neutral H and H_2 closest to the Sun to originate from dust while the interstellar neutral values begin to dominate much farther from the Sun (Fahr et al., 1981). From Figure 4.16, we find the ions are highly sensitive to the presence of neutrals below $15R_\odot$, for the slow, and $30R_\odot$, for the fast, where the dust component dominates. Therefore, we expect that the majority of solar He^+ predicted to be formed through charge exchange from outgassed dust neutrals rather than interstellar material.

We compare our results to the previously values of outgassed H_2 and H densities (Fahr et al., 1981). Following Fahr et al. (1981), the production rate for H and H_2 is given as, $\mathrm{P}_D(r) = n_p(r)v_{rel}(r)\epsilon\Gamma(r)$, where $n_p(r)$ is the proton density with radial distance, r, $v_{rel}(r)$ is the relative velocity between solar wind and the dust grains, $\epsilon = 0.9$ and $\epsilon = 0.05$ is the desorption efficiency for H_2 and H, respectively, $\Gamma(r)$ in cm^{-1} is the dust cross sectional area per unit volume of the dust,

$$\Gamma(r) = \int_{s_{min}}^{s_{max}} \pi s^2 f(s,r)ds \tag{4.10}$$

where s is the radius of the grain, $f(s,r)$ is the distribution of grains with grain size, s, and distance from the Sun, r.

Following equilibrium conditions, the P_D equates to destruction, $\mathrm{D}_D(r)$, of H and H_2. $\mathrm{D}_D(r) = n_{H,H_2}(r)(C^p(r) + C^e(r) + C^{exc}(r))$ where $C^p(r)$ is the photoionization rate, $C^e(r)$ is the electron impact ionization rate, and $C^{exc}(r)$ is the proton charge exchange rate of H and H_2 with distance from the Sun. Rearranging, density can be computed as the sum of $n_H(r) + n_{H_2}(r)$ in cm^{-3} as the following,

$$n_l(r) = \Sigma_l \frac{n_p(r)v_{rel}(r)\epsilon_l\Gamma(r)}{C_l^p(r) + C_l^e(r) + C_l^{exc}(r)} \tag{4.11}$$

for l = H$_2$ and H. Assuming, $C^p(r) = C_E^p(r_E/r)^2$, $C^e(r) = C_E^e(r_E/r)^2$, and $C^{exp}(r) = C_E^{exp}(r_E/r)^2$ where the subscript 'E' refers to that value at 1AU. $C_E^p = 3.67 \times 10^{-7}, 1 \times 10^{-7}$ s^{-1}, $C_E^e = 1 \times 10^{-7}, 1 \times 10^{-7}$ s^{-1}, and $C_E^{exc} = 1 \times 10^{-8}, 1 \times 10^{-7}$ s^{-1} for H$_2$ and H, respectively (Banks, 1971; Gruntman, 1996). There is still large uncertainty on the value of Γ and how it changes with radial distance from the Sun. Previous values of Γ span five orders of magnitude, $\sim 10^{-17} - 10^{-21}$ (Bame et al., 1968; Banks, 1971; Holzer, 1977). Fahr et al. (1981) approximated the geometric factor as $\Gamma(r) = \Gamma_E(r_E/r)^\zeta$ where $\Gamma_E = 2 \times 10^{-19}$ cm^{-1} and $\zeta = 1.3$. At $4R_\odot$, this produces $n_{H+H_2} \sim 5 \times 10^{-2}$ cm^{-3} which is 4 orders of magnitude lower compared to the minimum density that would generate He$^+$/He^{2+} to meet observational values for the $4R_\odot$ profile case, $a = 2.8$ and $\gamma = 1 \times 10^{-2}$. For an upper limit value of $\Gamma = 9 \times 10^{-17}$, the density predicted increases to $n_{H+H_2} \sim 10$ cm^{-3} at $4R_\odot$ which is two to three orders of magnitude lower compared to our required value, as shown with the solid black curve in Figure 4.15.

Generally, our results suggest a much larger dust density profile or distribution of grain size, as described by $\Gamma(r) = \Gamma_E(r_E/r)^\zeta$, than previously predicted in the vicinity of the Sun to generate the H and H$_2$ densities necessary to meet observational values.

Our results may also suggest that there could be an additional process contributing to the formation of solar-like He$^+$. One possibility would be the ionization of neutral He outgassed from the dust. This process would produce He$^+$ where the dust is present that could potentially have enough time to thermalize by 1AU. If so, this could generate a non-solar He$^+$ VDF with a Maxwellian-like profile rather than a typical PUI profile. This scenario would require further testing with the MIC, along with kinetic modeling of the VDF evolution from its creation in the corona to 1AU.

Moreover, our simulations predict the presence of neutral material in the extended corona which coincides with several decades of eclipse observations which observe He I 10830 in the vicinity of the Sun. The diffuse neutral helium found in eclipse observations was initially attributed to being geocoronal and to interstellar material (Kuhn et al., 1996, 2007); however, the most recent observations have linked the neutral He to the Sun (Moise et al., 2010; Dima et al., 2018). These studies suggest the diffuse He signal arises from the interaction between the solar wind alphas and surrounding dust, essentially acting to neutralize the alpha particles as they propagate from the Sun. In a similar manner to the present study, we can independently determine the density of neutral material in the extended corona by focusing on charge exchange reactions between H and H_2 that can neutralize alpha particles. This can be another method of further constraining neutrals near the Sun.

Furthermore, if the production of solar He^+ is due to the presence of the dust, then there will likely be a reduction in He^+/He^{2+} at higher latitudes where dust is depleted compared to the ecliptic. This can be achieved with future off ecliptic measurements from the Heavy Ion Sensor (HIS) on Solar Orbiter (Müller et al., 2020). The Ulysses spacecraft has previously sampled the solar wind above and below the ecliptic outside of the orbit of the Earth, however HIS will do this around the orbit of Mercury ($\sim 60R_\odot$) where we expect the majority of newly generated He^+ to be primarily formed through dust interaction in the inner heliosphere.

Another important observational constraint to the charge exchange process is the emission of X-ray and far-ultraviolet (FUV) radiation. Observations from the coma of Comet C/1996 B2 Hyakutake were discovered to emit a strong X-ray and EUV signal as a byproduct of charge exchange between neutral cometary material and solar wind ions (Lisse et al., 1996; Cravens, 1997). From laboratory experiments, photon emission through electron capture show that solar wind α particles and H and H_2 from interplanetary dust should produce emission in the FUV or EUV spectral range from He II 304Å, for He^+ produced, and He I 584Å, for neutralized He formed (Bodewits et al., 2006).

Lastly, in our simulations, we specified a static neutral distribution; however the dust can vary at different spatial scales. Solar transients and periodic deposits of fragmented comet material near the Sun can disrupt the homogeneity of the dust (Jones et al., 2018). This can develop local temporal and spatial changes in the dust allowing for periodic enhancements or depletions in neutral density that could result in sporadic fluctuations of He^+/He^{2+} values. This could explain the relatively large fluctuations that are occasionally observed, as shown in Figure 4.6.

4.7 Summary and Conclusions

In the present work, we investigate the presence of He^+ observed by ACE/SWICS in the solar wind throughout the majority of cycle 23 ($1998 - 2011$) in order to understand the origin and mechanism that produce this ion. From the ACE/SWICS dataset, we identified several periods where He^+ VDFs can be well modeled by a Maxwellian distribution traveling near the corresponding solar wind proton speed whose temperature follows a super mass proportional relationship that coincides with previous studies of ions in the solar wind. These properties suggest the He^+ ions resemble material of solar origin.

Furthermore, He^+ does not depend on the solar cycle, wind speed, composition, and source region, suggesting that the mechanism producing He^+ is independent of processes that generate the distinctive properties of the solar wind but rather a process common to wind traveling on the ecliptic and occurring before reaching 1AU.

Current simulations of He charge state distributions accounting for electron impact ionization and recombination along with photoionization and radiative recombination processes are shown to underestimate He^+/He^{2+} by $3 - 4$ orders of magnitude. This indicated the possibility of missing processes that may be active during the radial expansion of the solar wind. To reconcile the missing He^+, we tested the effectiveness of charge exchange between the solar wind and H and H_2 from dust in the production of He^+ to determine if this recombination process could explain the enhancement of

He^+/He^{2+} at 1AU. Our work estimates the radial distribution and density of neutrals that are required to be present during the solar wind's radial expansion which could make charge exchange an effective method of transforming a small fraction of solar alpha particles into singly ionized He to meet observational values. Results show that a distribution of dust neutrals (H, H_2) following a power law of the form γr^{-a}, with $\gamma > 0.05$ for $a = 2.8$, with an inner edge between $4 - 8R_\odot$ can produce the He^+/He^{2+} values. Our results predict a density of H and H_2 that is several orders of magnitude larger than previous models, suggesting; 1) that dust density and distribution of grain size in the vicinity of the Sun is larger than previously described, and/or 2) there may be additional processes contributing to the solar He^+ population below 1AU.

Further observations are needed to better constrain the density of H and H_2 near the Sun. However, our modeling results may be an indication of the importance in accounting for processes between the dust and solar wind. One of the key implications from our results is the importance of charge exchange processes during the radial propagation of the solar wind. This may be a significant process shaping the ion composition measured in the heliosphere.

Further constraints to the presence of neutrals are necessary to continue testing our hypothesis more rigorously. Remote observations remain limited to the progress of dust studies due to the loss of spatial information from intensities integrated along the line of sight. A more effective manner of probing the dust environment near the Sun is through a combination of remote and in situ observations.

CHAPTER V

Conclusions and Future Work

5.1 Thesis Summary and Conclusions

Throughout this thesis work, I address several aspects of the origin of low charge states within ICMEs and the solar wind. This section includes a brief summary of the main research goals in Chapter II − IV and details the three main science questions addressed, along with the main conclusions drawn from the body of work.

Chapter II provides insight to the following science question,

1. What is the fate of neutral and low ionized material in prominences and how is the CME heated?

In this Chapter, I investigated the energy evolution of a solar eruption by reconstructing a CME's thermodynamic evolution using near-Earth ion composition data collected within an ICME. Using a chi-squared minimizing algorithm that scanned an extensive parameter space, the temperature, density, and velocity profiles describing the CME's radial evolution are determined from its initial liftoff to ion freeze-in distances. The simulated ion distributions were closely matched to observations of C, O, and Fe distributions. Modeling results suggest the ion distributions are composed of multiple solar structures identified as; (1) cooler, chromospheric-like prominence material, (2) hot coronal plasma, and (3) interface plasmas, from the PCTR, possibly linking these structures. Through nonequilibrium modeling, we connected the low ionized C, O, and Fe observed to ions that originate from the prominence core that evolve among, but distinctly, from the adjacent structures of the CME. We also found the prominence component in the modeling results had photospheric composition, further confirming the cool ions belonged to prominence plasma which addresses the first part of Question 1.

To address the second part of the science question, we compute the heating rate per volume for each component. From our results, the cool ions can survive the level of heating experienced by the prominence plasma. However, the heating rate derived was different among the CME structures. The prominence core plasma experiences the highest heating rate at the solar surface that quickly descends to below the rate for the surrounding plasma by $2R_{\odot}$. The surrounding PCTR layers sustain an overall higher heating rate compared to the core and coronal plasma. These results suggest non-uniform heating throughout the CME that targets prominence plasma at the eruption site. However, the surrounding PCTR interface is consistently heated farther from the Sun. These results address the second part of Question 1 and signify the need for multi-point and -thermal plasma observations through a wider FOV from the solar surface.

Chapter III addressed the following science question,

2. Which spectral lines will enable the comprehensive study of solar eruptions with upcoming solar observatories?

In this Chapter, we investigated the diagnostic potential of several spectral lines spanning the EUV to near-Infrared, 100−14400Å, ranging between chromospheric and sub-flare temperatures to facilitate a more comprehensive examination of solar eruptions. The intensities were computed between the plasma's release and $2R_{\odot}$, taking into account the departures from ionization equilibrium experienced by each

CME plasma structure. We present several of the brightest lines along with a discussion of their diagnostic capability. We find many important spectral lines are within the planned observations of future DKIST, UCoMP, and instruments on the SO mission. We intend for the recommended lines to facilitate the planning of coordinated observations of CMEs between future ground- and space-based solar telescopes. Furthermore, additional lines are presented for planning and development of future solar telescopes.

Chapter IV focused on He^+ within the solar wind to provide insight to the following science question,

3. What is the origin of singly ionized He outside of CME cores and how is it formed?

In this Chapter, we analyze the velocity distribution functions of over a decade of He^+ measurements observed with the ACE/SWICS instrument located at L1. From this analysis, we found significant periods of enhanced singly ionized He outside of transients whose properties were unlike typical PUIs. These characteristics suggest the ions originate at the Sun and evolve as part of the solar wind, which addressed the first part of Question 3. However, models of the solar wind predict only a small fraction of the He^+ densities measured. To address the second part of Question 3, I reconcile the unaccounted for solar He^+ by testing charge exchange with outgassed dust neutrals as a mechanism driving the production of He^+ from He^{2+}. Modeling results indicate that charge exchange processes can be important below $10 - 15R_\odot$, however additional observations, both remote and in situ, are necessary to constrain neutrals at those distances and to confirm this as the primary source.

5.2 Future and Ongoing Work

5.2.1 Unprecedented Measurements of the Sun with New Solar and Heliospheric Missions

Ongoing measurements of the Sun throughout the heliosphere will enable the detailed study of the evolution of material from the Sun. Most recently, the Parker Solar Probe (PSP) and Solar Orbiter (SO) missions, which launched in August 2018 and February 2020, respectively. Figure 5.1 illustrates the orbit for PSP, in green, and SO, in purple. The trajectories are not to scale but are drawn to illustrate their relative locations. PSP travels on an elliptic orbit along the ecliptic plane with approximately 10-day perihelion passes at the Sun where the instruments will measure the solar wind, shown in the white portion of the orbit. At its closest approach, PSP will be within $10R_\odot$, at a distance where our work predicts CME ions will still be evolving. PSP carries several in situ instrument suites; 1) the Solar Wind Electrons Alphas and Protons (SWEAP) which measures electrons, protons, and alphas, 2) Fields Experiment (FIELDS) which measures the electric and magnetic fields, and 3) the Integrated Science Investigation of the Sun (IS$\odot$IS) which measures energetic particles (10s of keV to 100 MeV). It also includes one remote sensing instrument, the Wide-field Imager for Solar PRobe (WISPR) which is a white light telescope pointed away from the Sun, imaging solar material as it travels into the heliosphere.

SO will travel on an elliptic heliocentric orbit, in which throughout the course of the mission will climb off of the ecliptic, reaching 17° latitude in 2025 and 33° in 2029. SO will be the second mission to travel off the ecliptic to measure solar wind at large latitudes, the first to measure heavy ion composition below 1AU, and will be the first to take images of the Sun's poles. SO carries several remote and in situ instruments, which are all listed here for completeness. The remote sensing instrument suites include; 1) Polarimetric and Helioseismic Imager (PHI) which will be used to

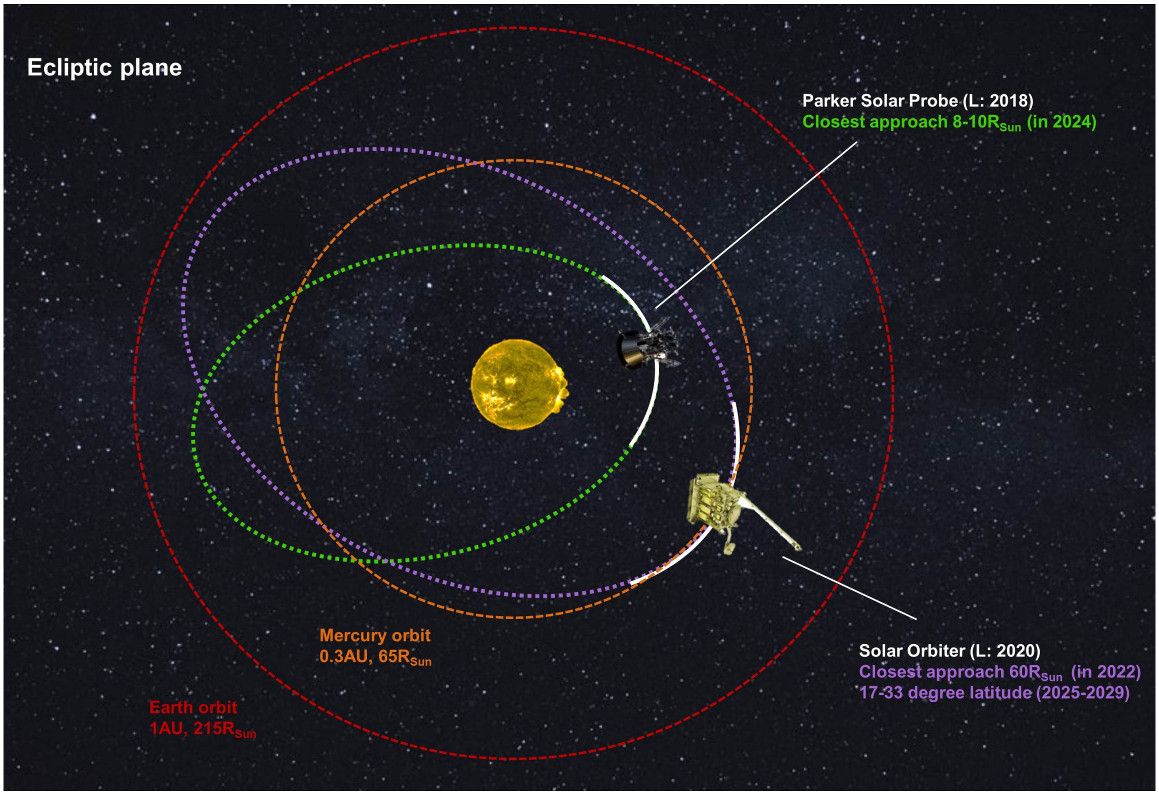

Figure 5.1: A top view of the ecliptic plane illustrating the orbits of Parker Solar Probe and Solar Orbiter (not to scale).

infer the photospheric magnetic field, 2) Extreme Ultraviolet Imager (EUI), 3) Spectral Imaging of the Coronal Environment (SPICE), 4) Spectrometer Telescope for Imaging X-rays (STIX), 5) Multi Element Telescope for Imaging and Spectroscopy (METIS) which is a coronagraph observing in Lyα and a broadband EUV channel, and 6) Solar Orbiter Heliospheric Imager (SoloHI). The in situ instrument suites include; 1) Solar Wind Plasma Analyser (SWA), 2) Energetic Particle Detector (EPD), 3) Magnetometer (MAG), and 4) Radio and Plasma Waves (RPW). Of particular interest to ongoing work, the SWA suite will carry a time-of-flight mass spectrometer, the Heavy Ion Sensor (HIS), that will measure heavy ion densities.

As described in Chapter III, ground-based DKIST and UCoMP will provide complementary observations on the Sun-Earth line to the orbiting spacecraft. DKIST will be targeting small on-disk, and just beyond the limb, regions of the Sun at high spatial resolution. UCoMP's coronagraphic capabilities will enable observations of the full corona, providing necessary context for DKIST observations as well as coverage of dynamics beyond the limb.

5.2.2 Future Nonequilibrum Ionization Modeling

Future nonequilibrium ionization modeling can be improved by examining ion and electron properties closer to the Sun with PSP and SO. Measurements of electron VDFs made with PSP, prior to the freeze-in distances to a large number of ions in CMEs, between $10 - 20R_\odot$, as shown in our results of Chapter II, can determine how similar the particle distributions are to Maxwellian at those distances. This can provide insight to where reaction coefficient rates begin to deviate from those calculated in the MIC, as well as which ion simulations are most reliable based on freeze-in distances.

Moreover, a combination of remote and in situ measurements can provide important boundary conditions to improve ion modeling. The ideal configuration to maximize CME coverage would require an eruption occurring on the solar limb, from the vantage point of one instrument, and for the CME to be intercepted by another instrument to measure local plasma properties. For example, through a combination of measurements from SWA's HIS and ESA combined with the UCoMP coronagraph at Earth, electron properties at the Sun and heliosphere can be combined with ion measurements to constrain charge state and plasma evolution.

5.2.3 Further Investigation of CME Heating with MHD Simulations

To build upon the energy results derived in Chapter II, future work plans to employ large scale MHD models to investigate the spatial dependence of energy supplied to different CME structures. Our plasma heating requirements will be compared to the energy evolution of the CME as a manner of constraining specific plasma structures as they travel through the corona. From the simulations, we can calculate the individual contributions from different heating sources to measure their potential viability.

For example, we can compare our heating rates to those generated from a 3D MHD simulation using the Alfvén Wave Solar Model (AWSoM; Oran et al. 2013; Sokolov et al. 2013; van der Holst et al. 2014) coupled with the Gibson-Low (GL; Gibson & Low 1998) flux rope model. AWSoM is a background solar wind model extending between the upper chromosphere to beyond $20R_{\odot}$. In past studies, AWSoM+GL has provided means of studying the CME's thermodynamic evolution through the corona, ion temperature anisotropy, as well as electron/ion temperature distribution within the ejecta (Jin et al., 2017; Manchester et al., 2014; Manchester & van der Holst, 2017). The code includes a self-consistent coronal heating term driven by the dissipation of counter-propagating Alfvén waves, as well as radiative cooling, and electron heat conduction terms. The GL magnetic flux rope inserted into the solar wind model can effectively capture the multi-part CME structure, allowing the heating experienced by different structures to be tracked. The MHD model would allow for the calculation of spatially dependent heating rates to compare with our results.

5.2.4 Further Analysis of He^+ in the Solar Wind

Future work will include additional constraints to the H and H_2 densities outgassed by interplanetary dust, derived in Chapter IV, using remote observations near the Sun. Additional charge exchange processes with solar wind protons and alphas can be included to further investigate the interplay between the solar wind and dust. For example, Table 5.1 includes reactions between protons and H and H_2, reactions between alpha particles and H and H_2 (as before), and a reaction between He^+ with H and H_2. Through a combination of He^+ ion densities from SO/HIS and neutralization of solar wind protons, which can form Lyα emission, additional constraints will be placed to the H and H_2 distribution at the Sun.

Table 5.1: Additional charge exchange processes.

Reaction #	Reaction	Line (Å)
1	$\mathbf{H}^{+} + \mathrm{H} \rightarrow \mathbf{H} + \mathrm{H}^{+}$	Ly α,β
2	$\mathbf{H}^{+} + \mathrm{H}_2 \rightarrow \mathbf{H} + \mathrm{H}_2^{+}$	
3	$\mathbf{H}^{+} + \mathrm{He} \rightarrow \mathbf{H} + \mathrm{He}^{+}$	
4	$\mathbf{He}^{2+} + \mathrm{H}_2 \rightarrow \mathbf{He}^{+} + \mathrm{H}_2^{+}$	He II 256, 304
5	$\mathbf{He}^{2+} + \mathrm{H}_2 \rightarrow \mathbf{He}^{+} + \mathrm{H}^{+} + \mathrm{H}$	
6	$\mathbf{He}^{2+} + \mathrm{H}_2 \rightarrow \mathbf{He}^{+} + \mathrm{H}^{+} + \mathrm{H}^{+} + e$	
7	$\mathbf{He}^{2+} + \mathrm{H} \rightarrow \mathbf{He}^{+} + \mathrm{H}^{+}$	
8	$\mathbf{He}^{2+} + \mathrm{H}_2 \rightarrow \mathbf{He} + \mathrm{H}_2^{2+}$	He I 584, 10830
+ 9	$\mathbf{He}^{2+} + \mathrm{He} \rightarrow \mathbf{He} + \mathrm{He}^{2+}$	
10	$\mathbf{He}^{+} + \mathrm{H}_2 \rightarrow \mathbf{He} + \mathrm{H}_2^{+}$	

For example, He^{+} densities from SO/HIS and Lyα measurements from the METIS, which can be compared to synthetic intensities produced by our distribution of neutral H, can be used together to constrain neutral densities in the MIC. Furthermore, the SO instruments will include the advantage of comparing measurements, of He^{+} and indirect H densities, for the same coronal environment which was previously not available.

APPENDIX

APPENDIX A

All Coronal Mass Ejection Intensities

A.1 Additional Figures for Remaining Intensities in Chapter III

We include figures showing the results for all lines above 1×10^{-3} phot cm^{-2} s^{-1} arcsec^{-2}, Figure A1-A10.

A.1.1 Non-equilibrium intensities

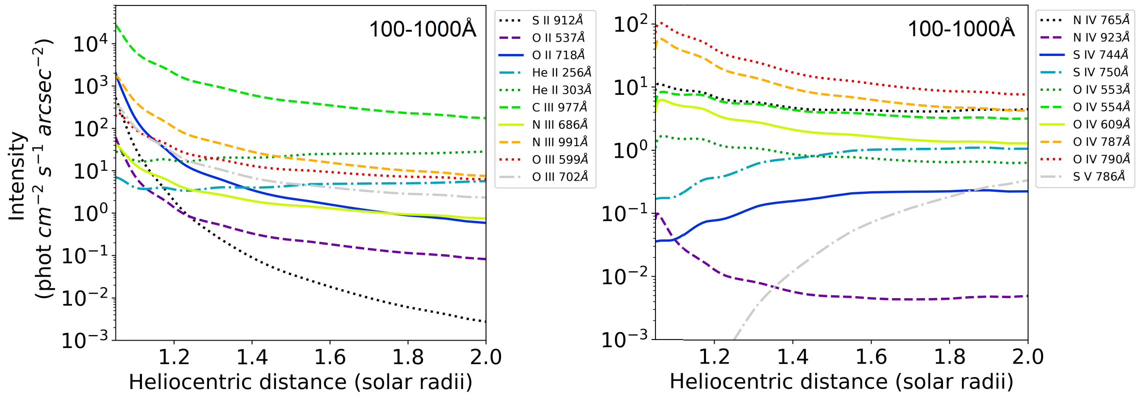

Figure A1: EUV intensities for all the lines between 1.05-2$R_\odot$ for PC$_1$.

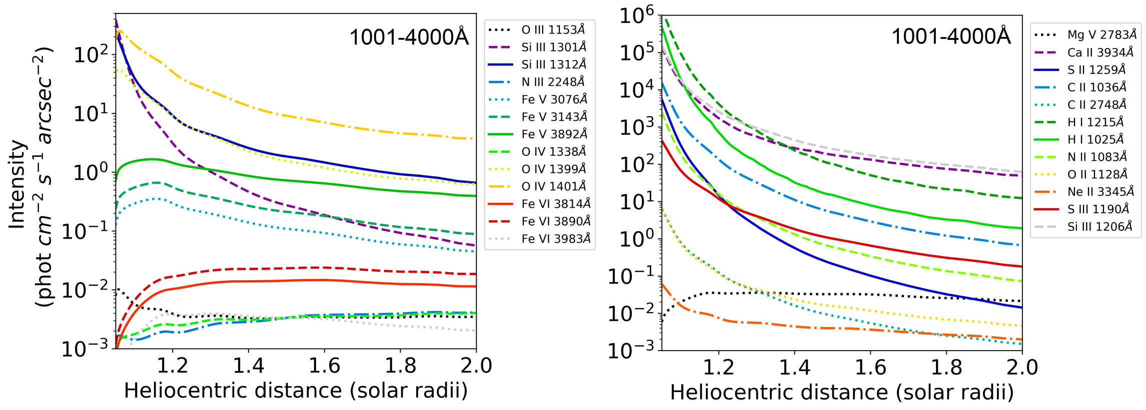

Figure A2: UV intensities for all the lines between 1.05-2$R_\odot$ for PC$_1$.

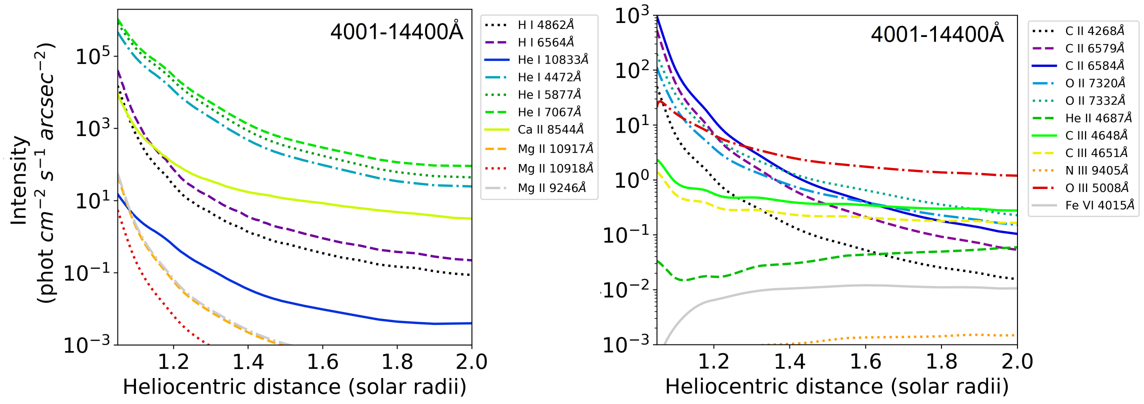

Figure A3: Visible and Infrared for all the lines between 1.05-2$R_\odot$ for PC$_1$.

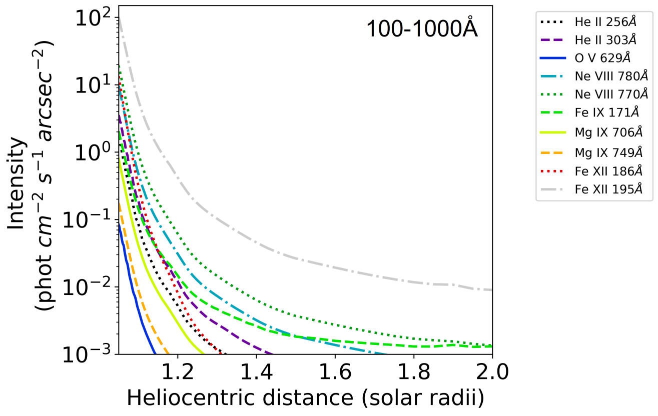

Figure A4: EUV intensities for all the lines between 1.05-2$R_\odot$ for PC$_2$.

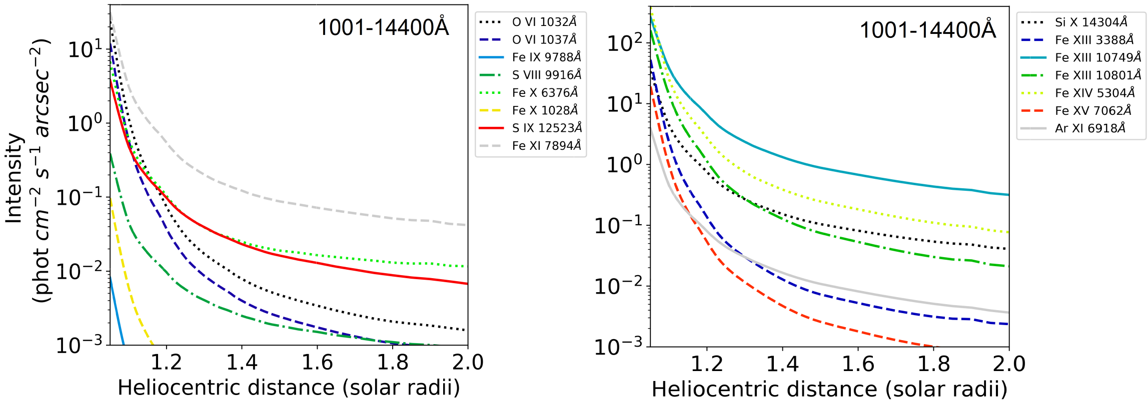

Figure A5: UV, visible, and infrared intensities for all the lines between 1.05-2$R_\odot$ for PC$_2$.

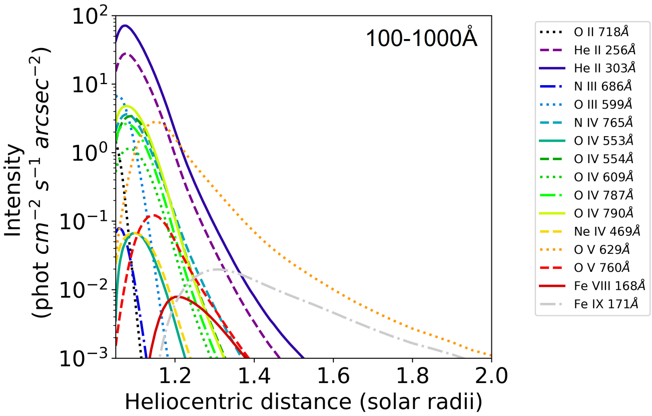

Figure A6: EUV intensities for all the lines between 1.05-2$R_\odot$ for PC$_3$.

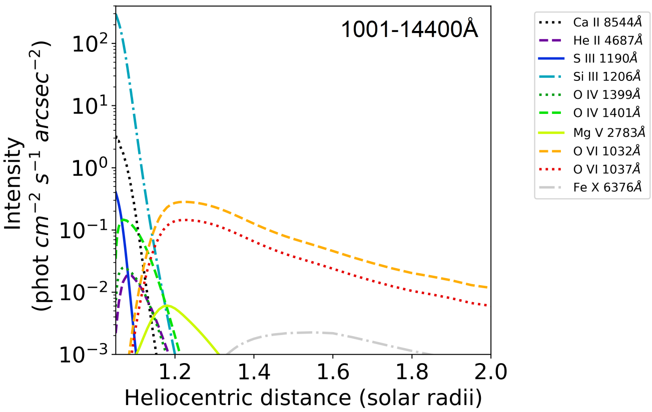

Figure A7: UV, visible, and infrared intensities for all the lines between 1.05-2$R_\odot$ for PC$_3$.

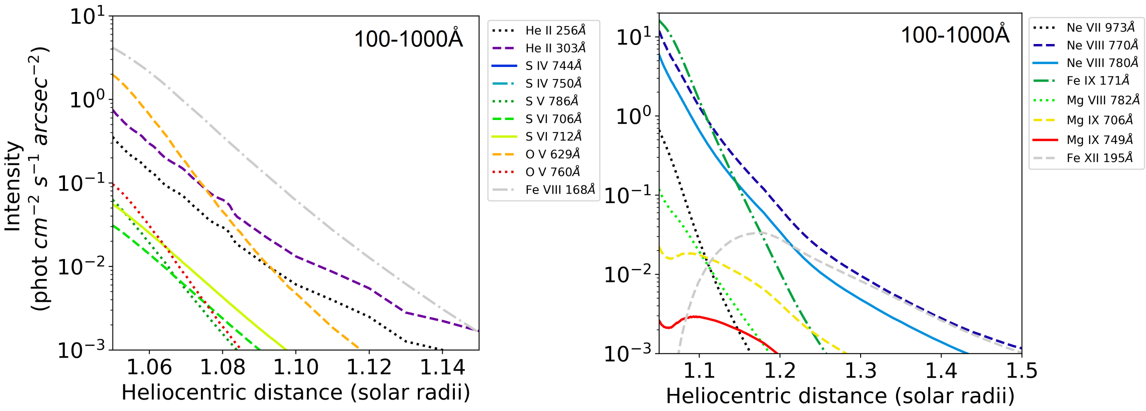

Figure A8: EUV intensities for all the lines between 1.05-15$R_{\odot}$ (left) and $1 - 1.5R_{\odot}$ (right) for PC$_4$.

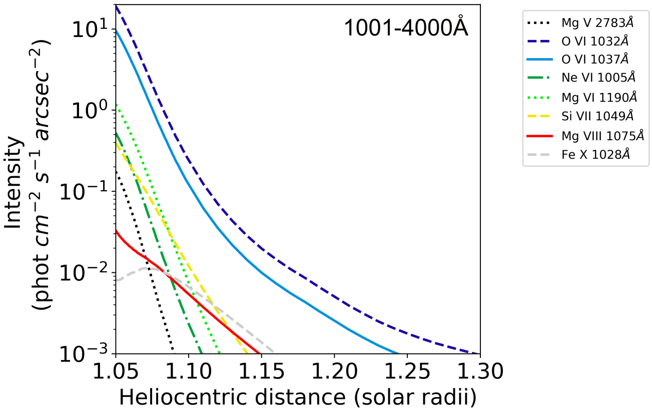

Figure A9: UV intensities for all the lines between 1.05-1.3$R_{\odot}$ for PC$_4$.

A.1.2 Elemental plots

We include elemental plots for all lines, Figure A11-A20.

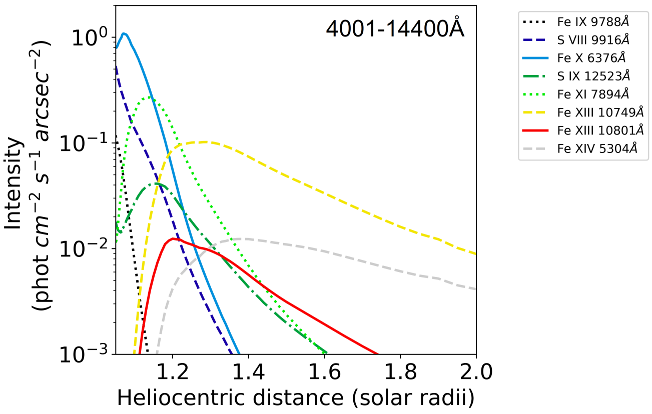

Figure A10: Visible and infrared intensities for all the lines between 1.05-2$R_\odot$ for PC$_4$.

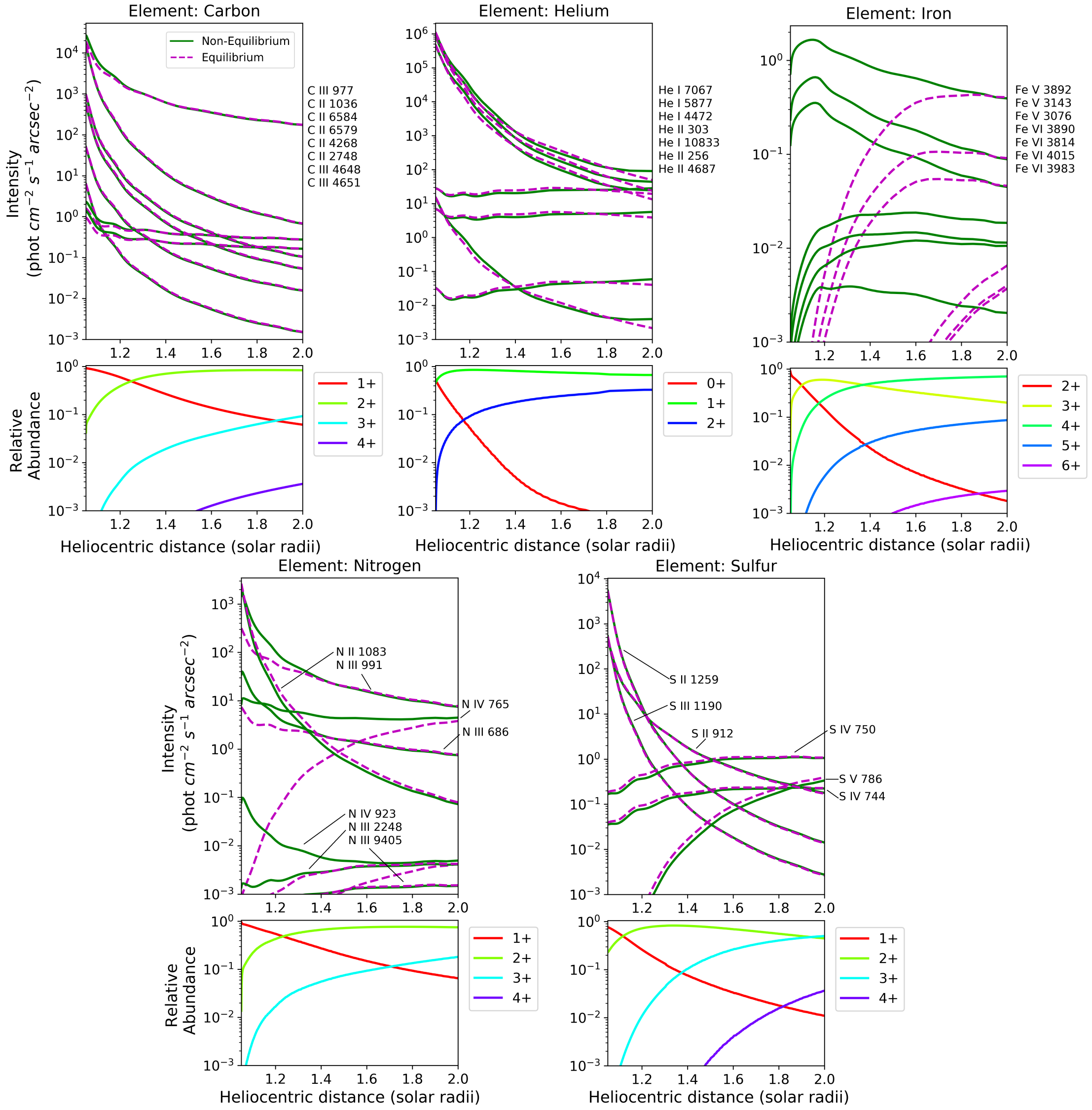

Figure A11: Results for PC_1; a vertical two panel plot for each element displaying the Non-equilibrium (green) and Equilibrium (magenta) intensity for each line (top), and the relative abundance of each ion (bottom). For plots with a list of lines appearing adjacent on the right, the lines are organized in descending order by each line's initial Non-equilibrium intensity value. In addition, as a note, the spectral lines include the common roman numeral convention describing the emitting ion while the relative abundance plots describe the charge states by the number of missing electrons which is typical heliospheric nomenclature. This results in mismatch of numbers such that Fe V is the Fe^{4+} charge state and so on.

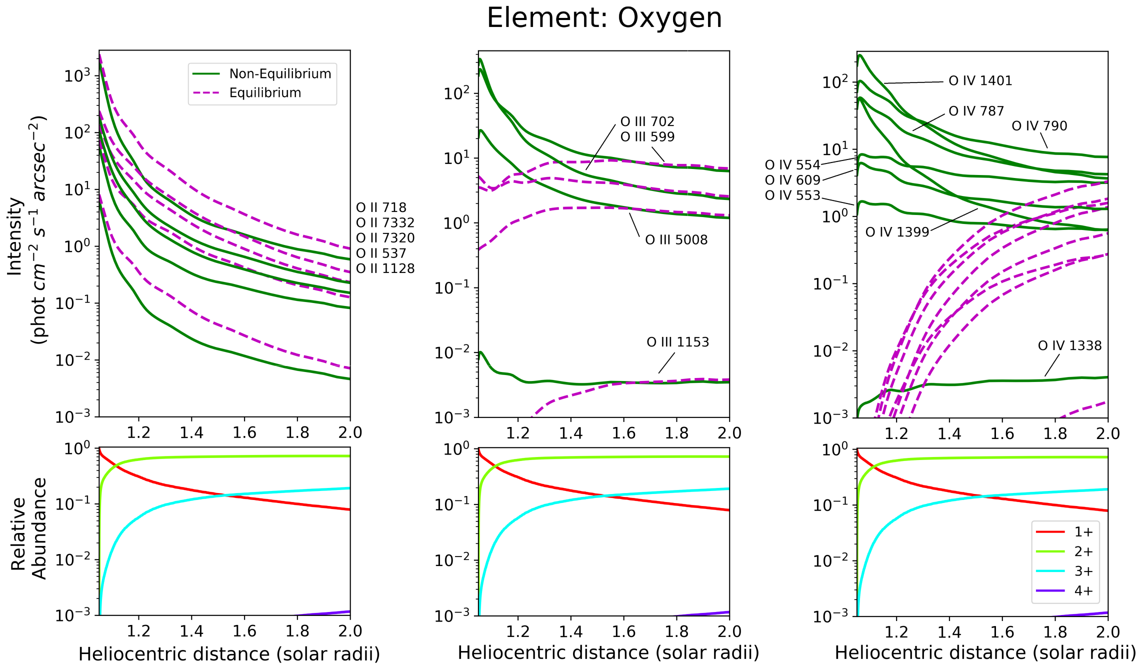

Figure A12: Same placement as Figure A11 for prominence plasma, PC_1.

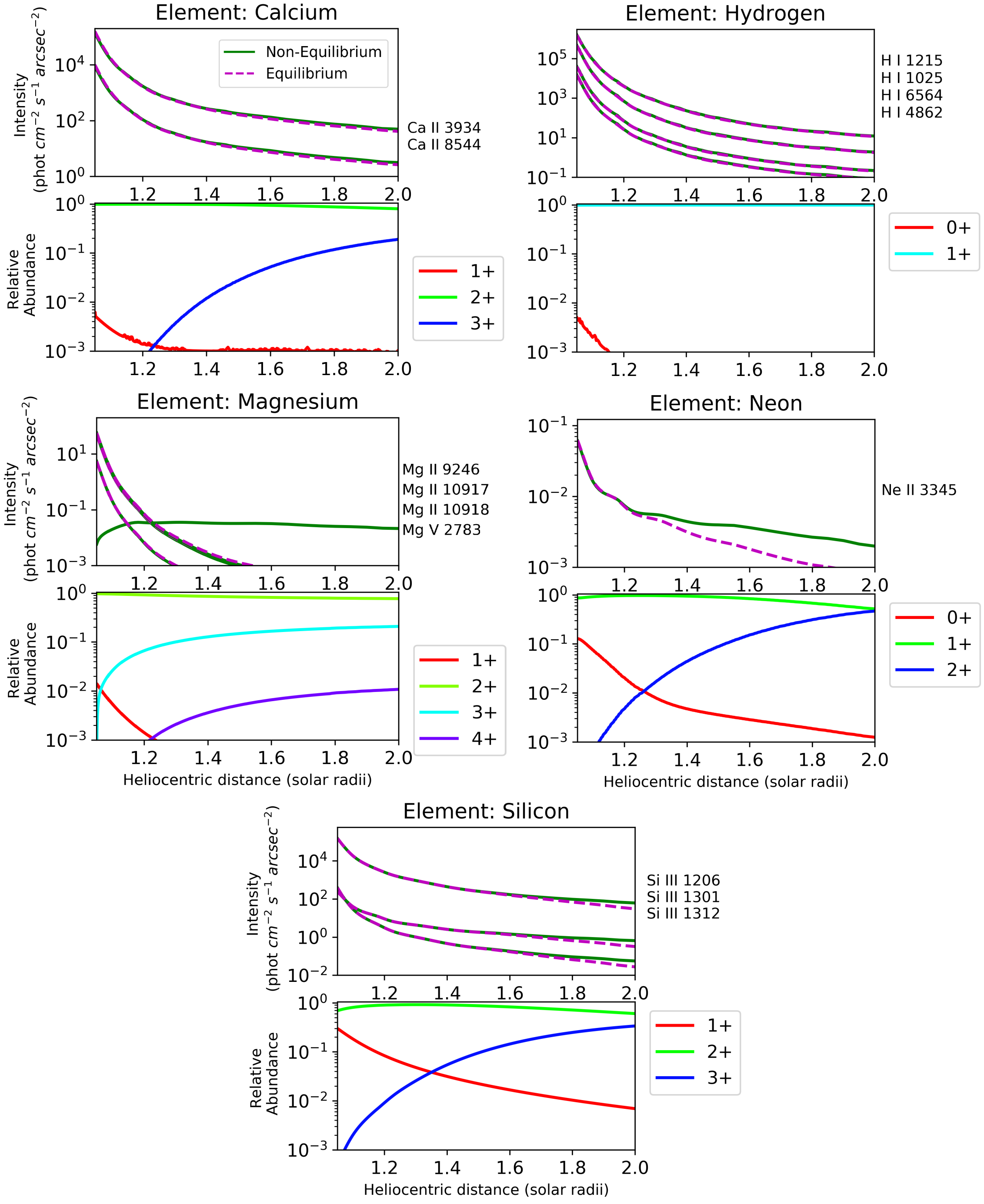

Figure A13: Same placement as Figure A11 for prominence plasma, PC_1.

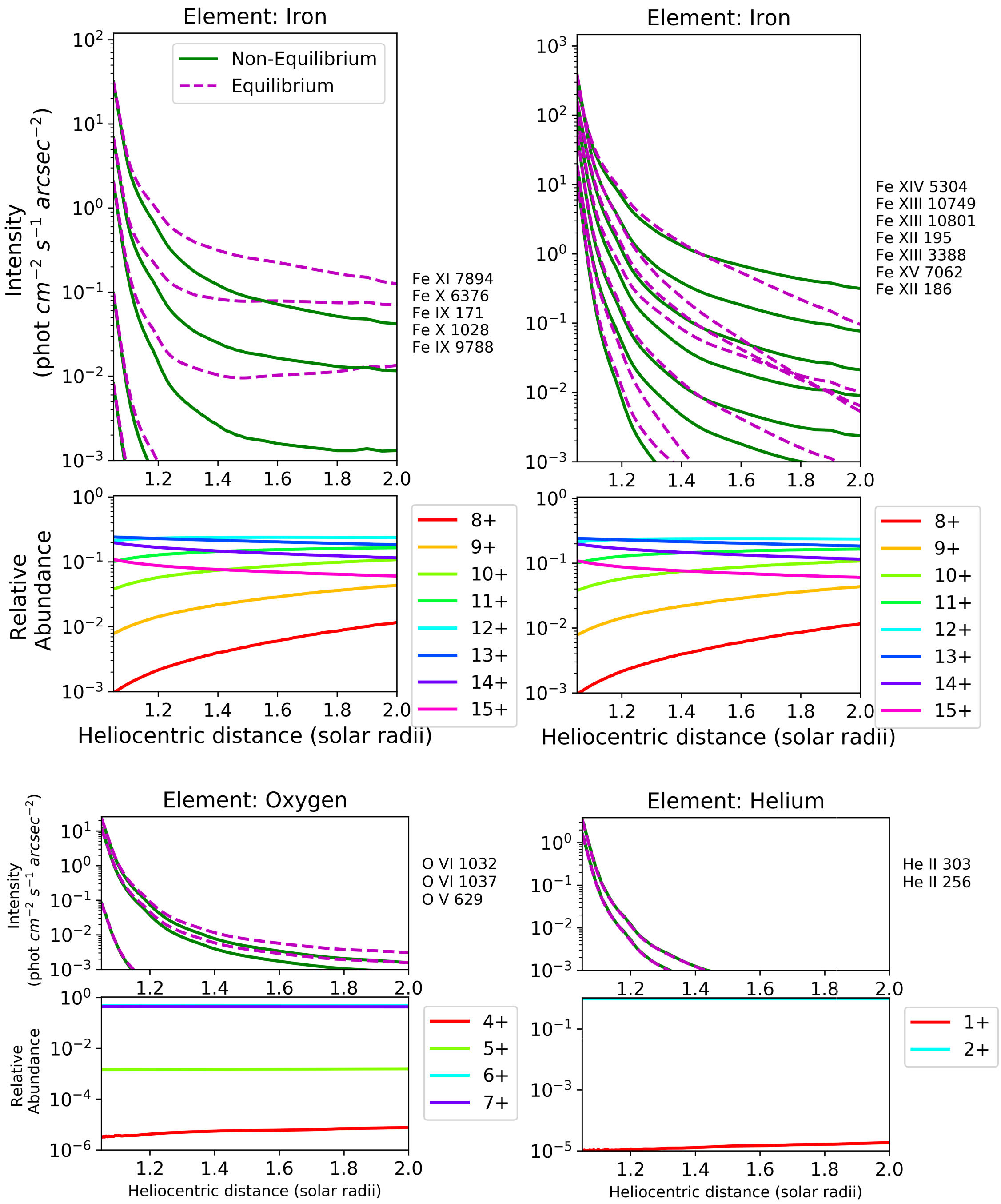

Figure A14: Same placement as Figure A11 for the coronal plasma, PC_2.

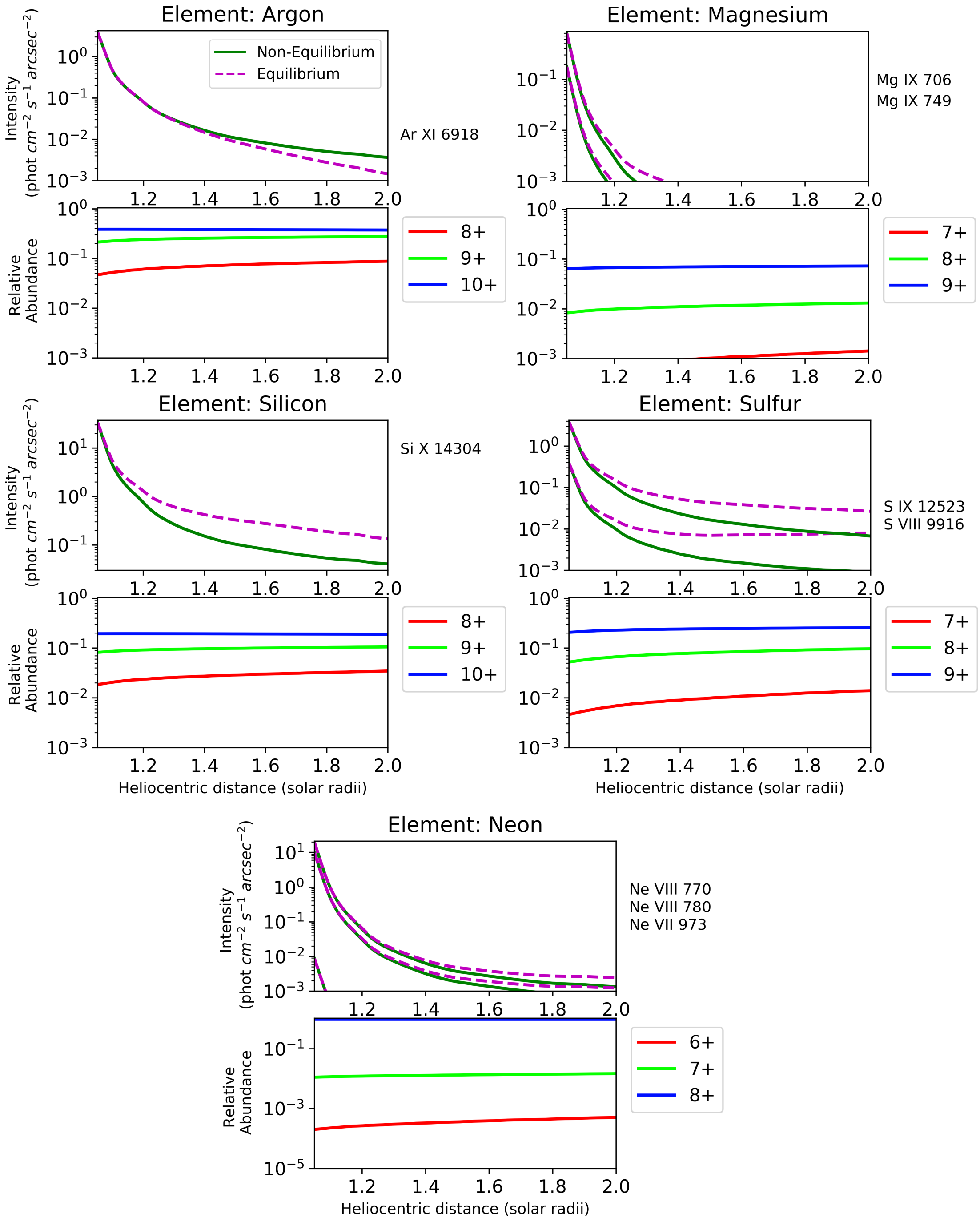

Figure A15: Same placement as Figure A11 for the coronal plasma, PC_2.

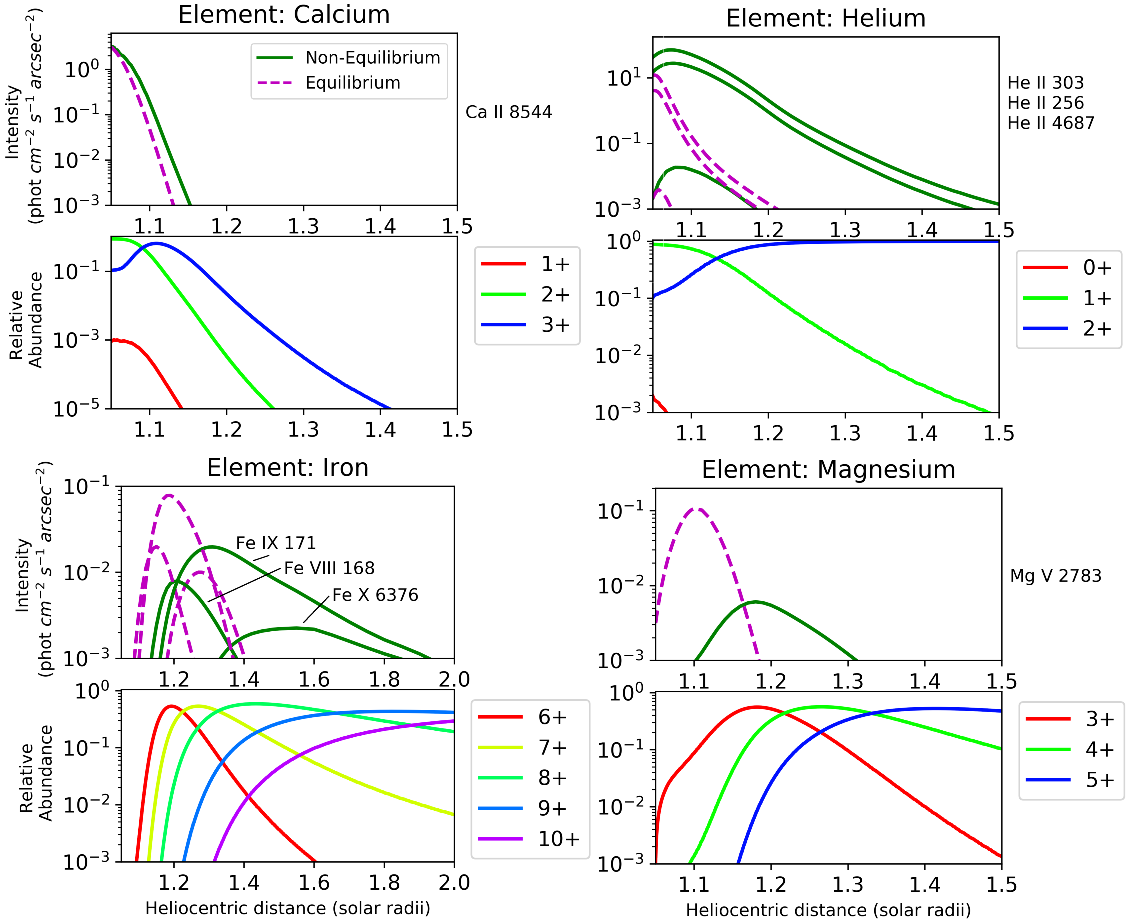

Figure A16: Same placement as Figure A11 for PCTR plasma, PC$_3$between $1-1.5R_\odot$.

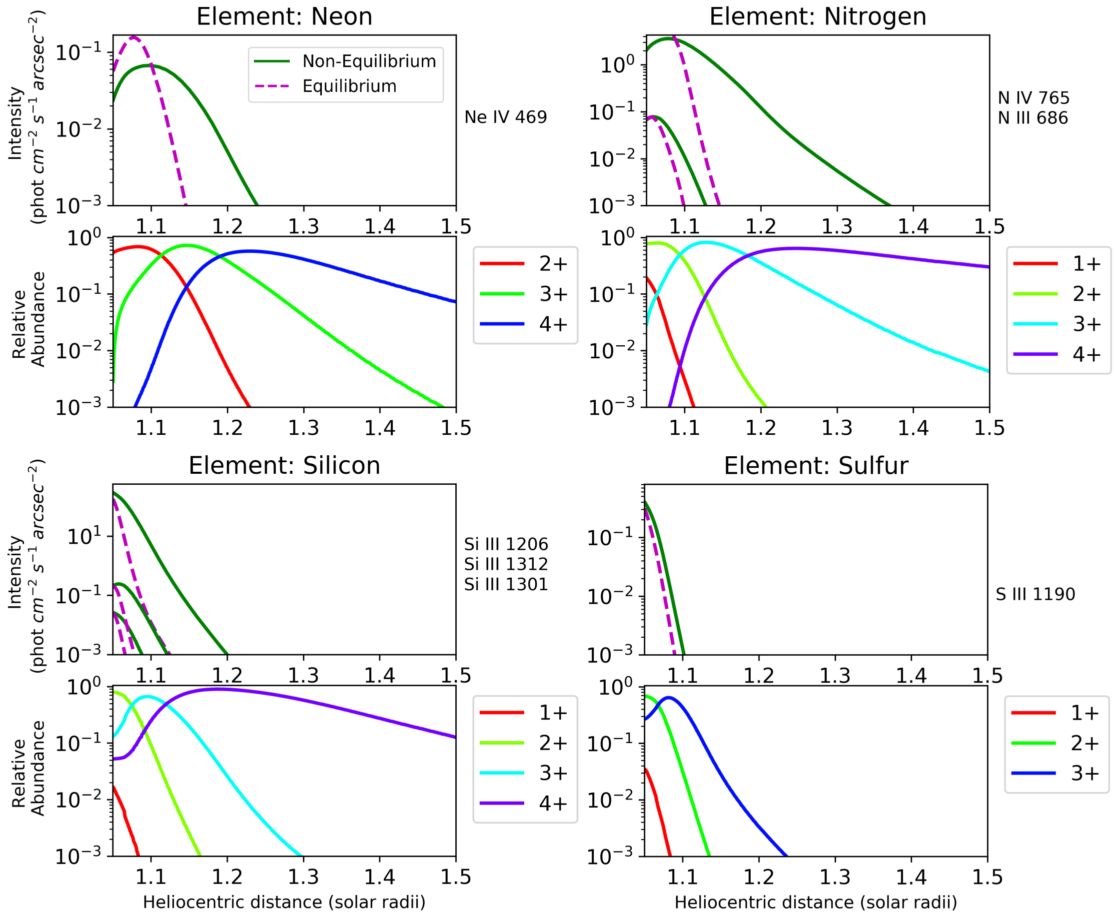

Figure A17: Same placement as Figure A11 for PCTR plasma, PC_3 between $1-1.5R_\odot$.

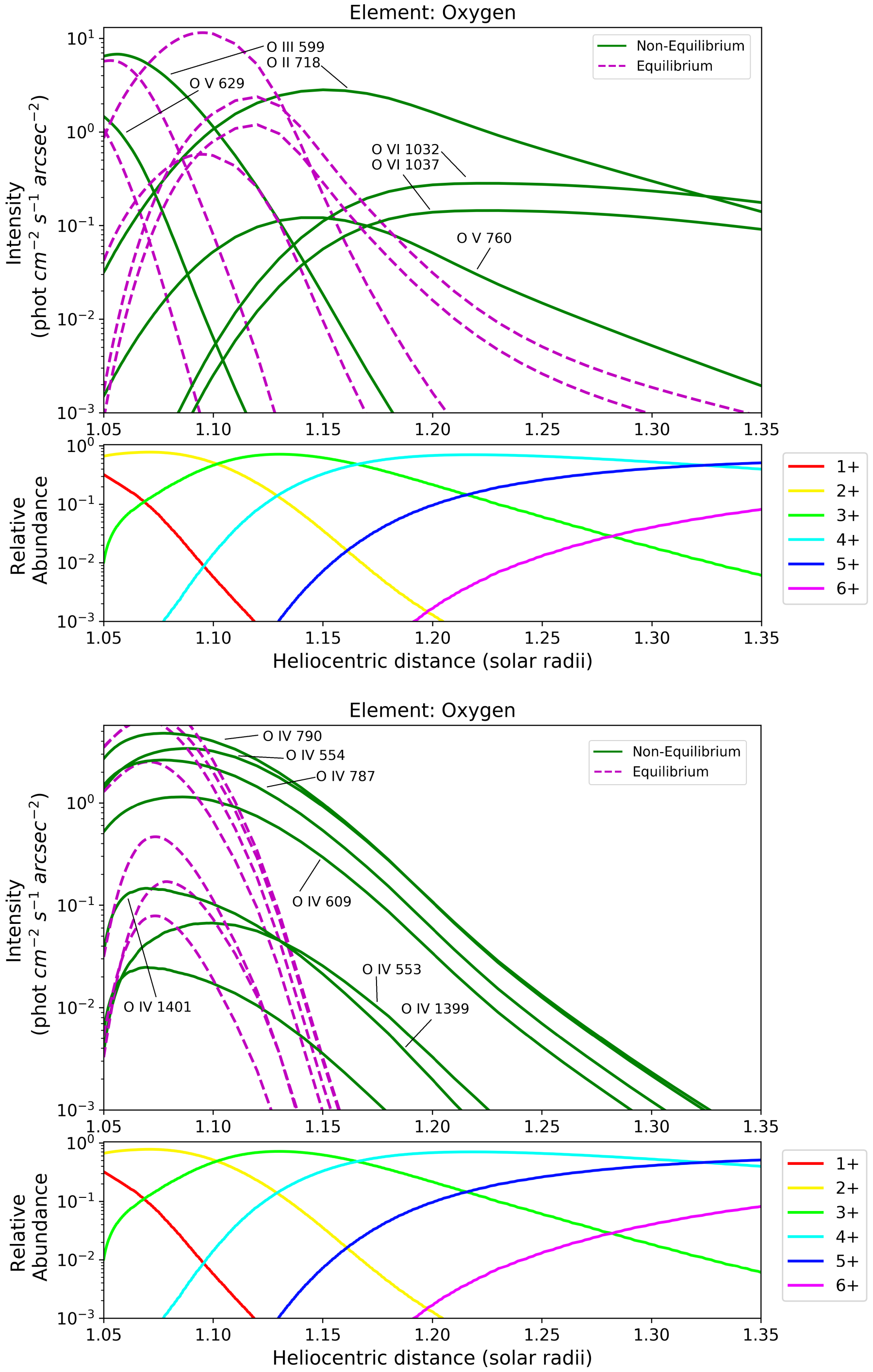

Figure A18: Same placement as Figure A11 for Oxygen lines in the PCTR, PC_3, between 1.05-1.35$R_{\odot}$.

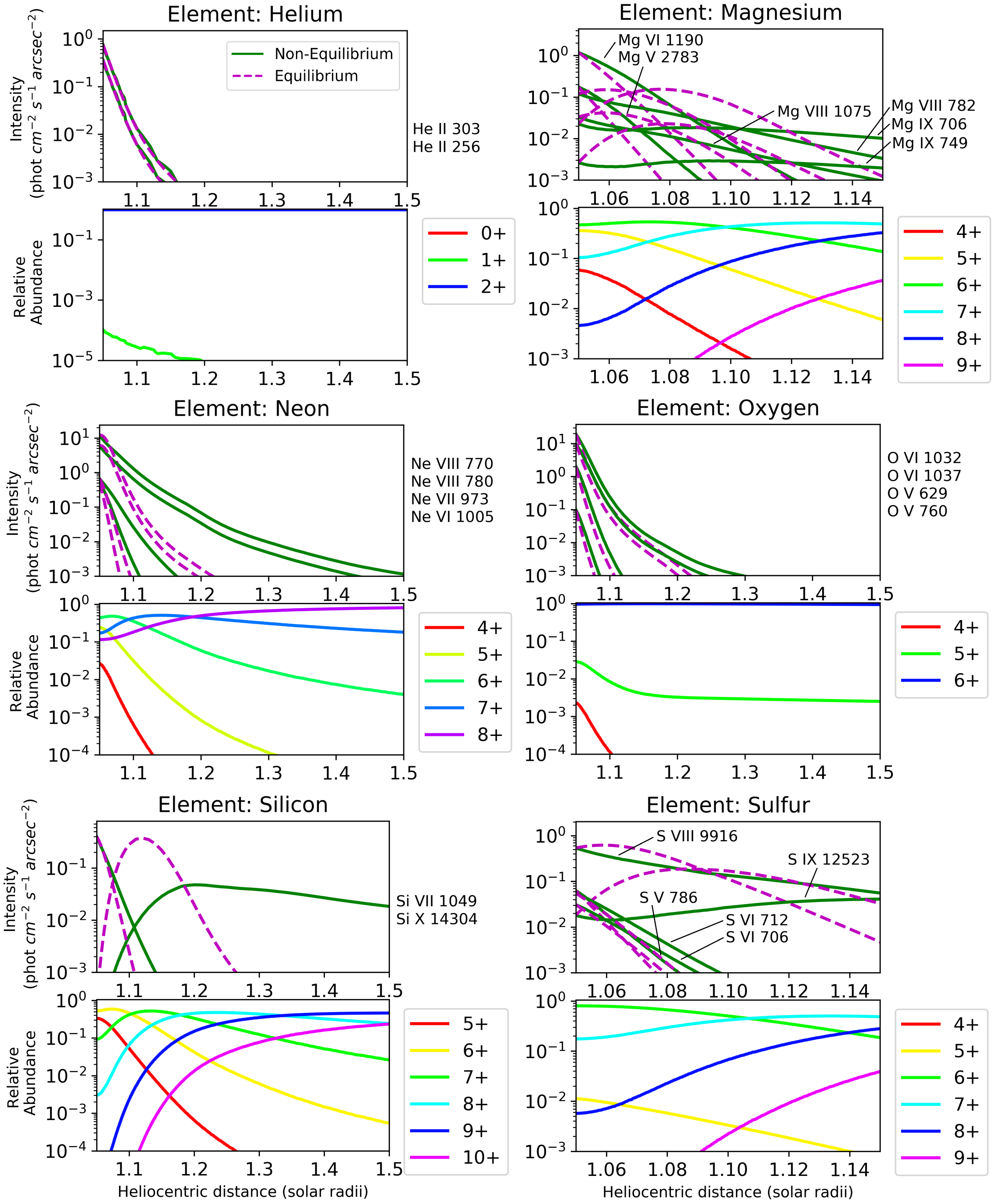

Figure A19: Same placement as Figure A11 for PCTR, PC_4, between 1.05-1.5$R_\odot$ for all lines except Mg and S which are plotted between 1.05-1.15$R_\odot$.

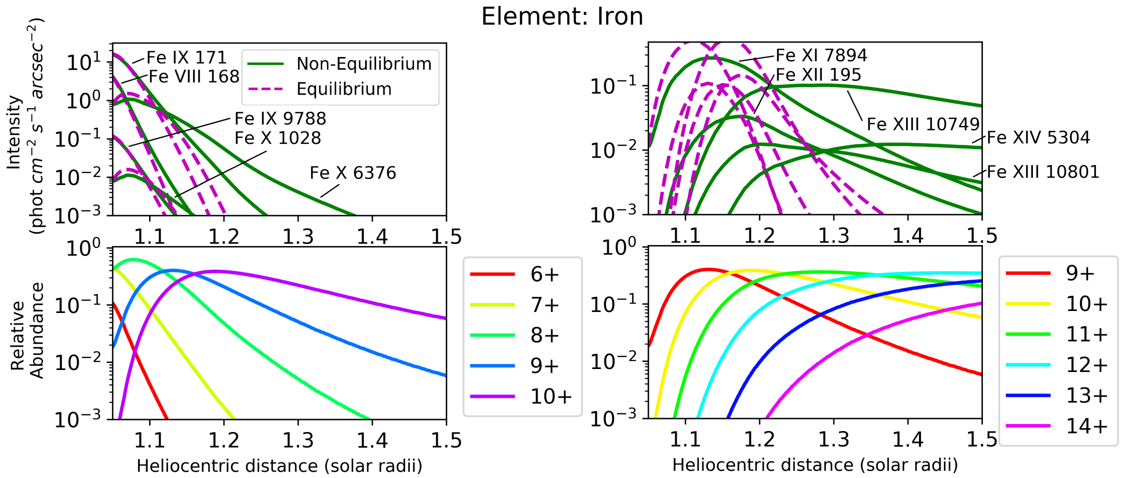

Figure A20: Same placement as Figure A11 for Iron lines in the PCTR, PC_4, between 1.05-1.5$R_\odot$.

BIBLIOGRAPHY

BIBLIOGRAPHY

Akmal, A., Raymond, J. C., Vourlidas, A., et al. 2001, The Astrophysical Journal, 553, 922

Alfvén, H., & Lindblad, B. 1947, Monthly Notices of the Royal Astronomical Society, 107, 211

Allegrini, F., Schwadron, N. A., McComas, D. J., Gloeckler, G., & Geiss, J. 2005, Journal of Geophysical Research: Space Physics, 110, A05105

Arnaud, J., & Newkirk, G. J. 1987, Astronomy and Astrophysics (ISSN 0004-6361), 178, 263

Aschwanden, M. J. 1999, Solar Physics, 190, 233

Asplund, M., Grevesse, N., Sauval, A. J., & Scott, P. 2009, Annual Review of Astronomy and Astrophysics, 47, 481

Bame, S. J., Hundhausen, A. J., Asbridge, J. R., & Strong, I. B. 1968, Physical Review Letters, 20, 393

Banks, P. M. 1971, J Geophys Res, 76, 4341

Bao, X., Zhang, Z., Deng, J., et al. 2009, Science in China, Series G: Physics, Mechanics and Astronomy, 52, 1794

Barnett, C. F. 1990, Atomic Data for Fusion, 1, doi:http://dx.doi.org/10.13140/2.1.4778.1442

Bein, B. M., Berkebile-Stoiser, S., Veronig, A. M., et al. 2011, The Astrophysical Journal, 738, 191

Berger, L., Drews, C., Taut, A., & Wimmer-Schweingruber, R. F. 2015, Astronomy and Astrophysics, 576, 54

Bethe, H. A., & Critchfield, C. L. 1938, Physical Review, 54, 248

Biermann, L. 1951, Zeitschrift fur Astrophysik, 29, 274

Bochsler, P., Geiss, J., & Joos, R. 1985, Journal of Geophysical Research, 90, 10,779

Bodewits, D., Hoekstra, R., Seredyuk, B., et al. 2006, The Astrophysical Journal, 642, 593

Bodewits, D., Juhsz, Z., Hoekstra, R., & Tielens, A. G. G. M. 2004, The Astrophysical Journal, 606, L81

Borrini, G., Gosling, J. T., Bame, S. J., & Feldman, W. C. 1982, Journal of Geophysical Research, 87, 7370

Bourdin, P.-A. 2017, The Astrophysical Journal Letters, 850, L29

Brownlee, D. 1996, in ASP Conference Series, Vol. 104, 216–264

Brueckner, G. E., Howard, R. A., Koomen, M. J., et al. 1995, Solar Physics, 162, 357

Burlaga, L., Sittler, E., Mariani, F., & Schwenn, R. 1981, Journal of Geophysical Research, 86, 6673

Bzowski, M., & Królikowska, M. 2005, Astronomy and Astrophysics, 435, 723

Cane, H. V., & Richardson, I. G. 2003, Journal of Geophysical Research: Space Physics, 108, 1156

Cargill, P. J., & Klimchuk, J. a. 1997, The Astrophysical Journal, 478, 799

Carrington, R. C. 1859, Monthly Notices of the Royal Astronomical Society, 20, 13

Casini, R., López Ariste, A., Paletou, F., & Léger, L. 2009, Astrophysical Journal, 703, 114

Chalov, S. V., & Fahr, H. J. 1998, Astronomy and Astrophysics, 335, 746

Chen, J. H., Möbius, E., Gloeckler, G., et al. 2013, Journal of Geophysical Research: Space Physics, 118, 3946

Chen, P. F. 2011, Living Reviews in Solar Physics, 8, 1

Cirigliano, D., Vial, J. C., & Rovira, M. 2004, Solar Physics, 223, 95

Cranmer, S. R., van Ballegooijen, A. A., & Edgar, R. J. 2007, The Astrophysical Journal Supplement Series, 171, 520

Cravens, T. E. 1997, Geophysical Research Letters, 24, 105

Culhane, J. L., Harra, L. K., James, A. M., et al. 2007, Solar Physics, 243, 19

Del Zanna, G., Dere, K. P., Young, P. R., Landi, E., & Mason, H. E. 2015, A&A, 582, 56

Del Zanna, G., & Mason, H. E. 2018, Living Reviews in Solar Physics, 15, 5

Delaboudinière, J. P., Artzner, G. E., Brunaud, J., et al. 1995, Solar Physics, 162, 291

Dere, K. P., Landi, E., Mason, H. E., Monsignori Fossi, B. C., & Young, P. R. 1997, Astronomy and Astrophysics Supplement Series, 125, 149

Dere, K. P., Zanna, G. D., Young, P. R., Landi, E., & Sutherland, R. S. 2019, The Astrophysical Journal Supplement Series, 241, 22

Dima, G. I., Kuhn, J. R., Mickey, D., & Downs, C. 2018, The Astrophysical Journal, 852, 23

Ding, A., & Habbal, S. R. 2017, The Astrophysical Journal, 842, L7

Domingo, V., Fleck, B., & Poland, A. I. 1995, Solar Physics, 162, 1

Drews, C., Berger, L., Taut, A., & Wimmer-Schweingruber, R. F. 2016, Astronomy and Astrophysics, 588, A12

Dudík, J., Dzifčáková, E., Meyer-Vernet, N., et al. 2017, Solar Physics, 292, 100

Eddington, A. 1920, The Observatory, A Monthly Review of Astronomy, 43, 341

Eddy, J. 1974, Astronomy and Astrophysics, 34, 235

Eddy, J. A., & McKim Malville, J. 1967, The Astrophysical Journal, 150, 289

Edlén, V. 1943, Zeitschrift fur Astrophysik, 22, 30

Engvold, O. 1988, Solar and stellar coronal structure and dynamics; Proceedings of the Ninth Sacramento Peak Summer Symposium, 151

Fahr, H., Ripken, H., & Lay, G. 1981, Astronomy and Astrophysics, 102, 359

Feldman, U. 1998, Space Science Reviews, 85, 227

Feldman, U., & Widing, K. G. 1993, ASTROPHYSICAL JOURNAL, 414, 381

Festou, M. C., Rickman, H., & West, R. M. 1993, The Astronomy and Astrophysics Review, 4, 363

Filippov, B., & Koutchmy, S. 2002, Solar Physics, 208, 283

Fludra, A., Griffin, D., Caldwell, M., et al. 2013, in Proceedings of SPIE - The International Society for Optical Engineering, ed. S. Fineschi & J. Fennelly, Vol. 8862, 88620F

Forland, B. C., Gibson, S. E., Dove, J. B., Rachmeler, L. A., & Fan, Y. 2013, Solar Physics, 288, 603

Galvin, A. B., Kistler, L. M., Popecki, M. A., et al. 2008, Space Science Reviews, 136, 437

Gary, G. A. 2001, Solar Physics, 203, 71

Geiss, J., Gloeckler, G., Mall, U., & Von Steiger, R. 1994, ASTRONOMY AND ASTROPHYSICS -BERLIN-, 282, 924

Geiss, J., Gloeckler, G., Von Steiger, R., et al. 1995, Science, 268, 1033

Gibson, S. E., Dalmasse, K., Rachmeler, L. A., et al. 2017, The Astrophysical Journal Letters, 840, L13

Gibson, S. E., Foster, D., Burkepile, J., de Toma, G., & Stanger, A. 2006, The Astrophysical Journal, 641, 590

Gibson, S. E., & Low, B. C. 1998, The Astrophysical Journal, 493, 460

Gilbert, H., Kilper, G., Alexander, D., & Kucera, T. 2011, Astrophysical Journal, 727, doi:10.1088/0004-637X/727/1/25

Gilbert, J. A., Gershman, D. J., Gloeckler, G., et al. 2014, Review of Scientific Instruments, 85, 091301

Gilbert, J. A., Lepri, S. T., Landi, E., & Zurbuchen, T. H. 2012, The Astrophysical Journal, 751, 20

Gilbert, J. A., Lepri, S. T., Rubin, M., Combi, M., & Zurbuchen, T. H. 2015, Astrophysical Journal, 815, 12

Giordano, S., Ciaravella, A., Raymond, J., Ko, Y.-K., & Suleiman, R. 2013, Journal of Geophysical Research: Space Physics, 118, 967

Gloeckler, G., Fisk, L. A., Geiss, J., Schwadron, N. A., & Zurbuchen, T. H. 2000, Journal of Geophysical Research: Space Physics, 105, 7459

Gloeckler, G., & Geiss, J. 1992, Astronomy and Astrophysics, 92, 267

—. 1998, Space Science Reviews, 86, 127

Gloeckler, G., Geiss, J., Balsiger, H., et al. 1993, Science, 261, 70

Gloeckler, G., Geiss, J., Roelof, E. C., et al. 1994, Journal of Geophysical Research, 99, 17637

Gloeckler, G., Cain, J., Ipavich, F. M., et al. 1998, Space Science Reviews, 86, 497

Gloeckler, G., Möbius, E., Geiss, J., et al. 2004, Astronomy & Astrophysics, 426, 845

Gopalswamy, N., Yashiro, S., Michalek, G., et al. 2009, Earth, Moon and Planets, 104, 295

Gouttebroze, P., Labrosse, N., Heinzel, P., & Vial, J. C. 2002, in European Space Agency, (Special Publication) ESA SP No. 505, 421–424

Grotian, W. 1939, Die Naturwissenschaften, 27, 214

Gruesbeck, J. R., Lepri, S. T., & Zurbuchen, T. H. 2012, The Astrophysical Journal, 760, 141

Gruesbeck, J. R., Lepri, S. T., Zurbuchen, T. H., & Antiochos, S. K. 2011, The Astrophysical Journal, 730, 103

Grün, E., & Landgraf, M. 2001in , 151–164

Gruntman, M. 1996, Journal of Geophysical Research, 101, 15,555

Gruntman, M. A. 1994, Journal of Geophysical Research: Space Physics, 99, 19,213

Grünwaldt, H., Neugebauer, M., Hilchenbach, M., et al. 1997, Geophysical Research Letters, 24, 1163

Habbal, S. R., Druckmuller, M., Morgan, H., et al. 2011a, American Astronomical Society, SPD meeting #42, id.13.05; Bulletin of the American Astronomical Society, Vol. 43, 2011, 43

Habbal, S. R., Druckmüller, M., Morgan, H., et al. 2010, Astrophysical Journal, 719, 1362

Habbal, S. R., Morgan, H., & Druckm, M. 2011b, First Asia-Pacific Solar Physics Meeting ASI Conference Series, 2, 259

Hale, G. E. 1892, Astronomy and Astrophysics, 11, 917

—. 1929, The Astrophysical Journal, 70, 265

—. 1931, The Astrophysical Journal, 73, 379

Hanle, W. 1924, Zeitschrift für Physik D Atoms, Molecules and Clusters, 18, 5

Harrison, R. A., Sawyer, E. C., Carter, M. K., et al. 1995, Solar Physics, 162, 233

Heasley, J. N., & Milkey, R. W. 1978, The Astrophysical Journal, 221, 677

Henke, T., Woch, J., Schwenn, R., et al. 2001, Journal of Geophysical Research: Space Physics, 106, 10597

Hirayama, T. 1971, Solar Physics, 19, 384

Hirshberg, J. 1971, 582

Hoffmeister, C. 1944, Zeitschrift für Astrophysik, 23, 1

Holzer, T. E. 1977, Neutral hydrogen in interplanetary space, doi:10.1029/RG015i004p00467

Hovestadt, D., Hilchenbach, M., Bürgi, A., et al. 1995, Solar Physics, 162, 441

Howard, T. A. 2015, The Astrophysical Journal, 806, 175

Hundhausen, A. J., Gilbert, H. E., & Bame, S. J. 1968, Journal of Geophysical Research Space Physics, 73, 5485

Ipavich, F. M., Lundgren, R. A., Lambird, B. A., & Gloeckler, G. 1978, Nuclear Instruments and Methods, 154, 291

Ipavich, F. M., Galvin, A. B., Gloeckler, G., et al. 1986, Journal of Geophysical Research, 91, 4133

Jess, D. B., Mathioudakis, M., & Keys, P. H. 2014, The Astrophysical Journal, 795, 172

Jin, M., Manchester, W. B., van der Holst, B., et al. 2017, The Astrophysical Journal, 834, 172

Jones, G. H., Knight, M. M., Battams, K., et al. 2018, Space Science Reviews, 214, 20

Kaiser, C. B. 1970, The Astrophysical Journal, 159, 77

Kaiser, M. L., Kucera, T. A., Davila, J. M., et al. 2008, Space Science Reviews, 136, 5

Kasper, J. C., Lazarus, A. J., & Gary, S. P. 2008, Physical Review Letters, 101, 1

Kasper, J. C., Stevens, M. L., Lazarus, A. J., Steinberg, J. T., & Ogilvie, K. W. 2007, The Astrophysical Journal, 660, 901

Kasper, J. C., Klein, K. G., Weber, T., et al. 2017, The Astrophysical Journal, 849, 126

Keenan, F., & Aggarwal, K. 1989, The Astrophysical Journal, 344, 522

Keil, S. L., Rimmele, T. R., & Wagner, J. 2009, Earth, Moon and Planets, 104, 77

Kimura, H., & Mann, I. 1998, Earth, Planets and Space, 50, 493

Kimura, H., Mann, I., & Mukai, T. 1998, Planetary and Space Science, 46, 911

Klein, L. W., & Burlaga, L. F. 1982, Journal of Geophysical Research, 87, 613

Klimchuk, J. A., Patsourakos, S., & Cargill, P. J. 2008, The Astrophysical Journal, 682, 1351

Ko, Y. K., Fisk, L. A., Geiss, J., Gloeckler, G., & Guhathakurta, M. 1997, Solar Physics, 171, 345

Kocher, M., Landi, E., & Lepri, S. T. 2018, The Astrophysical Journal, 860, 51

Kohl, J. L., Esser, R., Gardner, L. D., et al. 1995, Solar Physics, 162, 313

Koskinen, H. E., & Huttunen, K. E. 2006, Space Science Reviews, 124, 169

Koutchmy, S., & Lamy, P. L. 1985, in Properties and Interactions of Interplanetary Dust, 63–74

Kucera, T., Andretta, V., & Poland, A. 1998, Solar Physics, 183, 107

Kucera, T. A., & Landi, E. 2006, The Astrophysical Journal, 645, 1525

—. 2008, The Astrophysical Journal, 673, 611

Kuhn, J. R., Arnaud, J., Jaeggli, S., Lin, H., & Moise, E. 2007, The Astrophysical Journal Letters, 667, 203

Kuhn, J. R., Penn, M. J., & Mann, I. 1996, The Astrophysical Journal, 456, L67

Labrosse, N., Heinzel, P., Vial, J. C., et al. 2010, Space Science Reviews, 151, 243

Laming, J. M. 2015, Living Reviews in Solar Physics, 12, 1

Landi, E., Gruesbeck, J. R., Lepri, S. T., & Zurbuchen, T. H. 2012a, The Astrophysical Journal, 750, 159

Landi, E., Gruesbeck, J. R., Lepri, S. T., Zurbuchen, T. H., & Fisk, L. A. 2012b, The Astrophysical Journal, 758, L21

Landi, E., Habbal, S. R., & Tomczyk, S. 2016, Journal of Geophysical Research: Space Physics, 121, 8237

Landi, E., & Lepri, S. T. 2015, The Astrophysical Journal, 812, L28

Landi, E., Oran, R., Lepri, S. T., et al. 2014, The Astrophysical Journal, 790, 111

Landi, E., Raymond, J. C., Miralles, M. P., & Hara, H. 2010, The Astrophysical Journal, 711, 75

Landi, E., & Testa, P. 2015, Astrophysical Journal, 800, 110

Lee, J. Y., & Raymond, J. C. 2012, Astrophysical Journal, 758, 116

Lee, J.-Y., Raymond, J. C., Ko, Y.-K., & Kim, K.-S. 2009, The Astrophysical Journal, 692, 1271

Lee, J.-Y., Raymond, J. C., Reeves, K. K., Moon, Y.-J., & Kim, K.-S. 2015, The Astrophysical Journal, 798, 106

—. 2017, The Astrophysical Journal, 844, 3

Leinert, C., & Jackson, B. V. 1998, The Astrophysical Journal, 505, 984

Leinert, C., Richter, I., & Planck, B. 1982, Astronomy and Astrophysics, 110, 111

Leinert, C., Roser, S., & Buitrago, J. 1983, Astronomy and Astrophysics, 118, 345

Lemen, J. R., Title, A. M., Akin, D. J., et al. 2012, Solar Physics, 275, 17

Lepri, S. T., Laming, J. M., Rakowski, C. E., & von Steiger, R. 2012, The Astrophysical Journal, 760, 105

Lepri, S. T., & Zurbuchen, T. H. 2010, The Astrophysical Journal, 723, L22

Lepri, S. T., Zurbuchen, T. H., Fisk, L. A., et al. 2001, Journal of Geophysical Research, 106, 29231

Lin, H., Kuhn, J. R., & Coulter, R. 2004, The Astrophysical Journal, 613, L177

Lin, H., Penn, M. J., & Tomczyk, S. 2000, The Astrophysical Journal, 541, L83

Lisse, C. M., Dennerl, K., Englhauser, J., et al. 1996, Science, 274, 205

Liu, Y., Richardson, J. D., & Belcher, J. W. 2005in , 3–17

Liu, Y., Richardson, J. D., Belcher, J. W., Kasper, J. C., & Elliott, H. a. 2006, Journal of Geophysical Research, 111, A01102

Loch, S., Pindzola, M., Ballance, C., et al. 2013in , 242–251

Lopez, R. E., & Freeman, J. W. 1986, Journal of Geophysical Research, 91, 1701

Lynch, B. J., Reinard, A. A., Mulligan, T., et al. 2011, The Astrophysical Journal, 740, 112

Lyot, B. 1939, Monthly Notices of the Royal Astronomical Society, 99, 538

Lyot, P. 1930, Bulletin Astronomique, 6, 305

MacQueen, R. M., & Greeley, B. W. 1995, The Astrophysical Journal, 440, 361

Manchester, W. B., Kozyra, J. U., Lepri, S. T., & Lavraud, B. 2014, Journal of Geophysical Research: Space Physics, 119, 5449

Manchester, W. B., & van der Holst, B. 2017, J. Phys.: Conf. Ser, 900

Mann, I., Czechowski, A., & Meyer-Vernet, N. 2010, in AIP Conference Proceedings, Vol. 1216, 491–496

Mann, I., Kimura, H., Biesecker, D. A., et al. 2004, DUST NEAR THE SUN, Tech. rep.

Marsch, E. 1983, NASA Conference Publication, 228, 355

—. 2006, Living Reviews in Solar Physics, 3, 1

Marsch, E., Yao, S., & Tu, C.-Y. 2009, Annales Geophysicae, 27, 869

Martens, P. C. H., & Kuin, N. P. M. 1989, Solar Physics, 122, 263

McComas, D. J., Bame, S. J., Barker, P., et al. 1998, Space Science Reviews, 86, 563

McIntosh, S. W., De Pontieu, B., Carlsson, M., et al. 2011, Nature, 475, 477

Merkin, V. G., Lionello, R., Lyon, J. G., et al. 2016, The Astrophysical Journal, 831, 23

Möbius, E., Hovestadt, D., Klecker, B., et al. 1985, Nature, 318, 426

Möbius, E., Bzowski, M., Chalov, S., et al. 2004, Astronomy and Astrophysics, 426, 897

Moise, E., Raymond, J., & Kuhn, J. R. 2010, Astrophysical Journal, 722, 1411

Müller, D., Zouganelis, I., St. Cyr, O. C., Gilbert, H. R., & Nieves-Chinchilla, T. 2020, Nature Astronomy, 4, 205

Murphy, N. A., Raymond, J. C., & Korreck, K. E. 2011, The Astrophysical Journal, 735, 17

Neugebauer, M., & Snyder, C. W. 1962, Science, 138, 1095

Nordholt, J. E., Reisenfeld, D. B., Wiens, R. C., et al. 2003, Geophysical Research Letters, 30, 1465

Oran, R., van der Holst, B., Landi, E., et al. 2013, The Astrophysical Journal, 778, 176

Osterbrock, D. E. 1961, The Astrophysical Journal, 134, 347

Parenti, S. 2014, Living Reviews in Solar Physics, 11, 1

—. 2015, Spectral Diagnostics of Cool Prominence and PCTR Optically Thin Plasmas, ed. J.-C. Vial & O. Engvold (Cham: Springer International Publishing), 61–77

Parenti, S., Del Zanna, G., & Vial, J.-C. 2019, Astronomy & Astrophysics, 625, A52

Parenti, S., Schmieder, B., Heinzel, P., & Golub, L. 2012, The Astrophysical Journal, 754, 66

Parenti, S., & Vial, J. C. 2013in , 69–78

Parker, E. N. 1958, The Astrophysical Journal, 128, 664

—. 1988, The Astrophysical Journal, 330, 474

Peterson, A. W. 1971, in Bulletin of the Astronomical Society, 500

Phillips, K. J. H., Feldman, U., & Landi, E. 2008, Ultraviolet and X-Ray Spectroscopy of the Solar Atmosphere (Cambridge: Cambridge University Press), doi:10.1017/cbo9780511585968

Pilipp, W. G., Miggenrieder, H., Montgomery, M. D., et al. 1987a, Journal of Geophysical Research, 92, 1075

Pilipp, W. G., Miggenrieder, H., Mühlhäuser, K. H., et al. 1987b, Journal of Geophysical Research, 92, 1103

Pilleri, P., Reisenfeld, D. B., Zurbuchen, T. H., et al. 2015, Astrophysical Journal, 812, 1

Rakowski, C. E., Laming, J. M., & Lepri, S. T. 2007, The Astrophysical Journal, 667, 602

Rakowski, C. E., Laming, J. M., & Lyutikov, M. 2011, The Astrophysical Journal, 730, 30

Ranyard, A. C. 1872, Monthly Notices of the Royal Astronomical Society, 32, 84

—. 1878, The Astronomical Register, 190, 241

Raouafi, N. E., Riley, P., Gibson, S., Fineschi, S., & Solanki, S. K. 2016, Frontiers in Astronomy and Space Sciences, 3, 20

Raymond, J. 1999, Space Sci. Rev., 87, 55

Raymond, J. C., Kohl, J. L., Noci, G., et al. 1997, Solar Physics, 175, 645

Reeves, K. K., Linker, J. A., Mikić, Z., & Forbes, T. G. 2010, Astrophysical Journal, 721, 1547

Reinard, A. 2005, Astrophysical Journal, 620, 501

Reisenfeld, D. B., Burnett, D. S., Becker, R. H., et al. 2007, Space Science Reviews, 130, 79

Richardson, I. G., & Cane, H. V. 1995, Journal of Geophysical Research, 100, 23,397

—. 2004, Journal of Geophysical Research: Space Physics, 109, 9104

—. 2010, Solar Physics, 264, 189

Richardson, I. G., Farrugia, C. J., & Cane, H. V. 1997, Journal of Geophysical Research A: Space Physics, 102, 4691

Rivera, Y. J., Landi, E., & Lepri, S. T. 2019a, The Astrophysical Journal Supplement Series, 243, 34

Rivera, Y. J., Landi, E., Lepri, S. T., & Gilbert, J. A. 2019b, The Astrophysical Journal, 874, 164

—. 2020, The Astrophysical Journal, 899, 11

Robbrecht, E., Berghmans, D., & Van Der Linden, R. A. 2009, Astrophysical Journal, 691, 1222

Russell, C. T., & Neugebauer, M. 1981, Journal of Geophysical Research, 86, 5895

Sabine, C. E. 1852, Philosophical Transactions of the Royal Society of London, 142, 103

Schmahl, E., & Hildner, E. 1977, Solar Physics, 55, 473

Schmelz, J. T., Reames, D. V., Von Steiger, R., & Basu, S. 2012, Astrophysical Journal, 755, 33

Schwadron, N. A. 1998, Journal of Geophysical Research: Space Physics, 103, 20643

Schwadron, N. A., Gloeckler, G., Fisk, L. A., Geiss, J., & Zurbuchen, T. H. 1999in (AIP), 487–490

Sharma, R., & Srivastava, N. 2012, Journal of Space Weather and Space Climate, 2, A10

Sharma, R., Srivastava, N., Chakrabarty, D., M??stl, C., & Hu, Q. 2013, Journal of Geophysical Research: Space Physics, 118, 3954

Shearer, P., von Steiger, R., Raines, J. M., et al. 2014, The Astrophysical Journal, 789, 60

Simon Wedlund, C., Bodewits, D., Alho, M., et al. 2019, Astronomy & Astrophysics, 630, A35

Sittler, E. C., & Burlaga, L. F. 1998, Journal of Geophysical Research, 103, 17447

Sokolov, I. V., van der Holst, B., Oran, R., et al. 2013, The Astrophysical Journal, 764, 23

Song, H. Q., Chen, Y., Li, B., et al. 2017, The Astrophysical Journal, 836, L11

Spicer, D. S., Feldman, U., Widing, K. G., & Rilee, M. 1998, The Astrophysical Journal, 494, 450

Stellmacher, G., & Wiehr, E. 2017, Solar Physics, 292, 83

Stewart, B. 1861, Philosophical Transactions of the Royal Society of London, 151, 423

Stone, E. C., Frandsen, A. M., & Mewaldt, R. A. 1998, Space Science, 86, 1

Strömgren, B., Strömgren, & Bengt. 1933, Zeitschrift für Astrophysik, 7, 222

Susino, R., Bemporad, A., Jejčič, S., & Heinzel, P. 2018, A&A, 617, 21

Taut, A., Berger, L., Drews, C., Physik, A., & Kiel, C.-a.-u. 2015, A&A, 55, 1

Thomas, G. E. 1978, Annual Review of Earth and Planetary Sciences, 6, 173

Tomczyk, S., McIntosh, S. W., Keil, S. L., et al. 2007, Science, 317, 1192

Tomczyk, S., Card, G. L., Darnell, T., et al. 2008, Solar Physics, 247, 411

Tracy, P. J., Kasper, J. C., Raines, J. M., et al. 2016, Physical Review Letters, 116, 255101

Tracy, P. J., Kasper, J. C., Zurbuchen, T. H., et al. 2015, Astrophysical Journal, 812, 170

Tritschler, A., Rimmele, T. R., Berukoff, S., et al. 2016, Astronomische Nachrichten, 337, 1064

Tu, C.-Y., & Marsch, E. 2001, Journal of Geophysical Research: Space Physics, 106, 8233

van der Holst, B., Sokolov, I. V., Meng, X., et al. 2014, The Astrophysical Journal, 782, 81

Vasyliunas, V. M., & Siscoe, G. L. 1976, Journal of Geophysical Research, 81, 1247

von Steiger, R., & Zurbuchen, T. H. 2003, in Solar variability as an input to the Earth's environment, 835–840

von Steiger, R., Schwadron, N. a., Fisk, L. A., et al. 2000, Journal of Geophysical Research, 105, 27217

Webb, D. F., & Howard, T. A. 2012, Living Reviews in Solar Physics, 9, doi:10.12942/lrsp-2012-3

Weizsäcker, C. F. 1935, Zeitschrift für Physik, 96, 431

Widing, K. G., Feldman, U., & Bhatia, A. K. 1986, The Astrophysical Journal, 308, 982

Wiegelmann, T., Thalmann, J. K., & Solanki, S. K. 2014, Astronomy and Astrophysics Review, 22, 1

Wiehr, E., Stellmacher, G., & Bianda, M. 2019, The Astrophysical Journal, 873, 125

Wilhelm, K., Curdt, W., Marsch, E., et al. 1995, Solar Physics, 162, 189

Wimmer-Schweingruber, R. F., & Bochsler, P. 2003, Geophysical Research Letters, 30, doi:10.1029/2002GL015218

Wolf, M. 1852, Monthly Notices of the Royal Astronomical Society, 13, 29

Wood, B. E., Howard, R. A., & Linton, M. G. 2016, The Astrophysical Journal, 816, 67

Zhao, L., Zurbuchen, T. H., & Fisk, L. A. 2009, Geophysical Research Letters, 36, L14104

Zurbuchen, T. H., & Richardson, I. G. 2006, Space Science Reviews, 123, 31

Zurbuchen, T. H., Von Steiger, R., Gruesbeck, J., et al. 2012, Space Science Reviews, 172, 41

Zurbuchen, T. H., Weberg, M., Steiger, R. V., et al. 2016, The Astrophysical Journal, 826, 1